THE UNIVERSITY OF CHICAGO

ATOMIC ENGINEERING OF NANOMATERIALS IN MOLTEN SALTS AND LIQUID METALS

A DISSERTATION SUBMITTED TO

THE FACULTY OF THE DIVISION OF PHYSICAL SCIENCES

IN CANDIDACY FOR THE DEGREE OF

DOCTOR OF PHILOSOPHY

DEPARTMENT OF CHEMISTRY

BY

VLADISLAV KAMYSBAYEV

CHICAGO, ILLINOIS

JUNE 2020

TABLE OF CONTENTS

List of Figures

List of Tables

Acknowledgements

First, I would like to thank my research advisor Prof. Dmitri Talapin for his guidance and support throughout my graduate work. I learned from Dmitri about how to choose a challenging scientific problem, how to assemble necessary resources and how to present data as an engaging and coherent story. I am also in debt to Dmitri for having always pushed me outside of my comfort zone, be it the learning of new skills in the machine shop for building of an experimental setup or becoming an expert in analysis of X-ray diffraction. I would also like to thank my committee members Prof. John Anderson, Prof. Philippe Guyot-Sionnest and Prof. Jiwoong Park. Thank you both for reviewing my thesis and offering helpful comments and also for your advice during these five years.

My journey to becoming an independent scientist would not be possible without the senior student in our lab, Dr. Vishwas Srivastava, and our department crystallographer, Dr. Alexander Filatov. They taught me how to design a "realistic" experiment, maintain and reverse engineer X-ray equipment and gloveboxes and be pragmatic about research. I also thank them for advising me on my future career.

I was honored to collaborate with several excellent scientists during my graduate work. I would like to thank Prof. Yury Gogotsi and Prof. Babak Anasori of Drexel University for sharing their enthusiasm, knowledge and philosophy about MXenes during our collaboration on the metal matrix composite project and scientific conferences. In addition, I would like to thank our theory colleagues Dr. Nick Ludwig and Prof. Suri Vaikuntanathan for their dedicated collaboration on the Nanocrystals in ionic media. I am also grateful to our physics colleagues Dr. Nicole James and Prof. Heinrich Jaeger for their assistance with rheological measurements. In addition, I benefited tremendously by learning advanced X-ray techniques from the leading X-ray scientists at the

Argonne National Laboratory: Dr. Byeongdu Lee, Dr. Olaf Borkeiwicz, Dr. Chengjun Sun and Dr. Jan Ilavsky.

I was very fortunate to work with amazing colleagues in the Talapin lab. I am thankful to my seniors Dr. Michael Boles, Dr. Igor Fedin, Dr. Abhijit Hazarika, Dr. Yuanyuan Wang, Dr. Eric Janke and Dr. Hao Zhang for their advice. Special thanks are due to Dr. Xinzheng Lan and Dr. Margaret Hudson who not only taught me various essential lab skills, but also were the people I could talk to about life and philosophy of research. I would also like to thank everyone in the Talapin lab for their helpful conversations and assistance in lab: Huicheng Hu, Di Wang, Wooje Cho, Jia-Ahn Pan, Joshua Potner, Dr. Himchan Cho, Dr. Igor Coropceanu, Haoqi Wu and Min Chen. Finally, I would like to thank Tanya Shpigel for all that she does to make our lives easier.

I am certain that my success in the graduate school would have not been possible without support of my family. I am grateful to my parents, Liliya and Aidos, and my grandparents, Tanya and Gena, for their unconditional love. Finally, I am so thankful to the friends I made at the University of Chicago: Valerii, Youjin and Andrei. Last but not least, I am infinitely grateful to Polina for her companionship and tremendous support during the most difficult and uncertain times during my time in graduate school.

Abstract

The use of inorganic molten salts and liquid metals as solvents opens up the possibility to synthesize hard-to-crystallize colloidal nanomaterials as well as lower the diffusion barriers in covalent lattices. In this work, we demonstrate how molten inorganic salts and liquid metals can be used to fabricate a new class of ceramic two-dimensional (2D) materials and metal matrix composites, respectively.

We believe that detailed understanding of the solutes' solvation by highly ionized media of inorganic melts is necessary for the rational design of nanomaterials in these unconventional media. Chapter 2 focuses on the detailed analysis of X-ray total scattering patterns of nanocrystals (NCs) as typical solutes in ionic melts. With the aid of molecular dynamics (MD) simulations, we provide evidence for the formation of a layered ionic solvation shell around NCs dispersed in molten inorganic salts and organic ionic liquids. The solvation shell has enhanced ion-ion correlations compared to the ions in the bulk liquid and extends far beyond the Debye screening length. The charge density wave consisting of the restructured ions generates an oscillatory potential between NCs and hence constitutes a fundamentally different mechanism of colloidal stabilization in addition to the standard electrostatic and steric mechanisms.

In Chapter 3, we present versatile chemical transformations of surface functional groups in 2D transition-metal carbides (MXenes) which opens up a new design space for this broad class of functional materials. We introduce a general strategy to install and remove surface groups by performing substitution and elimination reactions in molten inorganic salts. Successful synthesis of MXenes with O, NH, S, Cl, Se, Br, and Te surface terminations, as well as bare MXenes (no surface termination) is demonstrated. These MXenes show distinctive structural and electronic properties. For example, the surface groups control interatomic distances in the MXene lattice, and

$Ti_{n+1}C_n$ (n = 1, 2) MXenes terminated with Te^{2-} ligands show a giant, (> 18%) in-plane lattice expansion compared to the bulk TiC lattice. And in Chapter 4, we show that Nb_2C MXenes synthesized in molten inorganic salts exhibit surface-group-dependent superconductivity.

In Chapter 5, we focus on liquid metals as the nanomaterials' dispersion media. For example, MXenes can be efficiently dispersed in liquid Ga and lightweight alloys of Al, Mg, Li. We show that the Lifshitz theory predicts strong van der Waals attraction between nanoscale objects interacting through liquid metals. However, a uniform distribution of MXenes in liquid metals can be achieved through colloidal gelation, where particles form self-supporting networks stable against macroscopic phase segregation. By choosing Mg-Li alloy as an example of ultra-lightweight metal matrix and $Ti_3C_2T_x$ MXene as a nanoscale reinforcement, we apply liquid metal gelation technique to fabricate functional nanocomposites with up to 57 % increase in the specific yield strength without compromising the matrix alloy's plasticity. This work expands applications for MXenes and shows the potential for developing MXene-reinforced metal matrix composites for structural alloys and other emerging applications with metal-MXene interfaces, such as batteries and supercapacitors.

1 Introduction to engineering nanomaterials in molten salts and liquid metals

1.1 Beyond "traditional solvents" for nanomaterials.

A wide variety of nanomaterials such as semiconductor quantum dots (QDs),[1] oxide[2] and metal[3] NCs can be synthesized in a precise manner in either organic or aqueous media. However, our ability to synthesize many hard-to-crystallize inorganic phases in a nanocrystalline form is limited by the inability of currently available solvents to reach desired crystallization temperatures.[4-5] Very few traditional solvents remain liquid and stable above 400 °C, but many inorganic phases require even higher temperatures to form and anneal out structural defects.[4]. The exploration of unconventional solvents systems and understanding their interaction with the NC surface is therefore essential for synthetic development of next-generation inorganic nanomaterials.

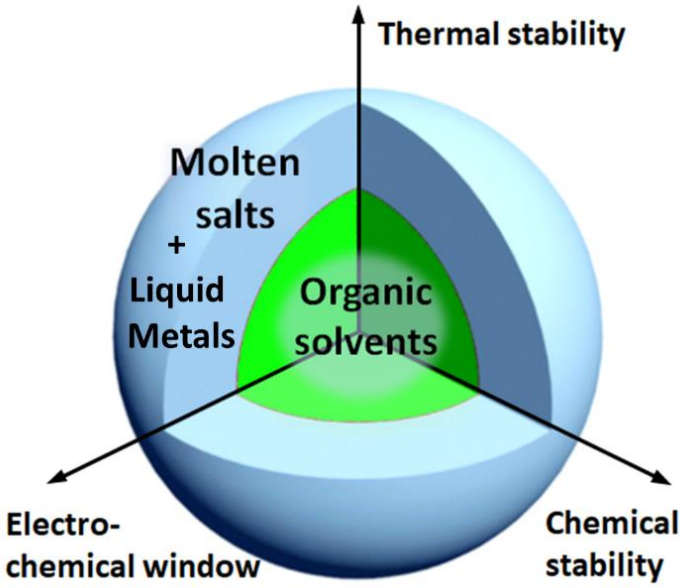

Figure 1.1. Justification for using molten salts and liquid metals for colloidal and flux syntheses of low-dimensional materials.

Our group recently reported on the formation of colloidal solutions of NCs dispersed in molten inorganic salts.[6] Molten inorganic salts represent a very attractive class of solvents for the synthesis and processing of nanomaterials due to their high temperature stability, wide electrochemical window, stability in the presence of highly reactive species, the ability to dissolve many ionic solids not soluble in traditional solvents, and transparency in a broad range of the electromagnetic spectrum (Figure 1.1).[6-7] Molten inorganic salts have long been used as inert or reactive fluxes for solid-state chemistry,[8] crystal growth,[9-10] and electrolysis of refractory metals.[11-12] Molten salt fluxes have been explored for the synthesis of nanostructured oxides, metal alloy NCs,[13] and covalent compounds (metal boride,[14] SiC,[15] Si,[16-17] graphene,[18] carbon nanotubes[19]). Colloidal stability is a critical requirement for precise synthesis and chemical manipulations of nanomaterials at high temperatures.

Liquid metals form another class of solvents that has been traditionally explored in the high temperature synthesis of intermetallic compounds[20] and semiconductors.[21] In addition to serving as flux media, liquid metals with homogeneously dispersed nanostructures can be used to fabricate metal matrix composites (MMCs) where mechanical properties of soft metal matrix are enhanced by the presence of hard ceramic particles. Uniform distribution of particles in liquid metal media is an essential prerequisite towards uniform MMCs with superior mechanical properties.

1.2 Mechanism of Nanocrystals' colloidal stabilization in ionic media.

The stability of NCs in ionic media cannot be explained by traditional electrostatic and steric mechanisms. A very high charge density of molten salt results in the Debye screening length, L_D, which is only ~ 1 Å. Such extremely short-ranged screening makes electrostatic stabilization in the classical sense impossible, while the absence of long chain ligands on the NC surfaces

eliminates the possibility of steric stabilization. Screening many solute–solvent combinations shows that colloidal stability can be traced to the strength of chemical bonding at the solute–solvent interface (Figure 1.2).[6] Chemical affinity of the NC surface to salt ions is necessary for colloidal stability. Empirically, it was observed that molten salts with ions which were able to function as X- or Z-type ligands to the nanoparticle surface were able to stabilize them. For example, halides are X-type ligands (Lewis basic) whereas $AlCl_3$ belongs to the category of Z-type ligands (Lewis acidic). $AlCl_4^-$ and BF_4^- are Lewis neutral and thus the associated ionic solvents were not able to stabilize NCs (Figure 1.2).

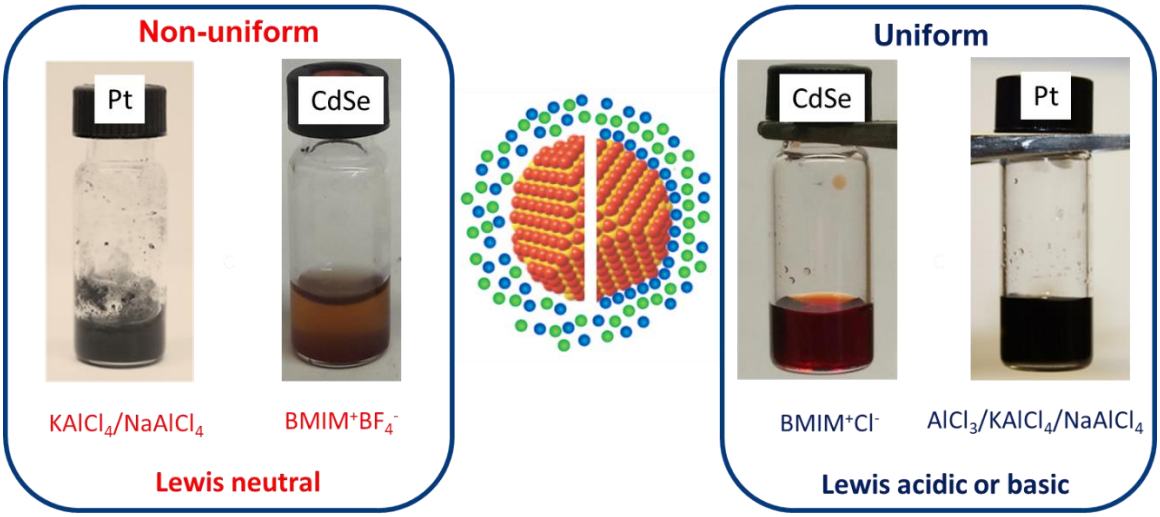

Figure 1.2. Phenomenological understanding of NCs' interaction with ionic media.
Representative photographs of NC colloids in molten salts and ionic liquids. BMIM stands for 1-butyl-3-methylimidazolium.

MD simulations of the interface between the CdSe crystal and molten KCl, provides an insight into the interaction of colloidal NCs with molten salts.[6] Figure 1.3 shows the modeled equilibrium structure of molten salt near the crystal surface and oscillatory density profiles of cations and anions in molten salt. MD simulations show how chemical properties of the NC surface translate into the layering and orientation order of molten salt around NCs, which result in long-

ranged charge density oscillations in molten salt around solute particles. For two spheroid NCs, the surface-templated charge density oscillations can interfere constructively or destructively, depending on the interparticle distance, which leads to an exponentially decaying oscillatory interaction energy. The phenomenological Ginsburg-Landau theory predicts existence of the repulsive-oscillatory potential of ion structuring which by far exceeds both the van der Waals and double-layer electrostatic contributions at 1 to 10 Å of interparticle separations.[6] As a result, the charge density wave generated by the NC surface can easily screen the van der Waals attraction and hence account for the colloidally stable dispersions in molten salts.

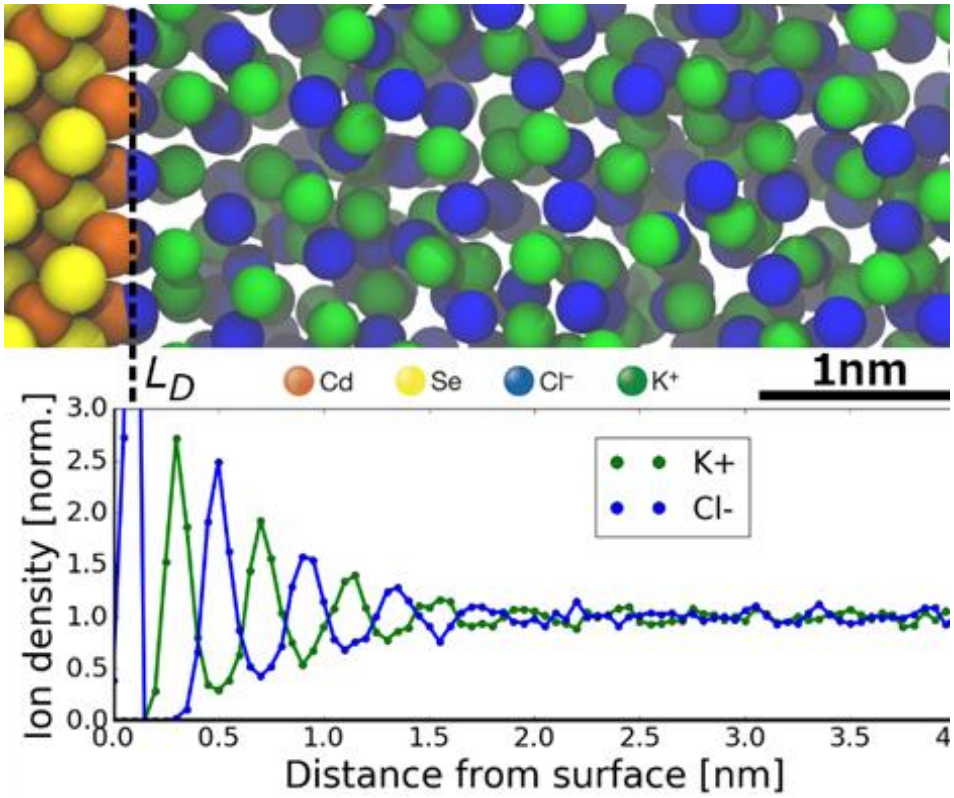

Figure 1.3. A snapshot of an MD simulation of the interface between a zinc-blende CdSe crystal surface and molten KCl.
Density profiles of K^+ and Cl^- ions showing structuring of molten salt near the Cd-terminated (100) CdSe surface. The crystal surface templates strong ordering of the molten salt. Adapted with permission from H. Zhang *et. al. Nature* **2017**, *542,* 328, copyright Springer Nature 2017.[6]

1.3 Improving optical properties of III-V Nanocrystals in molten salts.

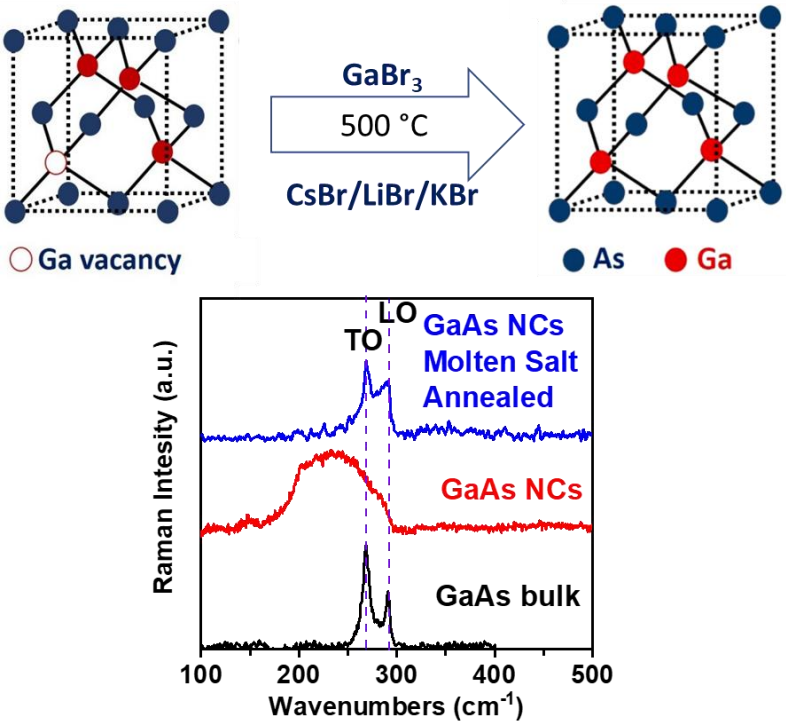

Figure 1.4. Curing Defects in colloidal GaAs NCs.
Adapted with permission from V. Srivastava *et. al. Nano Lett* **2017**, *17*, 2094.[4] Copyright 2017 American Chemical Society.

The ability to engineer interactions between the NC surface and the molten inorganic salt helps performing precise chemical manipulations on the NCs. One such example is the curing of defects in colloidal GaAs NCs. GaAs is arguably the most important member of the III−V semiconductor family due to its excellent electronic and opticalproperties.[22] The direct band gap (1.42 eV at 300 K), high electron mobility and saturation electron velocity, and reliable p-type and n-type doping make GaAs a material of choice for top-performing solar cells,[23] transistors, lasers, and LEDs.[24] However, as-synthesized GaAs NCs contain Ga vacancy defects which prevent these NCs from exhibiting size dependent excitonic properties typical for other classes of III-V QDs.[4] The structural defects in colloidal GaAs NCs can be alleviated by annealing the as-synthesized

NCs in alkali halide molten salts with the addition of Ga^{3+} cations. The Raman spectrum of the molten salt annealed NCs exhibited characteristic GaAs TO and LO phonon modes as well as complete disappearance of the disorder-related broad Raman feature (Figure 1.4). At the same time, the molten salt annealed GaAs NCs preserved their tight size distribution and for the first time exhibited size-dependent excitonic features in the steady state absorption spectrum.[4]

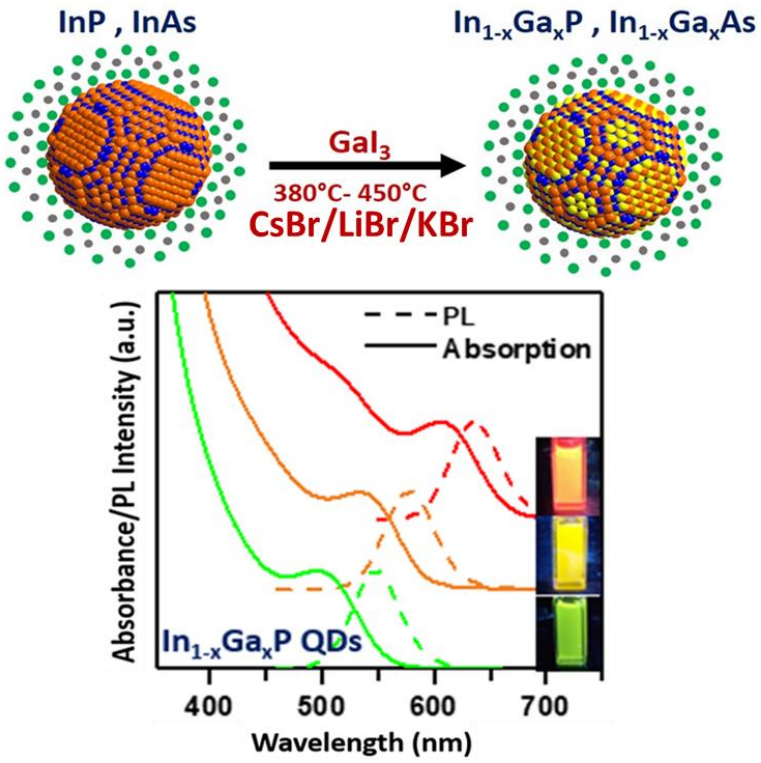

Figure 1.5. Ternary alloys of InP and InAs NCs *via* cation exchange in molten inorganic salts. Adapted with permission from V. Srivastava *et. al. J. Am. Chem. Soc.* **2018**, *140*, 12144.[25] Copyright 2018 American Chemical Society.

Another example of successful utilization of molten inorganic salts is related to the synthesis of colloidal ternary III-V NCs (Figure 1.5).[25] Ga-containing ternary III−V QDs, e.g., $In_{1-x}Ga_xP$ and $In_{1-x}Ga_xAs$ ($x \leq 1$), are technologically important compounds due to the flexibility they offer in terms of band gap and lattice constant engineering. For example, $In_{1-x}Ga_xP$ nanoparticles emitting green light are expected to be superior to their InP counterparts due to their

larger size and correspondingly larger absorption cross sections and smaller surface to volume ratio. However due to the low diffusivity of cations in covalent III-V lattices, even thermodynamically favorable cation exchange reactions in III-V NCs require high temperatures to overcome the diffusion barriers.[26] The ability to disperse colloidal NCs in molten salts offers us the unique possibility of performing precise chemical manipulations on them at high temperatures. The resultant ternary III−V NCs show absorption and emission features that are blue shifted in comparison to the starting materials, in line with the expected change in band gap upon homogeneous alloying with Ga^{3+} (Figure 1.5).

1.4 MXenes overview.

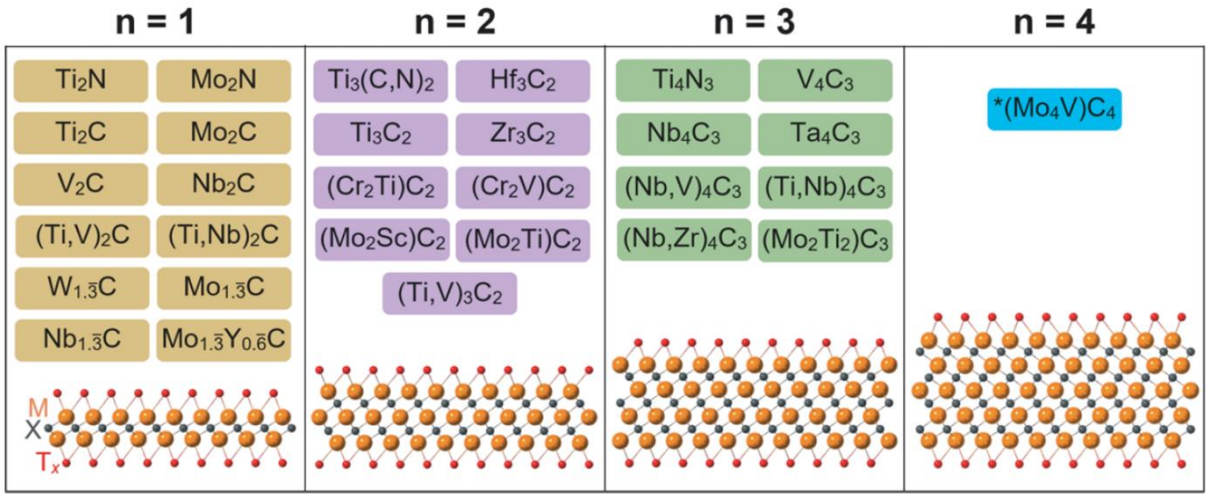

Figure 1.6. Experimentally synthesized MXenes reported to date.
Most MXenes have been synthesized by etching the parent MAX phases in concentrated aqueous HF solutions. Reproduced with permission from Deysher, G. et al. *ACS Nano* **2020,** *14*, 204. Copyright 2020 American Chemical Society.[27]

Early transition metal carbides and nitrides (MXenes) are 2D ceramic sheets. To date, MXenes represent the most diverse class of 2D materials (Figure 1.6). They have found applications in

supercapacitors,[28] batteries,[29] electromagnetic interference shielding,[30] composites,[31-32] and catalysts.[33] MXenes have the unit formula of $M_{n+1}X_nT_x$ where M stands for the early transition metal, X is C or N, *n* is an integer from 1 to 4 (Figure 1.6) and T_x are mixed surface terminations. MXenes are derived from the parent MAX phases by selectively etching the main group element A (e.g. Al, Ga, Si, *etc*.). The etching is usually performed in HF solutions resulting in MXenes terminated with a mixture of F, O, and OH functional groups (T_x). T_x surface groups render MXenes colloidally stable in various polar solvents in the form of single-layer flakes. These "inks" of delaminated 2D ceramic sheets open up the possibility to further process MXenes as thin films for electrochromic devices[34] or binder free 3D macrostructures for fiber-shaped supercapacitros.[35] However, better synthetic control over surface terminations is expected to impact nearly every physical property of MXenes thus potentially enabling new functionalities.[36]

Traditional colloidal NCs such as semiconductor QDs have achieved tremendous progress in terms of the diversity of organic and inorganic ligands that could be anchored on their surfaces.[37] The "toolkit" of surface ligands has made it possible to utilize NCs in the design of low-cost solution processable electronic and optoelectronic devices.[38] Selective surface functionalization of MXene with surface terminations as diverse as that available for solution processable NCs has not been demonstrated yet.

Electrochemical and hydrothermal methods have been recently applied for etching MAX phases without resorting to HF, but the use of aqueous solutions introduces a mixture of Cl, O, and OH surface groups.[39-40] Although there has been some progress in etching MAX phases in non-aqueous solutions containing NH_4HF_2 salt with the resultant MXene flakes rich in F terminations,[41] strong M-O and M-F bonds make it difficult to perform any postsynthetic covalent surface modifications of MXenes.

Because MAX phases and multilayer MXene stacks are present as extended 3D solids, the diffusion of ions and molecular species in between $M_{n+1}X_n$ layers is highly hindered at near ambient conditions. As a result, the ability to perform etching and exchange reactions at elevated temperatures could be a key to overcome the diffusion barriers and ultimately enable atomic engineering of MXenes beyond O, OH and F terminations. Due to their high temperature stability and processability, molten inorganic salts could potentially address the issue of water, oxygen and fluorine free etching of MAX phases and subsequent surface functionalization of MXenes.

1.5 Metal matrix composites enabled by liquid metals.

Nanomaterials dispersed in different media, such as liquids or polymers, generate a variety of functional composites with synergistic properties. Composites of nanostructures embedded in a second phase (matrix) enable emerging functionalities due to strong coupling between optical, electronic and mechanical properties.[42] Nanostructures in glasses and polymers have found applications in smart windows,[43] electromagnetic interference shielding[30] and energy storage.[44] Metallurgists combine nanostructures with metals to prepare metal-matrix composites (MMCs) with enhanced mechanical properties. The major challenge in fabrication of functional MMCs is the uniform distribution of ceramic particles. In addition, strong interfacial bonding between metal matrix and the nanostructures is required as well.[45] Although mixing of ceramic particles in solid state and metals in liquid state results in stronger bonding between the components,[46] phase segregation of particles in liquid metals usually cannot be avoided. Hence in order to prepare uniform MMCs using the liquid metal route, it is paramount to understand the fundamental forces governing the aggregation of particles in liquid metal media. Strong covalent bonding between M

and X atoms and surface group tunability make MXenes ideal candidates for exploring colloidal interactions inside liquid metals relevant for fabrication of functional MMCs.

1.6 Thesis motivation.

The generality of colloids composed of inorganic particles in inorganic melts offers opportunities for introducing colloidal techniques to various branches of solid-state science and engineering. In this thesis I first show experimentally that the interaction between the NC surfaces and molten salts leads to restructuring of ions around solutes. In order to probe the local structure of salts around colloidal NCs, I present a detailed investigation of NC dispersions in molten salts and ionic liquids using small-angle X-ray scattering (SAXS), atomic pair distribution function (PDF) analysis and molecular dynamics (MD) simulations. By using a combination of PDF analysis of X-ray total scattering and molecular modeling, I demonstrate that the NC surface induces a solvent restructuring with electrostatic correlations extending an order of magnitude beyond the Debye screening length. These strong oscillatory ion–ion correlations, which are not accounted by the traditional mechanisms of steric and electrostatic stabilization of colloids, offer additional insight into solvent–solute interactions and enable apparently "impossible" colloidal stabilization in highly ionized media.

I further explore the utility of molten salts as solvents for achieving precise surface functionalization of MXene multilayer stacks. I show the generality of this approach by successfully synthesizing MXenes with O, NH, S, Cl, Se, Br, and Te surface terminations, as well as bare MXenes (no surface terminations). The newly synthesized MXenes show unusual structural properties such as biaxial straining imposed by the surface groups. I further demonstrate how the surface groups affect electronic transport in multilayer Nb_2CT_n MXenes and for the first

time lead to observation of bulk superconductivity in MXenes. In the final section, I focus on liquid metals as the particle dispersion media. I show that liquid metals cannot support colloidal stabilization of ceramic NCs. I develop an alternative approach to uniformly disperse NCs in liquid metals based on colloidal gelation. I demonstrate the successful utilization of this new approach in fabrication of uniform composites of Mg-Li lightweight alloy and $Ti_3C_2T_x$ MXenes with superior mechanical properties compared to the base alloy.

1.7 Chapter 1 bibliography.

1. Murray, C. B.; Norris, D. J.; Bawendi, M. G., Synthesis and characterization of nearly monodisperse CdE (E = sulfur, selenium, tellurium) semiconductor nanocrystallites. *J. Am. Chem. Soc.* **1993,** *115* (19), 8706-8715.

2. Park, J.; An, K.; Hwang, Y.; Park, J.-G.; Noh, H.-J.; Kim, J.-Y.; Park, J.-H.; Hwang, N.-M.; Hyeon, T., Ultra-large-scale syntheses of monodisperse nanocrystals. *Nat. Mater.* **2004,** *3*, 891.

3. Sun, S.; Murray, C. B.; Weller, D.; Folks, L.; Moser, A., Monodisperse FePt Nanoparticles and Ferromagnetic FePt Nanocrystal Superlattices. *Science* **2000,** *287* (5460), 1989-1992.

4. Srivastava, V.; Liu, W.; Janke, E. M.; Kamysbayev, V.; Filatov, A. S.; Sun, C.-J.; Lee, B.; Rajh, T.; Schaller, R. D.; Talapin, D. V., Understanding and Curing Structural Defects in Colloidal GaAs Nanocrystals. *Nano Lett.* **2017,** *17* (3), 2094-2101.

5. Kanady, J. S.; Leidinger, P.; Haas, A.; Titlbach, S.; Schunk, S.; Schierle-Arndt, K.; Crumlin, E. J.; Wu, C. H.; Alivisatos, A. P., Synthesis of Pt3Y and Other Early–Late Intermetallic Nanoparticles by Way of a Molten Reducing Agent. *J. Am. Chem. Soc.* **2017,** *139* (16), 5672-5675.

6. Zhang, H.; Dasbiswas, K.; Ludwig, N. B.; Han, G.; Lee, B.; Vaikuntanathan, S.; Talapin, D. V., Stable colloids in molten inorganic salts. *Nature* **2017,** *542*, 328.

7. Liu, X.; Fechler, N.; Antonietti, M., Salt melt synthesis of ceramics, semiconductors and carbon nanostructures. *Chem. Soc. Rev.* **2013,** *42* (21), 8237-8265.

8. Sundermeyer, W., Fused salts and their use as reaction media. *Angew. Chem., Int. Ed. Engl.* **1965,** *4* (3), 222–238.

9. Volkov, S. V., Chemical reactions in molten salts and their classification. *Chem. Soc. Rev.* **1990,** *19* (1), 21–28.

10. Kerridge, D. H., Recent advances in molten salts as reaction media. *Pure Appl. Chem.* **1975,** *41* (3), 355–371.

11. Chen, G. Z.; Fray, D. J.; Farthing, T. W., Direct electrochemical reduction of titanium dioxide to titanium in molten calcium chloride. *Nature* **2000,** *407* (6802), 361–364.

12. Nohira, T.; Yasuda, K.; Ito, Y., Pinpoint and bulk electrochemical reduction of insulating silicon dioxide to silicon. *Nat. Mater.* **2003,** *2* (6), 397–401.

13. Cui, Z.; Chen, H.; Zhao, M.; Marshall, D.; Yu, Y.; Abruña, H.; DiSalvo, F. J., Synthesis of Structurally Ordered Pt3Ti and Pt3V Nanoparticles as Methanol Oxidation Catalysts. *J. Am. Chem. Soc.* **2014,** *136* (29), 10206-10209.

14. Portehault, D.; Devi, S.; Beaunier, P.; Gervais, C.; Giordano, C.; Sanchez, C.; Antonietti, M., A General Solution Route toward Metal Boride Nanocrystals. *Angew. Chem., Int. Ed.* **2011,** *50* (14), 3262-3265.

15. Liu, X.; Antonietti, M.; Giordano, C., Manipulation of Phase and Microstructure at Nanoscale for SiC in Molten Salt Synthesis. *Chem. Mater.* **2013,** *25* (10), 2021-2027.

16. Liu, X.; Giordano, C.; Antonietti, M., A molten-salt route for synthesis of Si and Ge nanoparticles: chemical reduction of oxides by electrons solvated in salt melt. *J. Mater. Chem.* **2012,** *22* (12), 5454–5459.

17. Shavel, A.; Guerrini, L.; Alvarez-Puebla, R. A., Colloidal synthesis of silicon nanoparticles in molten salts. *Nanoscale* **2017,** *9* (24), 8157-8163.

18. Liu, X.; Giordano, C.; Antonietti, M., A facile molten-salt route to graphene synthesis. *Small* **2014,** *10* (1), 193–200.

19. Schwandt, C.; Dimitrov, A. T.; Fray, D. J., High-yield synthesis of multi-walled carbon nanotubes from graphite by molten salt electrolysis. *Carbon* **2012,** *50* (3), 1311–1315.

20. Kanatzidis, M. G.; Pöttgen, R.; Jeitschko, W., The Metal Flux: A Preparative Tool for the Exploration of Intermetallic Compounds. *Angew. Chem., Int. Ed.* **2005,** *44* (43), 6996-7023.

21. Kubota, Y.; Watanabe, K.; Tsuda, O.; Taniguchi, T., Deep Ultraviolet Light-Emitting Hexagonal Boron Nitride Synthesized at Atmospheric Pressure. *Science* **2007,** *317* (5840), 932-934.

22. Adachi, S., *Properties of Semiconductor Alloys: Group-IV, III-V and II-VI Semiconductors*. John Wiley & Sons: West Sussex, U.K., 2009; Vol. 28.

23. Kayes, B. M.; Nie, H.; Twist, R.; Spruytte, S. G.; Reinhardt, F.; Kizilyalli, I. C.; Higashi, G. S. In *27.6% Conversion efficiency, a new record for single-junction solar cells under 1 sun illumination*, 2011 37th IEEE Photovoltaic Specialists Conference, 19-24 June 2011; 2011; pp 000004-000008.

24. Hall, R. N.; Fenner, G. E.; Kingsley, J. D.; Soltys, T. J.; Carlson, R. O., Coherent Light Emission From GaAs Junctions. *Phys. Rev. Lett.* **1962,** *9* (9), 366-368.

25. Srivastava, V.; Kamysbayev, V.; Hong, L.; Dunietz, E.; Klie, R. F.; Talapin, D. V., Colloidal Chemistry in Molten Salts: Synthesis of Luminescent In1- xGa xP and In1- xGa xAs Quantum Dots. *J. Am. Chem. Soc.* **2018,** *140* (38), 12144-12151.

26. Shaw, D., *Atomic diffusion in semiconductors*. Springer Science & Business Media: 2012.

27. Deysher, G.; Shuck, C. E.; Hantanasirisakul, K.; Frey, N. C.; Foucher, A. C.; Maleski, K.; Sarycheva, A.; Shenoy, V. B.; Stach, E. A.; Anasori, B.; Gogotsi, Y., Synthesis of Mo4VAlC4

MAX Phase and Two-Dimensional Mo4VC4 MXene with Five Atomic Layers of Transition Metals. *ACS Nano* **2020,** *14* (1), 204-217.

28. Xia, Y.; Mathis, T. S.; Zhao, M.-Q.; Anasori, B.; Dang, A.; Zhou, Z.; Cho, H.; Gogotsi, Y.; Yang, S., Thickness-independent capacitance of vertically aligned liquid-crystalline MXenes. *Nature* **2018,** *557* (7705), 409-412.

29. Zhang, C.; Park, S.-H.; Seral-Ascaso, A.; Barwich, S.; McEvoy, N.; Boland, C. S.; Coleman, J. N.; Gogotsi, Y.; Nicolosi, V., High capacity silicon anodes enabled by MXene viscous aqueous ink. *Nat. Commun.* **2019,** *10* (1), 849.

30. Shahzad, F.; Alhabeb, M.; Hatter, C. B.; Anasori, B.; Man Hong, S.; Koo, C. M.; Gogotsi, Y., Electromagnetic interference shielding with 2D transition metal carbides (MXenes). *Science* **2016,** *353* (6304), 1137-1140.

31. Kamysbayev, V.; James, N. M.; Filatov, A. S.; Srivastava, V.; Anasori, B.; Jaeger, H. M.; Gogotsi, Y.; Talapin, D. V., Colloidal Gelation in Liquid Metals Enables Functional Nanocomposites of 2D Metal Carbides (MXenes) and Lightweight Metals. *ACS Nano* **2019**.

32. Guo, J.; Legum, B.; Anasori, B.; Wang, K.; Lelyukh, P.; Gogotsi, Y.; Randall, C. A., Cold Sintered Ceramic Nanocomposites of 2D MXene and Zinc Oxide. *Adv. Mater.* **2018,** *30* (32), 1801846.

33. Zhang, J.; Zhao, Y.; Guo, X.; Chen, C.; Dong, C.-L.; Liu, R.-S.; Han, C.-P.; Li, Y.; Gogotsi, Y.; Wang, G., Single platinum atoms immobilized on an MXene as an efficient catalyst for the hydrogen evolution reaction. *Nature Catalysis* **2018,** *1* (12), 985-992.

34. Salles, P.; Pinto, D.; Hantanasirisakul, K.; Maleski, K.; Shuck, C. E.; Gogotsi, Y., Electrochromic Effect in Titanium Carbide MXene Thin Films Produced by Dip-Coating. *Adv. Funct. Mater.* **2019,** *29* (17), 1809223.

35. Zhang, J.; Uzun, S.; Seyedin, S.; Lynch, P. A.; Akuzum, B.; Wang, Z.; Qin, S.; Alhabeb, M.; Shuck, C. E.; Lei, W.; Kumbur, E. C.; Yang, W.; Wang, X.; Dion, G.; Razal, J. M.; Gogotsi, Y., Additive-Free MXene Liquid Crystals and Fibers. *ACS Central Science* **2020,** *6* (2), 254-265.

36. Anasori, B.; Lukatskaya, M. R.; Gogotsi, Y., 2D metal carbides and nitrides (MXenes) for energy storage. *Nature Reviews Materials* **2017,** *2*, 16098.

37. Boles, M. A.; Ling, D.; Hyeon, T.; Talapin, D. V., The surface science of nanocrystals. *Nat. Mater.* **2016,** *15*, 141.

38. Kagan, C. R.; Lifshitz, E.; Sargent, E. H.; Talapin, D. V., Building devices from colloidal quantum dots. *Science* **2016,** *353* (6302), aac5523.

39. Pang, S.-Y.; Wong, Y.-T.; Yuan, S.; Liu, Y.; Tsang, M.-K.; Yang, Z.; Huang, H.; Wong, W.-T.; Hao, J., Universal Strategy for HF-Free Facile and Rapid Synthesis of Two-dimensional MXenes as Multifunctional Energy Materials. *J. Am. Chem. Soc.* **2019,** *141* (24), 9610-9616.

40. Li, T.; Yao, L.; Liu, Q.; Gu, J.; Luo, R.; Li, J.; Yan, X.; Wang, W.; Liu, P.; Chen, B.; Zhang, W.; Abbas, W.; Naz, R.; Zhang, D., Fluorine-Free Synthesis of High-Purity Ti3C2Tx (T=OH, O) via Alkali Treatment. *Angew. Chem., Int. Ed.* **2018,** *57* (21), 6115-6119.

41. Natu, V.; Pai, R.; Sokol, M.; Carey, M.; Kalra, V.; Barsoum, M. W., 2D Ti3C2Tz MXene Synthesized by Water-free Etching of Ti3AlC2 in Polar Organic Solvents. *Chem* **2020,** *6* (3), 616-630.

42. Begley, M. R.; Gianola, D. S.; Ray, T. R., Bridging functional nanocomposites to robust macroscale devices. *Science* **2019,** *364* (6447), eaav4299.

43. Llordés, A.; Garcia, G.; Gazquez, J.; Milliron, D. J., Tunable near-infrared and visible-light transmittance in nanocrystal-in-glass composites. *Nature* **2013,** *500*, 323.

44. Luo, S.; Yu, J.; Yu, S.; Sun, R.; Cao, L.; Liao, W.-H.; Wong, C.-P., Significantly Enhanced Electrostatic Energy Storage Performance of Flexible Polymer Composites by Introducing Highly Insulating-Ferroelectric Microhybrids as Fillers. *Advanced Energy Materials* **2019,** *9* (5), 1803204.

45. Casati, R.; Vedani, M., Metal Matrix Composites Reinforced by Nano-Particles—A Review. *Metals* **2014,** *4* (1), 65.

46. Chen, L.-Y.; Xu, J.-Q.; Choi, H.; Pozuelo, M.; Ma, X.; Bhowmick, S.; Yang, J.-M.; Mathaudhu, S.; Li, X.-C., Processing and properties of magnesium containing a dense uniform dispersion of nanoparticles. *Nature* **2015,** *528*, 539.

2 Nanocrystals in molten salts and ionic liquids

2.1 Introduction to colloidal stability of Nanocrystals.

The colloidal state is realized by preventing irreversible aggregation of solute particles dispersed in a solvent. A "good" solvent inhibits the aggregation and disperses particles forming a stable colloidal solution. Traditionally, long chain hydrocarbons with a surface-binding head group have been employed as ligands to disperse NCs in non-polar organic solvents.[2] The basis for this type of stabilization (steric) is the minimization of the free energy associated with the chain-solvent mixing,[3] which is accomplished by the repulsion of hydrocarbon chains tethered to the surface of NCs.[4] A fundamentally different way to provide colloidal stability to NCs is through electrostatic effects, where charged groups are adsorbed on the NCs' surface and their charge is balanced by a diffuse cloud of counterions.[4] In this case, a good solvent is one with a high dielectric constant that can effectively screen the electrostatic attraction between oppositely charged surface-bound and dispersed ions.[3] Combined together, these two mechanisms complement each other in providing colloidal stability in a wide variety of solvents.

The stability of NCs in molten inorganic solvents has to be explained by a mechanism fundamentally different from traditional steric and electrostatic approaches. A very high charge density of molten salt results in the Debye screening length $L_D = 1/\sqrt{4\pi\rho q^2/\epsilon k_B T}$ (ρ is the ion concentration per unit volume, q is the unit charge, ε is the dielectric constant, k_BT is the thermal energy), which is only ~ 1 Å. Such extremely short-ranged screening makes electrostatic stabilization in the classical sense impossible, while the absence of long chain ligands on the NC surfaces eliminates the possibility of steric stabilization. Empirically, we found that only specific

salts with pronounced chemical affinity for the nanoparticle's surface were able to impart colloidal stability.[5] It was observed that molten salts with ions which were able to function as X- or Z-type ligands to the nanoparticle surface were able to stabilize them. Both halides and SCN^- are examples of X-type ligands (Lewis basic) whereas $AlCl_3$ belongs to the category of Z-type ligands (Lewis acidic).

Organic ionic liquids (ILs), a cousin of molten inorganic salts, were also found to provide colloidal stability to a variety of inorganic NCs. ILs with pronounced Lewis basicity but limited steric bulk, such as those belonging to the class of 1-butyl-3-methylimidazolium halides ($BMIM^+X^-$) formed stable dispersions of CdSe NCs where $X^- = Cl^-, Br^-, I^-$ but did not support any colloidal stability when $X^- = BF_4^-$.

Based on the recent direct force-distance measurements using Surface Force Apparatus, interactions between charged surfaces in aprotic organic ILs consist of the short-range oscillatory and long-range electrostatic components.[6-7] While the origin of the long-range repulsion is a subject of active experimental and theoretical studies,[8-10] the short-range oscillatory interaction is believed to be due to the ion layering near the surfaces. Experimentally, such structural changes of ionic solvents next to flat surfaces have been verified by X-ray reflectivity,[11] angle-resolved X-ray photoelectron spectroscopy (XPS)[12] and sum-frequency generation spectroscopy.[13] However, these surface sensitive techniques are not suitable for studying colloidal solutions. Recently X-ray pair distribution function (PDF) analysis has been successfully applied to study re-organization of molecular solvents around colloidal particles[14-15] and ILs confined inside carbon nanopores.[16]

Here, we report an experimental observation of enhanced layering of ions in the molten salt around colloidal NCs revealed by the PDF analysis of X-ray total scattering data. Such restructuring of the solvent is templated by the layer of surface-bound ions and responsible for the

formation of non-interacting colloids or, in some cases, weakly aggregated structures that do not precipitate, as evidenced by small-angle X-ray scattering (SAXS) measurements.

2.2 In-situ SAXS study of Nanocrystals in molten salts and ionic liquids.

An inorganic molten salt or IL with a pronounced Lewis acidic or Lewis basic character can be used to colloidally stabilize NCs of metals (Pt), oxides (ZrO_2) and binary semiconductors (CdSe, InP, InAs). We chose molten eutectics of $AlCl_3$/NaCl/KCl ($AlCl_3/AlCl_4^-$) and NaSCN/KSCN as representatives of salts with Lewis acidic and Lewis basic character, respectively. We also studied NC dispersions in $BMIM^+X^-$ (where X=Cl, Br, I) ILs which represent the organic analog of inorganic molten salts. In case of NaSCN/KSCN molten salt, NCs were first stripped of their original organic ligands and the dried NC powders were stirred in the molten salt for several hours until uniform dispersion was formed. In case of $AlCl_3/AlCl_4^-$ molten salt and $BMIM^+X^-$ ILs, NCs could phase transfer directly from the organic phase after interfacing it with the respective ionic media. A concentration of ~ 1 mg/ml NCs in molten salts and ILs was used for all experiments, unless specified otherwise. A complete list of NCs and molten salt combinations explored in this work is provided in Table 2.1.

Representative photographs of NC dispersions in ionic solvents are shown in Figure 2.1. The NCs retained their morphology as evidenced by TEM images taken before and after their dispersion in the molten salt (Figures 2.1B, C). Our choice of solvents was motivated by the following: (i) low melting points (97 °C for $AlCl_3/AlCl_4^-$ and 140 °C for NaSCN/KSCN and ~73 °C for $BMIM^+Cl^-$) for easy handling; (ii) sufficient transmission of X-rays for simultaneous SAXS and X-ray total scattering experiments; and (iii) chemical affinity of the molten salt to NC surfaces, as previously reported for halide-, halometallate- and SCN^- ions.[17-19]

Table 2.1. Summary of the experimental details of the ionic solutions of NCs used in this study.

Ionic solvent	NCs	m.p.	Preparation temperature	Temperature during in-situ X-ray measurement
$AlCl_3$/NaCl/KCl ($AlCl_3$/$AlCl_4^-$ eutectic)	Pt	90°C	150°C	140°C
NaSCN/KSCN (eutectic)	Pt, Pd, CdSe/CdS core-shell, InP, ZrO_2	140°C	250°C	200°C
$BMIM^+Cl^-$	Pt, CdSe, InP, InAs	73°C	100°C	100°C
$BMIM^+Br^-$	CdSe	65°C	100°C	100°C
$BMIM^+I^-$	CdSe, InAs	<R.T.	50°C	50°C

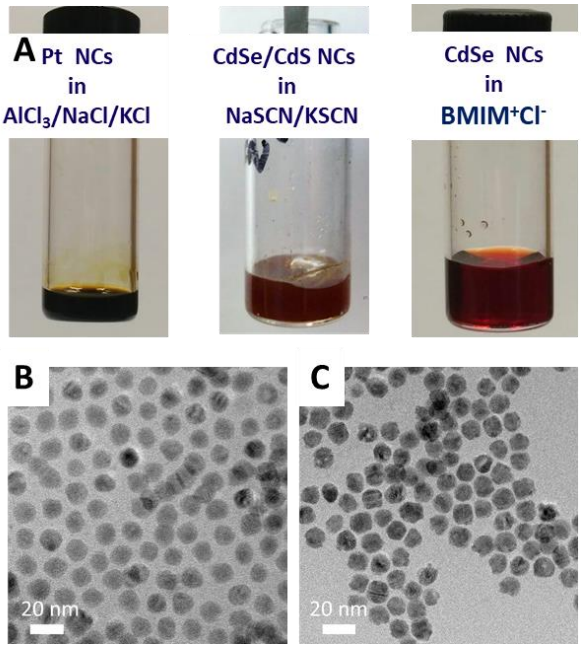

Figure 2.1. Photographs of NC colloids in ionic media.
Representative photographs of NC colloids in molten salts and ionic liquids. (B, C) TEM images of CdSe/CdS NCs (B) before dispersing in molten NaSCN/KSCN eutectic and (C) after their recovery from NaSCN/KSCN eutectic and functionalization with organic ligands.

A representative SAXS curve of Pt NCs in molten $AlCl_3/AlCl_4^-$ is shown in Figure 2.2A. The SAXS curve for the same Pt NCs in toluene is shown for comparison. In case of SAXS from NCs, it is common to assume that the scattering intensity, $I(q)$, is a product of the two terms (decoupling approximation), the form factor, $F(q)$, which defines particle shape and size polydispersity, and the structure factor, $S(q)$, which carries the information about organization and interactions between NCs: $I(q) = |F(q)|^2 S(q)$.[20] The fitting of the experimental data yielded $S(q)$ ~ 1 for Pt NCs in molten $AlCl_3/AlCl_4^-$ (Figure 2.3) meaning that the scattering is determined by the form factor only (dilute limit) and particles do not interact with each other, much like they behave in toluene.

Dispersions of NCs in NaSCN/KSCN eutectic show qualitatively similar behavior, forming non-precipitating colloidal solutions in the melt. However, SAXS measurements show that NCs in NaSCN/KSCN melt do not form a non-interacting (dilute limit) colloid but rather a loose network of particles, here shown for the dispersions of CdSe/CdS core-shell NCs in NaSCN/KSCN melt. CdSe/CdS core-shells were chosen for these experiments due to: (i) tight size distribution; (ii) good stability at temperatures above 200 °C; and (iii) affinity of the NC surface to SCN^- ions. Figure 2.2B shows a representative SAXS curve of core-shell NCs stripped of the original organic ligands (further referred to as "bare NCs") and dispersed in NaSCN/KSCN molten salt. In this case the NCs interacted with each other resulting in a non-constant $S(q)$ across the measured q range (Figure 2.4). The slope of -1.5 observed for the $I(q)$ curve at $q < 4*10^{-2}$ $Å^{-1}$ suggests that the NCs form mass fractal-like aggregates whose dimension can be inferred from the power law slope.[21] A low q slope of -1.5 corresponds to the fractal dimension of 1.5.[22] Fractal dimensions below 2 suggest formation of the open "worm-like" secondary structures. The reversible formation of chain structures has been previously reported for charged particles.[23-24] $I(q)$

for $q > 4*10^{-2}$ Å^{-1} (Figure 2B) shows the Bessel function oscillations with the Porod slope of -4, same as for CdSe/CdS NCs of similar size dispersed in toluene suggesting the preservation of the spherical shape and size distribution of NCs in the melt (Table 2.2).

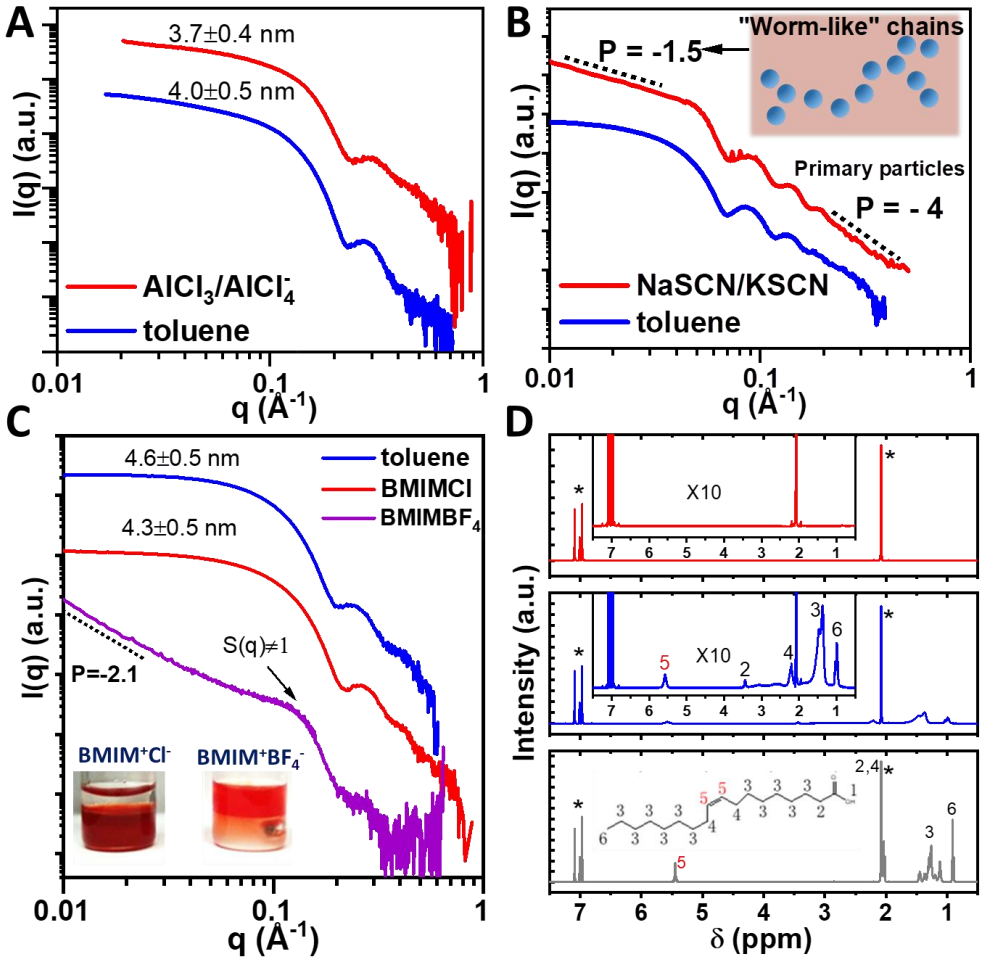

Figure 2.2. Characterization of NCs dispersed in different salts and comparison to the same NCs in toluene.
(A) SAXS curves for Pt NCs dispersed in molten $AlCl_3/AlCl_4^-$ eutectic (red) and the same NCs dispersed in toluene (blue). (B) SAXS curves for CdSe/CdS core-shells in molten NaSCN/KSCN eutectic (red) and the same NCs dispersed in toluene (blue). (C) SAXS curves of CdSe NCs in $BMIM^+X^-$ ILs and toluene (Note: In case of $BMIM^+BF_4^-$ solution the Porod region of CdSe NCs with the intensity decaying as q^{-4} is obscured due to the interference from the WAXS of $BMIM^+BF_4^-$). The inset shows a successful transfer of CdSe NCs from the top non-polar phase to Lewis basic $BMIM^+Cl^-$ IL and no transfer in case of Lewis neutral $BMIM^+BF_4^-$ IL. (D) ^{1}H-NMR spectra of oleic acid (grey curve), CdSe NCs capped with oleic acid in d^8-toluene (blue curve) with the assignments of resonances in the inset and diethyl ether extract of digested CdSe NCs recovered from $BMIM^+Cl^-$ (red curve) (* indicates residual solvent resonances).

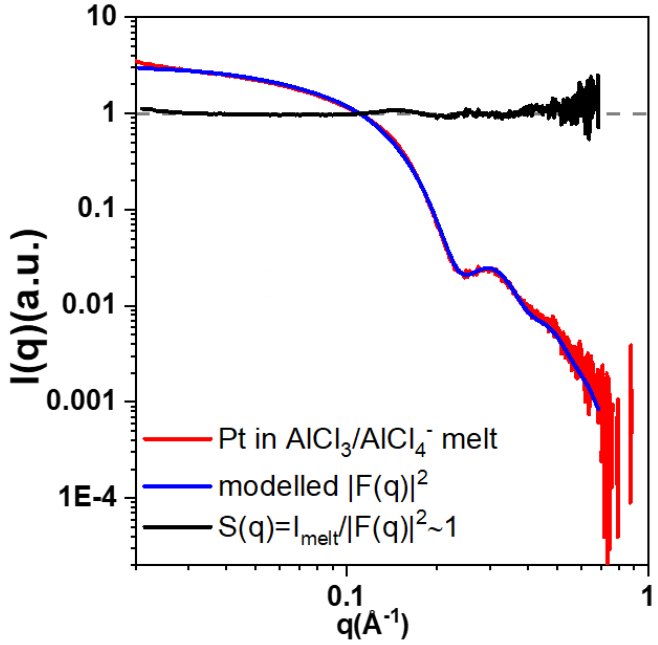

Figure 2.3. SAXS curve of Pt NCs in in molten $AlCl_3/AlCl_4^-$.
SAXS curve, modelled form factor, $|F(q)|^2$, and evaluated structure factor, $S(q)$. $S(q)$ was extracted by dividing scattering intensities by the corresponding modelled form factor of Pt NCs in $AlCl_3/AlCl_4^-$.

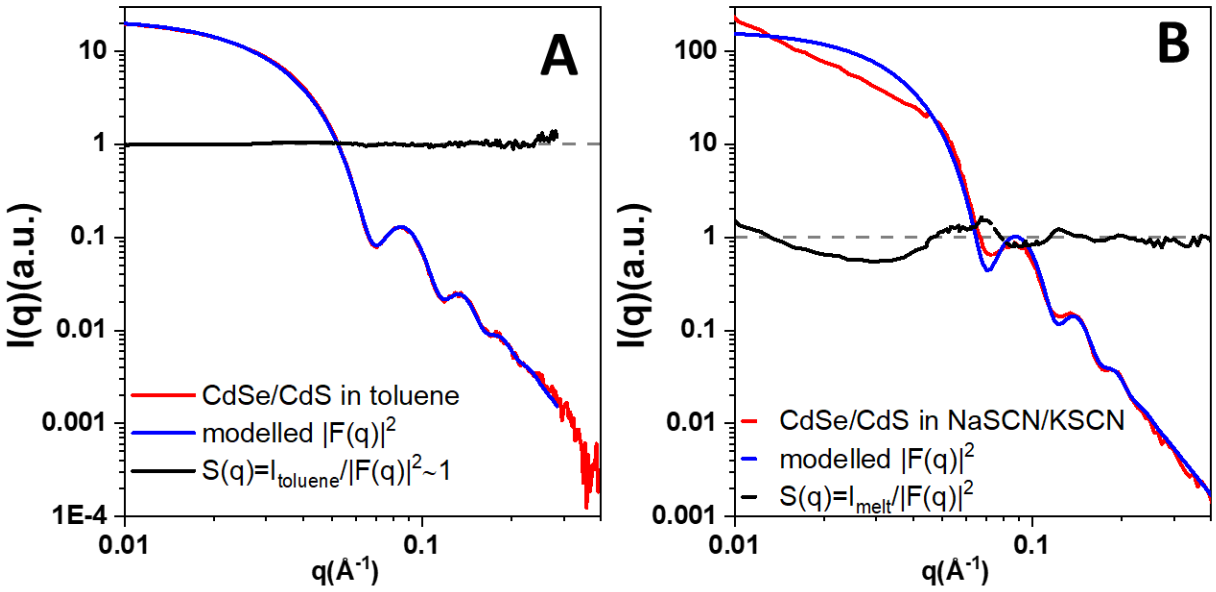

Figure 2.4. SAXS curves of CdSe/CdS core-shell NCs.
SAXS curves, modelled form factors, $|F(q)|^2$, and evaluated structure factors, $S(q)$, for CdSe/CdS core-shell NCs in: (A) toluene; (B) NaSCN/KSCN melt. S(q) of CdSe/CdS NCs in (b) is non-constant across the measured q range.

Table 2.2. Summary of the sizing parameters extracted for CdSe/CdS core-shell NCs. The average sizes were calculated from the size distributions extracted from the fits of the corresponding SAXS *I(q)* curves. The center-to-center distances were measured from the PDF-SAS curves in Figure S4. Interparticle distances are approximated as the difference between the first and second columns.

Sample	Center-to-center distance [Å]	Average Size [Å]	Interparticle distance [Å]
QDs in NaSCN/KSCN melt @ 250°C	133.4±9.8	128.7±10.9	~5
Bare QDs after annealing @ 250°C	131.6±12.8	131.0±14.4	~0
Bare QDs @ RT	134.2±10.0	131.0±10.9	~3

For the NCs dispersed in the NaSCN/KSCN melt, the average separation between individual particles can be assessed by Fourier transforming the structure factor S(*q*) resulting in the pair distribution function, PDF-SAS.[25] To understand the role of the molten salt in preserving particle separation, we compared PDF-SAS of bare CdSe/CdS NCs dispersed in molten NaSCN/KSCN eutectic at 250 °C with that of an annealed film of bare NCs (Figure 2.5). The average interparticle distance is ~5 Å for NCs in NaSCN/KSCN melt whereas it changed from ~3 Å for same NCs aggregated in-film at room temperature to ~0 Å (Table 2.2) after annealing the film at 250 °C. The average interparticle distance of 5 Å suggests on average ~5/3.3 = 1.5 ion pairs of K^+-SCN^- where 3.3 Å is the size of K^+-SCN^- ion-pair derived from the atomic PDF analysis detailed later in this report (Figure 2.13).[26] An approximate, phenomenological theory predicts a secondary free energy minimum when CdSe/CdS NCs are ~ 5 Å apart (Figure 2.6). Here the NCs have to surmount a potential barrier of at least an order of magnitude greater than k_bT before they

can contact directly. Moreover, CdSe/CdS NCs dispersed in NaSCN/KSCN melt and heated to 250 °C could be recovered and re-dispersed in a non-polar solvent such as hexane with the help of organic ligands, while the same NCs annealed at the same temperature without molten salts could not be re-dispersed into a solution. TEM images of these NCs showed a clear evidence of necking while no necking was observed for the CdSe/CdS core-shells recovered from the molten NaSCN/KSCN eutectic (Figure 2.7).

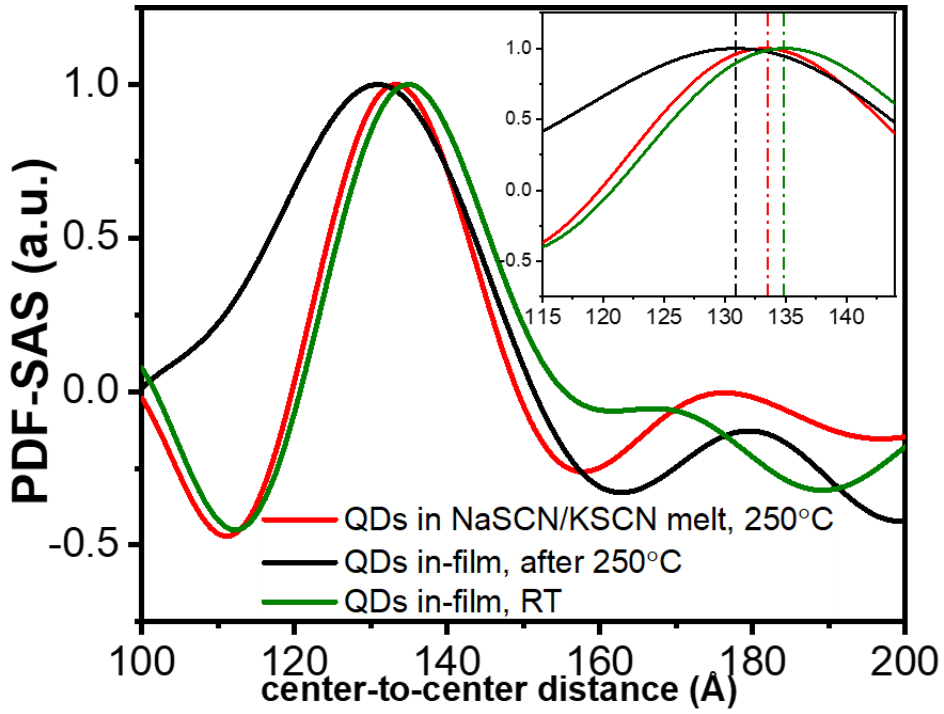

Figure 2.5. PDF-SAS of CdSe/CdS NCs.
PDF-SAS curves calculated from the corresponding structure factors of CdSe/CdS core-shell NCs in NaSCN/KSCN melt and the same bare NCs present as a spin-cast film at RT and after additional annealing the film at 250°C for 24h.

In addition to molten inorganic salts, SAXS measurements were carried out on NC dispersions in $BMIM^+X^-$ ILs. Similar to molten inorganic salts, $BMIM^+X^-$ ILs are unlikely to provide steric or electrostatic stabilization to NC colloids. However, CdSe NCs form stable non-interacting colloids in halide containing $BMIM^+X^-$ (X=Cl, Br, I) ILs. SAXS curves of CdSe NCs

in these ILs show $I(q)$ approaching the structure factor (Figure 2.8) in the Guinier region at $q < 1/R_g$, where R_g is the radius of gyration, 1.7 nm for CdSe NCs, suggesting absence of NC aggregates (Figure 2.2C).

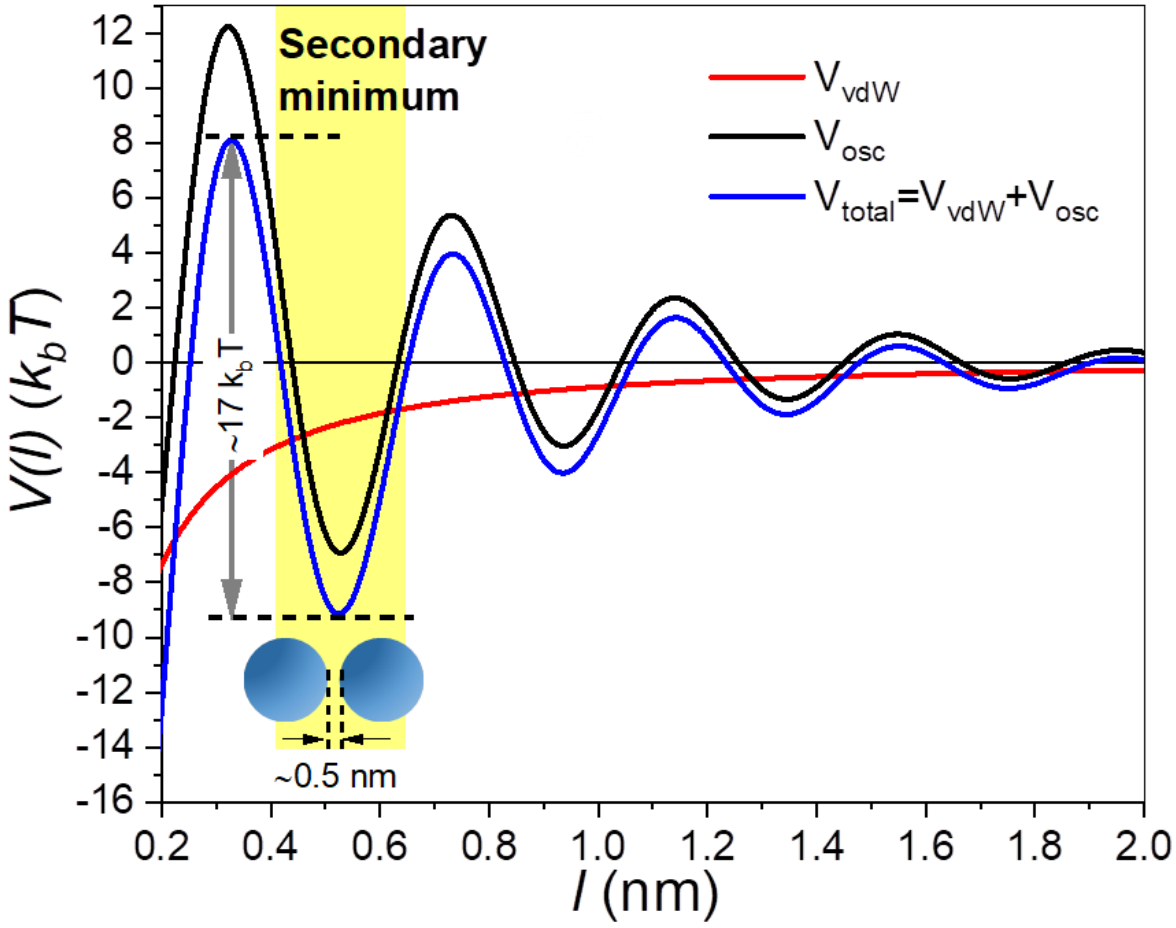

Figure 2.6. The free energy of interaction for CdSe/CdS NCs (approximated as CdS) in NaSCN/KSCN (approximated as KCl) molten salt at 473 K.
The vdW potential is computed using the non-retarded Lifshitz theory. The oscillatory potential is computed using the Ginsburg-Landau model under Derjaguin approximation (see Materials and methods for further details). The estimated location of the secondary attractive minimum at ~ 5 Å is in good agreement with the experimentally observed interparticle distance of ~ 5 Å in NaSCN/KSCN melt.

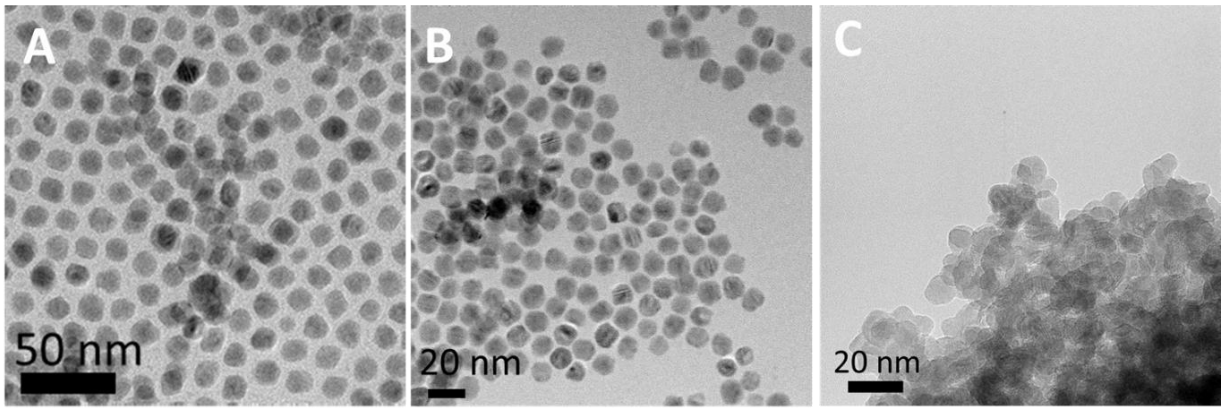

Figure 2.7. TEM images of CdSe/CdS NCs.
(a) TEM image of the initial CdSe/CdS NCs capped with organic ligands; (b) TEM image of CdSe/CdS NCs recovered after processing NCs in molten NaSCN/KSCN eutectic at 250°C for 24h. (c) TEM image of CdSe/CdS NCs recovered after annealing the bare NCs as a spin-cast film at 250°C for 24h.

We further confirmed the absence of organic ligands on CdSe NCs recovered from their IL dispersions by carrying out ^{1}H-NMR measurements and comparing them to CdSe NCs capped with oleic acid ligands. Characteristic resonances corresponding to the oleic acid ligands were completely absent in the ^{1}H-NMR spectrum of NCs recovered from $BMIM^{+}Cl^{-}$ IL (Figure 2.2D). Further, we observed a universal ~ 0.3 nm decrease of the average size of CdSe NCs in $BMIM^{+}X^{-}$ ILs from the fitting of SAXS curves, which can be attributed to the removal of bound $Cd(oleate)_2$ from the CdSe NC surface (Figure 2.8).

Although $BMIM^{+}BF_4^{-}$ IL could not directly transfer CdSe NCs from the non-polar phase (Figure 2.2C, inset), CdSe NCs could first be stripped of their native oleic acid and suspended in this Lewis neutral IL which does not contain ions capable of strongly binding to NC surface. In contrast to halide containing ILs, organic-ligand-free CdSe NCs in $BMIM^{+}BF_4^{-}$ IL exhibited a rising low q intensity with the power law slope of -2.1 indicating that they failed to form a stable colloidal solution (Figure 2.2C, purple curve and Figure 2.9).

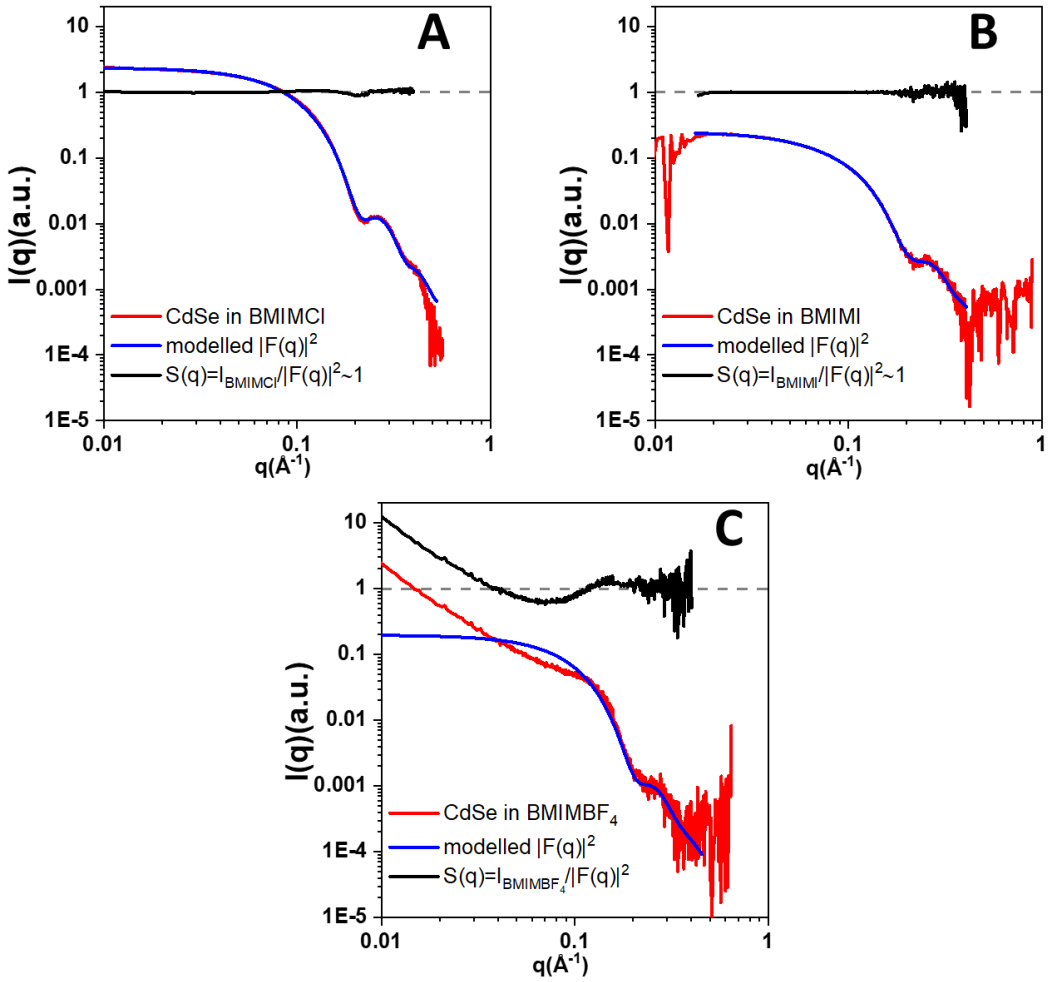

Figure 2.8. SAXS curves of CdSe NCs in in $BMIM^+X^-$ ILs.
SAXS curves, modelled form factors, $|F(q)|^2$, and evaluated structure factors, *S(q)*, for CdSe NCs in: (a) $BMIM^+Cl^-$ IL; (b) $BMIM^+I^-$ IL; and (c) $BMIM^+BF_4^-$ IL. *S(q)* of CdSe NCs in (a) and (b) does not change across the measured q range (remains ~1). *S(q)* of CdSe in (c) is non-constant across the same *q* range and rises at $q < 1/R_g$ (R_g=1.7 nm) suggesting presence of aggregates.

This observation demonstrates that absence of the native organic ligands alone is not sufficient to render particles stable in ionic media but a strong chemical affinity of the solvent ions to the NC surface is required to impart colloidal stability. InAs NCs could also form stable colloidal solutions in halide ionic liquids demonstrating the generality of this interaction. Similar to the dispersion of CdSe NCs, the SAXS intensity levels off at $q < 1/R_g$ (Guinier region) and exhibits $S(q) \sim 1$ (Figure 2.10).

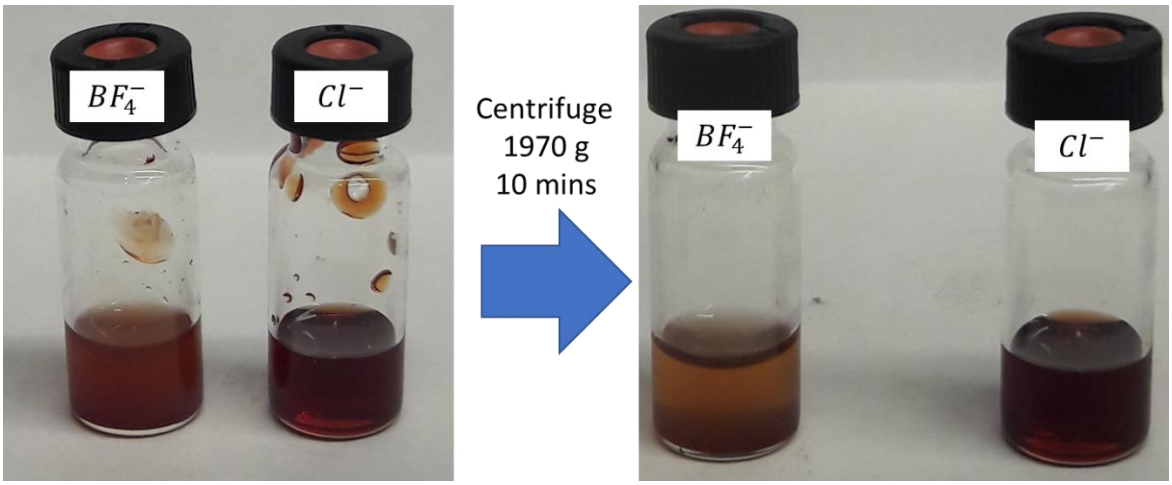

Figure 2.9. Photographs of CdSe NCs in $BMIM^+X^-$ ILs.
CdSe NCs in $BMIM^+BF_4^-$ IL form a cloudy solution where NCs precipitate after centrifuging the vial at 1970 g for 10 mins. CdSe NCs in $BMIM^+Cl^-$ remain colloidally stable after 1970 g, 10 mins centrifugation.

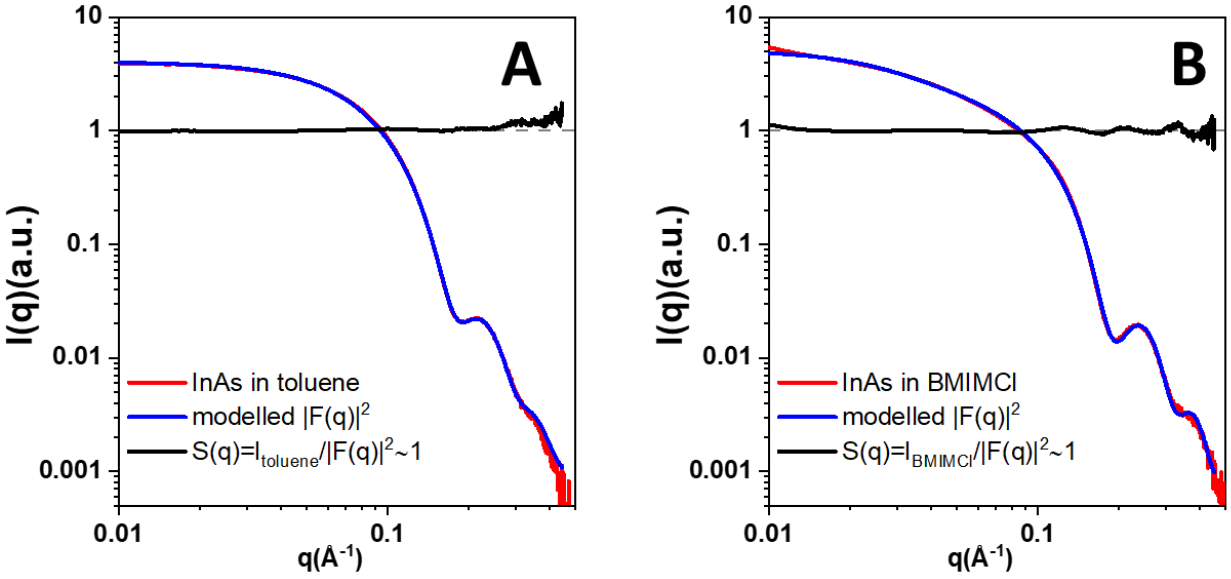

Figure 2.10. Figure 2.10. SAXS curves of InAs NCs.
SAXS curves, modelled form factors, $|F(q)|^2$, and evaluated structure factors, $S(q)$, for InAs NCs in: (a) toluene; (b) $BMIM^+Cl^-$ IL. In both cases the $S(q)$ remains constant ~ 1 across the measured q range.

2.3 Atomic PDF study of Nanocrystals in molten inorganic salts.

Any changes in local structure of molten inorganic salts and ILs induced by the addition of NC solute can be probed directly with the atomic Pair Distribution Function (PDF) analysis of the

high energy X-ray total scattering patterns. PDFs are extracted by the Fourier transform of the X-ray total scattering data and can give information about both short-range order (arrangement of atoms within molecules, sharp peaks at 1 to 5 Å) and intermediate-range order (intermolecular arrangements, broad oscillations at 3 to 20 Å) in a liquid sample. This ability to probe intermediate-range order can give us valuable information about the solvent layer immediately next to the NC surface. The compositional diversity in the $AlCl_3/AlCl_4^-$ eutectic due to the high vapor pressure of $AlCl_3$ and the presence of small amounts of $Al_2Cl_7^-$ and $Al_3Cl_{10}^-$ ions presented a hurdle for the interpretation of PDF data in these salts.[27] Therefore we focused our attention primarily on the NaSCN/KSCN eutectic and $BMIM^+X^-$ ILs. We obtained scattering data for the pure molten salt, NC powders without any solvent and, finally, for the NC/salt dispersions. To extract information about structure of solvent proximal to the NC surface (restructured melt), we first subtracted the total scattering of the pure melt from the NC/salt dispersions (Figure 2.11) before the Fourier transform.

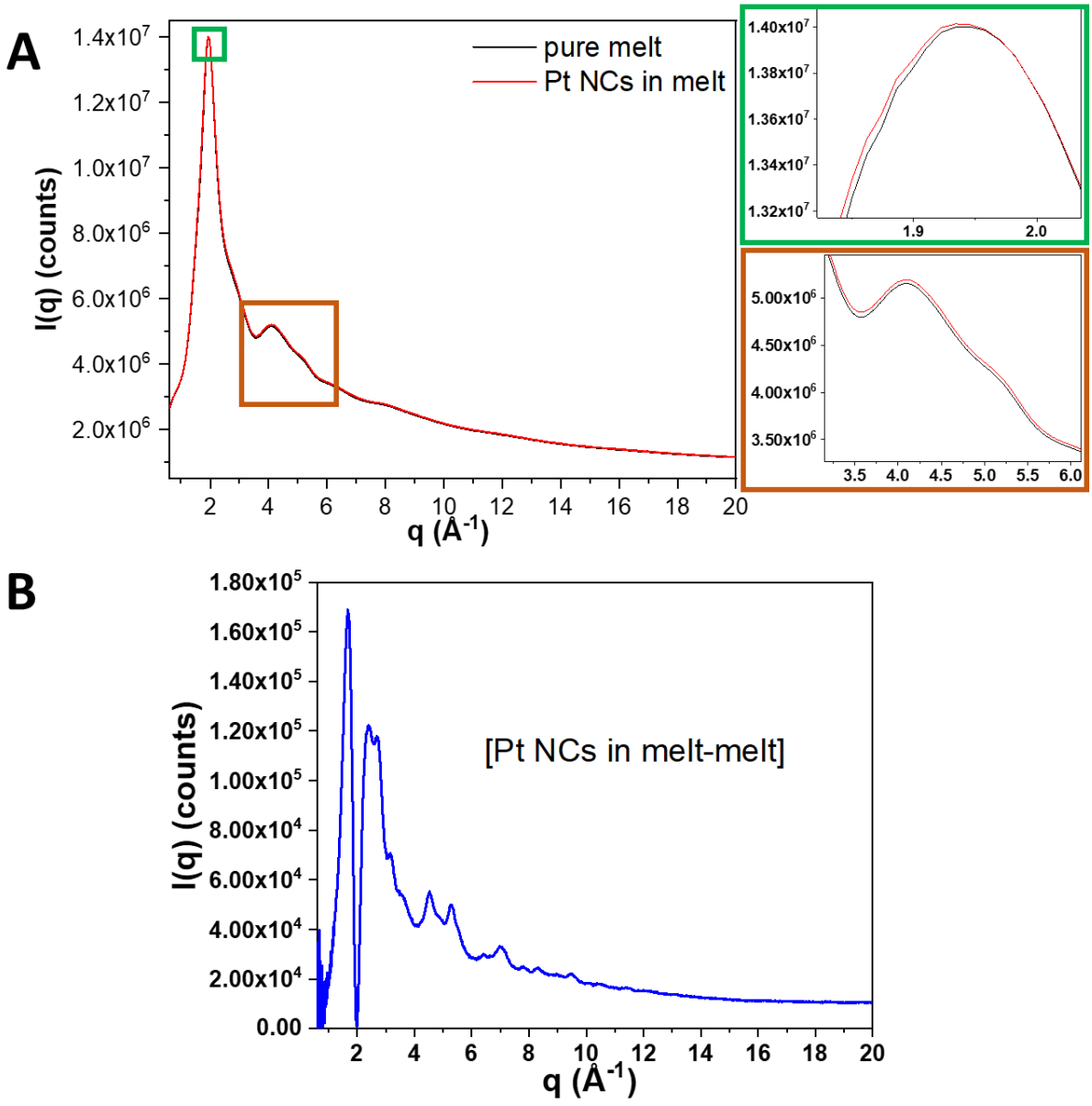

Figure 2.11. X-ray total scattering of Pt NCs in NaSCN/KSCN eutectic.
(A) Comparison between *I(q)* of the pure melt with that of Pt NCs dispersed in the same melt. (B) The difference curve with a new FSDP appearing at ~ 1.7 $Å^{-1}$ due to the interaction of ions in the melt with the NCs' surfaces.

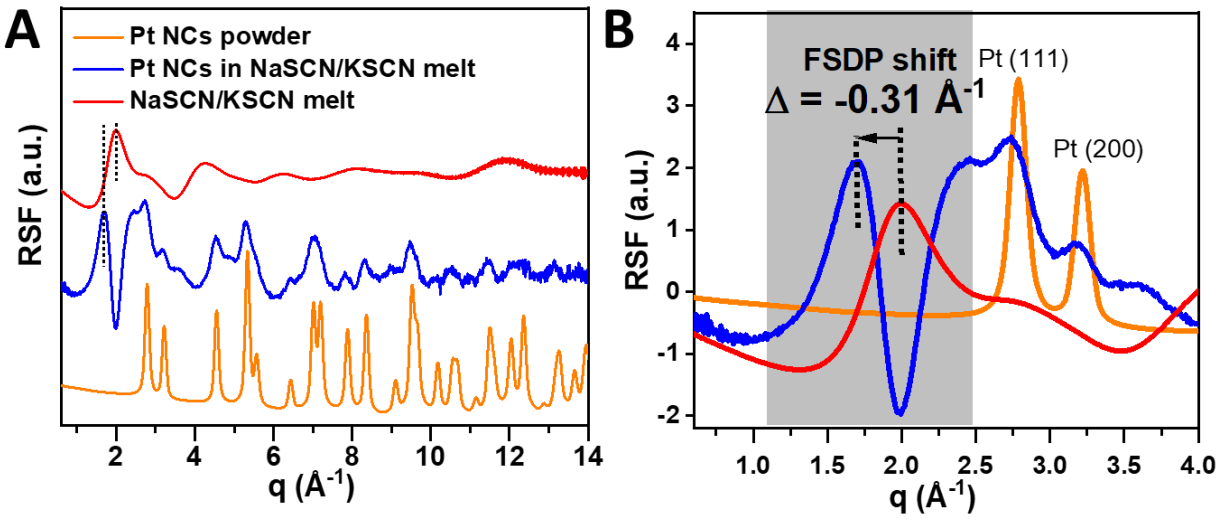

Figure 2.12. RSF of Pt NCs in NaSCN/KSCN melt.
(A) RSF plots for Pt NCs powder, Pt NCs in NaSCN/KSCN melt (after bulk NaSCN/KSCN subtraction), and NaSCN/KSCN melt. (B) Zoom-in of the RSF plots in (A) showing the shift in the FSDP of -0.31 $Å^{-1}$ in case of Pt NCs in NaSCN/KSCN melt.

The difference curve was further normalized by the atomic form factors of the elements in the melt rendering the reduced structure factor, *RSF=q[S(q)-1]*, which contains element-independent structural information (Figure 2.12). The Fourier transform of the RSF gives us the differential-PDF (d-PDF). Further subtraction of the contribution from the NC powders results in a double-differential PDF (dd-PDF). The amplitude of oscillations (if any) in dd-PDF varied for different NCs and was found to be dependent on the concentration of NCs in the melt. We found that dilute samples (~1 mg/ml) tended to give most pronounced oscillations. This can be attributed to two factors (1) dilute samples allowed a more precise subtraction of the contribution from crystalline nanoparticles that have higher scattering coefficients as compared to the amorphous salt matrix and (2) a ~ 1 mg/ml concentration for a ~ 4 nm Pt particle corresponds to an interparticle distance of ~ 86 nm in a colloidal solution which is sufficiently large to negate any interference between the restructured solvent shells around NCs.

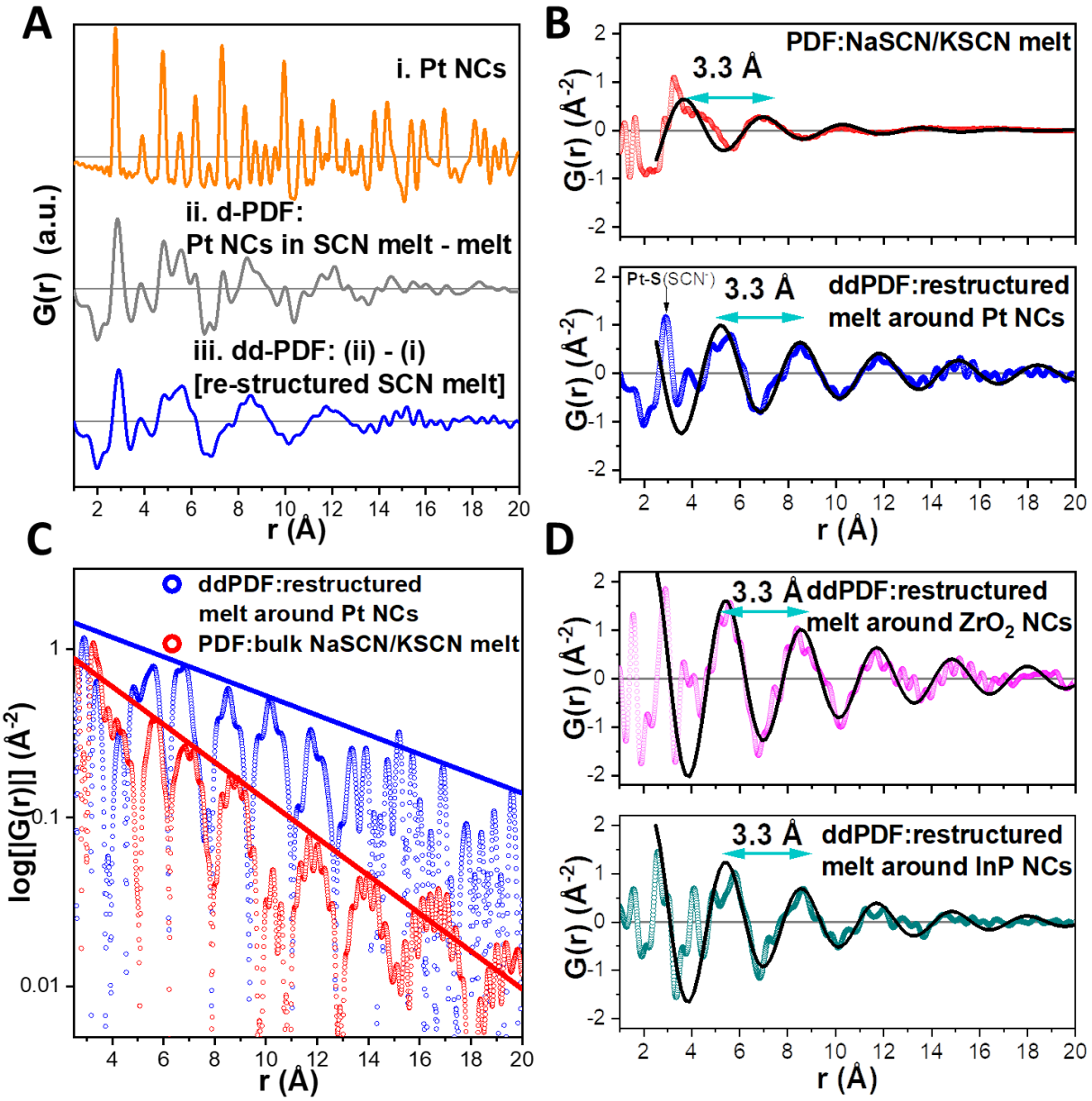

Figure 2.13. Restructuring of molten inorganic salts around NCs.
(A) Experimental PDF of Pt NCs in the dry powder, d-PDF of Pt NCs capped with S^{2-} ligands in NaSCN/KSCN after the bulk liquid PDF subtraction, and dd-PDF after additional subtraction of the NC contribution. (B) dd-PDF of Pt NCs and NaSCN/KSCN melt curves fitted using the exponentially damped sinusoidal functions (black curves). (C) Logarithmic plot of the curves from the panel (B) showing the difference in the decay lengths between the restructured and bulk melts. (D) Comparison of the dd-PDFs corresponding to the restructured NaSCN/KSCN melt around ZrO_2 and InP NCs (black curves represent the fits).

Using this PDF analysis, we see a change in the structure of the NaSCN/KSCN melt when Pt NCs are present. Any features in the d-PDF apart from the interatomic distances inside Pt NCs must be due to restructuring of the solvent induced by the presence of NCs.[14] Indeed, we observed that the d-PDF of NCs in NaSCN/KSCN melt contains peaks from the interatomic distances within Pt NCs (Figure 2.13A, i) superimposed over damped sinusoidal oscillations of the intermediate range order (Figure 2.13A, ii). In the RSF corresponding to this d-PDF, we observed the appearance of a first sharp diffraction peak (FSDP) which is distinct from that of the bulk liquid, with a shift of -0.31 $Å^{-1}$ relative to the bulk (Figure 2.12), and which does not appear in the Pt NC powder. After subtracting contribution of Pt NCs (Figure 2.13A, iii), the resultant dd-PDF contains broad oscillations corresponding to the restructured melt. In order to fit the intermediate range order with an exponentially damped sinusoidal function, the wavelength of the oscillation for the bulk and restructured NaSCN/KSCN melts was fixed at 3.3 Å which corresponds to the reported distance between K^+ and SCN^- ions in KSCN melt (Figure 2.14A).[26] In a highly ionic environment, the wavelength of the intermediate range order represents the physical size of the ion pair.[28] The contribution of Na^+-SCN^- distance to the intermediate range order oscillations in NaSCN/KSCN eutectic mixture is insignificant due to: (i) lower molar concentration (26.3 mol %) of NaSCN component; and (ii) smaller X-ray scattering cross-section of Na^+ compared to that of K^+ (Figure 2.14B). The dd-PDF of Pt NCs in NaSCN/KSCN melt shows oscillations with a distinct phase, amplitude and decay length relative to the original NaSCN/KSCN melt (Figure 2.13B). A sharp peak at ~2.9 Å in the dd-PDF plot for Pt NCs in NaSCN/KSCN melt likely corresponds to the distance between surface Pt atoms and S atoms of the chemisorbed sulfide and SCN^- ions forming a dense layer on Pt surface.

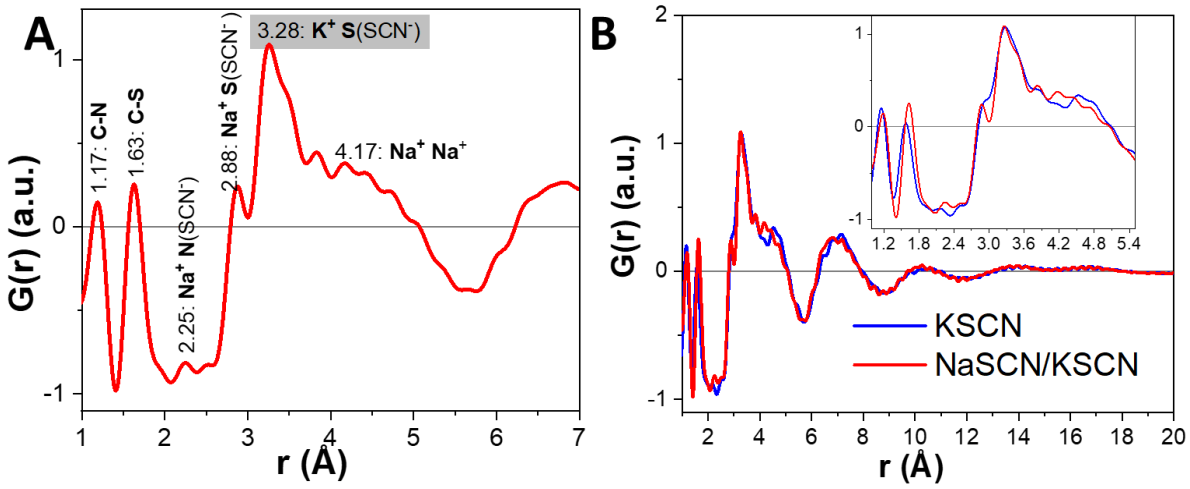

Figure 2.14. PDF of NaSCN/KSCN melt.
(A) Assignment of the sharp peaks in NaSCN/KSCN eutectic melt PDF based on the reported values. (B) Plot of the PDFs of NaSCN/KSCN eutectic melt and pure KSCN melt showing that KSCN has dominant contribution in the X-ray PDF of the eutectic mixture.

The phase change of the oscillatory component is primarily responsible for the observed shift in the FSDP of the restructured melt to smaller q position compared to that of the bulk melt (Figure 2.15A). As we show further for NCs in $BMIM^+Cl^-$ IL, this change in phase reflects correlations between ions in the melt and NC surface not present otherwise. An increase in the amplitude suggests higher local density of K^+/Na^+ and SCN^- ions near the Pt NC surface than in the bulk. The difference in the decay length can be more clearly visualized from a logarithmic plot of the absolute value of *G(r)* (Figure 2.13C). The *1/e* decay length increases from 3.9 Å in the bulk to 7.5 Å near the Pt NC surface suggesting that the ion-ion correlations near the Pt surface are more persistent than the ion-ion correlations in the bulk melt. This increase in the decay length is correlated with the observed increase in intensity and decrease in full width at half of the maximum of the FSDP of the restructured solvent compared to that of the bulk melt (Figures 2.15B, 2.12B). We observed a similar shift in FSDP (Figure 2.16) and phase as well as enhancement of the amplitude and decay length for other NCs, specifically ZrO_2 and InP NCs in NaSCN/KSCN melt

(Figure 2.13D) showing the generality of this picture for all classes of NCs. In a control experiment using toluene as the non-interacting solvent, we observed featureless dd-PDF (Figure 2.17) suggesting absence of toluene restructuring around InP NCs.

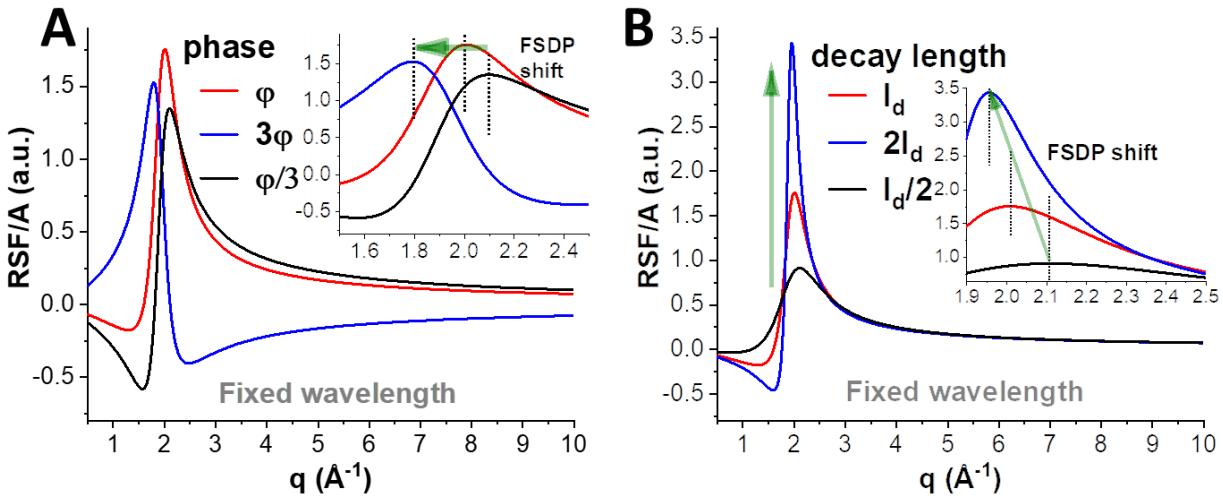

Figure 2.15. Influence of the phase and decay length on FSDP.
In order to isolate the influence of the phase (φ) and decay length (l_d) of the intermediate range order (G_{IRO}) on the FSDP, we calculated the Fourier transform of the fitting equation as a function of φ and l_d (see Materials and methods for details). Plots (a) and (b) show dependence of the calculated *RSF(q)/A* on the phase and decay length of $G_{IRO}(r)$ while the wavelength of oscillation (λ) is fixed. Here we use experimental parameters for NaSCN/KSCN melt with φ = 0.8, λ = 3.3 Å and l_d = 3.9 Å. (A) The change in phase primarily affects the FSDP position, where larger positive phase shift results in the low q shift of FSDP. (B) The change in the decay length primarily affects the peak FWHM where larger decay length results in sharper FSDP. These direct calculations show that the exponentially damped sinusoidal curve representing the IRO of the restructured melt can have the same λ as the bulk solvent and still exhibit FSDP with a distinct peak position and FWHM.

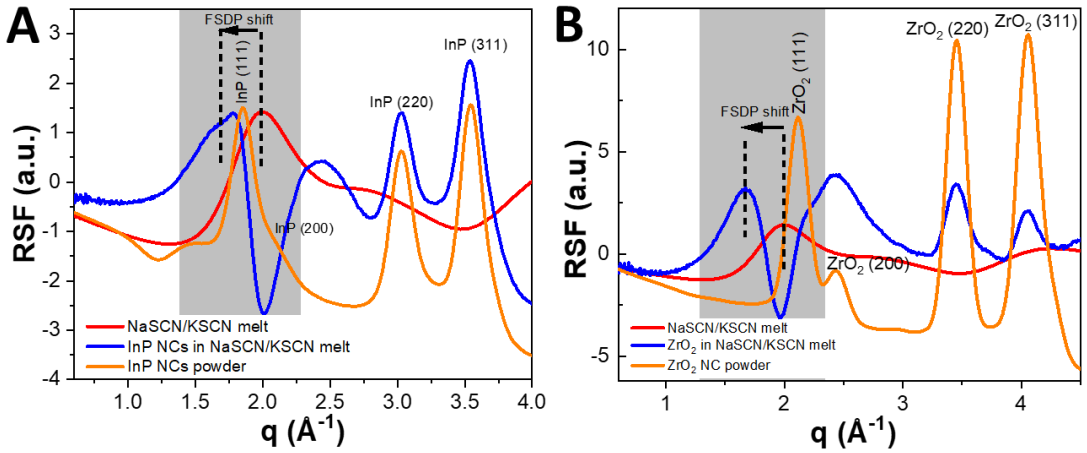

Figure 2.16. RSFs of InP and ZrO_2 NCs in NaSCN/KSCN melt.
(A) and (B) Zoomed-in regions of the RSFs of InP and ZrO_2 NCs in NaSCN/KSCN melt respectively showing that the FSDP shift for the restructured solvent is robust in semiconductor and oxide NC.

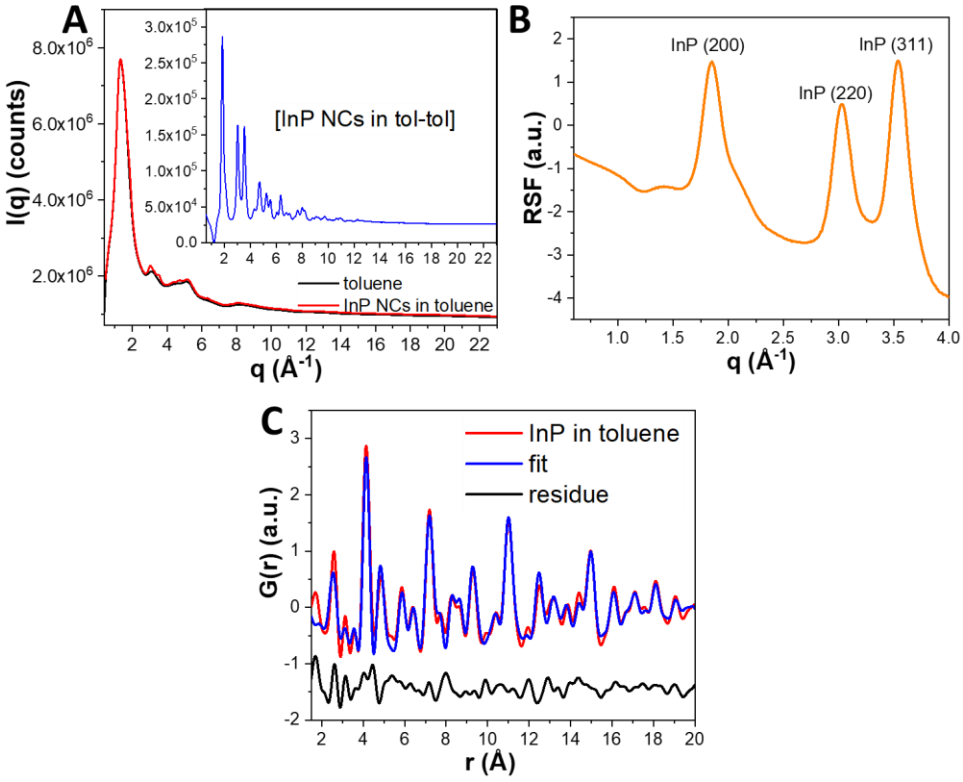

Figure 2.17. X-ray total scattering of InP NCs in toluene.
(A) and (B) Control experiment showing that *I(q)* and RSF of InP NCs in toluene after toluene background subtraction does not show any low q peaks corresponding to the restructured solvent FSDP. The resultant (C) *G(r)* can be fitted well as zinc-blende InP throughout the whole r region with R_w of 0.255.

2.4 Atomic PDF study of Nanocrystals in ionic liquids.

We performed a similar PDF analysis for Pt NCs dispersed in $BMIM^+Cl^-$ IL (Figure 2.18). The shift of -0.24 $Å^{-1}$ in the FSDP for Pt NCs in the IL as compared to pure IL shows that $BMIM^+Cl^-$ restructures around the NCs (Figure 2.19). The wavelength of the oscillation is larger for $BMIM^+Cl^-$ than for NaSCN/KSCN melt (Figure 2.20A). This corroborates the fact that the wavelength represents the physical size of the ion pair. Compared to molten inorganic salt, the PDF of the restructured $BMIM^+Cl^-$ shows no pronounced change in the amplitude. However, as in case of NaSCN/KSCN melt, the decay length increases from 3.6 Å for the bulk IL to 4.4 Å for the restructured IL (Figure 2.21). Faster decay of the ion-ion correlations and lower ionic density (smaller oscillation amplitude) near the nanostructured surfaces can be attributed to the bulkier and less polarizable nature of $BMIM^+$-Cl^- ion pair compared to small inorganic K^+/Na^+ and SCN^- ions. In addition to Pt NCs, CdSe and InP NCs in $BMIM^+Cl^-$ IL exhibited dd-PDFs with the distinct phase and increased decay length (Figure 2.20B).

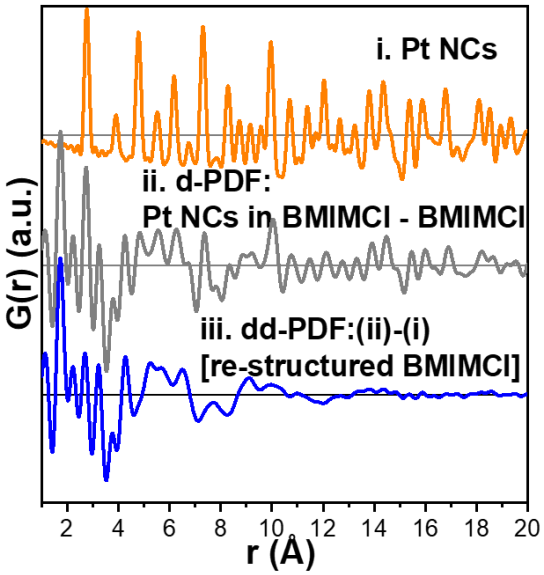

Figure 2.18. PDF of Pt NCs in $BMIM^+Cl^-$ IL.
Experimental PDF of Pt NCs in the dry powder, d-PDF of Pt NCs in $BMIM^+Cl^-$ after the bulk liquid PDF subtraction and dd-PDF after additional subtraction of the NC contribution.

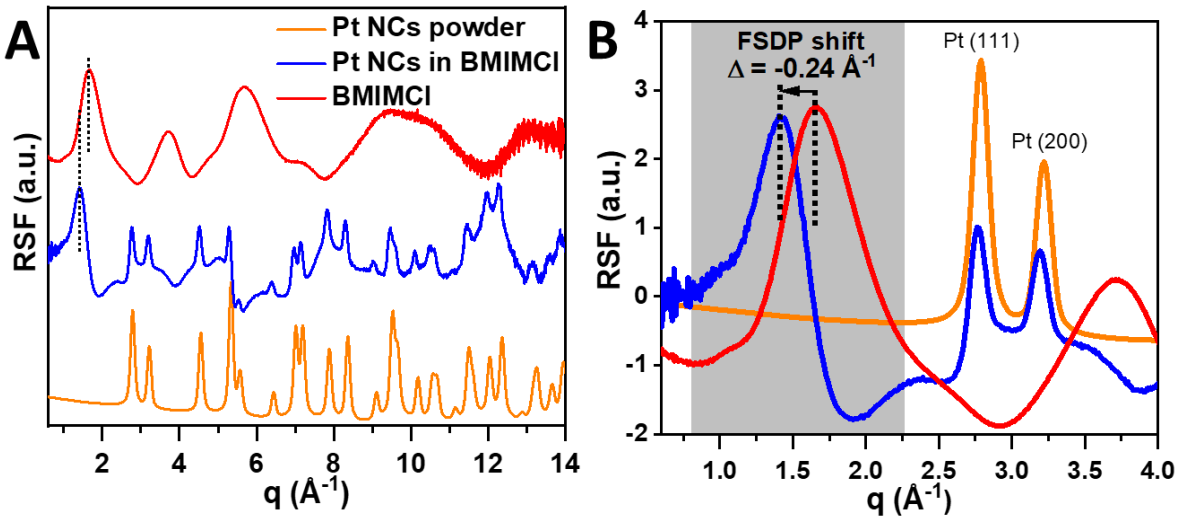

Figure 2.19. RSFs of Pt NCs in $BMIM^+Cl^-$ IL.
(A) RSF plots for Pt NCs powder, Pt NCs in $BMIM^+Cl^-$ IL (after bulk $BMIM^+Cl^-$ subtraction), and $BMIM^+Cl^-$. (B) Zoom-in of the RSF plots in (A) showing the shift in the FSDP of -0.24 $Å^{-1}$ in case of Pt NCs in $BMIM^+Cl^-$ IL.

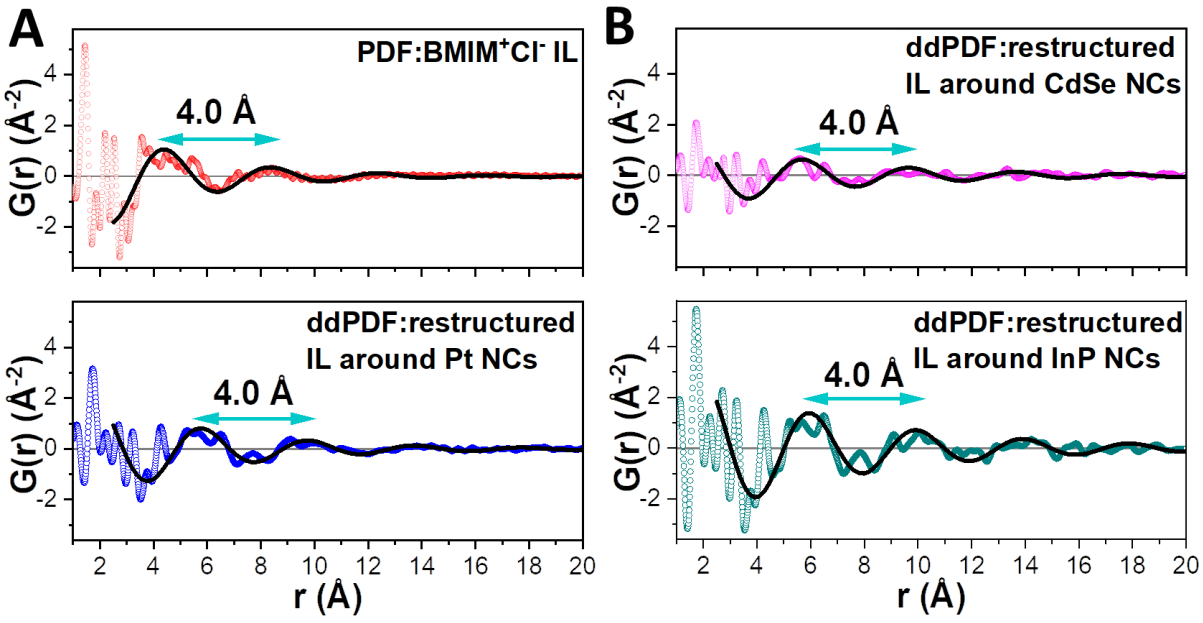

Figure 2.20. PDFs of NCs in $BMIM^+Cl^-$ IL.

(A) and (B) Comparison of the dd-PDFs corresponding to the restructured $BMIM^+Cl^-$ melt around Pt, CdSe and InP NCs with PDF of bulk $BMIM^+Cl^-$ IL (black curves represent the fits).

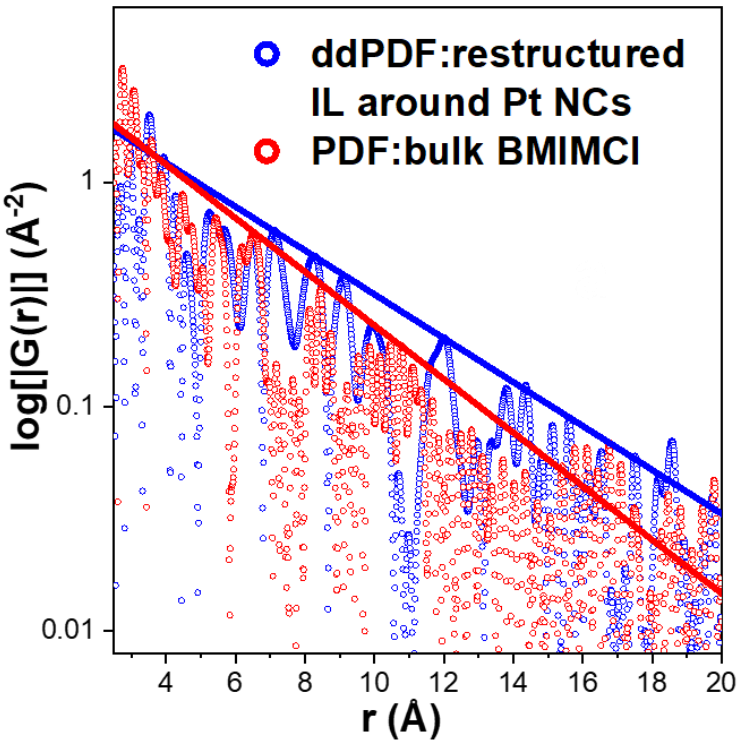

Figure 2.21. Change in the decay length for IL around NCs.
Logarithmic plot of the curves from panel Figure 2.20A showing an increase in the decay length from 3.6 Å (red curve) to 4.4 Å (blue curve) for $BMIM^+Cl^-$ IL.

MD simulations of NCs in $BMIM^+Cl^-$ further indicate that the distinct phase and decay length of the intermediate range oscillatory components in dd-PDFs originate from the correlations between ions and NC surface. Our choice to study $BMIM^+Cl^-$ was in part motivated by the availability of the force fields for this IL, which enabled direct comparison of experimental data and MD models.[29] Unfortunately, we could not find the force fields and parameterizations for NaSCN and KSCN molten salts which precluded modeling of that solvent system. We studied a system consisting of bulk $BMIM^+Cl^-$ as well as systems including NCs (see Materials and methods for model details). Figure 2.22 shows the simulated PDF of the bulk $BMIM^+Cl^-$ which is well matched to the experimental data obtained from the total X-ray scattering from pure $BMIM^+Cl^-$. The computed partial PDFs suggest that the intermolecular intermediate range order is dominated by $BMIM^+$ - Cl^- correlations (orange curve).

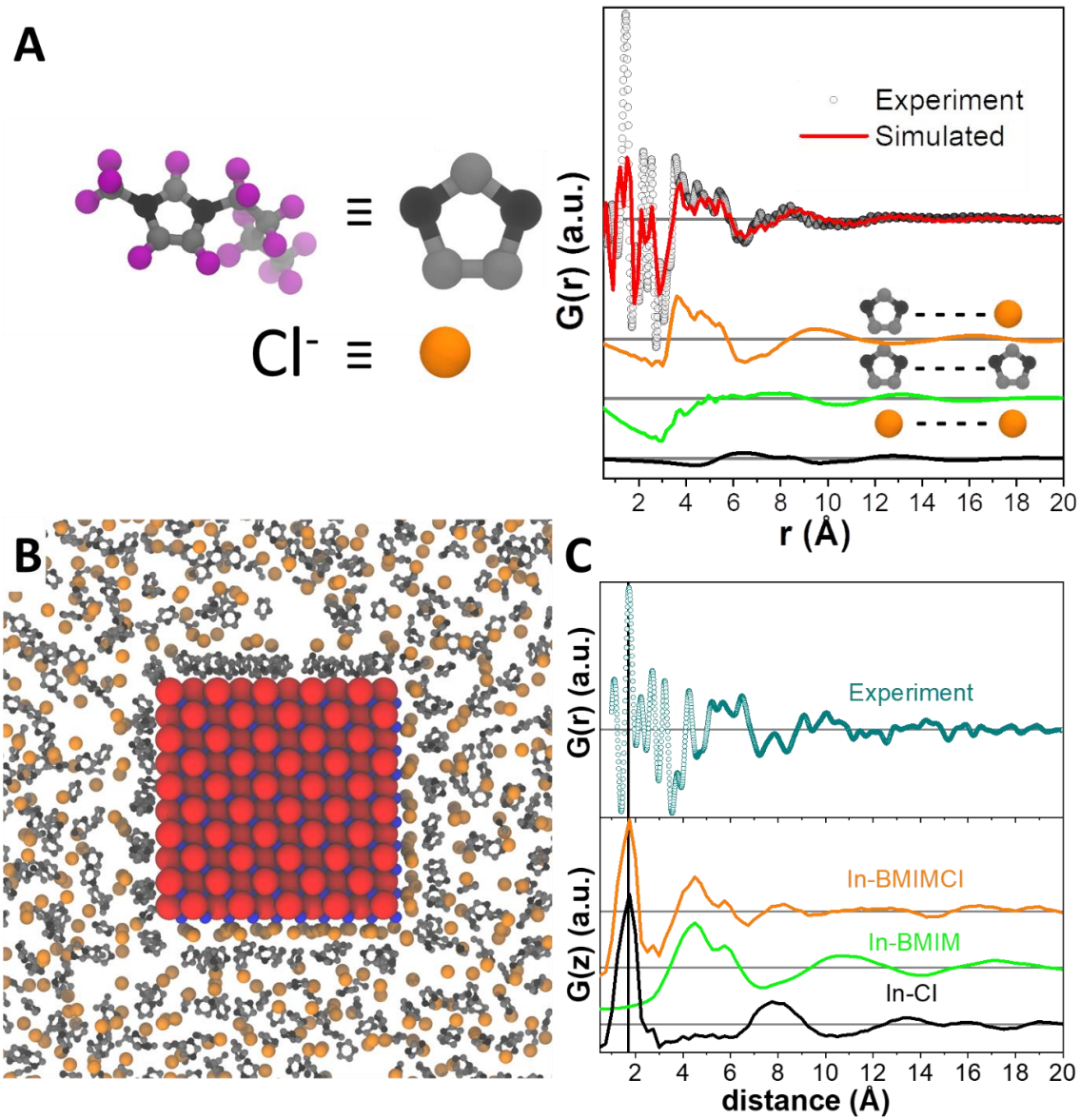

Figure 2.22. InP NCs in $BMIM^+Cl^-$ IL: theory-experiment comparison.
(A) Comparison of the experimental PDF with the simulated radial PDF of the bulk $BMIM^+Cl^-$ IL, and contributions from the inter-ion structures of $BMIM^+$-Cl^-, $BMIM^+$-$BMIM^+$, Cl^- -Cl^-. (B) MD snapshot (zoomed in view) of $BMIM^+Cl^-$ in the vicinity of the cubic zinc blende InP NC (In atoms are blue circles; P atoms are red circles). (C) Comparison of the experimental PDF with the simulated linear PDF in the direction normal to In-rich NC surface, and contributions from the surface-ion correlations of In-$BMIM^+$, In-Cl^-.

We also extracted the density profiles of $BMIM^+Cl^-$ normal to the In-terminated (001) surface of a cubic zinc-blende InP NC. We plot these profiles, which vary with distance (z) from

the NC surface along with experimental dd-PDF, which varies with the radial distance (*r*) (Figure 2.22C). Interestingly, these measurements show a good match, in particular, between the small-distance large peak (at 1.7 Å), identified from the simulations as the Cl^- ion adhered to the In surface, and the second broad peak (~ 4-6 Å) identified as a layer of $BMIM^+$ ions immediately following the first Cl^- layer. A snapshot of the simulation (Figure 2.22B) clearly suggests that Cl^- ions form a dense layer on the In-terminated surface followed by a dense layer of $BMIM^+$ ions before the density correlations become bulk-like. Recent elemental analysis of InP NCs with Rutherford backscattering spectroscopy and XPS suggest that InP NCs are almost 100 % In terminated.[30] Hence there should be little contribution from the correlations between negatively-charged (P terminated) facets and $BMIM^+$ ions to the total pair distribution function (Figure 2.23).

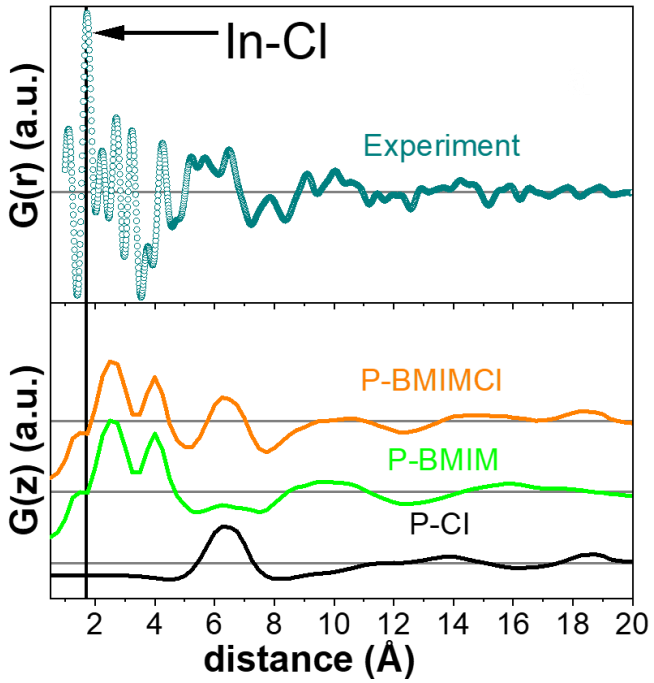

Figure 2.23. $BMIM^+Cl^-$ IL around P-rich facet of InP NC.
Comparison of the experimental PDF with the simulated linear PDF in the direction normal to P-rich NC surface, and contributions from the surface-ion correlations of $P\text{-}BMIM^+$, $P\text{-}Cl^-$. The most significant difference between the positive surface interaction with the solvent and the negative surface interaction with the solvent is that in the case of the In – Cl^- correlations, there is a very large peak for small z which doesn't appear in the P – $BMIM^+$ correlations.

The features of this surface-induced density profile do not change significantly for the different surfaces presented by InP and CdSe NCs in simulation (Figure 2.24), nor Pt NCs in experiment (Figure 2.20A). Thus, the restructuring of the $BMIM^+Cl^-$ solvent by a metal rich surface is robust to changes in the specific composition of the surface. Further, the restructuring observed in the experiment appears to consist largely of the order induced normal (z) to the NC surface.

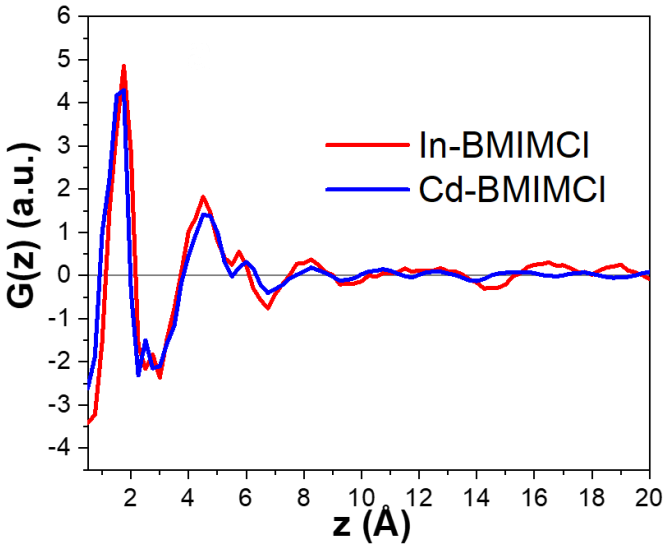

Figure 2.24. Linear PDFs of $BMIM^+Cl^-$ IL normal to metal rich NCs surfaces.
MD simulation results for the linear PDFs normal to the In-rich InP NC and Cd-rich CdSe NC surface showing that there is little difference in the restructured $BMIM^+Cl^-$ – surface correlations.

In a control experiment, we dispersed organic ligand free CdSe NCs in the Lewis neutral $BMIM^+BF_4^-$ IL and performed analogous PDF analysis. The RSF obtained after bulk IL background subtraction contained the diffraction peaks of CdSe phase only and there were no signs of the restructured solvent FSDP (Figure 2.25). Together with the SAXS results presented in Figure 2.2 for CdSe dispersed in $BMIM^+BF_4^-$, it is evident that solvent restructuring around the NC surface correlates with the observation of colloidal stability of NCs in highly ionic media.

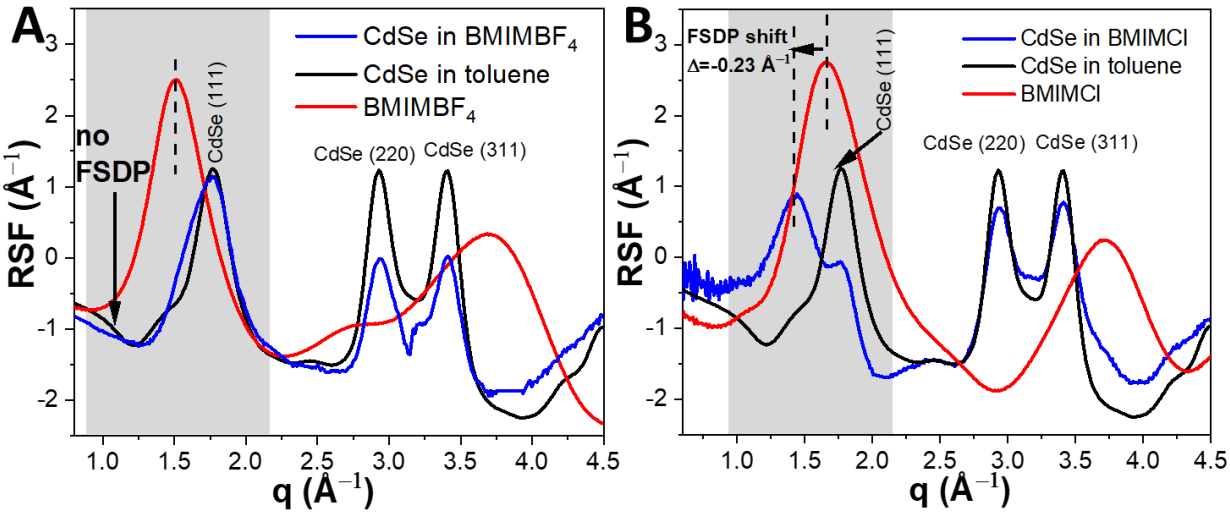

Figure 2.25. RSFs of CdSe NCs in BMIM$^+$BF$_4^-$ and BMIM$^+$Cl$^-$ ILs.
(A) RSF plots for CdSe NCs in toluene and BMIM$^+$BF$_4^-$ IL and pure BMIM$^+$BF$_4^-$ IL showing absence of the restructured BMIM$^+$BF$_4^-$ around CdSe NCs. (B) RSF plots of CdSe in toluene and BMIM$^+$Cl$^-$ IL and pure BMIM$^+$Cl$^-$ IL showing presence of the restructured BMIM$^+$Cl$^-$ FSDP shifted by -0.23 Å^{-1} from that of the bulk IL.

2.5 Conclusion.

The universal restructuring observed in Lewis basic NaSCN/KSCN melt and BMIM$^+$Cl$^-$ IL around various classes of NCs and its absence in Lewis neutral BMIM$^+$BF$_4^-$ IL supports the hypothesis of Zhang *et al.*[5] that the intermediate-range ionic ordering near the NC interface is responsible for the colloidal stability. SCN$^-$ and Cl$^-$ ions are able to act as X-type ligands which bind to electron deficient metal rich facets of NCs and hence form a dense surface-bound layer (Figure 2.22B). BF$_4^-$ ions, on the other hand, cannot act as X-type ligands and hence do not form a surface-bound layer. A layer of negatively charged surface-bound Cl$^-$ in case of BMIM$^+$Cl$^-$ IL and SCN$^-$ in case of NaSCN/KSCN molten salt in-turn electrostatically templates a charge density wave consisting of layers of alternating ions with opposite charges (Figure 2.22C). Guided by local Coulomb forces, the charge density wave propagates into the solvent for a distance greatly exceeding the Debye screening length, which is limited to one ion layer. These long-range ionic

correlations in molten salts are not predicted by the Debye–Hückel theory and require accounting for both long-range Coulomb and short-range molecular interactions.[9] The charge density wave represented by the typical dd-PDF of 4.0 nm Pt NCs in NaSCN/KSCN melt (Figure 2.13B) decays to the bulk melt density at the distance of more than 20 Å away from the Pt surface. The associated oscillatory potential is only weakly perturbed by the van der Waals attraction in the interparticle distance range of 1 Å to 20 Å (Figure 2.26). As a result, the charge density wave generated by the NC surface can easily screen the van der Waals attraction and hence account for the colloidally stable dispersions in molten salts. The charge density wave consisting of the restructured ions generates an oscillatory potential between NCs and hence constitutes a fundamentally different mechanism of colloidal stabilization in addition to the standard electrostatic and steric mechanisms.

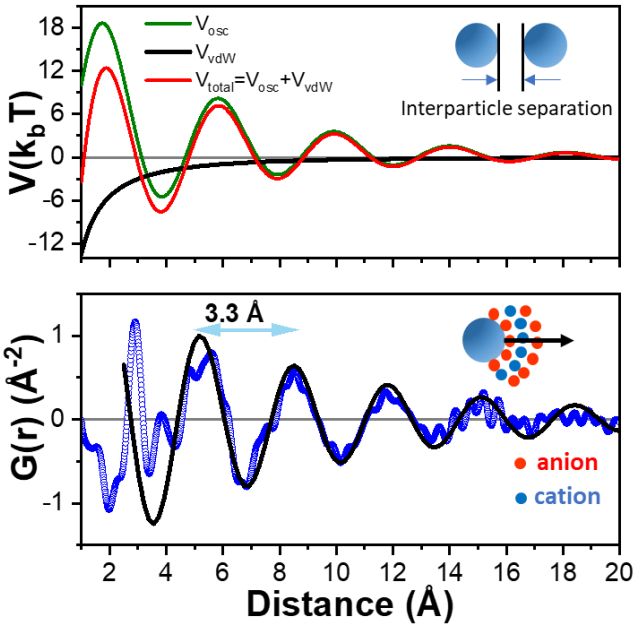

Figure 2.26. Comparison of the van der Waals and oscillatory potentials for Pt NCs (4.0 nm) interacting through NaSCN/KSCN melt with the experimental PDF of the restructured solvent around Pt NCs.
"Distance" corresponds to the interparticle separation for the van der Waals and oscillatory potentials. The oscillatory potential is estimated using a modified phenomenological Ginsburg-Landau theory (see Materials and methods for further details).

2.6 Materials and methods.

Chemicals and materials

Sodium thiocyanate (NaSCN, ≥99.99 %, trace metal basis, Aldrich), Potassium thiocyanate (KSCN, ACS reagent, ≥99.0 %, Aldrich), Aluminum chloride ($AlCl_3$, 99.99 %, trace metal basis, Aldrich), Sodium chloride (NaCl, puratronic, 99.999 %, metal basis, Alfa Aesar), Potassium chloride (KCl, 99.999 %, trace metal basis, Aldrich), 1-butyl-3-methylimidazolium chloride (98 %, Strem Chemicals), 1-butyl-3-methylimidazolium tetrafluoroborate (98 %, Strem Chemicals), 1-butyl-3-methylimidazolium iodide (99 %, Aldrich), 1-butyl-3-methylimidazolium bromide (≥98.5 %, HPLC grade, Aldrich), Didodecylammonium bromide (DDAB, 98 %, Aldrich), Ammonium sulfide (40-48% in water, Aldrich), Nitrozonium tetrafluoroborate powder ($NOBF_4$, 97 % Aldrich), Tetrafluoroboric acid (HBF_4, 48 % in water, Aldrich), Oleylamine (70 %, Aldrich), octadecene (90 %, Aldrich), oleic acid (90 %, Aldrich), Tri-n-octylphosphine oxide (TOPO, 99 %, Aldrich), Formamide (99.5 %, Aldrich), Toluene (Anhydrous, 99.8 %, Aldrich), acetonitrile (Anhydrous, 99.8 %, Aldrich) Zirconium (IV) isopropoxide isopropanol complex (99.9 %, Aldrich), Zirconium (IV) chloride (sublimed grade, >99.95 %, Strem Chemicals), Indium (III) chloride ($InCl_3$, anhydrous, 99.99 %, Puratrem),) tris(trimethylsilyl) arsine ($(TMS)_3As$) was prepared as detailed in the literature[31], tri-n-octylphosphine (TOP, 97 %, Strem Chemicals), Tri(trimethylsilyl) phosphine ($(TMS)_3P$, 98 %, Strem Chemicals), CdO (≥99.99 %, Aldrich), Se (99.99 %, 100 mesh, Aldrich), Iron (0) pentacarbonyl (>99.99 %, Aldrich), Platinum (II) acetylacetonate (97 %, Aldrich). Oleylamine, octadecene and formamide were dried under vacuum before use. $AlCl_3$ was purified by sublimation in a nitrogen filled glovebox prior to use.

Synthesis of NCs capped with organic ligands

All NC syntheses were performed according to reported protocols using conventional air-free techniques including Schlenk line and N_2-filled glovebox. Pt NCs (mean size 4.0±0.5 nm),[32] zinc-blende CdSe NCs (mean size 4.6±0.5 nm),[33] ZrO_2 NCs (mean size 4.0±0.4 nm),[34] InAs (mean size 5.0±0.7 nm),[35] InP (mean size 4.7 nm±0.6 nm),[36] CdSe/CdS core-shell QDs (13.1±1.3 nm)[37] were used in this work. Mean sizes were measured from SAXS analysis and verified with TEM measurements. All manipulations with molten salts and ILs were performed in a N_2-filled glovebox with moisture and oxygen levels under 0.1 ppm.

Pt NCs in $AlCl_3$/NaCl/KCl

Pt NCs were dispersed in a ternary mixture of $AlCl_3$/NaCl/KCl (63.5/20/16.5 mol. %) through a direct phase transfer process. In this procedure, a solution of Pt NCs in anhydrous decane (capped with the original organic ligands, washed multiple times to remove excess organics) was interfaced with the molten salt mixture (4:1 vol. ratio) in a glass vial. The resulting mixture was stirred at 120 °C using a Pyrex-glass-coated stir bar until NCs transferred completely from the upper decane phase to the molten salt phase. The upper phase was later discarded and fresh decane was added to the vial. This procedure was repeated several times to ensure complete removal of organic ligands.

CdSe/CdS and ZrO_2 NCs in NaSCN/KSCN

CdSe/CdS core-shell NCs were stripped of their organic ligands using tetrafluoroboric acid (HBF_4) as described in the reference.[38] ZrO_2 NCs were stripped of their organic ligands (tri-n-octyl phosphorous oxide) using nitrosonium tetrafluoroborate powder ($NOBF_4$).[39] Bare NCs form stable

colloidal solutions in dimethylformamide and were precipitated with CH_3CN multiple times and dried as powders. A eutectic mixture of NaSCN/KSCN (26.3/73.7 mol. %) was taken in a vial and heated to 250 °C until molten. The molten salt was cooled down to room temperature and ground into fine powder. Bare NC powder was then mixed with the finally ground eutectic mixture mixed and heated at 250 °C under stirring (using a Pyrex-glass-coated stir bar) for several hours until a stable solution was obtained.

Pt and InP NCs in NaSCN/KSCN

InP and Pt NCs were functionalized with S^{2-} using $(NH_4)_2S$ dissolved in formamide to form a stable colloidal solution.[40] Particles These NCs were further transferred into toluene phase using didodecyldimethylammonium bromide (DDAB) as the phase transfer agent. This ligand decomposes cleanly into gaseous products *via* Hoffman elimination, leaving no organics behind.[41] The toluene phase containing NCs was transferred to a centrifuge tube, precipitated with ethanol to get rid of excess ligands, and redispersed in minimal amount of anhydrous toluene. The finally ground eutectic mixture of NaSCN/KSCN (see above) was combined with the solution of NCs capped with S^{2-}/DDA^+ ion-pair in toluene and slowly heated at 250 °C under stirring (using the Pyrex-glass-coated stir bar) for several hours until a stable solution was obtained.

CdSe, InP and InAs in $BMIM^+X^-$ ILs (X = Cl, Br, I, BF_4)

NCs were dispersed in $BMIM^+X^-$ through a direct phase transfer process. In this procedure, a solution of NCs in anhydrous decane was combined with the respective IL (4:1 vol. ratio) in a glass vial. Upon vigorous stirring at 100 °C (for $BMIM^+Cl^-$ and $BMIM^+Br^-$) and 50 °C ($BMIM^+I^-$), NCs gradually transferred into ILs within several hours, resulting in a colorless decane top phase.

The bottom phase of the IL containing NCs was rinsed with fresh decane and ethyl acetate several times to get rid of the residual organic ligands. Afterwards, a slightly turbid NC solution in IL was dissolved in CH_3CN and NCs were precipitated and supernatant discarded. The recovered NCs can be redispered in fresh halide containing $BMIM^+X^-$, forming a stable colloidal solution. Since BF_4^- anion is Lewis neutral and hence it is not able to displace the original organic ligands, CdSe NCs were stripped off their organic ligands using $BMIM^+Cl^-$ IL as described above. The recovered CdSe NCs (after dissolution of $BMIM^+Cl^-$ matrix with CH_3CN) were further combined with $BMIM^+BF_4^-$ IL (liquid at room temperature). The resultant mixture failed to form a colloidally stable solution and remained turbid even after several hours of continuous stirring.

^{1}H NMR of CdSe NCs

Oleic acid (OA) capped CdSe NCs in hexane were dried thoroughly and redispersed in d^8-toluene with the concentration of 25 mg/ml. To test the existence of OA ligands on CdSe NC surface after their phase transfer to $BMIM^+Cl^-$ IL, we recovered the organic ligands (if any) by digesting CdSe to avoid interferences from imidazolium ring. In brief, DI water was used to dissolve IL matrix. The NC precipitates were rinsed with water several times to completely remove IL residue. Afterward, CdSe NCs were dissolved in half concentrated aqua regia using standard procedures.[42] The organic ligands (if any) were then extracted with diethyl either, dried under vacuum and dissolved in d^8-toluene for NMR study. ^{1}H-NMR spectroscopy was recorded at 500 MHz on a Bruker Ultrashield 500 plus spectrometer.

Small Angle X-ray Scattering (SAXS)

Molten inorganic salt and IL samples were prepared by drawing the solution into 1.1 mm outer diameter (0.1 mm thickness) borosilicate glass capillaries and were further flame sealed to avoid exposure to ambient atmosphere. The concentration for all the samples was ~ 1mg/mL. All SAXS for the NC dispersions, except for CdSe/CdS core-shell NCs in NaSCN/KSCN molten salt, were collected at 12-ID-B at the Advanced Photon Source, Argonne National Laboratory, with the X-ray wavelength of 0.9341 Å. The *in-situ* heating experiments were performed using Linkam stage. SAXS of CdSe/CdS core-shell NCs in NaSCN/KSCN molten salt were collected at 9-ID using X-ray wavelength of 0.6902 Å.

SAXS fitting

The SAXS curves were analyzed by fitting to a quantitative model in Igor Pro using the Irena package (available at https://usaxs.xray.aps.anl.gov/software/irenafrom the APS).[43] Structure factor free scattering curves (*S(q)~1*) (after appropriate background subtraction) were fitted with the model independent maximum entropy approach. Based on TEM data, the particles' form factor was assumed to be spherical with the aspect ratio of 1.

Modeling of dispersions of interacting particles ($S(q)\neq1$) was performed in Modeling II module in Irena package. The primary particles (population 1) were modelled using the Gaussian size distribution with the hard sphere structure factor. The secondary structures (population 2) were modelled using the Unified Fit level.[44] To further extract approximate *S(q)*: (i) the interparticle interactions were "switched off" (dilute limit) in the appropriate model and population 2 was removed as well, thus rendering $|F(q)|^2$ of the primary particles; (ii) background corrected experimental intensity was normalized by the form factor from (i), $S(q) = I(q)/|F(q)|^2$.

PDF-SAS analysis

We use the same definition of the PDF-SAS as for the atomic PDF (see eq. 4 below):

$$PDF - SAS = \frac{2}{\pi} \int_{q_{min}}^{q_{max}} dqq(S(q) - 1)\sin(qr) \quad (1)$$

Here *S(q)* is the structure factor extracted from the corresponding SAXS intensity curves (as in section 2.2), q_{min} = 0.02 Å^{-1} and q_{max} = 0.18 Å^{-1} for CdSe/CdS core-shell NCs.

X-ray total scattering

Molten inorganic salt and IL samples were prepared by drawing the solution into 1.1 mm outer diameter (0.1 mm thickness) borosilicate glass capillaries and were further flame sealed to avoid exposure to ambient atmosphere. High energy X-ray scattering data was collected at 11-ID-B at the Advanced Photon Source, Argonne National Laboratory, with the X-ray wavelength of 0.2113 Å. The *in-situ* heating set-up[45] was used to melt samples and collect X-ray data for various dispersions of NCs. KSCN/NaSCN samples were heated to 200 °C and $BMIM^+Cl^-$ IL samples were heated to 100°C to ensure complete melting. The collected high energy X-ray scattering data was reduced to 1D in GSAS-II[46] using CeO_2 powder as a calibrant to determine sample to detector distance. Please refer to the supporting information for details on PDF extraction and analysis.

Atomic PDF extraction

Conversion to the respective structure factor and pair distribution function was performed in PDFGetX2.[47] A typical procedure for the extraction of the structure factor and PDF was as following and it is similar to that of Zobel *et al*.:[14]

1. Molten salt without NCs in 1.1 mm outer diameter (0.1 mm thickness) borosilicate capillary was used as a background to subtract the scattering corresponding to bulk liquid, glass and experimental set-up from the dispersion of NCs in the same molten salt formulation (empty glass capillary was used as a background for pure molten salt and NCs in dry powdered state).

2. The background subtracted scattering intensity was corrected for Compton scattering and detector effects ($I_{corrected}$) and further converted to the respective structure factor ($S(q)$) using the atomic form factors (f) of the known elemental composition of NCs (or elemental composition of salt or ILs in case of the structure factor for bulk liquid):

$$S(q) = 1 + \frac{I_{corrected} - \langle f^2 \rangle}{\langle f \rangle^2} \tag{2}$$

The reduced structure factor can be further calculated as following:

$$RSF = q\left(S(q) - 1\right) \tag{3}$$

3. The PDF function was extracted by the Fourier transformation of the respective reduced structure factor (eq. 3) using the transferred momentum range ($q = \frac{4\pi \sin(2\theta/2)}{\lambda}$ where λ is X-ray wavelength and 2θ is the scattering angle) from q_{min} = 0.6 Å^{-1} to q_{max} = 14 to 20 Å^{-1} in case of solutions of NCs in molten salt and ILs and 20 to 24 Å^{-1} in case of NC powders and bulk liquids:

$$G(r) = \frac{2}{\pi} \int_{q_{min}}^{q_{max}} dq q(S(q) - 1)\sin(qr) \quad (4)$$

The chosen q_{min} of 0.6 Å^{-1} guarantees that there is minimum contribution from the SAXS region of NCs and at the same time it should capture all FSDPs of the restructured and bulk molten salts and ILs.

4. The double differential PDFs (dd-PDF) for NCs in molten salts and ILs were obtained using PDFGui.[47] The differential PDF (d-PDF) of NCs in molten salt has almost no contribution from the oscillatory component of the restructured solvent at r > 20 Å. Hence the region of the d-PDF at r > 20 Å was modelled using the refined crystal structure of NCs only to render the scaling factor for the NC phase. The refined parameters such as lattice constants and atomic displacement factors were extracted from modeling of NCs powder without any solvent. The particle diameter was not refined and determined independently from SAXS size distributions and TEM data. The obtained parameters corresponding to the respective NC phase (scaling factor, lattice constant, atomic displacement factors, diameter) were fixed and the model was propagated into the region of r < 20 Å where there is significant contribution from the oscillatory component of the restructured solvent. The resultant difference curve (residue) is the dd-PDF free of atomic correlations corresponding to bulk liquid and distances within individual NCs.

Atomic PDF fitting

Intermediate range order (IRO) component in dd-PDF of the restructured and bulk molten salt was fit with the exponentially damped sinusoidal curve:

$$G_{IRO}(r) = Acos\left(2\pi r/\lambda - \varphi\right)e^{-r/l_d} \quad (5)$$

Where l_d is the decay length of layering, λ is the wavelength fixed for the same type of the ion-pair (3.3 Å for K^+ - SCN^- and 4.0 Å for $BMIM^+$ - Cl^-), φ is the phase and *A* is the amplitude.

Relation between $G_{IRO}(r)$ and *RSF(q)*

The Fourier transform of eq. 5 yields the following reduced structure factor (normalized by the amplitude of G_{IRO}):

$$\frac{RSF}{A} = \frac{q(S(q)-1)}{A} = q\,\frac{(q^2-(2\pi/\lambda)^2+(1/l_d)^2)cos(\varphi)+2(2\pi/\lambda l_d)sin(\varphi)}{(q^2-(2\pi/\lambda)^2)^2+(1/l_d)^4+2(q^2+(2\pi/\lambda)^2)(1/l_d)^2} \quad (6)$$

From eq. 6 it is evident that the peak position of *RSF(q)* (which as defined as the first sharp diffraction peak, FSDP) is a complex function of the phase and decay length of G_{IRO}. Figure 2.15 further illustrates this dependence for the experimentally relevant values of λ, φ and l_d.

Molecular dynamics simulations

$BMIM^+Cl^-$ IL system was studied using the CLDP forcefield for ionic liquids, a timestep of 0.5 fs and a short-ranged pairwise cutoff distance of 12 Angstroms.[29] We ran molecular dynamics simulations using the LAMMPS software package,[48] and visualized trajectories using the VMD package.[49] The long-range part of the Coulomb interaction was implemented using the particle-particle particle-mesh scheme, with relative error of 10^{-4}.

Nanoparticles of CdSe, InP, and chemically inert types were implemented by setting short-range interactions equivalent to those of C2 carbons in the CLDP force field and including

appropriate partial charges.[50-51] Mixing the partial charges from a crystal model with the CLDP force field is necessarily approximate, but we expect it to be a reasonable approximation – and agreement between the simulation and experimental results bears out that expectation. The interatomic distances in the nanoparticle solutes were rigidly fixed. Our choice to model the short-range interaction in such an approximate way was informed by simulation work on ionic liquid interactions with Au electrodes where the Au short-range interactions were set as graphite carbons.[52] The most important factor by far appears to be the charge of the surface, with the short-range interactions providing only a perturbation. Since most of the ion specific interactions between the NC and the solvent is due to the Coulomb interaction, setting the charge of the NC to zero is effectively the same as making it chemically inert. And indeed, we observed that the structuring of the IL did not occur when the Coulomb interaction between nanoparticle and solvent was set to zero. Though not meant to be physically meaningful, this test confirms that the short-range interactions and exclusion volume due to the nanoparticle is not responsible for the restructuring of the IL.

Simulations were run at constant temperature and pressure with a temperature of 400K using the Nose-Hoover thermostat and a pressure of 1 bar using the Nose-Hoover barostat with coupling parameters of 500 fs and 1000 fs respectively. In runs with nanoparticles, the nanoparticles were allowed to rotate freely and were subject to a Langevin thermostatting at 400K.

Bulk simulations consisted of 480 $BMIM^+$ and 480 Cl^- ions. Simulations with nanoparticles consisted of two sets. In the first set, nanoparticles were cubic with sides approximately 3 nm in length. The nanoparticles were cut such that for CdSe (InP) there were three Cd (In) coated facets and three Se (P) coated facets. All facets were (100). For these simulations, 3630 $BMIM^+$ and 3630 Cl^- ions were used, leading to a cubic periodic box of roughly 10.5 nm in length. Larger simulations

with 3 nm nanoparticles and box sizes up to 20 nm in length were used to confirm finite size effects were not an issue for the 10.5 nm box size.

Radial distribution functions for all ion pairs were extracted from simulation trajectories. These were convoluted with appropriate atomic form factors for comparison with experiment.[53-55] Atomic form factors were approximated using sums of four Gaussians, which is a good approximation for small q.[56] The surface-induced correlations were also measured by computing the probability of observing the various fluid atom types in front of each surface of the nanoparticle as a function of the distance along surface normal. Similar post-processing with atomic form factors was required for comparison with experiment.

For comparison with experimental restructured reduced structure factors, the radial distribution functions of ion pairs were also extracted from solvent systems including nanoparticles. In these RSFs, crystal-crystal (Cd-Cd, Cd-Se, *etc*.) correlations were excluded from sums over all particle pairs, as otherwise, the crystal-crystal contributions dominate the less-ordered liquid-liquid and crystal-liquid contributions.

Estimation of the free energy of interaction for NCs in molten salt

The van der Waals (vdW) attraction V_{vdW} between CdSe/CdS NCs in NaSCN/KSCN molten salt can be evaluated using the Lifshitz theory. Since the distances of interest are on the order of a few nanometers, the retardation effects due to the finite speed of light can be ignored. The general expression for the vdW potential between the two spheres of radius R separated by a distance l at the point of the closest approach:[3]

$$V_{VdW}(l) = -\frac{A}{6}\left(\frac{2R^2}{(4R+l)l} + \frac{2R^2}{(2R+D)^2} + \ln\left(\frac{(4R+l)l}{(2R+l)^2}\right)\right) \quad (7)$$

Where *A* is a Hamaker coefficient defined by the medium's and interacting particles' dielectric functions:

$$A = \frac{3}{2}k_b T \sum_{q=1}^{\infty} \frac{1}{q^3} \sum_{n=0}^{\infty}{}' \left[\Delta(i\omega_n)\right]^{2q} \quad (8)$$

$$\Delta(i\omega_n) = \frac{\varepsilon_1(i\omega_n) - \varepsilon_3(i\omega_n)}{\varepsilon_1(i\omega_n) + \varepsilon_3(i\omega_n)} \quad (9)$$

Here T is temperature (= 473 K in case of NaSCN/KSCN molten salt) and k_b is the Boltzmann constant; ε_1 and ε_3 are the complex dielectric functions of particles (MXenes) and medium (liquid metal), respectively, evaluated at imaginary Matsubara frequencies, $\omega_n = n \cdot 2\pi k_b T / \hbar$. The subscript (') in the second sum in eq. 8 indicates that the zero frequency ($n = 0$) term has contribution of ½. However, since molten salts are infinitely polarizable media, the zero frequency term (equivalent to the electrostatic interaction) is screened as $e^{-\frac{l}{l_d}}$.[3] Hence, we can ignore the $n = 0$ term contribution to the Hamaker coefficient in eq. 8.

Here we approximate the dielectric functions of CdSe/CdS core-shell NC and NaSCN/KSCN molten salt as CdS and KCl, respectively. Since complex dielectric functions at 473 K (excluding the zero frequency term) are evaluated at integral multiples of $\omega_1 = 3.887 \cdot 10^{14} rad/s$ the spectral parameters in the near infrared and UV-visible ranges are of interest. It is common to approximate ε_1 and ε_3 using one UV and one IR relaxation terms:[57]

$$\varepsilon(i\omega_n) = 1 + \frac{C_{UV}}{1+\frac{\omega_n^2}{\omega_{UV}^2}} + \frac{C_{IR}}{1+\frac{\omega_n^2}{\omega_{IR}^2}} \tag{10}$$

Parameters for ε_1 of CdS

ω_{UV} (rad/s)	C_{UV}	ω_{IR} (rad/s)	C_{IR}
$6.92*10^{15}$	4.114	$4.6*10^{13}$	4.86

Parameters for ε_3 of KCl

ω_{UV} (rad/s)	C_{UV}	ω_{IR} (rad/s)	C_{IR}
$1.58*10^{16}$	1.17	$2.7*10^{13}$	2.23

The numerical calculation using eq. 8 with q_{max} = 30 and n_{max} = 20000 results in $A_{CdS/KCl/CdS}$ = 22.2 zJ.

The dielectric function for Pt NCs (R = 2 nm) can be represented with the familiar Drude free-electron model whose parameters are readily available in the literature:[58]

$$\varepsilon_1(i\omega_n) = 1 + \frac{\omega_{p1}^2}{\omega_n^2 + \gamma_1\omega_n} \tag{11}$$

Parameters for ε_1 of Pt

ω_{p1}(eV)	γ_1 (meV)
5.156	69.32

The numerical calculation using eq. 8 with q_{max} = 30 and n_{max} = 20000 results in $A_{Pt/KCl/Pt}$ = 71.9 zJ.

The oscillatory potential between CdSe/CdS NCs interacting through NaSCN/KSCN (approximated as KCl) molten salt V_{ocs} is evaluated using the continuum Ginsburg-Landau model under Derjaguin ($l << R$) approximation:[5]

$$V_{osc}(l) = \pi R F_0 q_0^{-1} \, \mathrm{e}^{-\frac{l}{l_d}} \left(\cos\left(q_0 l + \varphi\right) + \frac{l_d}{R} \right) \tag{12}$$

Here R is the radius of a NC, l is the interparticle separation, l_d = 0.496 nm is the decay length of layering (as in eq. 5), q_o = 15.373 nm^{-1} is the preferred wavenumber of layering, $\varphi = tan^{-1}\left(\frac{1}{l_d q_0}\right) = 7.472$ is the phase and F_0 is the energy scale. For KCl interacting with the Cd-terminated (100) facet of CdS NCs the energy scale can be estimated as $F_0 \sim \frac{\psi_0 l_d k_b T}{\sigma^3} = \frac{1*0.496*1.38*10^{-23}*473}{0.31^3} = 108.7\ zJ/nm^2$ (σ is related to the size of ions in the melt, 3.1 Å for KCl, ψ_0 is the ion density at the NC surface fixed by the strong binding affinity).

The purely repulsive contribution in eq. 12 scales as 1/R suggesting that larger particles are more likely to get kinetically trapped by large oscillatory barrier. This is likely the case for CdSe/CdS NCs with R = 6.45 nm in NaSCN/KSCN melt for which the experimentally observed interparticle distance of ~ 5 Å in "worm-like" aggregates is close to the computed secondary minimum at ~ 5 Å (Figure 2.6).

For smaller particles (e.g 4 nm Pt NCs) the Derjaguin approximation is no longer valid. Since majority of NCs are faceted, it is reasonable to approximate shape of Pt NCs by a spheroidal shape. Here we represent Pt NCs as a truncated icosidodecahedron. The total oscillatory potential is then a linear combination of the oscillatory potentials between one pair of parallel facets (decagons) and 5 pairs of tilted facets (squares and hexagons):

$$V_{osc}(l) = Area_{decagon} V_{\parallel}(l) + 5a \frac{1}{2\sin(\theta_{4,10})} \int_{l}^{l+2a\sin(\theta_{4,10})} dz\left[V_{\parallel}(z) + V_{tilt}(z, 2\theta_{4,10})\right]$$
$$+5\frac{1}{2\sin(\theta_{6,10})} \int_{l}^{l+4a\sin(\theta_{6,10})\cos(\pi/6)} dz\left[V_{\parallel}(z) + V_{tilt}(z, 2\theta_{6,10})\right] w(z-l) \quad (13)$$

$$V_{\parallel}(z) = -\frac{F_0}{2} e^{-\frac{z}{l_d}} \cos(q_0 z + \varphi) \quad (14)$$
$$V_{tilt}(z,\theta) = \frac{F_0}{l_d q_0} e^{-\frac{z}{l_d}} \theta^2$$
$$w(z-l) = a + (z-l)\frac{\tan(\pi/6)}{\sin(\theta_{6,10})}, (z-l) \le 2a\sin(\theta_{6,10})\cos(\pi/6)$$
$$w(z-l) = a(1+4\sin(\pi/6)) - (z-l), (z-l) > 2a\sin(\theta_{6,10})\cos(\pi/6)$$

Here F_0, q_0, l_d and φ have the same values as for the spherical geometry mentioned above; $\theta_{4,10}$ is the dihedral angle between decagon and square (142.62°); $\theta_{6,10}$ is the dihedral angle between decagon and hexagon (148.28°); and $a = R\sqrt[3]{\frac{4\pi}{3(95+50\sqrt{5})}} = 0.5452\ nm$ corresponds to the edge length of a truncated icosidodecahedron for a R = 2 nm Pt NC.

2.7 Chapter 2 bibliography.

1. Kamysbayev, V.; Srivastava, V.; Ludwig, N. B.; Borkiewicz, O. J.; Zhang, H.; Ilavsky, J.; Lee, B.; Chapman, K. W.; Vaikuntanathan, S.; Talapin, D. V., Nanocrystals in Molten Salts and Ionic Liquids: Experimental Observation of Ionic Correlations Extending beyond the Debye Length. *ACS Nano* **2019,** *13* (5), 5760-5770.

2. Murray, C. B.; Kagan, C. R.; Bawendi, M. G., Synthesis and Characterization of Monodisperse Nanocrystals and Close-Packed Nanocrystal Assemblies. *Annu. Rev. Mater. Sci.* **2000,** *30* (1), 545-610.

3. Israelachvili, J. N., *Intermolecular and surface forces*. Academic press: London, 2011.

4. Boles, M. A.; Ling, D.; Hyeon, T.; Talapin, D. V., The surface science of nanocrystals. *Nat. Mater.* **2016,** *15*, 141.

5. Zhang, H.; Dasbiswas, K.; Ludwig, N. B.; Han, G.; Lee, B.; Vaikuntanathan, S.; Talapin, D. V., Stable colloids in molten inorganic salts. *Nature* **2017,** *542*, 328.

6. Gebbie, M. A.; Dobbs, H. A.; Valtiner, M.; Israelachvili, J. N., Long-range electrostatic screening in ionic liquids. *Proc. Natl. Acad. Sci. U.S.A.* **2015,** *112* (24), 7432-7437.

7. Smith, A. M.; Lee, A. A.; Perkin, S., The Electrostatic Screening Length in Concentrated Electrolytes Increases with Concentration. *J. Phys. Chem. Lett.* **2016,** *7* (12), 2157-2163.

8. Lee, A. A.; Perez-Martinez, C. S.; Smith, A. M.; Perkin, S., Scaling Analysis of the Screening Length in Concentrated Electrolytes. *Phys. Rev. Lett.* **2017,** *119* (2), 026002.

9. Ludwig, N. B.; Dasbiswas, K.; Talapin, D. V.; Vaikuntanathan, S., Describing screening in dense ionic fluids with a charge-frustrated Ising model. *J. Chem. Phys.* **2018,** *149* (16), 164505.

10. Gebbie, M. A.; Smith, A. M.; Dobbs, H. A.; Lee, A. A.; Warr, G. G.; Banquy, X.; Valtiner, M.; Rutland, M. W.; Israelachvili, J. N.; Perkin, S.; Atkin, R., Long range electrostatic forces in ionic liquids. *Chem. Commun.* **2017,** *53* (7), 1214-1224.

11. Mezger, M.; Schröder, H.; Reichert, H.; Schramm, S.; Okasinski, J. S.; Schöder, S.; Honkimäki, V.; Deutsch, M.; Ocko, B. M.; Ralston, J.; Rohwerder, M.; Stratmann, M.; Dosch, H., Molecular Layering of Fluorinated Ionic Liquids at a Charged Sapphire (0001) Surface. *Science* **2008,** *322* (5900), 424-428.

12. Cremer, T.; Stark, M.; Deyko, A.; Steinrück, H. P.; Maier, F., Liquid/Solid Interface of Ultrathin Ionic Liquid Films: [C1C1Im][Tf2N] and [C8C1Im][Tf2N] on Au(111). *Langmuir* **2011,** *27* (7), 3662-3671.

13. Jeon, Y.; Sung, J.; Bu, W.; Vaknin, D.; Ouchi, Y.; Kim, D., Interfacial Restructuring of Ionic Liquids Determined by Sum-Frequency Generation Spectroscopy and X-Ray Reflectivity. *J. Phys. Chem. C* **2008,** *112* (49), 19649-19654.

14. Zobel, M.; Neder, R. B.; Kimber, S. A. J., Universal solvent restructuring induced by colloidal nanoparticles. *Science* **2015,** *347* (6219), 292-294.

15. Thomä, S. L. J.; Krauss, S. W.; Eckardt, M.; Chater, P.; Zobel, M., Atomic insight into hydration shells around facetted nanoparticles. *Nat. Commun.* **2019,** *10* (1), 995.

16. Futamura, R.; Iiyama, T.; Takasaki, Y.; Gogotsi, Y.; Biggs, M. J.; Salanne, M.; Ségalini, J.; Simon, P.; Kaneko, K., Partial breaking of the Coulombic ordering of ionic liquids confined in carbon nanopores. *Nat. Mater.* **2017,** *16*, 1225.

17. Zhang, H.; Jang, J.; Liu, W.; Talapin, D. V., Colloidal Nanocrystals with Inorganic Halide, Pseudohalide, and Halometallate Ligands. *ACS Nano* **2014,** *8* (7), 7359-7369.

18. Dirin, D. N.; Dreyfuss, S.; Bodnarchuk, M. I.; Nedelcu, G.; Papagiorgis, P.; Itskos, G.; Kovalenko, M. V., Lead Halide Perovskites and Other Metal Halide Complexes As Inorganic Capping Ligands for Colloidal Nanocrystals. *J. Am. Chem. Soc.* **2014,** *136* (18), 6550-6553.

19. Fafarman, A. T.; Koh, W.-k.; Diroll, B. T.; Kim, D. K.; Ko, D.-K.; Oh, S. J.; Ye, X.; Doan-Nguyen, V.; Crump, M. R.; Reifsnyder, D. C.; Murray, C. B.; Kagan, C. R., Thiocyanate-Capped Nanocrystal Colloids: Vibrational Reporter of Surface Chemistry and Solution-Based Route to Enhanced Coupling in Nanocrystal Solids. *J. Am. Chem. Soc.* **2011,** *133* (39), 15753-15761.

20. Li, T.; Senesi, A. J.; Lee, B., Small Angle X-ray Scattering for Nanoparticle Research. *Chem. Rev.* **2016,** *116* (18), 11128-11180.

21. Beaucage, G., Small-angle scattering from polymeric mass fractals of arbitrary mass-fractal dimension. *J. Appl. Crystallogr.* **1996,** *29* (2), 134-146.

22. Sorensen, C. M., Light Scattering by Fractal Aggregates: A Review. *Aerosol Sci. Technol.* **2001,** *35* (2), 648-687.

23. Liu, Y.; Han, X.; He, L.; Yin, Y., Thermoresponsive Assembly of Charged Gold Nanoparticles and Their Reversible Tuning of Plasmon Coupling. *Angew. Chem., Int. Ed.* **2012,** *51* (26), 6373-6377.

24. Zhang, H.; Wang, D., Controlling the Growth of Charged-Nanoparticle Chains through Interparticle Electrostatic Repulsion. *Angew. Chem., Int. Ed.* **2008,** *47* (21), 3984-3987.

25. Lee, B.; Podsiadlo, P.; Rupich, S.; Talapin, D. V.; Rajh, T.; Shevchenko, E. V., Comparison of Structural Behavior of Nanocrystals in Randomly Packed Films and Long-Range Ordered Superlattices by Time-Resolved Small Angle X-ray Scattering. *J. Am. Chem. Soc.* **2009,** *131* (45), 16386-16388.

26. Johnson, K.; Inman, D.; Saboungi, M.; Newman, D. *Proceedings of the fifth international symposium on molten salts*; The Electrochemical Society, Pennington, NJ: 1985.

27. Fannin, A. A.; King, L. A.; Seegmiller, D. W., Chloroaluminate Equilibria in AlCl3 - NaCl Melts. *J. Electrochem. Soc.* **1972,** *119* (7), 801-807.

28. Leote de Carvalho, R. J. F.; Evans, R., The decay of correlations in ionic fluids. *Mol. Phys.* **1994,** *83* (4), 619-654.

29. Canongia Lopes, J. N.; Deschamps, J.; Pádua, A. A. H., Modeling Ionic Liquids Using a Systematic All-Atom Force Field. *J. Phys. Chem. B* **2004,** *108* (6), 2038-2047.

30. Kim, T.-G.; Zherebetskyy, D.; Bekenstein, Y.; Oh, M. H.; Wang, L.-W.; Jang, E.; Alivisatos, A. P., Trap Passivation in Indium-Based Quantum Dots through Surface Fluorination: Mechanism and Applications. *ACS Nano* **2018,** *12* (11), 11529-11540.

31. Becker, G.; Gutekunst, G.; Witthauer, C., Trimethylsilylverbindungen der Vb-Elemente. II. Molekül- und KristallStruktur des Tetrakis(trimethylsilyl)-diarsans. *Z. Anorg. Allg. Chem.* **1982,** *486* (1), 90-101.

32. Wang, C.; Daimon, H.; Onodera, T.; Koda, T.; Sun, S., A General Approach to the Size- and Shape-Controlled Synthesis of Platinum Nanoparticles and Their Catalytic Reduction of Oxygen. *Angew. Chem., Int. Ed.* **2008,** *47* (19), 3588-3591.

33. Mohamed, M. B.; Tonti, D.; Al-Salman, A.; Chemseddine, A.; Chergui, M., Synthesis of High Quality Zinc Blende CdSe Nanocrystals. *J. Phys. Chem. B* **2005,** *109* (21), 10533-10537.

34. Joo, J.; Yu, T.; Kim, Y. W.; Park, H. M.; Wu, F.; Zhang, J. Z.; Hyeon, T., Multigram Scale Synthesis and Characterization of Monodisperse Tetragonal Zirconia Nanocrystals. *J. Am. Chem. Soc.* **2003,** *125* (21), 6553-6557.

35. Guzelian, A. A.; Banin, U.; Kadavanich, A. V.; Peng, X.; Alivisatos, A. P., Colloidal chemical synthesis and characterization of InAs nanocrystal quantum dots. *Appl. Phys. Lett.* **1996,** *69* (10), 1432-1434.

36. Xie, R.; Battaglia, D.; Peng, X., Colloidal InP Nanocrystals as Efficient Emitters Covering Blue to Near-Infrared. *J. Am. Chem. Soc.* **2007,** *129* (50), 15432-15433.

37. Chen, O.; Zhao, J.; Chauhan, V. P.; Cui, J.; Wong, C.; Harris, D. K.; Wei, H.; Han, H.-S.; Fukumura, D.; Jain, R. K.; Bawendi, M. G., Compact high-quality CdSe–CdS core–shell nanocrystals with narrow emission linewidths and suppressed blinking. *Nat. Mater.* **2013,** *12*, 445.

38. Huang, J.; Liu, W.; Dolzhnikov, D. S.; Protesescu, L.; Kovalenko, M. V.; Koo, B.; Chattopadhyay, S.; Shenchenko, E. V.; Talapin, D. V., Surface Functionalization of Semiconductor and Oxide Nanocrystals with Small Inorganic Oxoanions (PO43–, MoO42–) and Polyoxometalate Ligands. *ACS Nano* **2014,** *8* (9), 9388-9402.

39. Dong, A.; Ye, X.; Chen, J.; Kang, Y.; Gordon, T.; Kikkawa, J. M.; Murray, C. B., A Generalized Ligand-Exchange Strategy Enabling Sequential Surface Functionalization of Colloidal Nanocrystals. *J. Am. Chem. Soc.* **2011,** *133* (4), 998-1006.

40. Nag, A.; Kovalenko, M. V.; Lee, J.-S.; Liu, W.; Spokoyny, B.; Talapin, D. V., Metal-free Inorganic Ligands for Colloidal Nanocrystals: S2–, HS–, Se2–, HSe–, Te2–, HTe–, TeS32–, OH–, and NH2– as Surface Ligands. *J. Am. Chem. Soc.* **2011,** *133* (27), 10612-10620.

41. Kovalenko, M. V.; Bodnarchuk, M. I.; Talapin, D. V., Nanocrystal Superlattices with Thermally Degradable Hybrid Inorganic−Organic Capping Ligands. *J. Am. Chem. Soc.* **2010,** *132* (43), 15124-15126.

42. Kovalenko, M. V.; Scheele, M.; Talapin, D. V., Colloidal Nanocrystals with Molecular Metal Chalcogenide Surface Ligands. *Science* **2009,** *324* (5933), 1417-1420.

43. Ilavsky, J.; Jemian, P. R., Irena: tool suite for modeling and analysis of small-angle scattering. *J. Appl. Crystallogr.* **2009,** *42* (2), 347-353.

44. Beaucage, G., Approximations Leading to a Unified Exponential/Power-Law Approach to Small-Angle Scattering. *J. Appl. Crystallogr.* **1995,** *28* (6), 717-728.

45. Chupas, P. J.; Chapman, K. W.; Kurtz, C.; Hanson, J. C.; Lee, P. L.; Grey, C. P., A versatile sample-environment cell for non-ambient X-ray scattering experiments. *J. Appl. Crystallogr.* **2008,** *41* (4), 822-824.

46. Toby, B. H.; Von Dreele, R. B., GSAS-II: the genesis of a modern open-source all purpose crystallography software package. *J. Appl. Crystallogr.* **2013,** *46* (2), 544-549.

47. Qiu, X.; Thompson, J. W.; Billinge, S. J. L., PDFgetX2: a GUI-driven program to obtain the pair distribution function from X-ray powder diffraction data. *J. Appl. Crystallogr.* **2004,** *37* (4), 678.

48. Plimpton, S., Fast Parallel Algorithms for Short-Range Molecular Dynamics. *J. Comput. Phys.* **1995,** *117* (1), 1-19.

49. Humphrey, W.; Dalke, A.; Schulten, K., VMD: Visual molecular dynamics. *J. Mol. Graphics* **1996,** *14* (1), 33-38.

50. Grünwald, M.; Zayak, A.; Neaton, J. B.; Geissler, P. L.; Rabani, E., Transferable pair potentials for CdS and ZnS crystals. *J. Chem. Phys.* **2012,** *136* (23), 234111.

51. Han, P.; Bester, G., Interatomic potentials for the vibrational properties of III-V semiconductor nanostructures. *Phys. Rev. B* **2011,** *83* (17), 174304.

52. Hu, Z.; Vatamanu, J.; Borodin, O.; Bedrov, D., A molecular dynamics simulation study of the electric double layer and capacitance of [BMIM][PF6] and [BMIM][BF4] room temperature ionic liquids near charged surfaces. *Phys. Chem. Chem. Phys.* **2013,** *15* (34), 14234-14247.

53. Migliorati, V.; Serva, A.; Aquilanti, G.; Pascarelli, S.; D'Angelo, P., Local order and long range correlations in imidazolium halide ionic liquids: a combined molecular dynamics and XAS study. *Phys. Chem. Chem. Phys.* **2015,** *17* (25), 16443-16453.

54. Pings, C. J.; Waser, J., Analysis of Scattering Data for Mixtures of Amorphous Solids or Liquids. *J. Chem. Phys.* **1968,** *48* (7), 3016-3018.

55. Santos, C. S.; Annapureddy, H. V. R.; Murthy, N. S.; Kashyap, H. K.; Jr., E. W. C.; Margulis, C. J., Temperature-dependent structure of methyltributylammonium bis(trifluoromethylsulfonyl)amide: X ray scattering and simulations. *J. Chem. Phys.* **2011,** *134* (6), 064501.

56. Brown, P. J.; Fox, A. G.; Maslen, E. N.; O'Keefe, M. A.; Willis, B. T. M., International Tables for Crystallography. 2006; Vol. C, pp 554-595.

57. Bergström, L., Hamaker constants of inorganic materials. *Adv. Colloid Interface Sci.* **1997,** *70*, 125-169.

58. Ordal, M. A.; Bell, R. J.; Alexander, R. W.; Long, L. L.; Querry, M. R., Optical properties of fourteen metals in the infrared and far infrared: Al, Co, Cu, Au, Fe, Pb, Mo, Ni, Pd, Pt, Ag, Ti, V, and W. *Appl. Opt.* **1985,** *24* (24), 4493-4499.

3 Covalent surface modification of 2D titanium carbides (MXenes)

3.1 Introduction to MXenes with selective surface terminations, T_n.

In contrast to more mature 2D materials, such as graphene and transition metal dichalcogenides, MXenes have chemically modifiable surfaces that offer additional engineerability. MXenes are typically synthesized from the corresponding MAX phases, where M stands for the transition metal (e.g., Ti, Nb, Mo, V, W, etc.) and X stands for C or N, by selectively etching the main group element A (e.g., Al, Ga, Si, etc.). The etching is usually performed in aqueous HF solutions rendering MXenes terminated with a mixture of F, O, and OH functional groups, commonly denoted as T_x (Figure 3.1). Recent theoretical studies predict that selective terminations of MXenes with different surface groups can lead to remarkable properties, such as opening or closing bandgap,[1] room-temperature electron mobility exceeding 10^4 $cm^2/V{\cdot}s$,[2] widely tunable work functions,[3] half-metallicity, and 2D ferromagnetism.[4] Covalent functionalization of MXene surfaces is expected to uncover new directions for rational engineering of 2D functional materials.

The surface of MXene sheets is defined during MAX phase etching. Electrochemical and hydrothermal methods have been recently applied for etching MAX phases without resorting to HF, but the use of aqueous solutions introduces a mixture of Cl, O, and OH surface groups.[5-6] The etching of Ti_3AlC_2 MAX phase in molten $ZnCl_2$ and several other Lewis acidic molten salts above 500°C results in $Ti_3C_2Cl_2$ MXene with pure Cl termination (Figure 3.1).[7-8] Since etching of MAX phases in molten salts eliminates undesired oxidation and hydrolysis, we used a variation of this method for synthesis of $Ti_3C_2Cl_2$ and Ti_2CCl_2 MXenes in $CdCl_2$ molten salt. Moreover, the use of Lewis acidic $CdBr_2$ allowed us to extend the molten salt etching route beyond chlorides to prepare the first Br-terminated $Ti_3C_2Br_2$ and Ti_2CBr_2 MXenes. The morphology, structure, and

composition of all new MXenes were characterized using high-resolution scanning transmission electron microscopy (STEM), Raman spectroscopy, and a combination of X-ray methods, including energy-dispersive elemental mapping, diffraction, fluorescence, absorption and photoelectron spectroscopy.

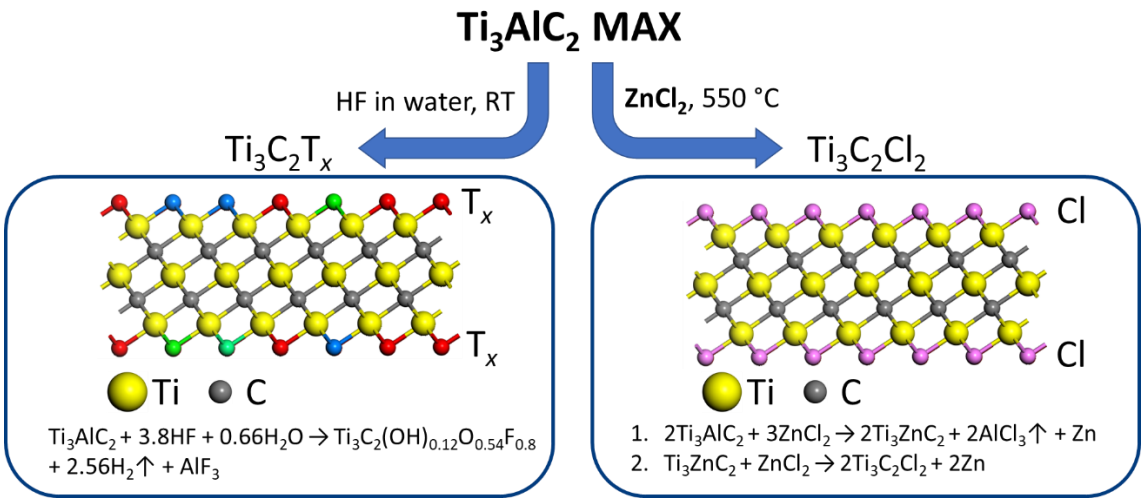

Figure 3.1. Schematic for synthesis of MXenes with mixed (T_x) and controlled (T_n = Cl_2) surface terminations.
Side views of $Ti_3C_2T_x$ and $Ti_3C_2Cl_2$ MXenes.

The transition metal atoms from the outer layers of MXene sheets (Ti, Mo, Ta, V) form relatively weak M-Cl and M-Br bonds, in comparison to M-F and M-OH bonds typical for MXenes with T_x surface groups. This point can be demonstrated by the enthalpies of formation for $TiBr_4$ (-617 kJ mol^{-1}), $TiCl_4$ (-804 kJ mol^{-1}) vs. TiF_4 (-1649 kJ mol^{-1}), as well as by direct comparison of the bond energies (Table 3.1). Strong Ti-F and Ti-O bonds make it difficult to perform any postsynthetic covalent surface modifications of MXenes.[9] In contrast, Cl- and Br-terminated MXenes with labile surface bonding act as versatile synthons for further chemical transformations.

Table 3.1. Bond dissociation energies for M-O and M-X bonds relevant for this study.

Bond	Bond dissociation energy at 298 K (kJ/mol)
Ti-O	666.5±5.6
Ti-F	569±33
Ti-Cl	405.4±10.5
Ti-Br	373
Nb-O	726.5±10.6
Nb-Cl	393
Nb-Br	347

Here we show that Cl- and, especially, Br-terminated MXenes can efficiently engage in a new type of surface reactions where halide ions exchange for other atoms and functional groups. In addition to Cl and Br terminated MXenes, successful synthesis of MXenes with O, NH, S, Se, and Te surface terminations, as well as bare MXenes (no surface termination) is demonstrated. These MXenes show unique structural and electronic properties.

3.2 $Ti_3C_2T_n$ MXenes.

The structure of $Ti_3C_2Cl_2$ MXene can be approximated using $P6_3/mmc$ space group (space group of the parent Ti_3AlC_2 MAX phase) with the two lattice parameters: in-plane, *a*, and out of plane, *c* (Figure 3.2A). The successful MXene synthesis can be visualized from the shift of (0002) and $(11\bar{2}0)$ peaks to lower angles compared to that of the parent MAX phase (Figure 3.2B, C). In the direct space these changes are reflected by the increase of both *a* and *c* lattice parameters. Initial Ti_3AlC_2 MAX phase contains small amounts of bulk fcc-TiC_x (*Fm-3m* space group) which propagates into the final MXene product.

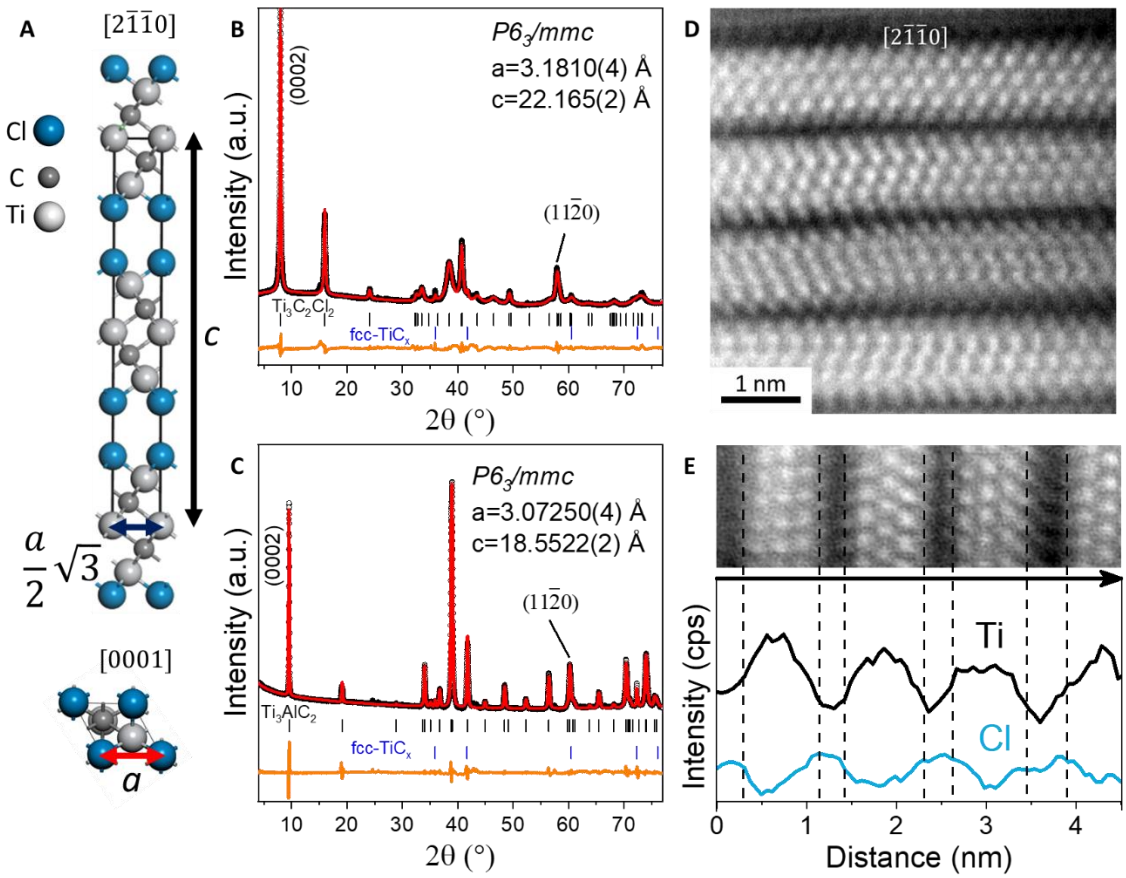

Figure 3.2. Structure of $Ti_3C_2Cl_2$ MXene.
(A) Side and top views of $Ti_3C_2Cl_2$ MXene structure. Experimental XRD patterns (Cu Kα, reflection, black curve), Le Bail fits (red curve) and the corresponding residues (orange curves) of (B) $Ti_3C_2Cl_2$ MXene derived from Ti_3AlC_2 MAX phase in (C). (D) STEM-HAADF image of $Ti_3C_2Cl_2$ MXene. (E) Ti Kα and Cl Kα EDX elemental line scans.

Atomic-column resolved scanning transmission electron microscopy (STEM) high angle annular dark field (HAADF) image of $Ti_3C_2Cl_2$ MXenes along [2$\bar{1}\bar{1}$0] zone axis (Figure 3.2D) clearly shows presence of 7 atom thick MXene sheets (2 layers of carbon atoms are not visualized due to their low Z constrast). The energy dispersive X-ray (EDX) elemental line scans further suggest that the outermost layers of Ti_3C_2 sheet are Cl atoms.

In contrast to etching in $ZnCl_2$ molten salt, where formation of $Ti_3C_2Cl_2$ MXene proceeds through Ti_3ZnC_2 MAX phase as an intermediate (Figure 3.1),[7] etching in $CdCl_2$ molten salt results

in $Ti_3C_2Cl_2$ MXene directly due to the absence of a thermodynamically stable Ti_3CdC_2 MAX phase.[10] This difference has strong implications on the purity of final product (Figure 3.3). Etching in $CdCl_2$ results in $Ti_3C_2Cl_2$ MXene with minimum Cd contamination (~ 1 mol. % w.r.t. Ti) unlike contamination with Zn (10 mol. % w.r.t. Ti) in case of etching in $ZnCl_2$ molten salt.

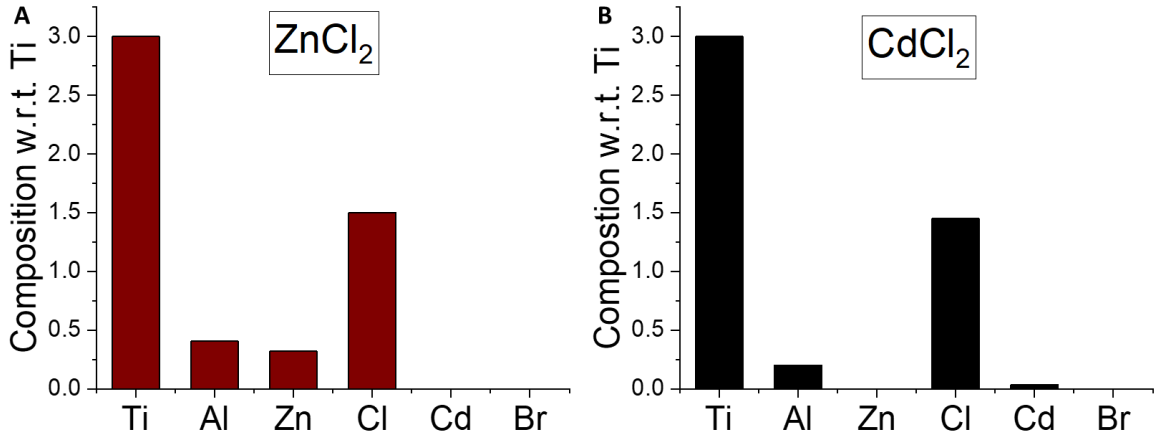

Figure 3.3. XRF analysis for the purified $Ti_3C_2Cl_{1.5}$ MXene (approximated as $Ti_3C_2Cl_2$). $Ti_3C_2Cl_2$ MXene obtained through etching of Ti_3AlC_2 in (A) $ZnCl_2$ and (B) $CdCl_2$ molten salts.

The use of $CdBr_2$ with a boiling point of 844 °C allows us to further extend the molten salt etching route to obtain the purely Br terminated $Ti_3C_2Br_2$ MXene (Figure 3.4). $Ti_3C_2Br_2$ MXene have enlarged *a* and *c* lattice parameters compared to that of $Ti_3C_2Cl_2$ MXene, consistent with Br having larger van der Waals radius.

MXene surface exchange reactions typically require temperatures of 300 °C to 600 °C, which are difficult to achieve using traditional solvents. Instead, we used molten alkali metal halides as solvents with unmatched high-temperature stability, high solubility of various ionic compounds, and wide electrochemical windows.[11-13] For example, $Ti_3C_2Br_2$ MXene (Figure 3.5B) dispersed in CsBr/KBr/LiBr eutectic (m.p. 236°C) can react with Li_2Te, Li_2Se and Li_2S to form new Ti_3C_2Te (Figure 3.5D and Figure 3.6), Ti_3C_2Se (Figure 3.7) and Ti_3C_2S (Figure 3.5E and Figure 3.8) MXenes, respectively.

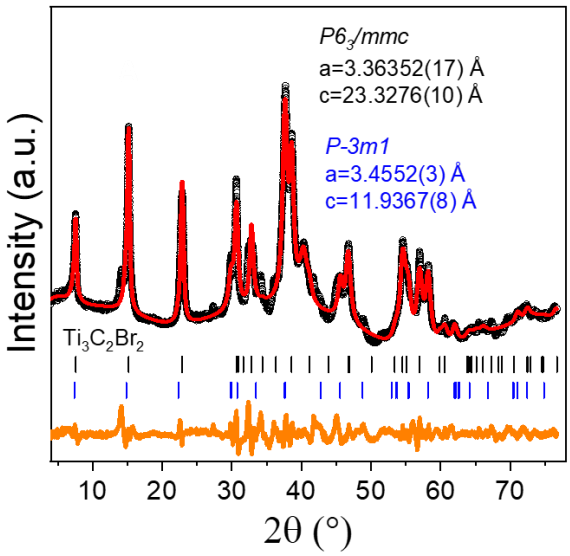

Figure 3.4. XRD pattern of $Ti_3C_2Br_2$.
XRD pattern (Cu Kα, reflection, black curve) and corresponding Le Bail fit (red curve) of $Ti_3C_2Br_2$ MXene. In contrast to $Ti_3C_2Cl_2$ MXene for which *P6₃/mmc* space group can account for all the peaks in the diffraction pattern, $Ti_3C_2Br_2$ MXene requires addition of *P-3m1* space group with a slightly different *a* lattice parameter.

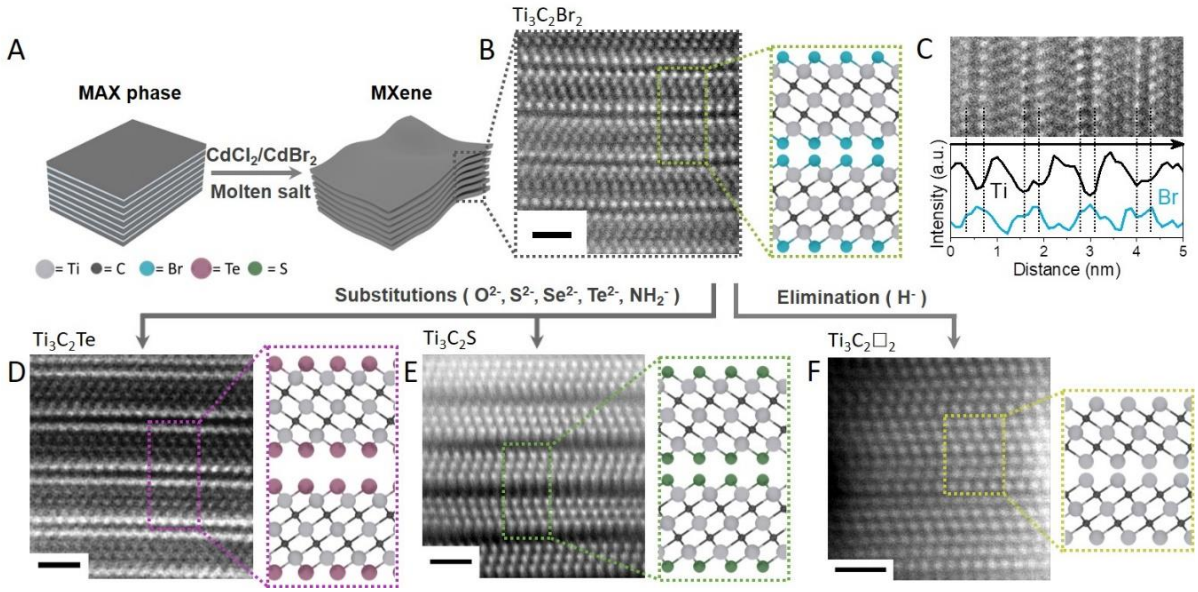

Figure 3.5. Surface reactions of $Ti_3C_2T_n$ MXenes in molten inorganic salts.
(A) Schematics for etching of MAX phases in Lewis acidic molten salts. (B) Atomic resolution STEM-HAADF image of $Ti_3C_2Br_2$ MXene sheets synthesized by etching Ti_3AlC_2 MAX phase in $CdBr_2$ molten salt. The electron beam is parallel to $[2\bar{1}\bar{1}0]$ zone axis. (C) EDX elemental analysis (line scan) of $Ti_3C_2Br_2$ MXene sheets. HAADF images of (D) Ti_3C_2Te and (E) Ti_3C_2S MXenes obtained by substituting Br for Te and S surface groups, respectively. (F) HAADF image of $Ti_3C_2□_2$ MXene (□ stands for the vacancy) obtained by reactive elimination of Br surface groups. All scale bars are 1 nm.

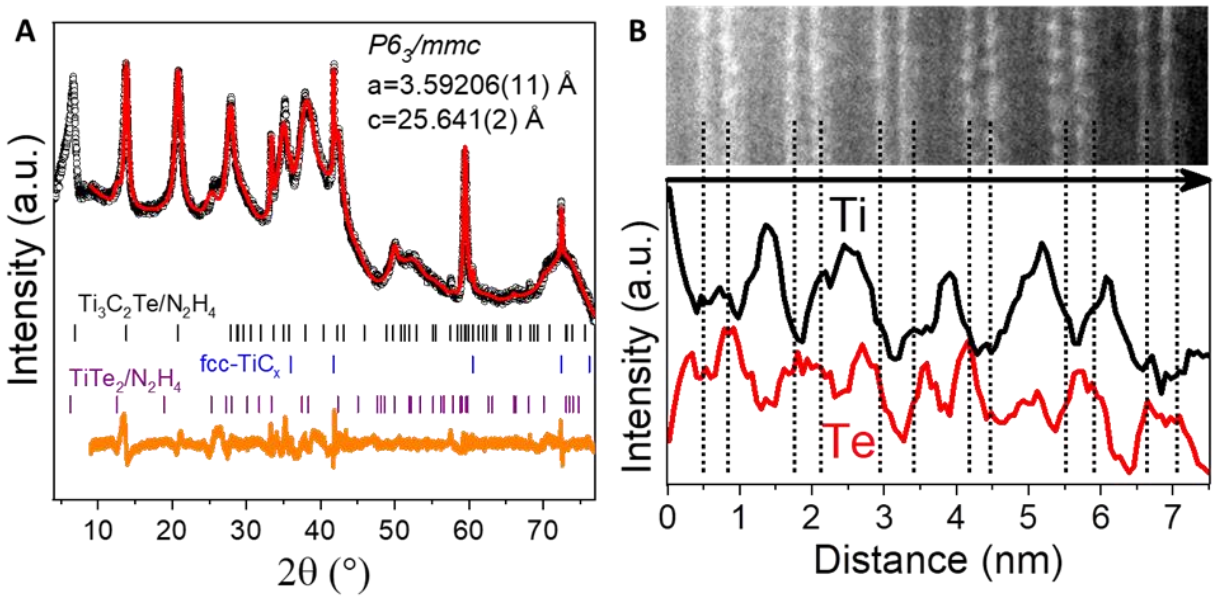

Figure 3.6. Characterization of Ti_3C_2Te MXene.
(A) Experimental XRD pattern (Cu Kα, reflection, black curve) and Le Bail fit (red curve) of Ti_3C_2Te MXene derived from $Ti_3C_2Br_2$ MXene. Ti_3C_2Te MXene was recovered from the salt matrix using anhydrous N_2H_4. (B) The EDX elemental line scans of Ti_3C_2Te MXene using Ti Kα and Te Lα suggest presence of Te surface groups on each Ti_3C_2 sheet.

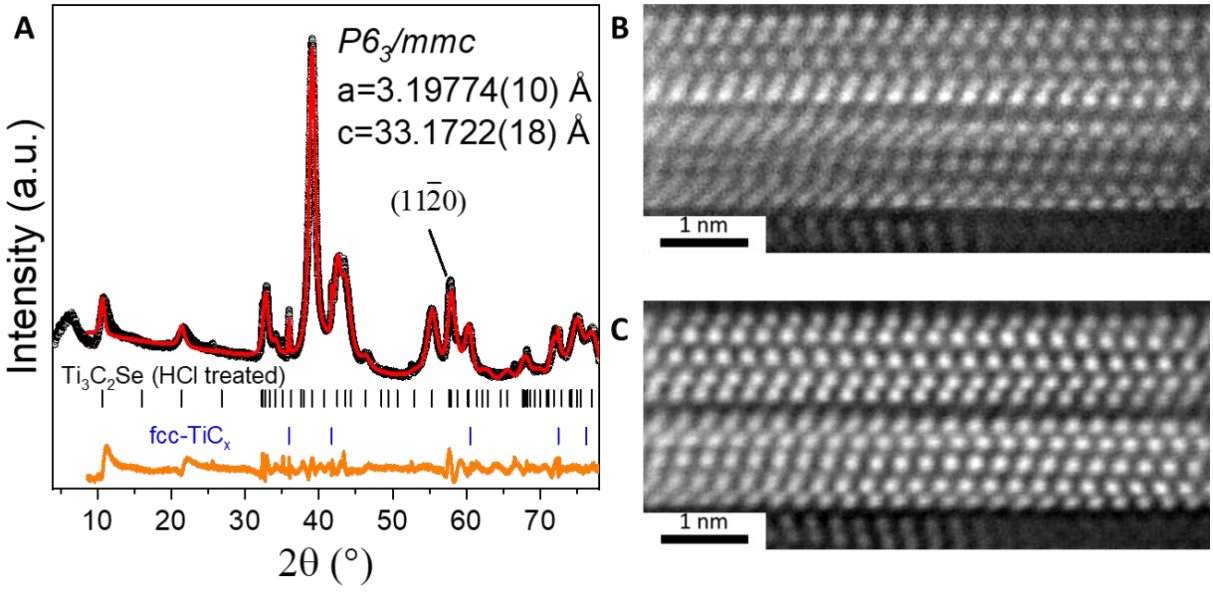

Figure 3.7. Characterization of Ti_3C_2Se MXene.
(A) Experimental XRD pattern (Cu Kα, reflection, black curve) and Le Bail fit (red curve) of Ti_3C_2Se MXene recovered from the salt matrix using anhydrous hydrazine and subsequently washed with aqueous HCl (black curve) to remove traces of bulk zb-CdSe. (B) HAADF and (C) LAADF images of Ti_3C_2Se MXene.

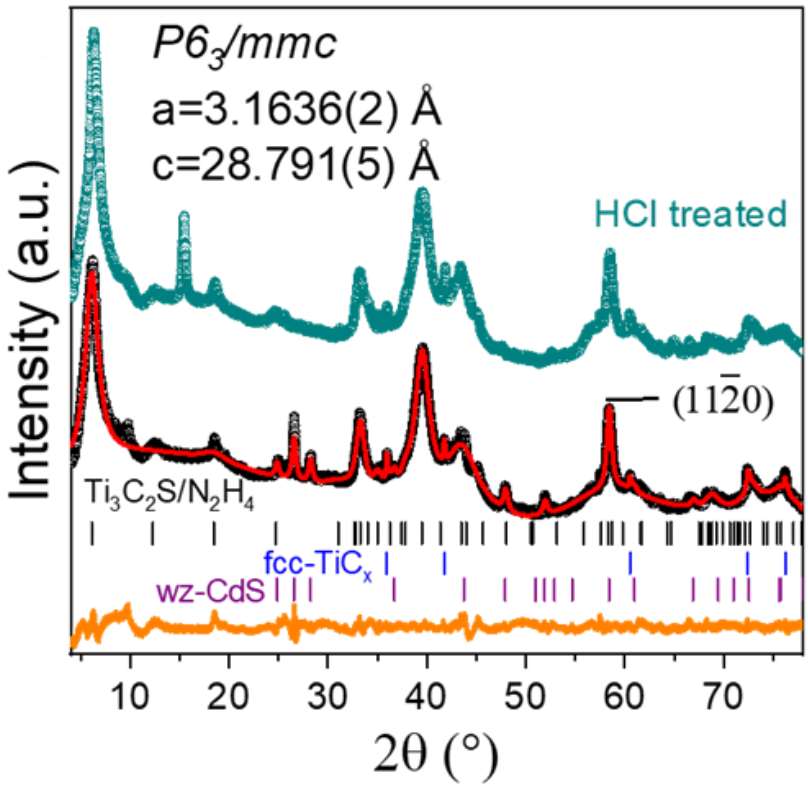

Figure 3.8. XRD pattern of Ti_3C_2S MXene.
Experimental XRD pattern (Cu Kα, reflection, black curve) and Le Bail fit (red curve) of Ti_3C_2S MXene derived from $Ti_3C_2Br_2$ MAX phase. Ti_3C_2S MXene was recovered from the salt matrix using anhydrous hydrazine (black curve) and subsequently washed with aqueous HCl (dark cyan) to remove traces of bulk wz-CdS.

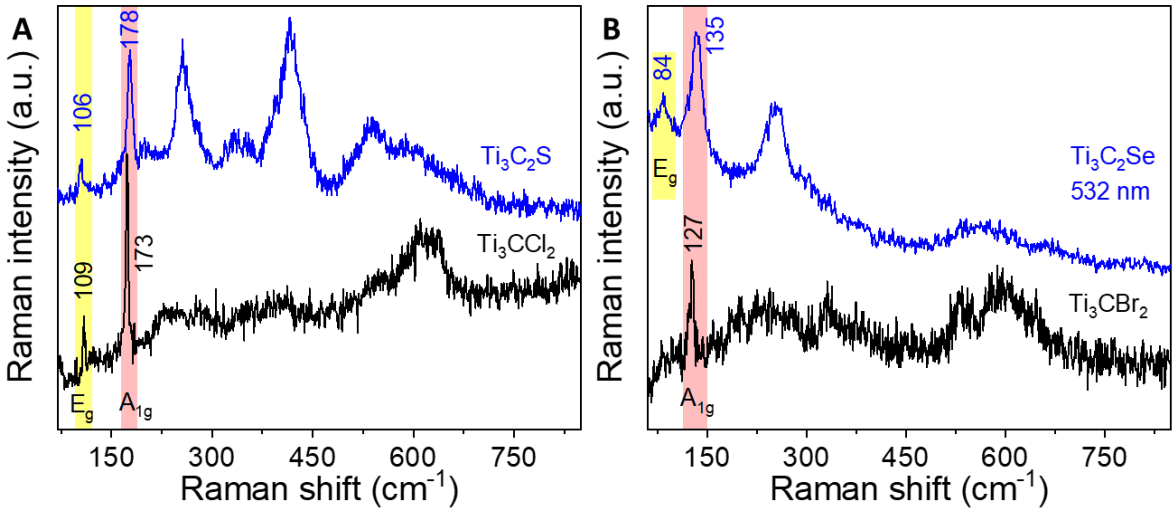

Figure 3.9. Raman spectra of Ti_3C_2(S, Cl, Se, Br) MXene.
Raman spectra of Ti_3C_2 MXene functionalized with (A) Cl, S and (B) Br, Se surface groups.

Figure 3.9 shows Raman spectra for $Ti_3C_2T_n$ MXenes with S, Cl, Se and Br surface groups. The position of the A_{1g} mode (red area) corresponding to the out-of-plane vibration of the surface groups is primarily determined by the atomic mass of the surface group with Br and Se resulting in lower frequencies than Cl and S. Similar trend holds for the E_g mode (yellow area) corresponding to the in-plane vibration of the surface groups and outer Ti atoms.[14]

XPS shows that the original Br peaks were replaced with the Te peaks after surface exchange in molten salt (Figure 3.8). High resolution XPS spectra (Figure 3.9 and Table 3.2) suggest that the Ti-C component binding energy of $Ti_3C_2Br_2$ MXene shifts to a lower value after Br^- has been substituted for Te^{2-}. This Br. Te 3d region of Ti_3C_2Te MXene can be modelled using two components: Te^{2-} as the major component (83 %) and Te in higher oxidation state (probably in the form of Te_n^{2-}) as the minor component (17 %).

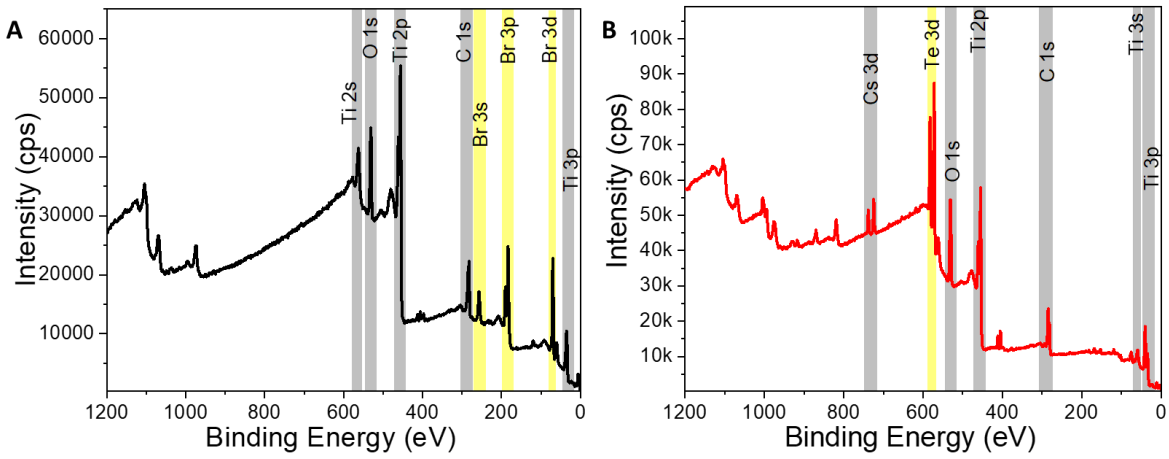

Figure 3.10. XPS survey spectra of $Ti_3C_2Br_2$ and Ti_3C_2Te MXenes.
The Cs 3d peak in (B) corresponds to either intercalated Cs^+ ions or residue Cs^+X^- salt.

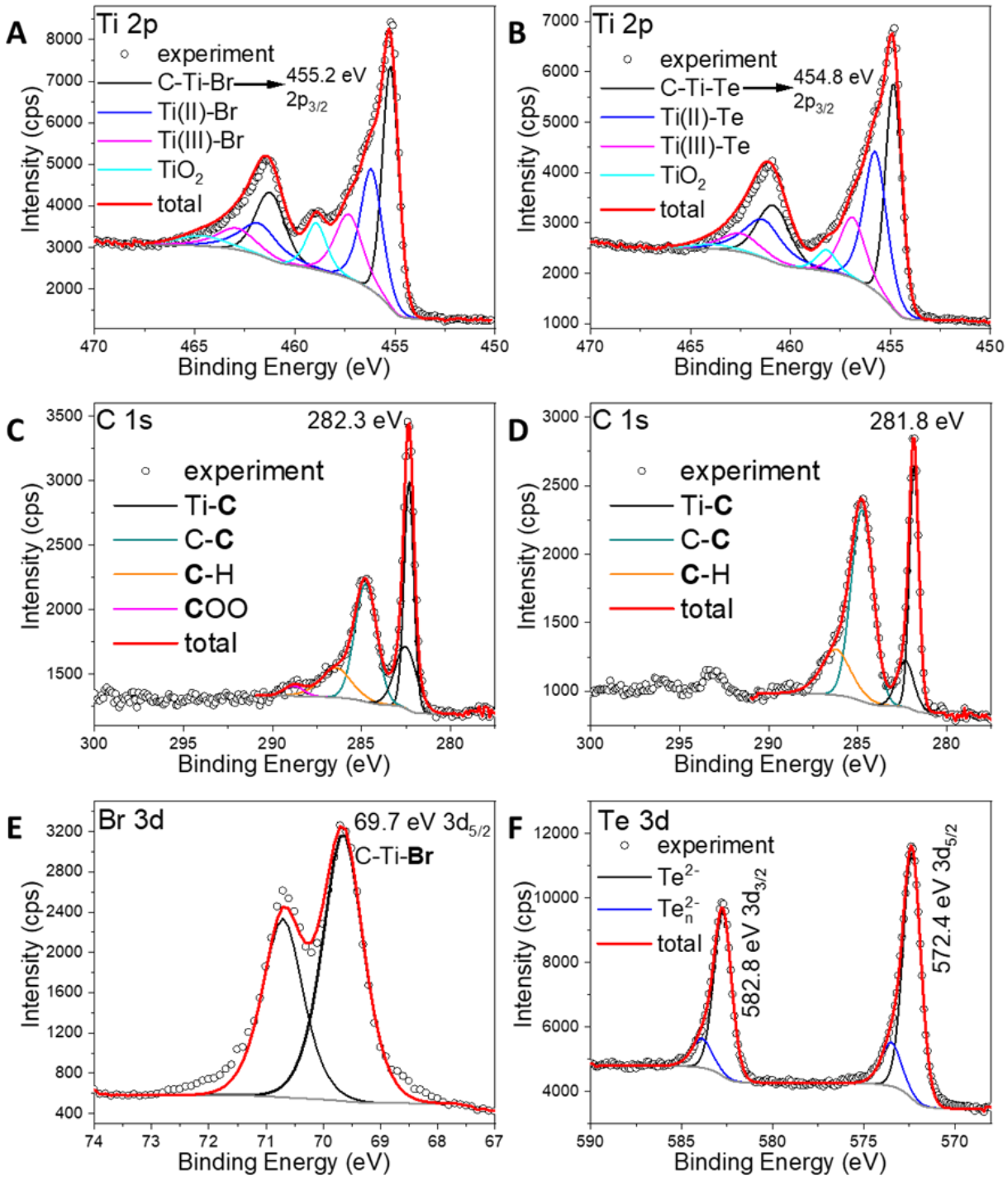

Figure 3.11. High resolution XPS spectra of $Ti_3C_2Br_2$ and Ti_3C_2Te MXenes.
See materials and methods section for XPS fitting details.

Table 3.2. $Ti_3C_2Br_2$ and Ti_3C_2Te MXene XPS fitting results.

	BE (eV)	FWHM (eV)	Fraction	Assigned to
Ti $2p_{3/2}$ ($2p_{1/2}$)	455.2 (461.2)	0.95 (1.71)	0.41	C-Ti-Br
	456.2 (461.8)	1.28 (2.3)	0.29	Ti(II)-Br
	457.3 (462.9)	1.63 (2.3)	0.19	Ti(III)-Br
	458.9 (464.6)	1.21 (2.8)	0.11	TiO_2
C 1s	282.3	0.63	0.31	C-Ti-Br
	282.5	1.42	0.19	C-Ti-Br
	284.8	1.44	0.35	C-C
	286.4	2	0.13	C-H
	288.8	1.25	0.02	-COO
Br $3d_{5/2}$ ($3d_{3/2}$)	69.7 (70.7)	0.83 (0.83)	1	C-Ti-Br

	BE (eV)	FWHM (eV)	Fraction	Assigned to
Ti $2p_{3/2}$ ($2p_{1/2}$)	454.8 (460.8)	0.95 (1.9)	0.41	C-Ti-Te
	455.8 (461.4)	1.34 (2.3)	0.37	Ti(II)-Te
	456.9 (462.5)	1.48 (2.3)	0.18	Ti(III)-Te
	458.2 (463.9)	1.18 (2.8)	0.04	TiO_2
C 1s	281.8	0.60	0.26	C-Ti-Te
	282.3	1.14	0.09	C-Ti-Te
	284.8	1.46	0.48	C-C
	286.2	1.91	0.17	C-H
Te $3d_{5/2}$ ($3d_{3/2}$)	572.4 (582.8)	1.14 (1.14)	0.83	Te^{2-}
	573.5 (583.9)	1.30 (1.30)	0.17	Te_n^{2-}

The reactions of $Ti_3C_2Cl_2$ and $Ti_3C_2Br_2$ with Li_2O, $NaNH_2$ and LiH yield Ti_3C_2O, $Ti_3C_2(NH)$ and bare $Ti_3C_2\square_2$ MXenes (where □ stands for the vacancy site), respectively (Figure 3.12 and Figure 3.5F). Since H-terminations are difficult to reveal by STEM (Figure 3.5F) and other methods, we based this conclusion on the experimental value of the center-to-center distance

between the Ti_3C_2 sheets (7.59 Å), which is substantially smaller than the theoretical prediction for $Ti_3C_2H_2$ MXene (8.26 Å) and close to the smallest theoretically possible spacing of 7.23 Å.[15] Since XPS shows reduction of Ti after removal of the hydride groups (Figure 3.13), this process can be formally described as a reductive elimination step following the exchange reaction.

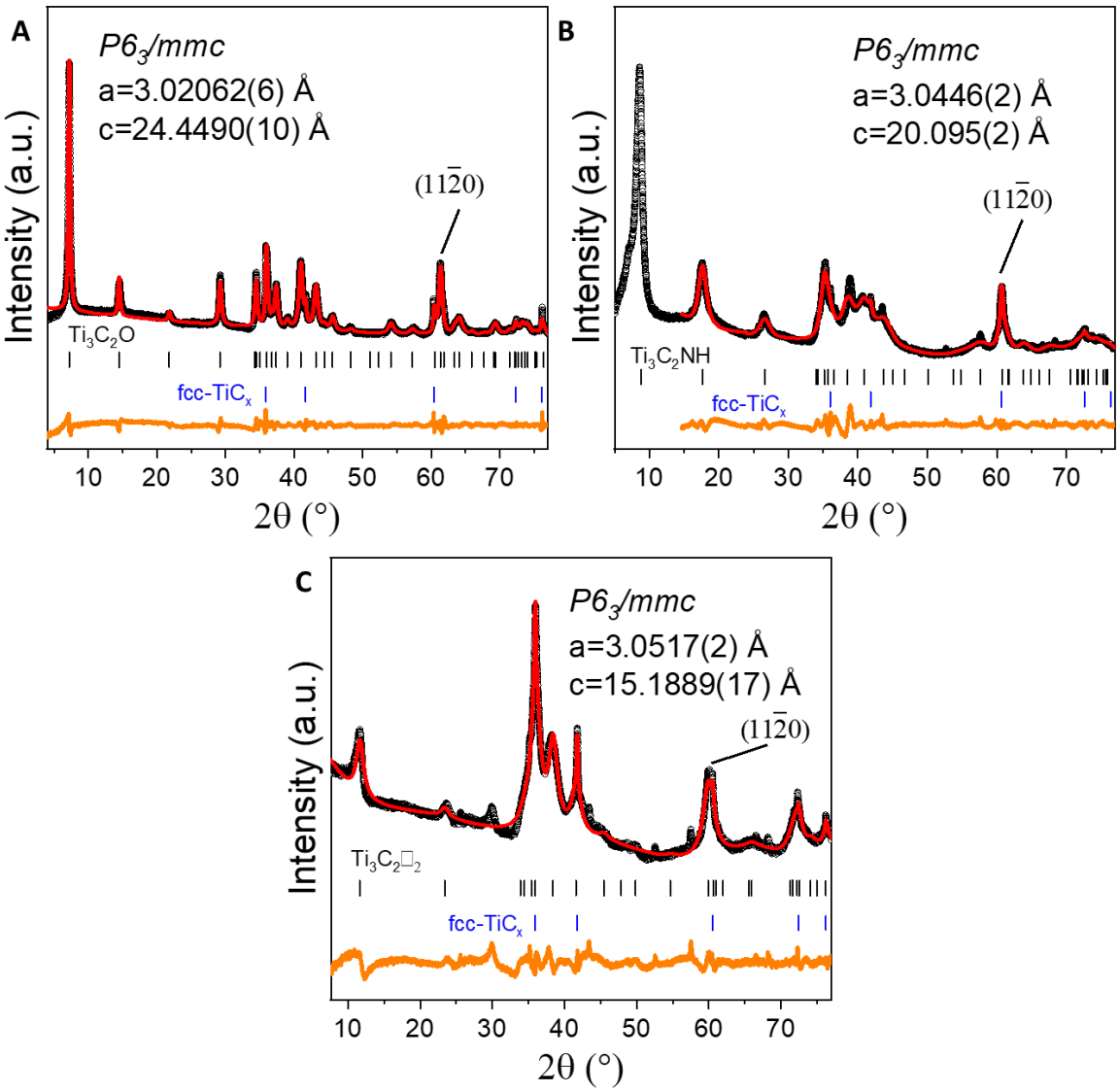

Figure 3.12. XRD patterns of Ti_3C_2(O, NH, □) MXenes.
Experimental XRD patterns (Cu Kα, reflection, black curves) and Le Bail fits (red curves) of: (A) Ti_3C_2O; (B) Ti_3C_2(NH); (C) bare $Ti_3C_2□_2$.

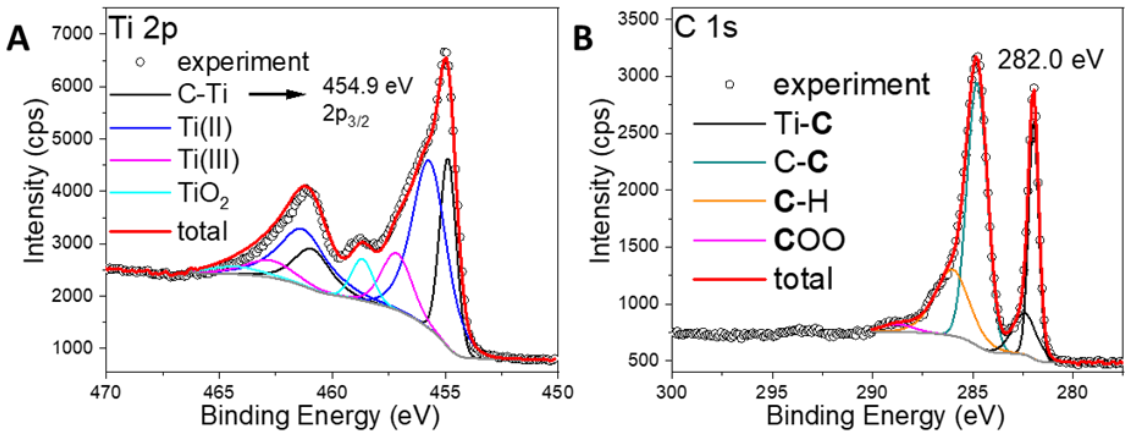

Figure 3.13. XPS spectra of $Ti_3C_2□_2$ MXene.
(A), (B) High resolution XPS spectra (see XPS section and Table S9 for fitting details) of $Ti_3C_2□_2$ MXene. The Ti-C component binding energy of $Ti_3C_2Br_2$ MXene (Figure 3.11) shifts to a lower value after Br^- has been eliminated with H^-.

Table 3.3. Ti3C2□2 MXene XPS fitting results.

	BE (eV)	FWHM (eV)	Fraction	Assigned to
Ti $2p_{3/2}$ ($2p_{1/2}$)	454.9 (460.9)	0.86 (1.89)	0.26	C-Ti
	455.7 (461.3)	1.78 (2.5)	0.51	Ti(II)
	457.1 (462.7)	1.58 (2.5)	0.15	Ti(III)
	458.7 (464.3)	1.14 (2.8)	0.08	TiO_2
C 1s	282.0	0.58	0.21	C-Ti
	282.4	1.44	0.09	C-Ti
	284.8	1.19	0.47	C-C
	286.0	2.00	0.21	C-H
	288.8	1.83	0.02	-COO

Elemental analysis of the XPS survey spectrum of Ti_3C_2NH MXenes (Figure 3.14A) results in Ti:N ratio of 3:1.1. Analysis of the high resolution N 1s spectrum suggests presence of three components. The 396.2 eV peak (59 %) belongs to the chemisorbed β-N on Ti surface.[16] The 397.5

eV peak (26 %) could correspond to the chemisorbed α-N_2 on Ti surface. The 399.9 eV peak (16 %) likely corresponds to N-H bond.

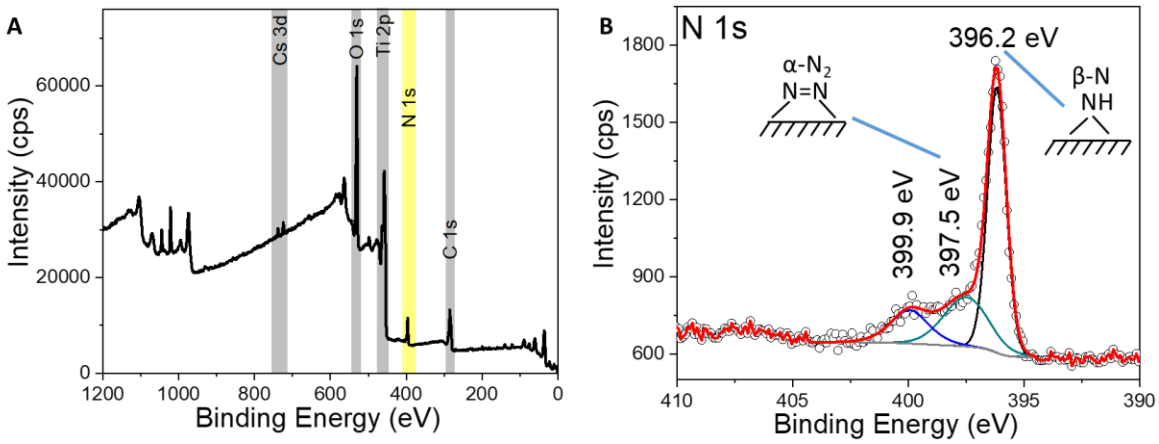

Figure 3.14. XPS spectra of Ti_3C_2NH MXene.

Figure 3.15 shows Raman spectra for $Ti_3C_2T_n$ MXenes with T_x (mixed), O and NH surface groups as well as bare MXenes. The E_g mode corresponding to the in-plane vibration of the surface groups in 300-400 cm^{-1} region (grey area) is absent in the case of the bare Ti_3C_2 MXene. The assignment of the vibrational modes (marked with *) of the bare Ti_3C_2 is based on the work of Hu *et al.* [14] The appearance of the Raman forbidden (IR allowed) E_u mode at 277 cm^{-1} is probably related to the disorder present in the stacks of the bare Ti_3C_2 MXene sheets.

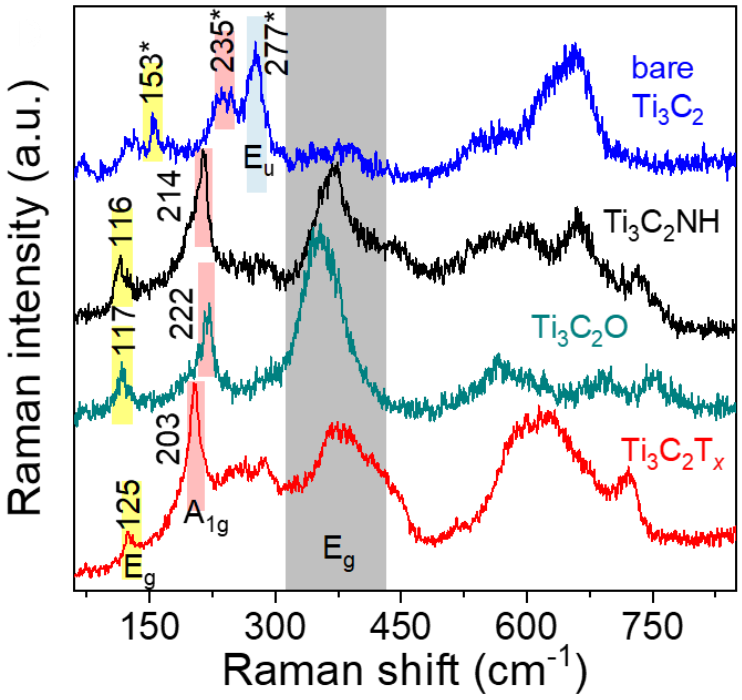

Figure 3.15. Raman spectra of $Ti_3C_2(T_x$, O, NH, □) MXenes.

3.3 Mechanism of surface exchanges in molten inorganic salts.

The chemical transformations of solids are generally impeded by slow diffusion, which severely limits the scope of synthesizable solid state compounds.[17] The complete exchange of surface groups in stacked MXenes is also expected to be kinetically cumbersome, especially if the entering ions are bulkier than the leaving ones, as in the case of Cl^- (the ionic radius, R_i = 1.81 Å) exchanged for Te^{2-} (R_i = 2.21 Å). Counterintuitively, the reactions of $Ti_3C_2Cl_2$ MXenes with O^{2-}, S^{2-}, Se^{2-}, and Te^{2-} occur at similar temperatures and with comparable reaction rates.

To understand this behavior, we followed the evolution of the (0002) diffraction peak during surface exchange reactions. In the initial state, $Ti_3C_2Cl_2$ sheets form stacks (Figure 3.2) with d = 11.25 Å. Analysis of the high-resolution STEM images of $Ti_3C_2Cl_2$ MXene stack (Figure 3.2) suggests that each layer is ~ 8.4 Å thick. Hence the van der Waals gap between adjacent $Ti_3C_2Cl_2$

MXene sheets is 11.25 - 8.42 (±0.32) = 2.83 (±0.32) Å ~ 2.8 Å. which is smaller than the dimensions of entering or leaving ions. No measurable changes of the *d*-spacing were detected upon heating $Ti_3C_2Cl_2$ in KCl-LiCl molten salt to 500°C (Figure 3.16).

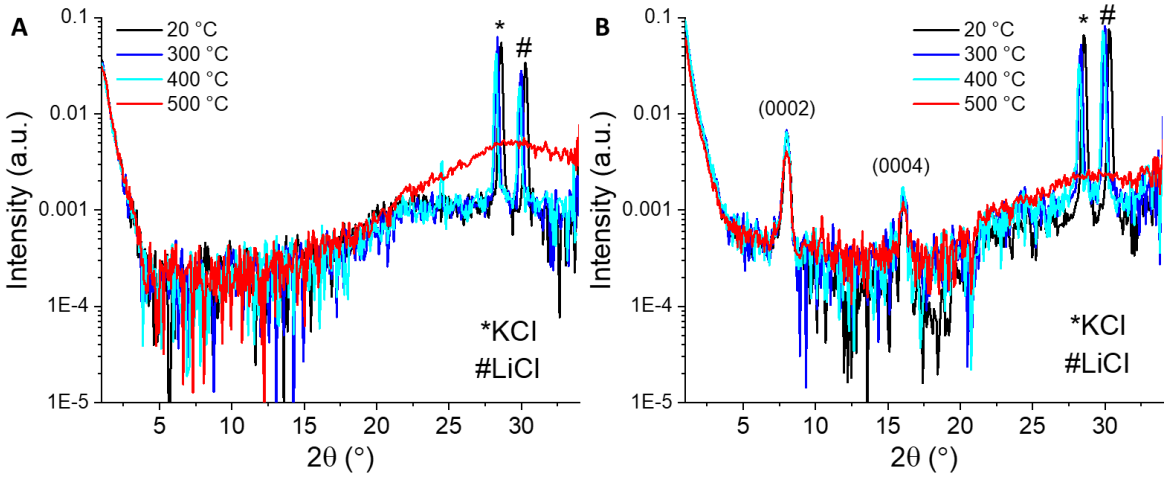

Figure 3.16. Temperature dependent in-situ WAXS patterns.
Temperature dependent WAXS patterns of: (A) pure KCl/LiCl salt; (B) KCl/LiCl salt with $Ti_3C_2Cl_2$ MXene. The peaks corresponding to KCl and LiCl salts shift to lower angles at high temperatures, consistent with the expansion of the ionic lattice. The (000*l*) peaks corresponding to the multi-layer $Ti_3C_2Cl_2$ MXene remain temperature independent up to 500 °C.

However, heating MXenes in the same molten salt but in the presence of Li_2O resulted in *d* = 13.2 Å (Figure 3.17). The van der Waals gap between adjacent Ti_3C_2O MXene sheets is similar to that of between $Ti_3C_2Cl_2$ MXene, 9.46 – 6.87 = 2.59 Å ~ 2.6 Å.[15, 18] Hence the upper bound (assuming 100 % reaction yield) on the interlayer distance (including the van der Waals gap) between adjacent Ti_3C_2O sheets in KCl/LiCl salt is 13.16 - 6.87 = 6.29 Å ~ 6.3 Å. The lower bound (assuming no Cl substitution took place) on the interlayer distance (including the van der Waals gap) between adjacent $Ti_3C_2Cl_2$ sheets in KCl/LiCl salt is 13.16 – 8.42 (±0.32) = 4.74 (±0.32) Å ~ 4.7 Å. The gap of 4.7–6.3 Å between the surface atoms on adjacent MXene sheets is thus large enough to allow ions as big as Te^{2-} (R_i = 2.21Å) to access MXene's surface sites.

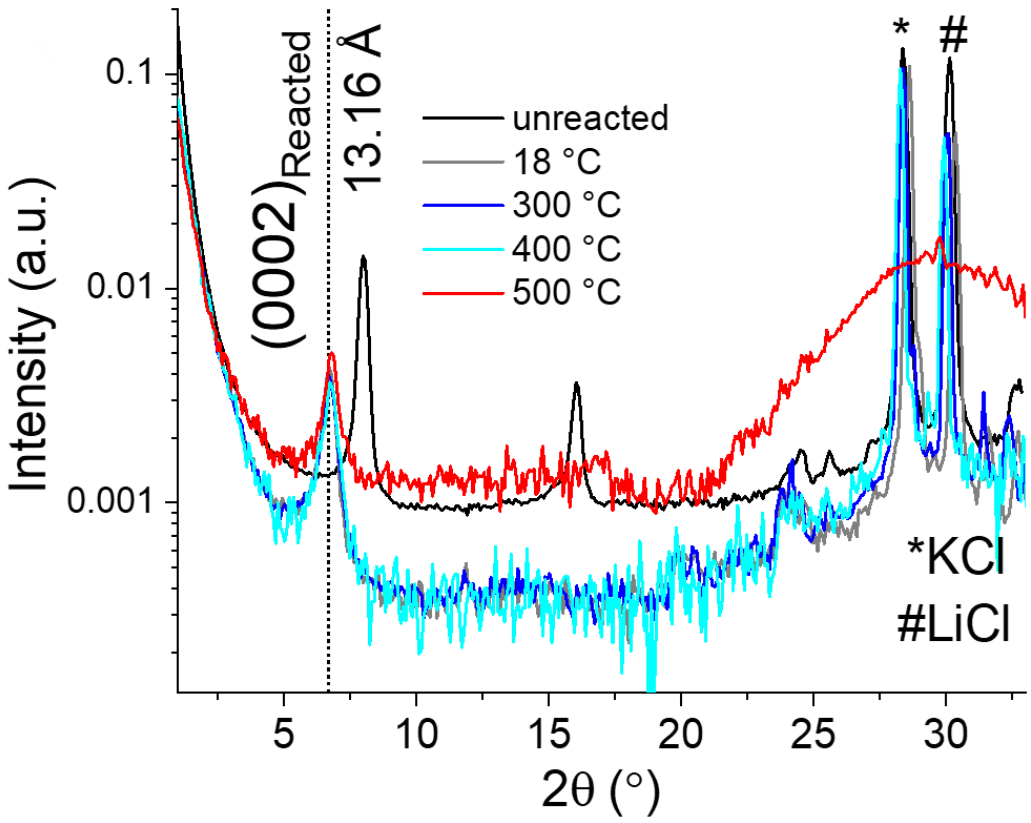

Figure 3.17. Temperature dependent in-situ WAXS patterns for the reaction with Li_2O. WAXS patterns of $Ti_3C_2Cl_2$ MXene in KCl/LiCl salt with Li_2O added before reaction (black curve) and after reaction at 550 °C for 16 h (grey curve). Temperature dependent (18-500 °C) WAXS patterns are shown for $Ti_3C_2Cl_2$ MXene reacted with Li_2O.

A similar d = 13.5 Å was observed during reaction of $Ti_3C_2Cl_2$ MXene with Li_2Se, although with a larger disorder (Figure 3.18). Hence the lower bound (assuming 100 % reaction yield) on the interlayer distance (including the van der Waals gap) between adjacent Ti_3C_2Se sheets in KCl/LiCl salt is 13.49 – 9.11 (±0.22) = 4.38 (±0.22) Å ~ 4.4 Å. The upper bound (assuming no Cl substitution took place) on the interlayer distance (including the van der Waals gap) between adjacent $Ti_3C_2Cl_2$ sheets in KCl/LiCl salt is 13.49 – 8.42 (±0.32) = 5.07 (±0.32) Å ~ 5.1 Å.

The unstacking of MXene sheets in molten salts greatly facilitates diffusion of ions and makes MXene surfaces sterically accessible. The interaction potential of MXenes in a molten salt is likely

to be similar to the interactions between inorganic nanoparticles dispersed in molten salts. For two parallel surfaces, surface-templated ion layering in a molten salt leads to an exponentially decaying oscillatory interaction energy.[19] We speculate that the free energy released in the surface exchange reaction causes MXene sheets to "swell" into one of the energy minima and stay in this state during chemical transformation.

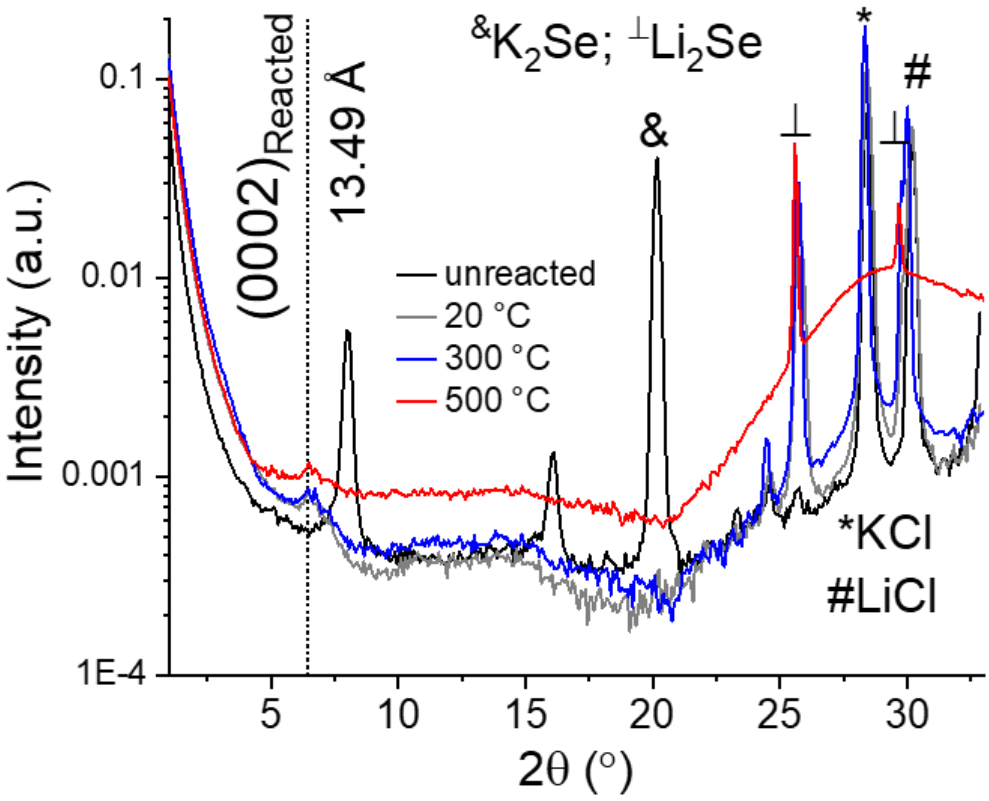

Figure 3.18. Temperature dependent in-situ WAXS patterns for the reaction with K_2Se. WAXS patterns of $Ti_3C_2Cl_2$ MXene in KCl/LiCl salt with K_2Se added before reaction (black curve) and after reaction at 500 °C for 24 h (grey curve). Temperature dependent (20-500 °C) WAXS patterns are shown for $Ti_3C_2Cl_2$ MXene reacted with K_2Se.

3.4 Ti_2CT_n MXenes.

Similar covalent surface modifications can be achieved for Ti_2CCl_2, and Ti_2CBr_2. The ability to perform surface exchange reactions on the thinnest MXenes demonstrates that the 2D sheets stay intact during all stages of the transformation.

Moreover, Ti_2CT_n MXenes can provide additional structural information. Due to their larger thickness, $Ti_3C_2T_n$ MXenes can only adopt a pseudo-*P6₃/mmc* space group and thus are not suitable for Rietveld refinement.[20-21] This fact limits our understanding of the structure of $Ti_3C_2T_n$ MXenes to the unit cell parameters extracted from the Le Bail fitting of the XRD patterns.

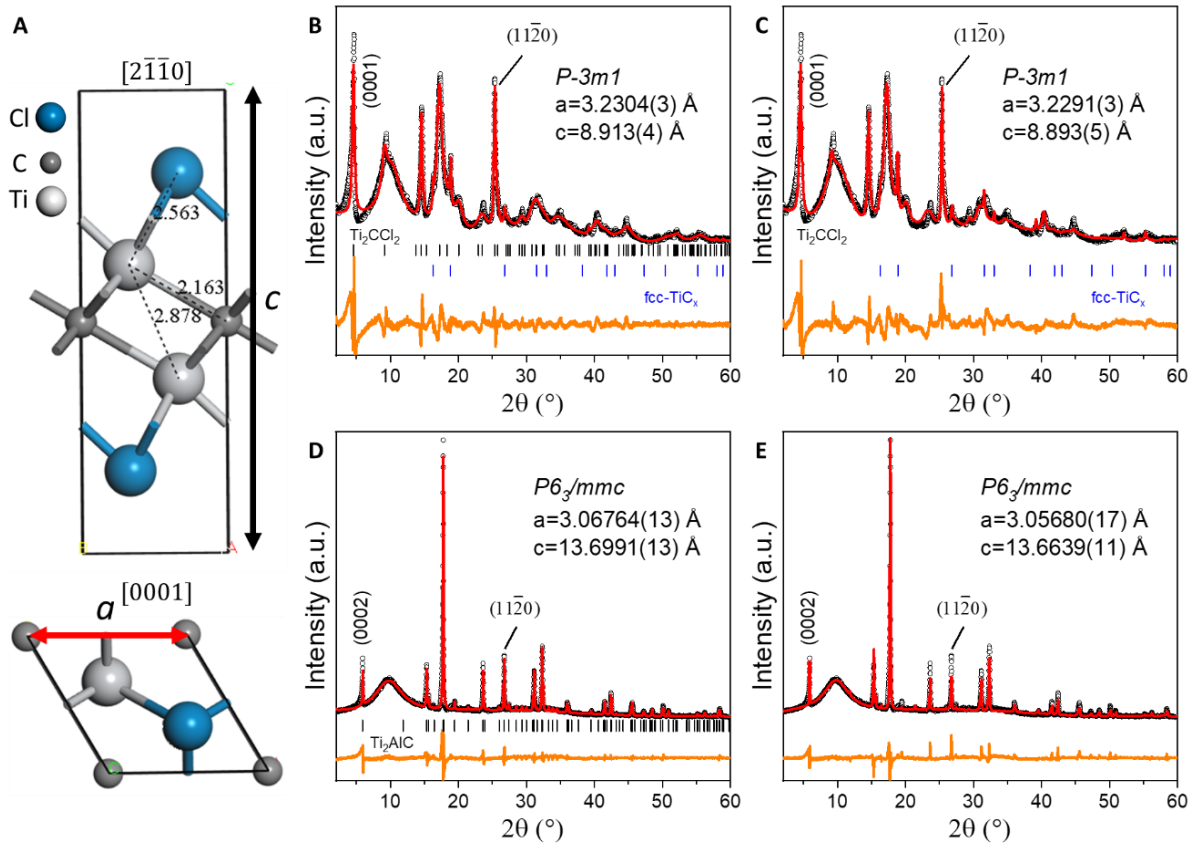

Figure 3.19. Structure of Ti_2CCl_2 MXene.
(A) Side and top views of the structure of Ti_2CCl_2 MXene derived from the Rietveld refinement in (C). Experimental XRD patterns (Mo Kα1, transmission, black curves) and Le Bail fits (red curves) of (B) Ti_2CCl_2 MXene derived from Ti_2AlC MAX phase in (D). Experimental XRD patterns (black curves) and Rietveld refinements (red curves) of (C) Ti_2CCl_2 MXene derived from (E) Ti_2AlC MAX phase.

In contrast to the parent Ti_2AlC MAX phase, Ti_2CCl_2 MXene adopts *P-3m1* space group (Figure 3.19). The transmission geometry based XRD pattern can be used for the subsequent Rietveld refinement (Table 3.4).

Table 3.4. Rietveld refinement results for Ti_2AlC MAX phase and Ti_2CCl_2 MXene.

Ti_2AlC, *$P6_3/mmc$*, a = 3.05680(17) Å, c = 13.6639(11) Å, V = 110.571(15) Å^3
R_{wp} = 10.49 %, R_p = 6.85 %

Atom	x	y	z	Occ.
Ti	0.33333	0.66667	0.5828(3)	1
Al	0.33333	0.66667	0.75	0.980(10)
C	0	0	0.5	1

Ti_2CCl_2, *P-3m1*, a = 3.2291(3) Å, c = 8.893(5) Å, V = 80.30(5) Å^3
R_{wp} = 12.31 %, R_p = 8.88 %

Atom	x	y	z	Occ.
Ti	0.33333	0.66667	0.6233(9)	1
Cl	0.33333	0.66667	0.1790(8)	1
C	0	0	0.5	1

The fitting of the experimental Fourier-transformed extended X-ray absorption fine structure (EXAFS) functions of Ti_2CCl_2 MXene (Figure 3.20 and Table 3.5) demonstrates that the local structure around Ti is consistent with the respective crystallographic model. For example, the Ti-Cl bond distance is 2.56 Å based on the Rietveld refinement (Figure 3.19) and 2.50 Å based on the EXAFS modeling (Table 3.5).

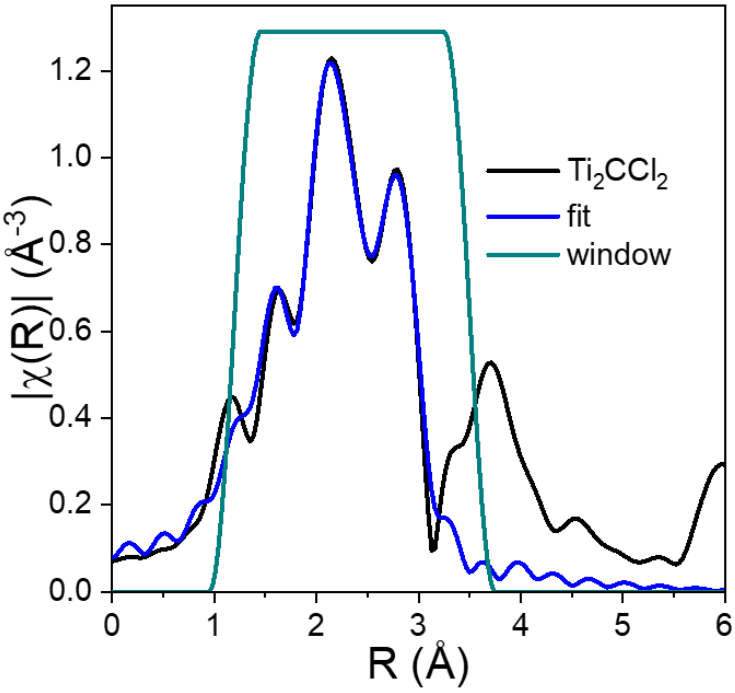

Figure 3.20. EXAFS fit for Ti_2CCl_2 MXene.

Magnitude of the Fourier-transformed EXAFS experimental datum (k^2-weighted) and fit for Ti_2CCl_2 MXene.

Table 3.5. EXAFS fitting parameters for Ti_2CCl_2 MXene.

	R (Å)	N	σ^2 (Å^2)
Ti-C	2.14(4)	3	0.005(5)
Ti-Cl	2.50(2)	3	0.004(3)
Ti-Ti1	2.87(2)	3	0.004(3)
Ti-Ti2	3.23(2)	6	0.009(3)
Ti-Cl in $TiCl_3$[22]	2.42		
Ti-Ti in $TiCl_3$[22]	3.55		

ΔE_0 = 0.65 ± 2.39 eV; S_0^2 = 0.68 ± 0.16; Independent Points: 12.9; Number of Variables: 10; R factor: 0.024; Fitting Range: k: 3.0-12.0 Å^{-1}; R: 1.2-3.5 Å.

Ti_2CBr_2 also crystallizes in *P-3m1* space group (Figure 3.21 and Table 3.6). The Ti-Br bond distance is 2.72 Å based on the Rietveld refinement and 2.62 Å based on the EXAFS modeling (Figure 3.22 and Table 3.7).

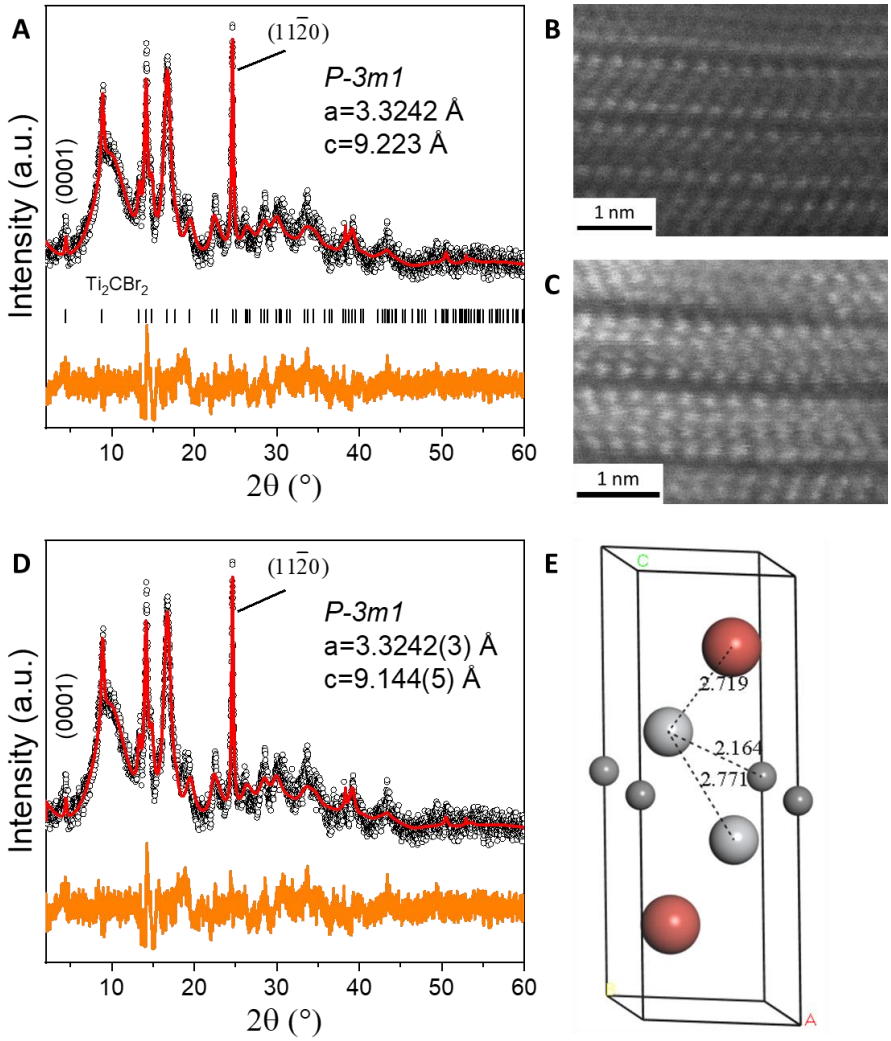

Figure 3.21. Structure of Ti_2CBr_2 MXene.
(A) Experimental XRD pattern (Mo Kα1, transmission, black curve) and Le Bail fit (red curve) of Ti_2CBr_2 MXene. Atomically resolved (B) STEM-HAADF and (C) low angle annular dark field (LAADF) images of Ti_2CBr_2 MXene. Experimental XRD pattern (black curve) and Rietveld refinement (red curve) of Ti_2CBr_2 MXene. (E) Structure of Ti_2CBr_2 MXene derived from (D).

Table 3.6. Ti_2CBr_2 Rietveld refinement results.

Ti_2CBr_2, *P-3m1*, a = 3.3242(3) Å, c = 9.144(5) Å, V = 87.51(5) Å^3
R_{wp} = 2.58 %, R_p = 2.00 %

Atom	x	y	z	Occ.
Ti	0.33333	0.66667	0.6093(8)	1
Br	0.33333	0.66667	0.1801(5)	1
C	0	0	0.5	1

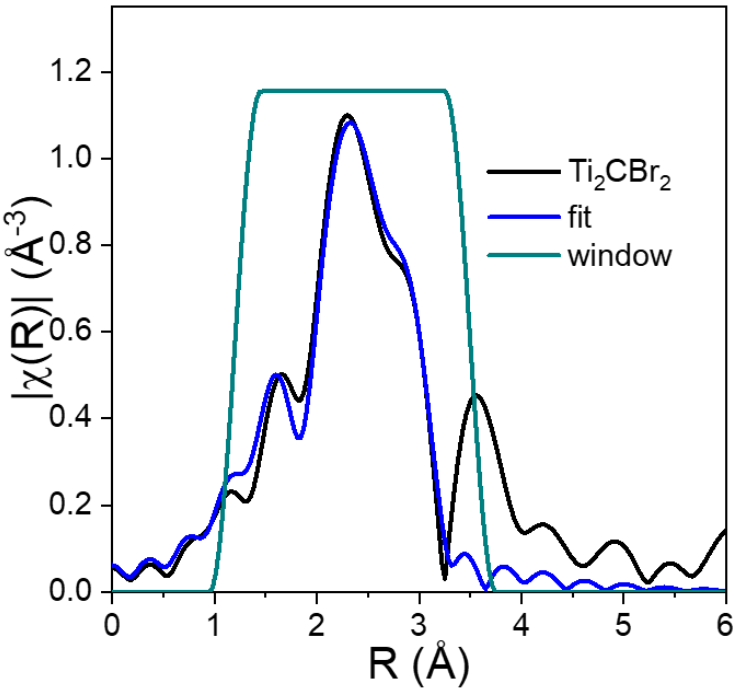

Figure 3.22. EXAFS fit for Ti_2CBr_2 MXene.

Magnitude of the Fourier-transformed EXAFS experimental datum (k^2-weighted) and fit for Ti_2CBr_2 MXene.

Table 3.7. EXAFS fitting parameters for Ti_2CBr_2 MXene.

	R (Å)	N	σ^2 (Å^2)
Ti-C	2.14(4)	3	0.007(5)
Ti-Br	2.62(2)	3	0.005(2)
Ti-Ti1	2.86(2)	3	0.009
Ti-Ti2	3.28(2)	6	0.012
Ti-Br in $TiBr_3$[23]	2.58		
Ti-Br in $TiBr_2$[24]	2.65		

ΔE_0 = -1.8 ± 2.7 eV; S_0^2 = 0.84 ± 0.12; Independent Points: 11.8; Number of Variables: 8; R factor: 0.028; Fitting Range: k: 3.0-11.0 Å^{-1}; R: 1.2-3.5 Å.

Ti_2CCl_2 and Ti_2CBr_2 MXenes dispersed in CsBr/KBr/LiBr eutectic can react with Li_2S, Li_2Se and Li_2Te to form new Ti_2CS (Figures 3.23, 3.24 and Tables 3.8, 3.9), Ti_2CSe (Figure 3.25, 3.26 and Table 3.10) and Ti_2CTe (Figure 3.27, 3.28 and Tables 3.11, 3.12) MXenes, respectively. The

exact metal/surface group elemental ratios for new MXenes are close to the expected values as summarized in Table 3.13.

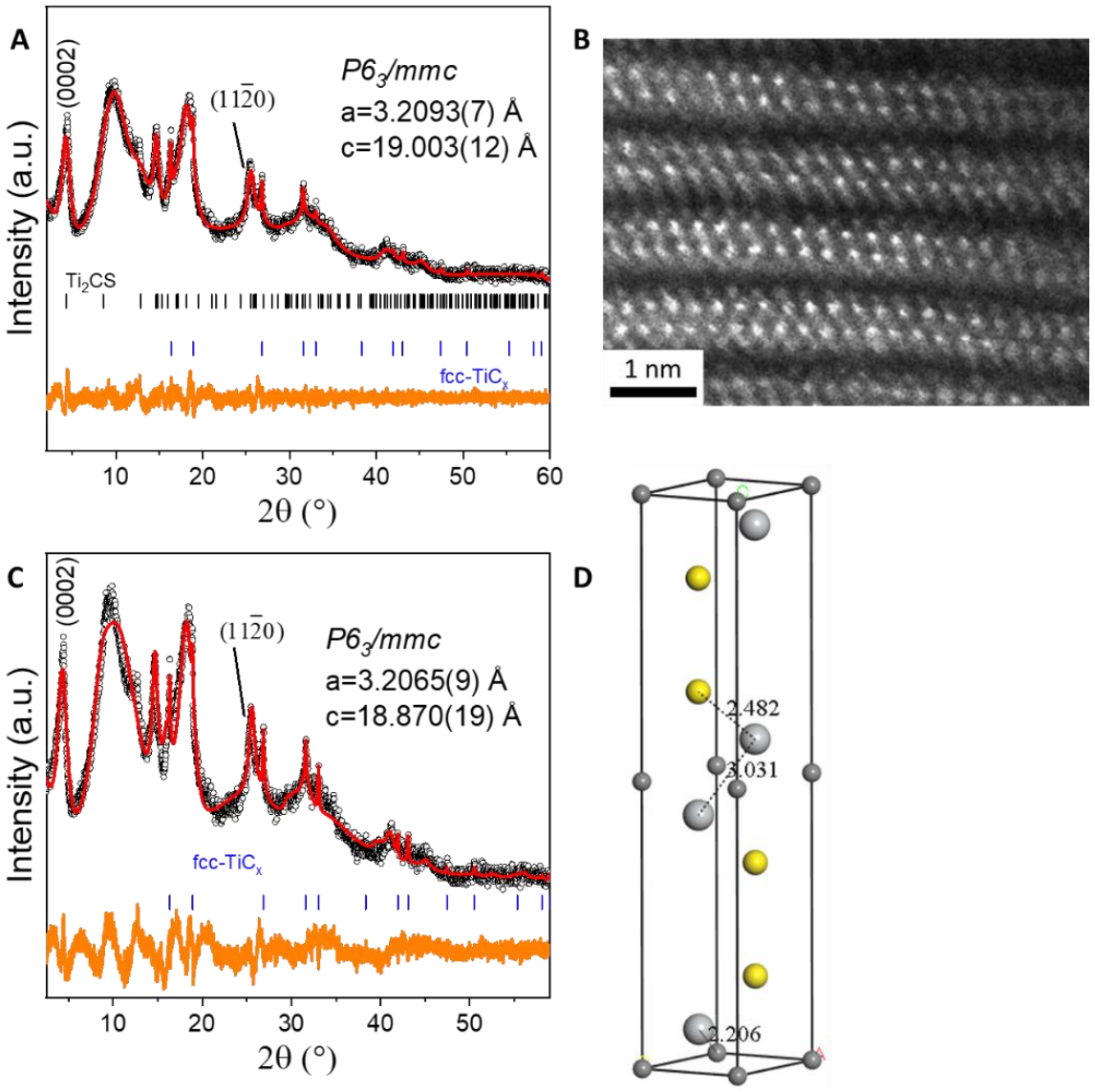

Figure 3.23. Structure of Ti_2CS MXene.
(A) Experimental XRD pattern (Mo Kα1, transmission, black curve) and Le Bail fit (red curve) of Ti_2CS MXene. (B) Atomically resolved STEM-HAADF image of Ti_2CS MXene. (C) Experimental XRD pattern (black curve) and Rietveld refinement (red curve) of Ti_2CS MXene. (D) Structure of Ti_2CS MXene derived from (C).

Table 3.8. Ti_2CS Rietveld refinement results.

Ti_2CS, $P6_3/mmc$, a = 3.2065(9) Å, c = 18.870(19) Å, V = 168.0(2) Å^3 R_{wp} = 4.61 %, R_p = 3.73 %				
Atom	x	y	z	Occ.
Ti	0.33333	0.66667	0.4364(3)	1
S	0.33333	0.66667	0.6512(3)	0.611(4)
C	0	0	0.5	1

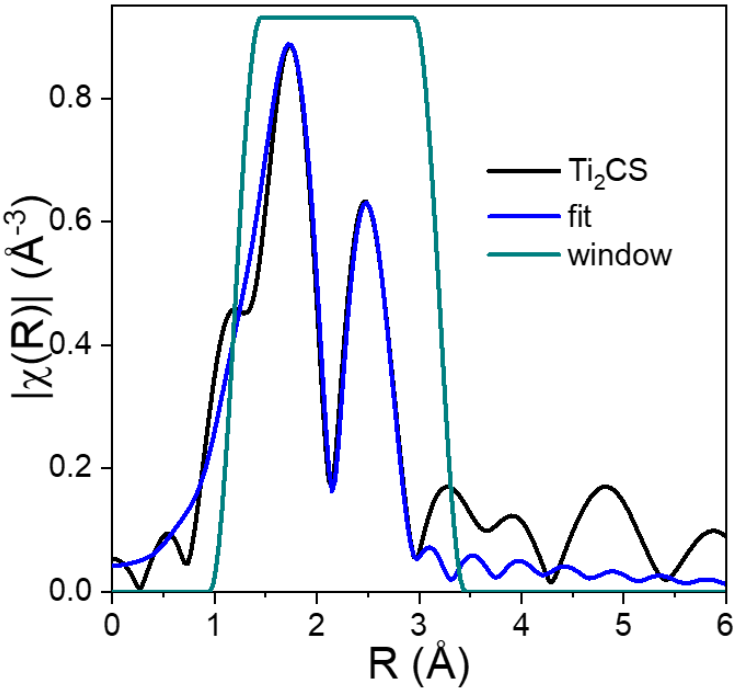

Figure 3.24. EXAFS fit for Ti_2CS MXene.

Magnitude of the Fourier-transformed EXAFS experimental datum (k^2-weighted) and fit for Ti_2CS MXene.

Table 3.9. EXAFS fitting parameters for Ti_2CS MXene.

	R (Å)	N	σ^2 (Å^2)
Ti-C	2.14(3)	3	0.014
Ti-S	2.41(2)	2.5	0.011
Ti-Ti1	3.06(2)	3	0.012
Ti-Ti2	3.23(4)	6	0.034
Ti-S in TiS_2[25]	2.43		
Ti-S in TiS[26]	2.48		

ΔE_0 = 4.35 ± 1.1 eV; S_0^2 = 0.88; Independent Points: 8.4; Number of Variables: 5; R factor: 0.019; Fitting Range: k: 2.2-9.0 Å^{-1}; R: 1.2-3.2 Å.

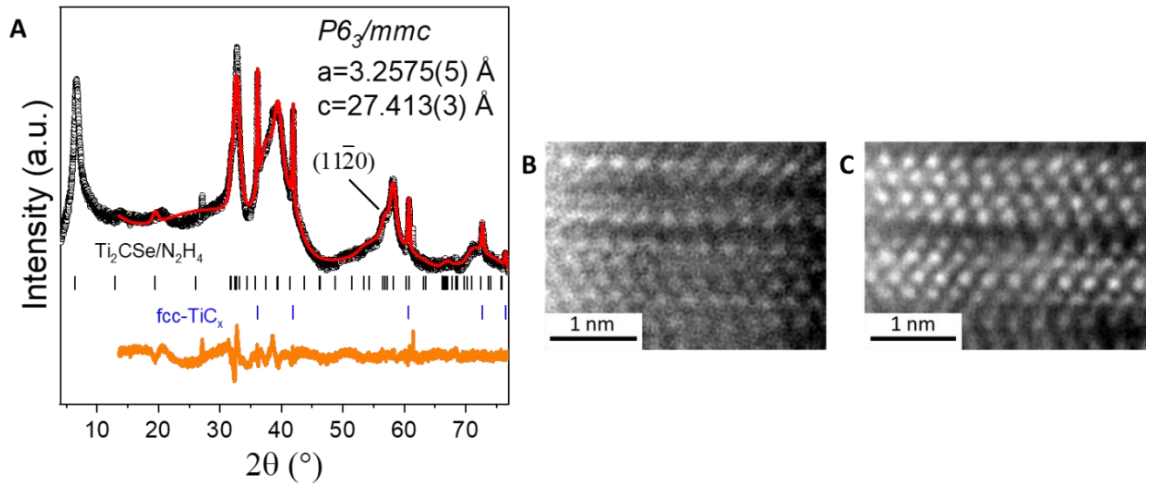

Figure 3.25. Characterization of Ti_2CSe MXene.
(A) Experimental XRD pattern (Cu Kα, reflection, black curve) and Le Bail fit (red curve) of Ti_2CSe MXene recovered from the salt matrix using anhydrous hydrazine. (B) HAADF and (C) LAADF images of Ti_2CSe MXene.

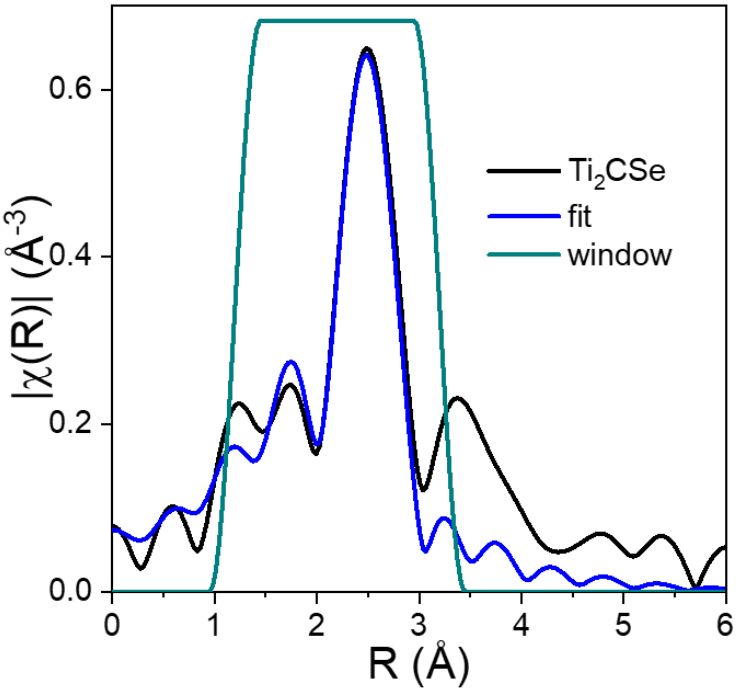

Figure 3.26. EXAFS fit for Ti_2CSe MXene.

Magnitude of the Fourier-transformed EXAFS experimental datum (k^2-weighted) and fit for Ti_2CSe MXene.

Table 3.10. EXAFS fitting parameters for Ti_2CSe MXene.

	R (Å)	C.N.	σ^2 ($Å^2$)
Ti-C	2.14(9)	3	0.034(21)
Ti-Se	2.55(3)	3	0.013(5)
Ti-Ti1	3.08	3	0.015
Ti-Ti2	3.28	6	0.051
Ti-Se in $TiSe_2$ [25]	2.54		
Ti-Se in TiSe [25]	2.58		

ΔE_0 = 0.57 ± 1.89 eV; S_0^2 = 0.92 ± 0.28; Independent Points: 7.4; Number of Variables: 6; R factor: 0.041; Fitting Range: k: 3.0-9.0 $Å^{-1}$; R: 1.2-3.2 Å. The TiTi1 and TiTi2 distances were not refined.

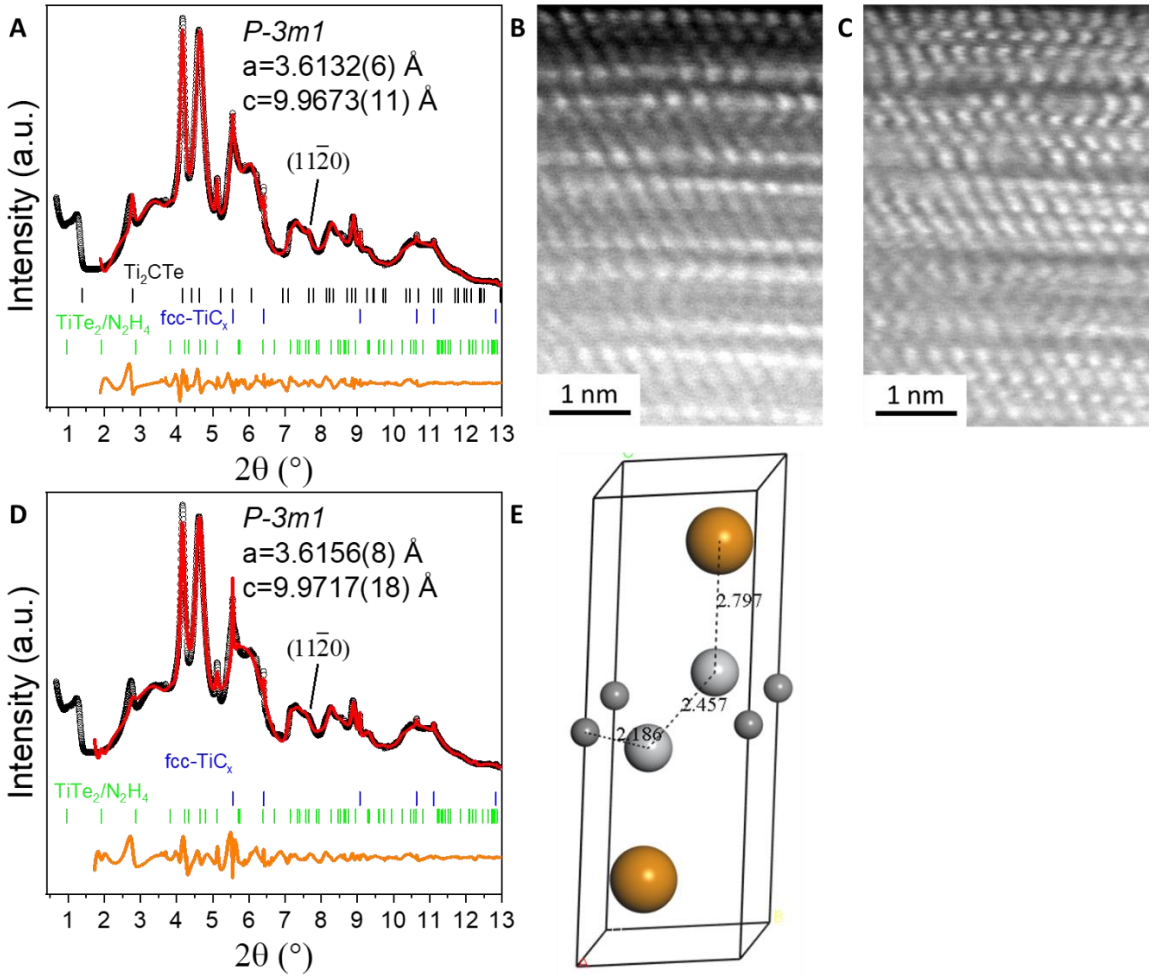

Figure 3.27. Structure of Ti_2CTe MXene.
(A) Experimental XRD pattern (0.2412 Å, transmission, black curve) and Le Bail fit (red curve) of Ti_2CTe MXene. (B) HAADF and (C) LAADF images of Ti_2CTe MXene. Experimental XRD pattern (black curve) and Rietveld refinement (red curve) of Ti_2CTe MXene. (E) Structure of Ti_2CTe MXene derived from (D).

Table 3.11. EXAFS fitting parameters for Ti_2CS MXene.

Ti_2CTe, *P-3m1*, a = 3.6156(8) Å, c = 9.9717(18)Å, V = 112.89(5) Å^3 R_{wp} = 2.77 %, R_p = 1.91 %				
Atom	x	y	z	Occ.
Ti	0.33333	0.66667	0.565	1
Te	0.66667	0.33333	0.8455(6)	0.934(7)
C	0	0	0.5	1

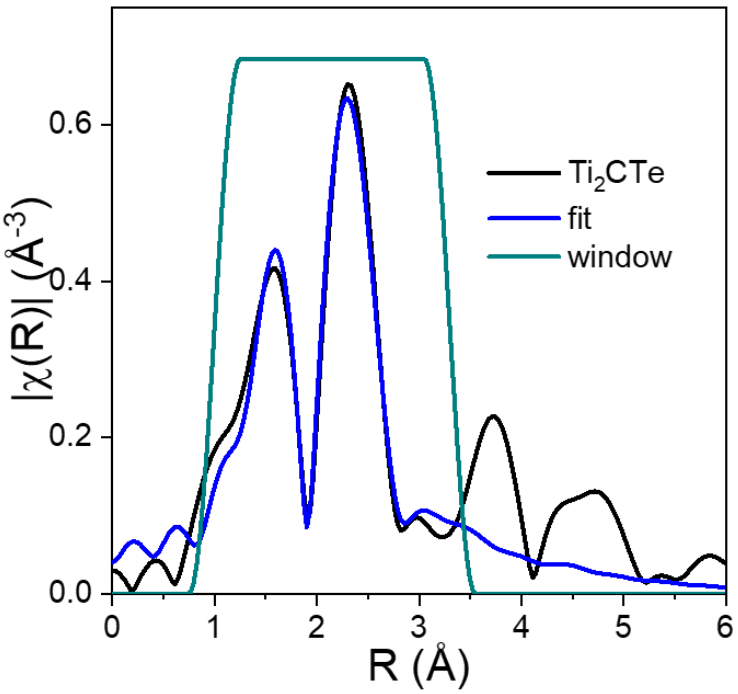

Figure 3.28. EXAFS fit for Ti_2CTe MXene.

Magnitude of the Fourier-transformed EXAFS experimental datum (k^2-weighted) and fit for Ti_2CTe MXene.

Table 3.12. EXAFS fitting parameters for Ti_2CTe MXene.

	R (Å)	N	σ^2 (Å^2)
Ti-C	2.19(1)	3	0.004(2)
Ti-Te	2.80(2)	2.8	0.013(3)
Ti-Ti1	2.58(2)	3	0.012(2)
Ti-Ti2	3.47(3)	6	0.026(5)
Ti-Te in $TiTe_2$[25]	2.72		
Ti-Te in TiTe[25]	2.74		

ΔE_0 = 2.34 eV; S_0^2 = 0.59; Independent Points: 10.3; Number of Variables: 8; R factor: 0.010; Fitting Range: k: 2.0-9.2 Å^{-1}; R: 1.0-3.3 Å.

Table 3.13. Summary of the metal to surface group (M/T) elemental ratios for the MXenes.

EDX elemental mapping was performed in SEM (marked with *) and STEM. Light element (NH, O) terminated MXenes and bare MXenes are not included. XRF analysis was performed on the sample area of 79 mm^2. If the bonding between transition metal atoms and surface functional groups were purely ionic, we would expect 1 halide (charge -1) and 0.5 chalcogenide (charge -2) ion per every transition metal atom in the outer MXene layer.[27] The results in this table seem to agree with this simple argument. The deviations of the MXene surface group density from the canonical one surface group per every transition metal atom in the outer layer have been observed in mixed terminated $Ti_3C_2T_x$ MXenes.[28] The slight substoichiometry in the case of Br/Cl-terminated MXenes can be as a result of surface vacancies.

Material	M/T ratio EDX	M/T ratio XRF
$Ti_3C_2Cl_2$	3/1.9*	3/1.5
$Ti_3C_2Br_2$	3/1.8*	3/1.8
Ti_3C_2S	3/1.1	3/1.1
Ti_3C_2Se	3/1.1	3/1.2
Ti_3C_2Te	3/1.0	3/1.2
Ti_2CCl_2	2/1.7	2/1.5
Ti_2CBr_2	2/1.6	2/2.0
Ti_2CS	2/1.2*	2/1.2
Ti_2CSe	2/1.1*	2/1.2
Ti_2CTe	2/1.2	2/1.2

Based on the simulated XRD patterns of Ti_2CT_n MXenes (Figures 3.29, 3.30) and recent theoretical studies,[29] we hypothesize that due to their large size, Te^{2-} groups may be positioned on top of the neighboring Ti atoms. This contrasts with the smaller surface groups which are positioned on top of the opposite Ti atoms of the same Ti_2CT_n sheet. For example, without changing *P-3m1* space group and unit cell parameters (a = 3.229 Å, c = 8.893 Å), there are three possible ways to position Cl atoms: on top of neighboring Ti atoms (model 1), on top of bottom Ti atoms (model 2) and on top of C atoms (model 3) (Figure 3.29). It is evident that model 2

generates an XRD pattern most consistent with the experimental XRD pattern. This result is in accordance with the recent theoretical prediction where Cl terminated MXenes are expected to adopt model 2 structure.[29]

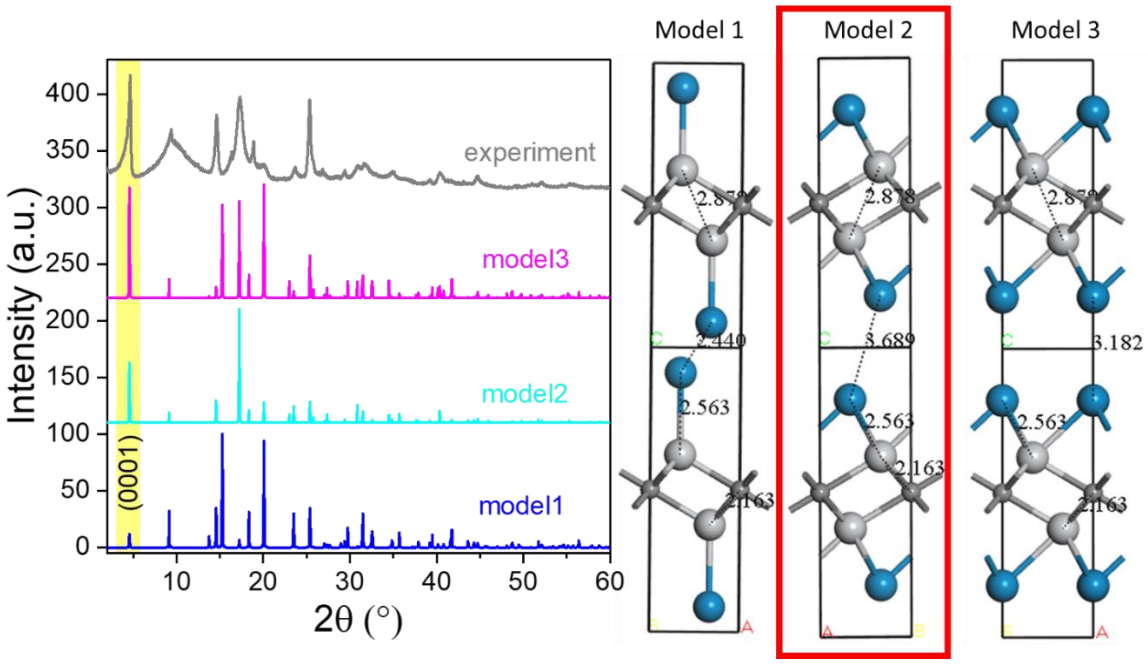

Figure 3.29. Simulated XRD patterns for Ti_2CCl_2 MXene.

Comparison between simulated and experimental XRD patterns for Ti_2CCl_2 MXene. The nearest neighbor distances were fixed in all three models (Ti-Cl at 2.563 Å, Ti-Ti1 at 2.878 Å and Ti-C at 2.163 Å). The X-ray wavelength was fixed at Mo Kα1 (0.7093 Å).

The situation is different in case of Ti_2CTe MXene. Without changing *P-3m1* space group and unit cell parameters (a = 3.616 Å, c = 9.971 Å) there are also three possible ways to position Te atoms: on top of neighboring Ti atoms (model 1), on top of bottom Ti atoms (model 2) and on top of C atoms (model 3) (Figure 3.30). It is evident that model 1 generates an XRD pattern most consistent with the experimental XRD pattern. Model 1 is the only model out of three that has (0003) peak dominating among (000*l*) family peaks.

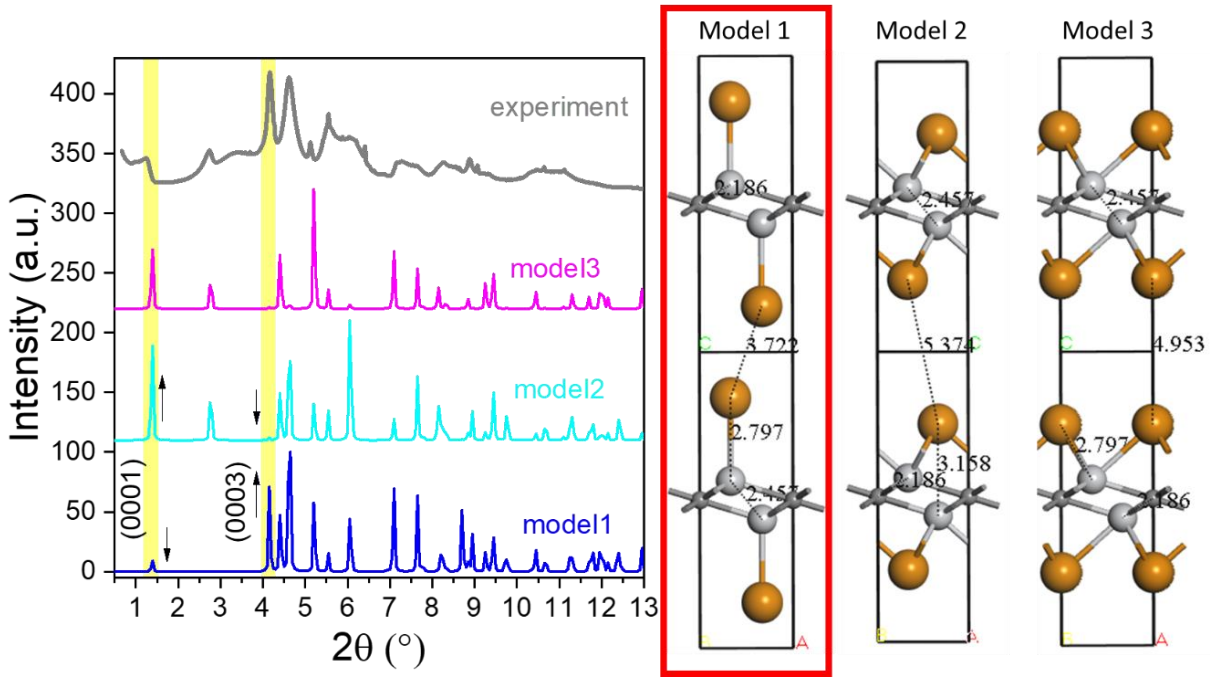

Figure 3.30. Simulated XRD patterns for Ti_2CTe MXene.

Comparison between simulated and experimental XRD patterns for Ti_2CTe MXene. The nearest neighbor distances were fixed in all three models (Ti-Te at 2.797 Å, Ti-Ti1 at 2.457 Å and Ti-C at 2.186 Å). The X-ray wavelength was fixed at 0.2412 Å.

We also performed additional verification of the EXAFS and Rietveld refinement based structural models by mapping the interatomic distances on the atomic pair distribution functions (PDFs) (Figures 3.31, 3.32). The peak positions in PDFs seem to be consistent with our EXAFS/Rietveld refinement-based models (Figure 3.32).

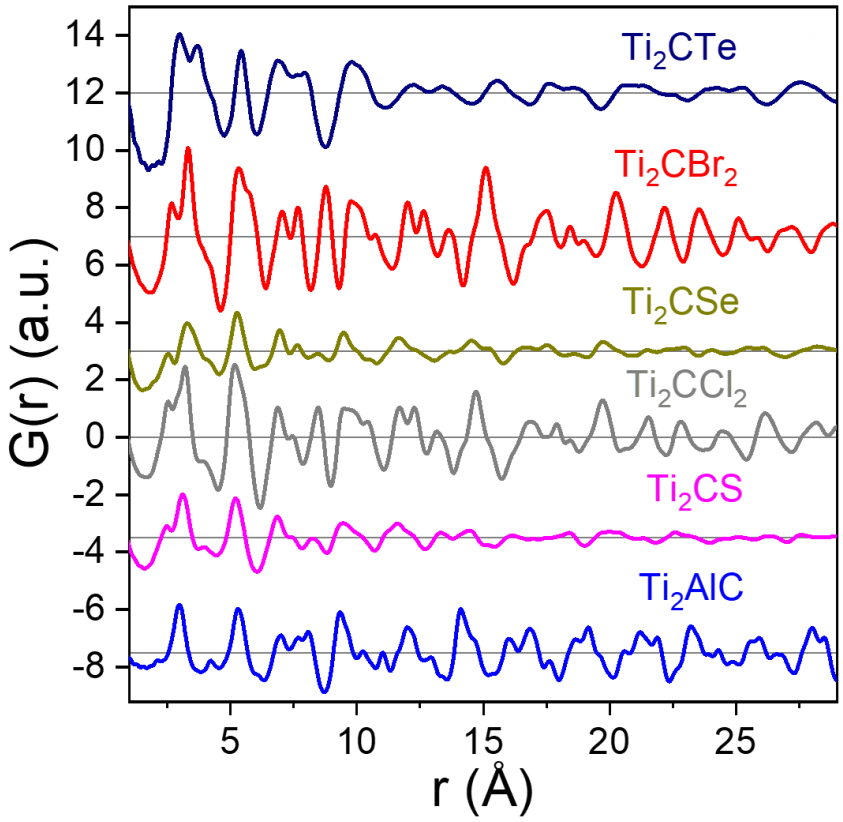

Figure 3.31. Atomic PDFs for Ti_2CT_n MXenes and Ti_2AlC MAX phase.
Ti_2CCl_2, Ti_2CBr_2 and Ti_2AlC have atomic correlations extending farther than in case of S, Se and Te functionalized MXenes. This could be related to greater amount of disorder along c-axis in chalcogenide MXenes, consistent with broader peaks observed in the corresponding XRD patterns.

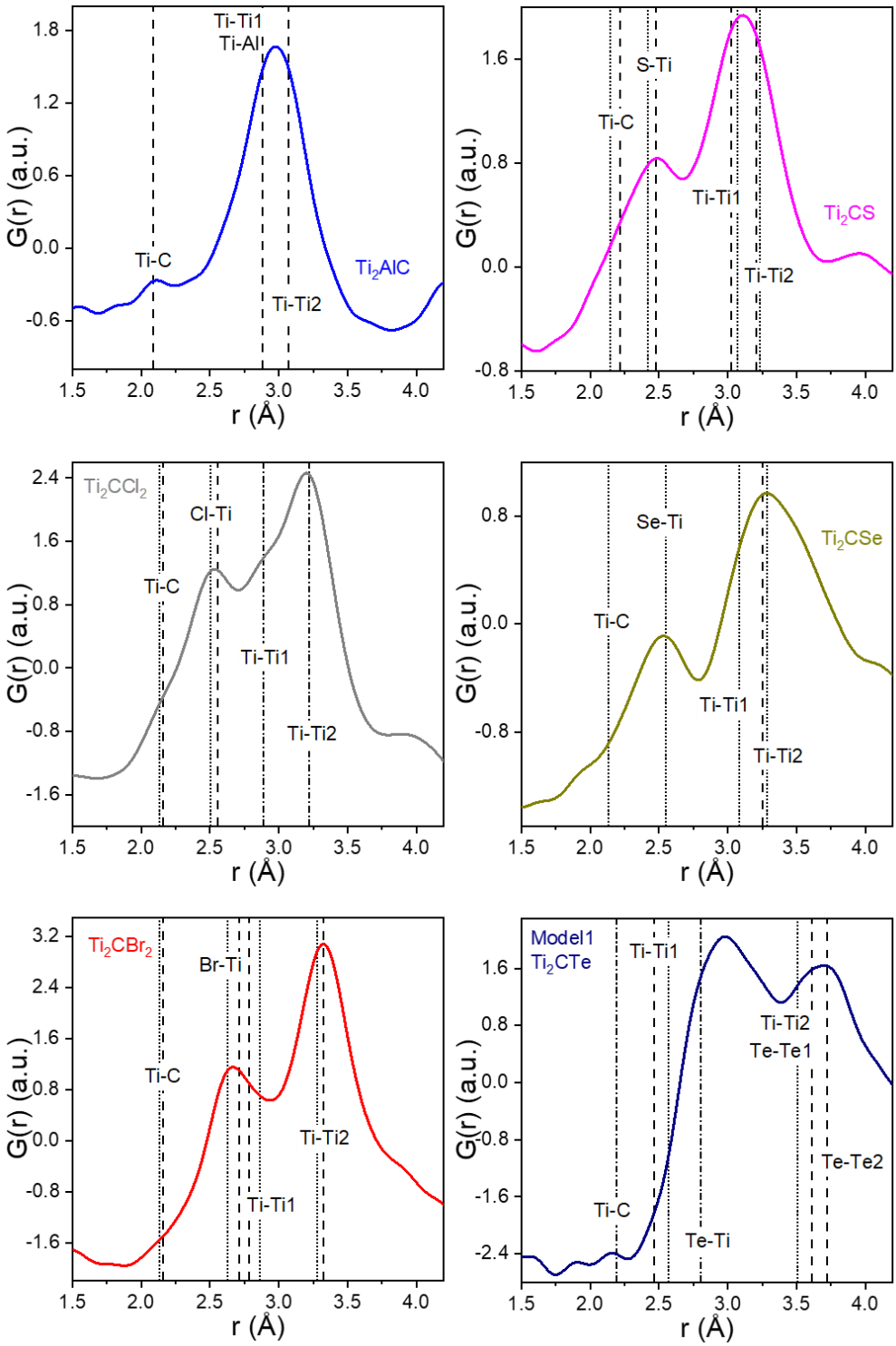

Figure 3.32. Low *r* atomic PDFs for Ti_2CT_n MXenes and Ti_2AlC MAX phase.
Low *r* atomic PDFs of Ti_2CT_n MXenes (T = S, Cl, Se, Br and Te) and Ti_2AlC MAX phase. The marked bond lengths of Ti-C, Ti-T as well as nearest neighbor Ti-Ti1 and Ti-Ti2 distances are based on the Rietveld refinement of powder XRD patterns (dashed lines) and EXAFS modeling (dotted lines). Distances which are within 0.01 Å from both methods are marked as dash-dotted lines.

As in case of $Ti_3C_2T_n$ MXenes, the reactions of Ti_2CCl_2 and Ti_2CBr_2 with Li_2O, $NaNH_2$ and LiH yield Ti_3C_2O, $Ti_3C_2(NH)$ and bare $Ti_3C_2\square_2$ MXenes, respectively (Figure 3.33). Bare Ti_2C MXene has the smallest *c* lattice constant of just ~10.5 Å.

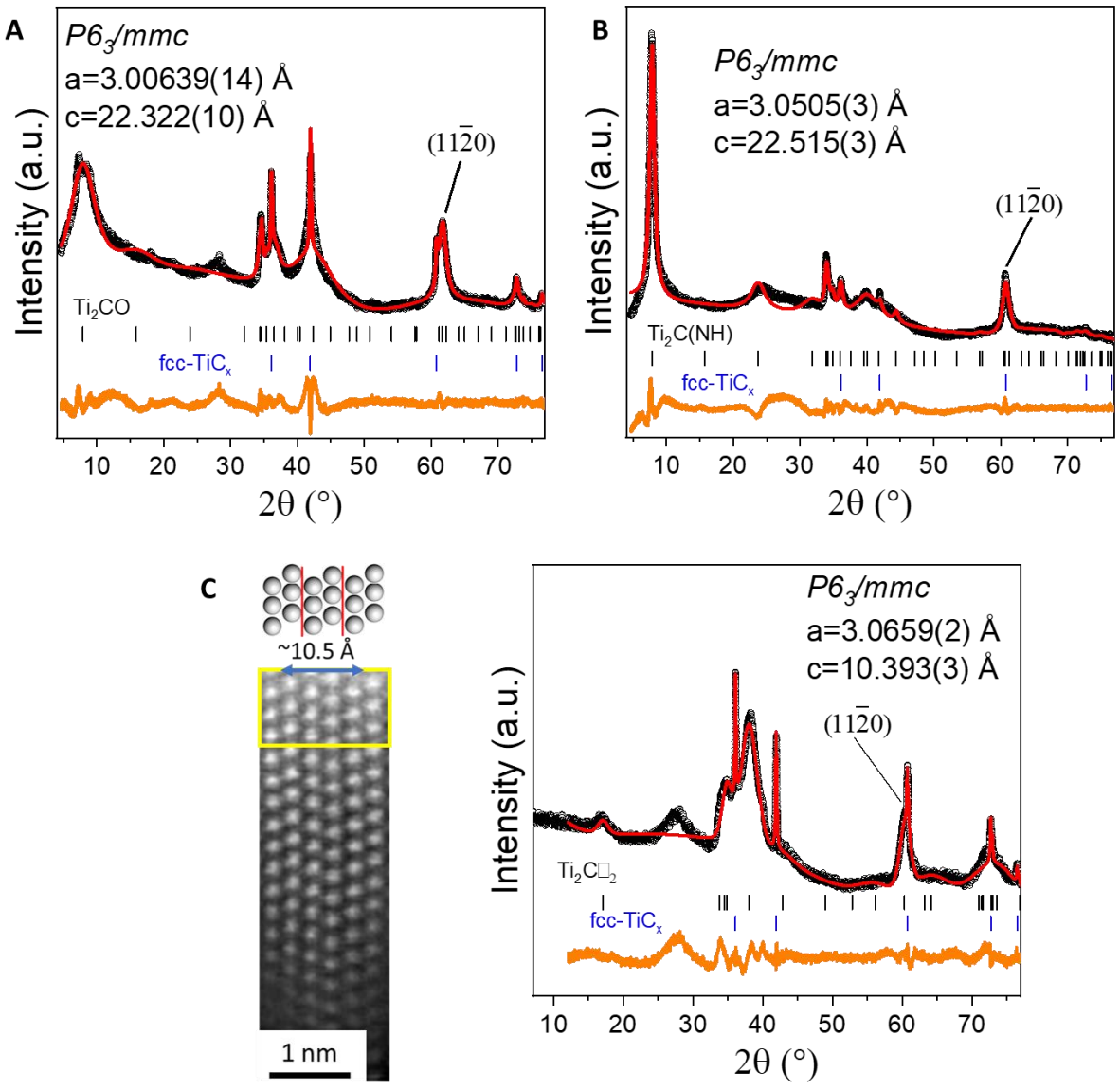

Figure 3.33. Characterization of $Ti_2C(\square, NH, O)$ MXenes.
Experimental XRD patterns (Cu Kα, reflection, black curves) and Le Bail fits (red curves) of: (A) Ti_2CO; (B) $Ti_2C(NH)$; (C) Bare Ti_2C (Inset shows STEM-HAADF image of the bare Ti_2C sheets).

3.5 Strain in $Ti_3C_2T_n$ and Ti_2CT_n MXenes.

Both EXAFS and XRD modeling give a = 3.32 Å for Ti_2CBr_2 (Figure 3.32). After exchanging Br^- for O^{2-}, the resultant MXene shows a = 3.01 Å, while the reaction with Te^{2-} produces MXene with a = 3.62 Å (Figure 3.34). Figure 3.34A shows that the van der Waals radius and packing density of surface atoms have a huge effect on a, and Figure 3.34B compares these values with available computational predictions. For comparable ion radii, e.g., S *vs*. Cl and Se *vs*. Br, halido-terminated MXenes show larger a. This is likely due to the smaller number of chalcogenide ions required for charge compensation of the MXene surface. To estimate the in-plane strain ($\varepsilon_{||}$) imposed on the titanium carbide lattice by surface groups in the new MXene species, we compared a to the nearest neighbor distance between Ti atoms in (111) plane of bulk cubic TiC that is structurally equivalent to the basal (0001) MXene plane. For $Ti_3C_2T_n$ and Ti_2CT_n MXene families, the mixed (T_x = F, O, OH) and pure O^{2-} terminations result in a compressive $\varepsilon_{||}$. Bare (□) and NH-terminated MXenes are nearly strain-free, while Cl, S, Se, and Br-terminated MXenes all experience tensile $\varepsilon_{||}$. The thinner Ti_2CT_n MXenes experience, on average, a slightly larger in-plane expansion or contraction with respect to the bulk TiC lattice, compared to the thicker $Ti_3C_2T_n$ MXenes. The Ti_2CTe MXene (Figure 3.34) experiences the largest magnitude of tensile $\varepsilon_{||}$ of 18.2 % in accordance with Te^{2-} having the largest van der Waals radius among all groups used in this study. This degree of lattice expansion in a crystalline solid is unprecedented. For comparison, the lattice of bulk TiC expands by "only" 2.5% when heated from room temperature to 2700°C.[30]

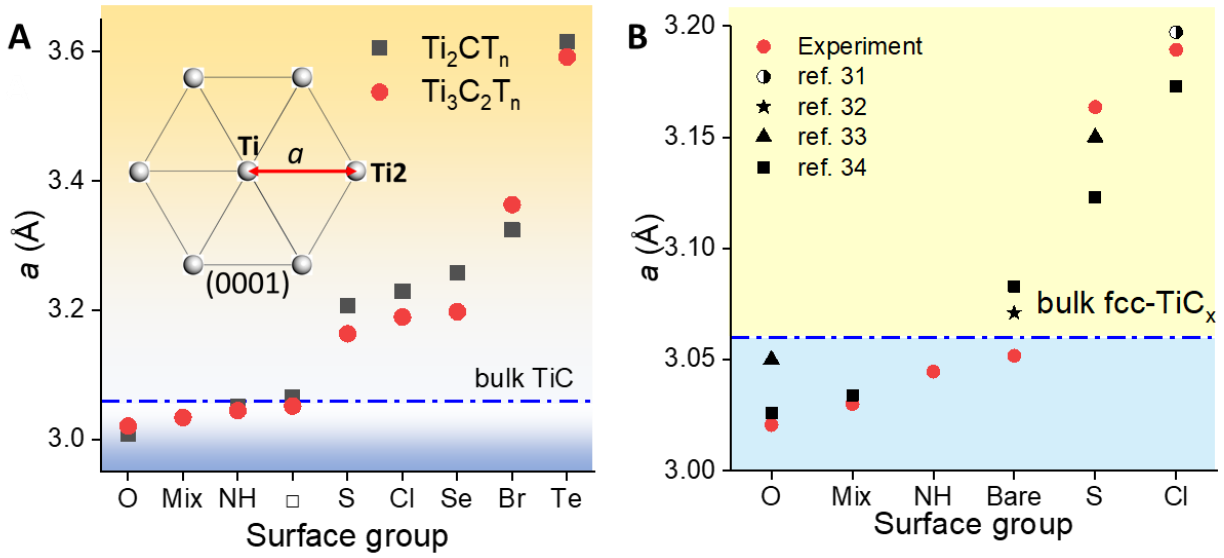

Figure 3.34. Surface groups can induce giant in-plane strain in the MXene lattice.
(A) Dependence of the in-plane lattice constant *a* (equivalent to Ti-Ti2 distance) for Ti_2CT_n and $Ti_3C_2T_n$ MXenes on the chemical nature of the surface group (T_n). (B) Zoomed in version of panel A showing comparison between the experimental and theoretically predicted in-plane *a* lattice parameters[31-34] of the light element functionalized $Ti_3C_2T_n$ MXene. For the mixed terminated $Ti_3C_2T_x$ MXene obtained *via* aqueous LiF-HCl method, *a* is calculated using the Vegard's Law[35] with the stoichiometry determined previously as $Ti_3C_2(OH)_{0.06}(F)_{0.25}(O)_{0.84}$.[27] No theoretical values for NH, Se, Br and Te terminated Ti_3C_2 MXenes are currently available.

Since the out-of-plane *c* lattice constant is strongly affected by the intercalation of ions and solvent molecules between MXene sheets,[36] we used high-resolution STEM images to assess the distances between the Ti planes along the *c* axis of the unit cell (Table 3.14). The magnitude of the out-of-plane strain in the MXene core ($\varepsilon_\perp$) can be calculated by referencing experimental distances between Ti planes inside the MXene sheets ($M_\perp$) to the distance between the (111) planes of bulk TiC. Figure 3.35 shows that the expansion of the *a*-lattice parameter in $Ti_3C_2T_n$ MXenes functionalized with S, Cl, Se, Br, and Te atoms is accompanied by the corresponding contraction of the Ti_3C_2 layers along the *c* axis. This observation is consistent with the behavior of the Ti_3C_2 layers as an elastic 2D sheet under tensile stress imposed by the surface atoms (Figure 3.35). The Poisson effect can account for the relations between the stress and the strain components reflected

Table 3.14. Summary of the STEM and XRD derived parameters for $Ti_3C_2T_n$ MXenes.

The strain paraments ($\varepsilon_\perp$, $\varepsilon_{||}$) and Poisson ratios (ν) were calculated according to Equations in "Estimation of the Poisson ratio". The XRD CtC distances are not available for S, Se and Te functionalized MXenes due to the presence of intercalated N_2H_4 solvent.

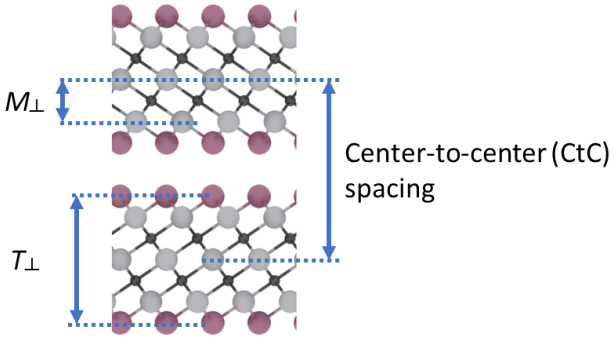

Material	$M_\perp$ (Å) (STEM)	$\Delta M_\perp$ (Å)	$T_\perp$ (Å) (STEM	$\Delta T_\perp$ (Å)	CtC (Å) (STEM)	Δ CtC Spacing (Å)	a (Å) (XRD)	c (Å) (XRD)	CtC (Å) (XRD)	$\varepsilon_\perp$ (%)	Δ (%)	$\varepsilon_{||}$ (%)	ν	Δν
Ti_3C_2	2.54	0.03	NA	NA	7.88	0.18	3.0517	15.1889	7.59	1.6	1.2	-0.3	NA	NA
Ti_3C_2S	2.45	0.07	8.66	0.1	11.00	0.12	3.1636	NA	NA	-2.0	2.8	3.4	0.23	0.33
$Ti_3C_2Cl_2$	2.39	0.06	8.42	0.32	11.36	0.17	3.18935	22.502	11.08	-4.4	2.4	4.2	0.34	0.2
Ti_3C_2Se	2.41	0.07	9.11	0.22	11.79	0.39	3.19774	NA	NA	-3.6	2.8	4.5	0.29	0.23
$Ti_3C_2Br_2$	2.36	0.07	8.45	0.2	12.12	0.2	3.36352	23.3276	11.66	-5.6	2.8	9.9	0.22	0.11
Ti_3C_2Te	2.34	0.06	9.15	0.08	13.11	0.12	3.59206	NA	NA	-6.4	2.4	17.4	0.16	0.06

by observed changes of a and $M_\perp$ distances. Unfortunately, our atomic-resolution STEM images of MXenes measure $M_\perp$ values with relatively large error bars (due to projection effects and bending of the MXene sheets) which complicates an accurate estimation of the Poisson's ratio (ν) for new MXenes. In order to estimate the Poisson ratio (ν) for the MXene sheets, we assume that the sheet can be approximated as an elastic isotropic solid. S, Cl, Se, Br and Te result in the tensile stress of the MXene basal (0001) plane, $\sigma_{xx} = \sigma_{yy} = \sigma$. The surface groups do not cause stress along the c-axis, $\sigma_{zz} = 0$. The in-plane strain, $\varepsilon_{xx} = \varepsilon_{yy} = \varepsilon_{||}$, and out-of-plane strain, $\varepsilon_{zz} = \varepsilon_\perp$, can be related to the tensile stress using the 3D Hooke's Law:

$$\varepsilon_{||} = \frac{1}{E}\left(\sigma_{xx} - \nu\left(\sigma_{zz} + \sigma_{yy}\right)\right) = \frac{1}{E}(\sigma - \nu\sigma)$$

$$\varepsilon_{\perp} = \frac{1}{E}\left(\sigma_{zz} - \nu\left(\sigma_{xx} + \sigma_{yy}\right)\right) = \frac{1}{E}(0 - 2\nu\sigma)$$

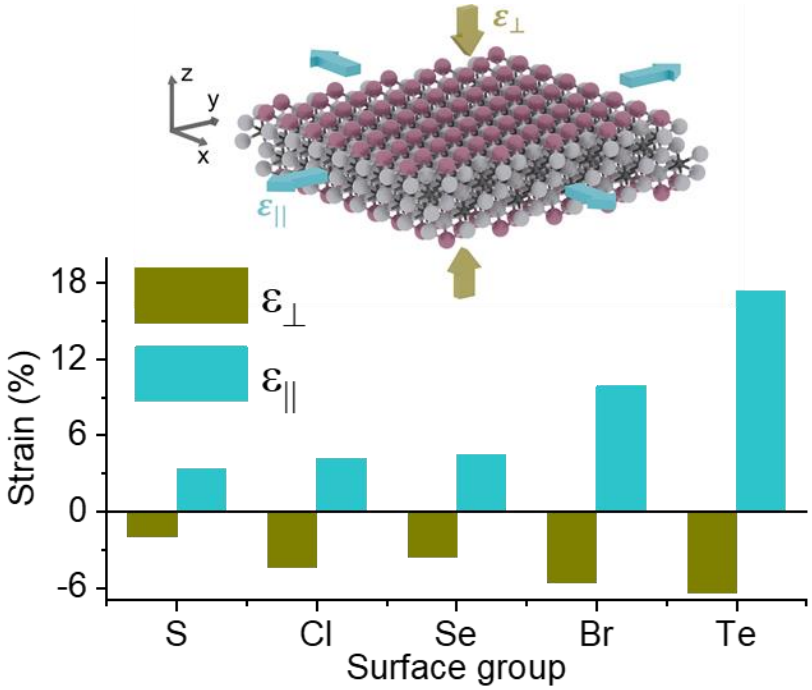

Figure 3.35. Surface groups can induce biaxial strain in the MXene lattice.

Biaxial straining of $Ti_3C_2T_n$ MXene lattice induced by the surface groups. The in-plane ($\varepsilon_{||}$) and out-of-plane ($\varepsilon_{\perp}$) strain components are evaluated with respect to the bulk cubic TiC lattice with $a_{TiC}/\sqrt{2}$ = 3.06 Å.

From the above equations the Poisson ratio can be expressed in terms of $\varepsilon_{||}$ and $\varepsilon_{\perp}$:

$$\nu = \frac{-\varepsilon_{\perp}/\varepsilon_{||}}{2 - \varepsilon_{\perp}/\varepsilon_{||}}$$

The in-plane strain can be calculated as following:

$$\varepsilon_{||} = \frac{a - a_{TiC}/\sqrt{2}}{a_{TiC}/\sqrt{2}}$$

Where a is the MXene in-plane lattice constant as estimated from the Le Bail fit of the corresponding XRD patterns and a_{TiC} (= 4.32 Å) is the lattice constant of cubic TiC.

The out-of-plane strain can be calculated as following:

$$\varepsilon_{\perp} = \frac{M_{\perp} - {a_{TiC}}/{\sqrt{3}}}{{a_{TiC}}/{\sqrt{3}}}$$

Where $M_{\perp}$ is the distance between Ti planes along c – axis, equivalent to the distance between (111) planes in cubic TiC. This distance can be obtained from the analysis of the MXene high resolution STEM images (Table 3.14).

A simple elastic model applied to $Ti_3C_2T_n$ yields $\nu \sim 0.22$ for T = S and Br, which is comparable to the recently predicted ν value for $Ti_3C_2T_x$.[15, 37] On the other hand, Ti_3C_2Te shows $\nu = 0.16 \pm 0.06$, likely due to the additional stiffening of the Ti_3C_2 layers under very large in-plane stress.

3.6 Delamination of $Ti_3C_2T_n$ MXenes.

The multilayers of $Ti_3C_2T_n$ MXenes (T = Cl, S, NH) can be further treated with n-butyl lithium resulting in Li^+ intercalated sheets (Figure 3.36) with a negative surface charge (Figures 3.37A, 3.38). Subsequent dispersion in a polar organic solvent such as N-methyl formamide (NMF) results in a stable colloidal solution of single-layer flakes (Figures 3.37B, C). The delaminated MXenes preserve their original T_n surface groups (Figures 3.38, 3.39, 3.40). X-ray diffraction pattern of spin-coated films shows a single (0002) diffraction peak corresponding to the center-to-center separation (*d*) between two adjacent MXene sheets. Absence of $(10\bar{1}l)$ and $(11\bar{2}0)$ reflections is consistent with the horizonal alignment of delaminated flakes (Figures 3.37D, 3.39A).[38] Grazing incidence wide angle X-ray scattering (GIWAXS) pattern of a thin film further supports that all MXenes are oriented parallel to the substrate (Fig. 3.37E).

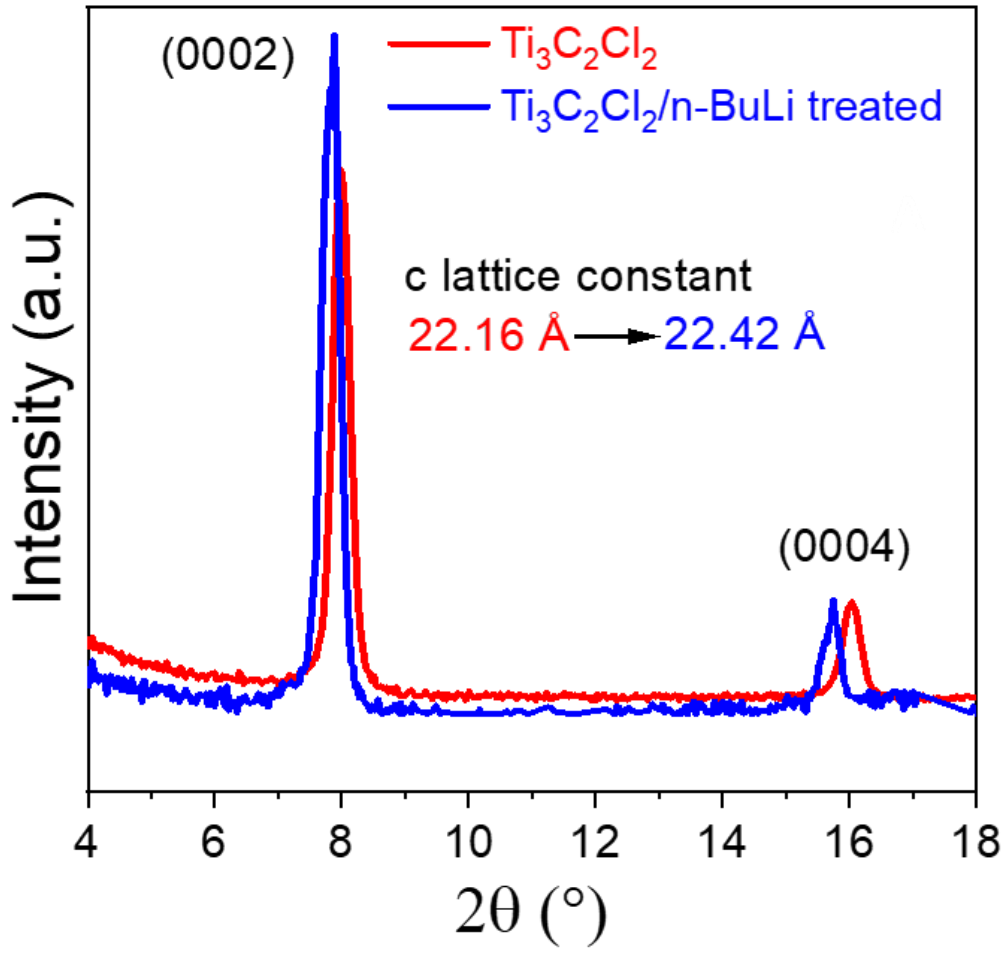

Figure 3.36. Effect of n-BuLi treatment on $Ti_3C_2Cl_2$ MXene.
WAXS patterns of the multilayer and Li^+ intercalated $Ti_3C_2Cl_2$ MXene. The *c*-lattice parameter expands after Li^+ intercalation.

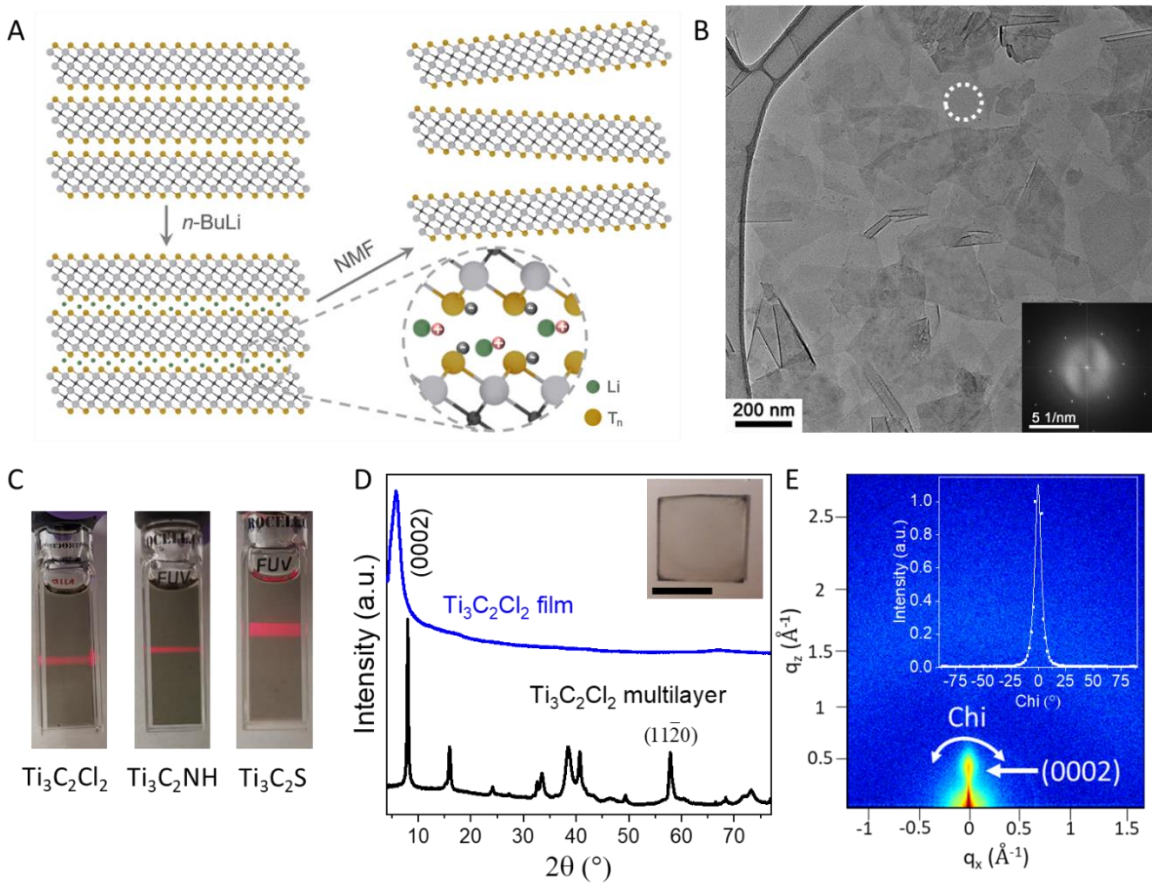

Figure 3.37. Delamination of multilayer $Ti_3C_2T_n$ MXenes.
(A) Schematic for delamination. (B) TEM image of $Ti_3C_2Cl_2$ MXenes deposited from a stable colloidal solution. Inset: Fast Fourier transform (FFT) of the highlighted region showing single-crystallinity and hexagonal symmetry of the individual flake. (C) Photographs of stable colloidal solutions of $Ti_3C_2T_n$ MXenes (T = Cl, S, NH) in NMF exhibiting Tyndall effect. (D) XRD patterns of delaminated and multilayer $Ti_3C_2Cl_2$ MXene. Inset: a photograph of $Ti_3C_2Cl_2$ MXene film spin casted on a glass substrate (scale bar 1 cm). (E) GIWAXS pattern of the film in (D). Inset: chi-integrated and normalized scattering intensity.

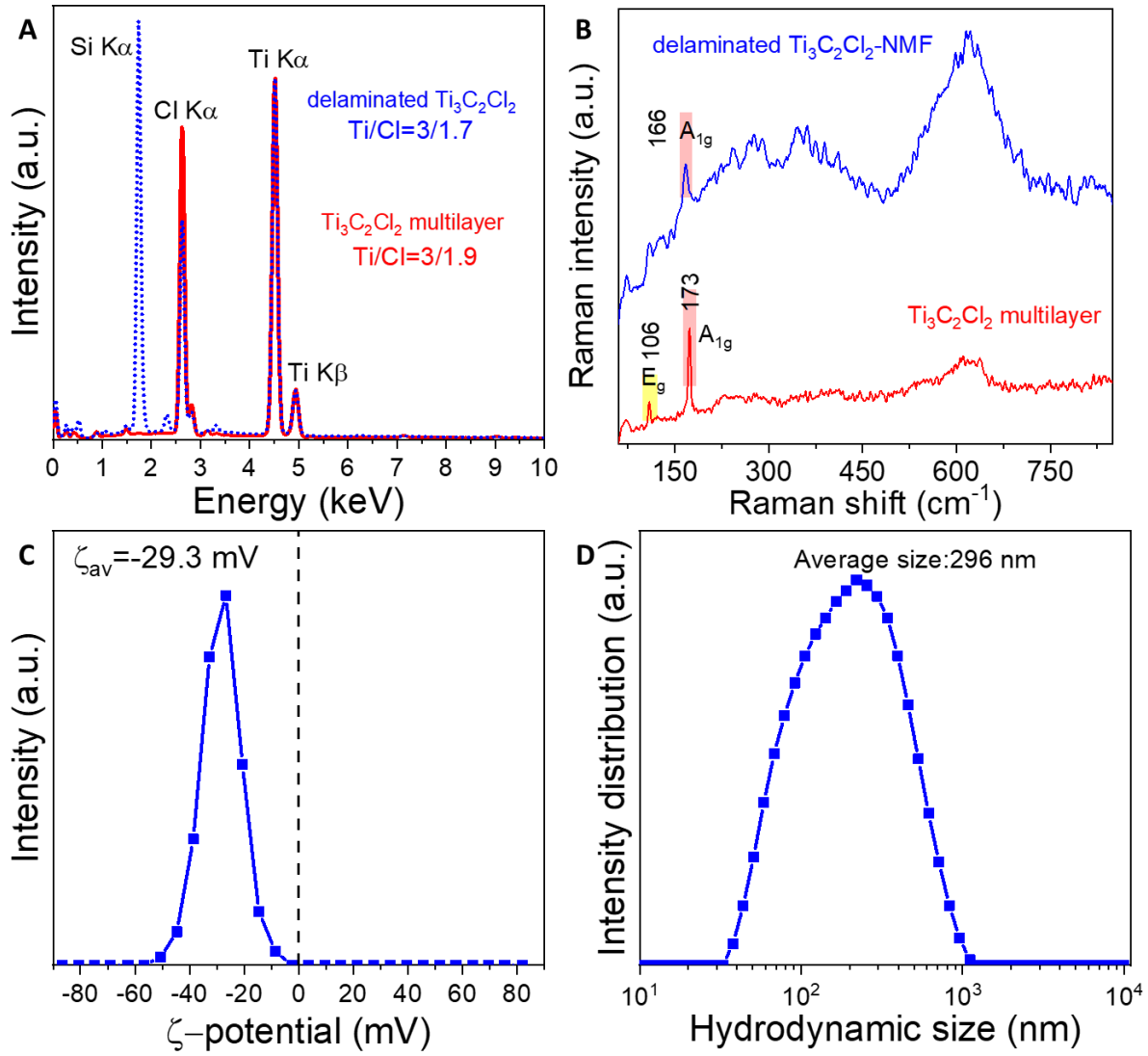

Figure 3.38. Characterization of delaminated $Ti_3C_2Cl_2$ MXene.
(A) Comparison of EDX spectra (normalized w.r.t. Ti Kα) for multilayer and delaminated MXene. Slight increase in Ti/Cl ratio in delaminated MXenes can be associated with the partial breakage of Ti-Cl bonds. (B) The Raman spectrum of delaminated $Ti_3C_2Cl_2$ MXene still contains A_{1g} peak associated with the out-of-plane vibration of surface Cl groups. (C) Zeta potential is negative for the delaminated MXenes, consistent with the injection of electron after n-BuLi treatment. (D) Size distribution of MXene flakes measured by DLS with the average flake size ~ 300 nm.

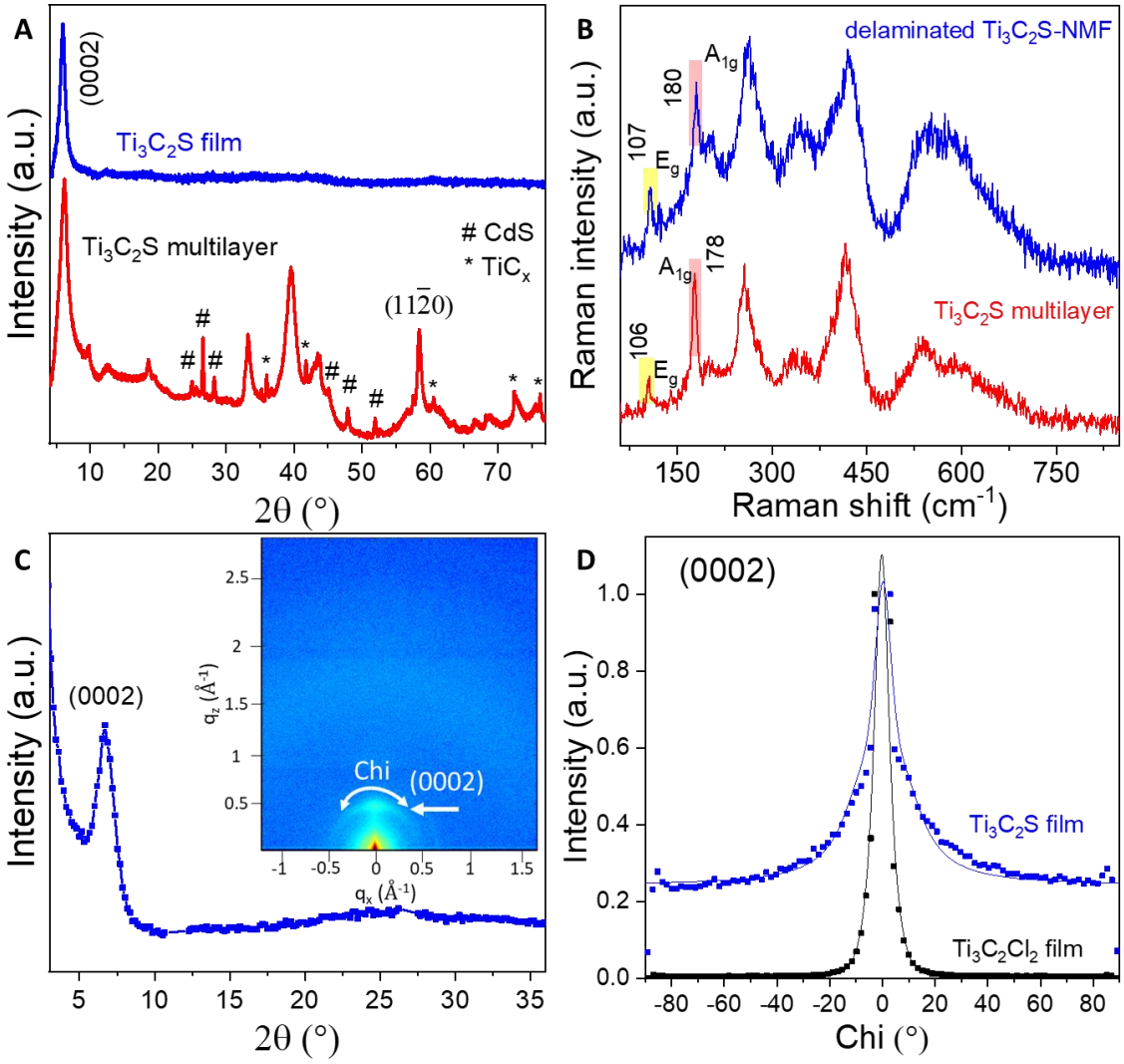

Figure 3.39. Characterization of delaminated Ti_3C_2S.
(A) XRD patterns of delaminated and multilayer Ti_3C_2S MXene. The MXene film does not contain TiC_x and CdS impurities present in the multilayer sample. The MXene film XRD pattern contains only (0002) peak consistent with most flakes aligned parallel to the substrate. (B) The Raman spectrum of delaminated Ti_3C_2S MXene still contains A_{1g} and E_g peak associated with the vibration of surface S groups. (C) 1D line cut along q_z of the 2D GIWAXS pattern (inset) shows a (0002) peak similar to that of panel (a). (D) Chi integrated intensity for Ti_3C_2S MXene film does not decay to 0 as in case of $Ti_3C_2Cl_2$ MXene film. This suggests that Ti_3C_2S MXene flakes are not as well aligned as $Ti_3C_2Cl_2$ flakes. This might be related to poorer colloidal stability of Ti_3C_2S flakes in NMF which results in lower quality MXene film.

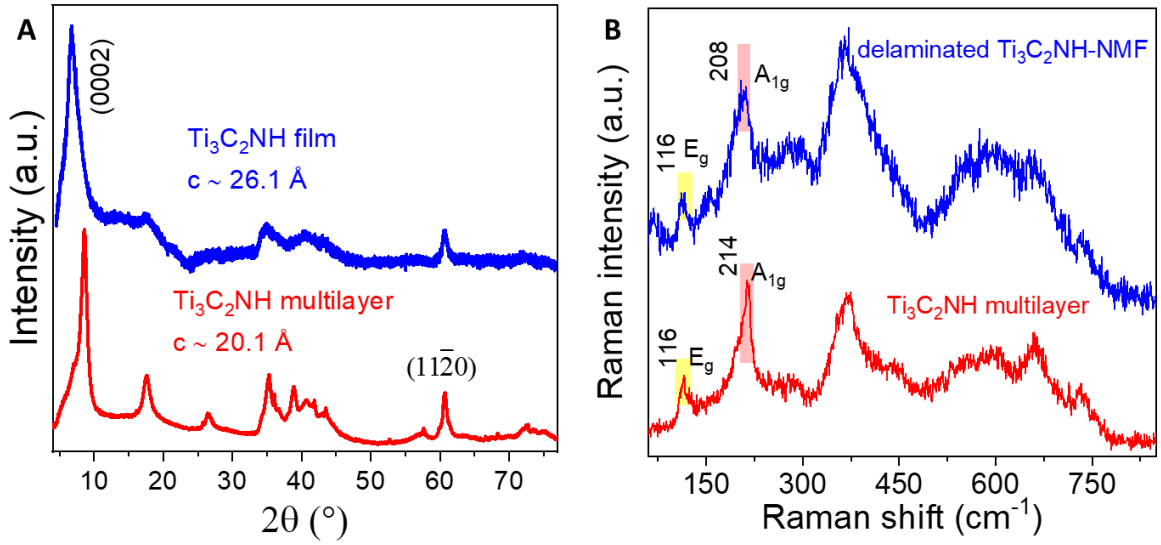

Figure 3.40. Characterization of delaminated Ti_3C_2NH.
(A) XRD patterns of delaminated and multilayer Ti_3C_2NH MXene. (0002) peak is shifted to a lower angle in case of Ti_3C_2NH film, consistent with NMF intercalation. However, presence of $(10\bar{1}l)$ and $(11\bar{2}0)$ peaks suggests incomplete alignment of the flakes parallel to the substrate. (B) The Raman spectrum of delaminated Ti_3C_2NH MXene still contains A_{1g} and E_g peak associated with the vibration of surface NH groups.

3.7 Conclusion.

In conclusion, the synthesis of MXenes with controlled functional groups opens up a general strategy for engineering this broad class of 2D materials toward previously inaccessible compositions and properties. The MXene exchange reactions represent an exciting counter example to traditional perception of solids as hard to post-synthetically modify entities. Instead, we show that chemical bonds inside an extended MXene stack can be rationally designed in a way more typical for molecular compounds. Moreover, we show that the multilayers of $Ti_3C_2Cl_2$ MXenes can be delaminated into single-layer flakes forming a stable colloidal solution. We envision we could potentially access various other surface groups including bare MXenes by adopting a reversed synthetic scheme, where the halide functionalized MXenes can be first delaminated and then their surface groups can be exchanged. For example, an already thin film of

$Ti_3C_2Cl_2$ MXenes can be further subjected to LiH treatment in a molten salt to render $Ti_3C_2\square_2$ MXene film directly.

3.8 Materials and methods.

Chemicals and materials

Al powder (99.5 %, 325 mesh, Alfa Aesar), C (graphite, 99.8 %, 325 mesh, Alfa Aesar), Ti powder (99.5 %, 325 mesh, Alfa Aesar), KCl (99.95 %, ultra dry, Alfa Aesar), NaCl (99.99 %, ultra dry), $CdCl_2$ (99.996 %, ultra dry, Alfa Aesar), $ZnCl_2$ (99.999 %, ultra dry, Alfa Aesar), $CdBr_2$ (99.999 %, ultra dry, Alfa Aesar), CsBr (99.9 %, ultra dry, Alfa Aesar), KBr (99.9 %, ultra dry, Alfa Aesar), LiBr (99.9 %, ultra dry, Alfa Aesar), LiCl (99.995 %, ultra dry, Alfa Aesar), LiH (99.4 %, Alfa Aesar), $NaNH_2$ (99 %, extra pure, Acros Organics), Li_2O (99.5 %, Alfa Aesar), Li_2S (98 %, Strem), Te shot (99.9999 %, Alfa Aesar), Se pellets (99.99 %, Alfa Aesar), Superhydride solution (1.0 M lithium triethylborohydride in tetrahydrofuran, Sigma), N_2H_4 (98 %, anhydrous, Sigma), HCl (36.5-38 %, Fisher), HBr (48 %, Sigma), MeCN (99.8 %, anhydrous, Sigma), MeOH (99.8 %, anhydrous, Sigma), LiF (98.5 %, Alfa Aesar), HF (48 %, Sigma), *n*-butyllithium (2.5 M in hexanes, Sigma), hexane (95 %, anhydrous, Sigma), THF (99.9 %, anhydrous, Sigma), N-methyl formamide (NMF, 99 %, Sigma) was purified by distillation before handling in a glovebox. Alumina crucibles were 99.8 % grade from CoorsTek. Borosilicate glass capillaries were 0.5 mm in diameter and 10 μm wall thickness from Hampton Research.

Li_2Se and Li_2Te were synthesized according to the published procedure.[39] In order to avoid oxidation of MXenes at high temperatures, it is paramount that the alkali metal chalcogenide precursors do not contain polysulfides, polyselenides and polytellurides.

MAX phase synthesis

Ti_3AlC_2 MAX phase was synthesized from TiC, Ti and Al according to a well-established procedure described in details elsewhere.[40] Ti_2AlC MAX phase was synthesized using the modified molten salt approach.[7] In brief, Ti (0.356 g), C (0.045 g) and Al (0.12 g) (2:1:1.2 molar ratio) powders were mixed with NaCl (0.87 g) and KCl (1.109 g) salts using mortar and pestle. The resultant mixture was heated in an alumina crucible at 1080 °C for 2 h under the flow of Ar.

Synthesis of MXenes with mixed (F, OH, O) termination

Mixed terminated $Ti_3C_2T_x$ were synthesized by etching Ti_3AlC_2 MAX phase in aqueous LiF-HCl solution as described in details elsewhere.[40]

Synthesis of Cl- and Br-terminated MXenes

Molten salt-based etching of MAX phases and surface group substitution/elimination reactions were all performed in an Ar-filled glovebox with oxygen and moisture levels below 1 ppm unless stated otherwise.

Ti_3AlC_2 (0.5 g) and Ti_2AlC (0.346 g) MAX phases were mixed with $CdCl_2$/$CdBr_2$ salts in 1:8 molar ratio using mortar and pestle. The resultant mixture was heated in an alumina crucible at 610 °C for at least 6 h. The Cl functionalized MXenes were recovered from the reaction mixture by dissolving excess $CdCl_2$ and Cd metal in concentrated HCl followed by washing with deionized water until neutral pH. The Br functionalized MXene were recovered from the reaction mixture by dissolving excess $CdBr_2$ and Cd metal in concentrated HBr for at least 24 h followed by washing with deonized water until neutral pH. The resultant MXene powders were dried under vacuum at 45 °C for > 12 h for further use.

Substitution/elimination of Cl/Br surface groups

The Cl- and Br-terminated MXenes act similarly during the substitution/elimination reactions.

In a typical reaction procedure, $Ti_3C_2Br_2$ MXene (70 mg) was stirred in CsBr/KBr/LiBr (25:18.9:56.1 molar ratio, m.p. 236 °C) eutectic (1.777 g) at 300 °C for 60 minutes in an alumina crucible using a glass coated stir bar. At least 3 times mole excess of the reactive ionic compound was further added to the MXene/salt mixture and stirred at 300 °C. In the case of LiH and $NaNH_2$, the elimination and surface functionalization with NH respectively were complete after 2 h of stirring at 300 °C. In the case of Li_2O, Li_2S, Li_2Se and Li_2Te, the stir bar was first removed with a magnet before annealing the reaction mixture at 500-550 °C (functionalization with S, Se and Te) or 600 °C (functionalization with O) for 12-24 h in a muffle furnace. All products were recovered by dissolving the salt matrix in anhydrous N_2H_4 followed by washing with anhydrous MeCN and anhydrous MeOH inside N_2 filled glovebox in order to avoid possible oxidation of the surface groups, especially chalcogenide groups.

Delamination of $Ti_3C_2T_n$ MXenes

In a typical delamination process, 500 mg $Ti_3C_2Cl_2$ was immersed in 5 mL of 2.5 M *n*-butyllithium hexanes solution in a sealed vial. Then, the mixture was stirred at 50 °C for 24 h inside N_2 filled glovebox. The lithium intercalated MXene was washed with hexane followed by THF to remove excess lithium and organic residues. After that, 100 mg of intercalated powder and 10 mL anhydrous NMF were added in a centrifuge tube which was further sealed inside N_2 filled glovebox. After bath sonication (< 10 °C to avoid possible oxidation) for 1 h, the supernatant was collected by centrifuging at 1500 r.p.m. for 15 min. Finally, the supernatant was centrifuged at

9000 r.p.m. for 15 min to remove small impurity. The sediment was further redispersed in fresh NMF or hydrazine to form stable colloidal solutions.

Thin film fabrication

A glass substrate was treated in piranha solution (H_2SO_4:H_2O_2 = 5:2) for 30 min, and thoroughly washed with DI water and treated with oxygen plasma for 30 min. The MXene film was obtained by spin-coating colloidal $Ti_3C_2Cl_2$ in NMF onto a substrate at ~ 90 °C inside a N_2 filled glovebox.

In-situ WAXS experiment

Due to the high attenuation coefficient of Cu Kα X-rays by CsBr salt (995.8 cm^{-1}), a mixture of KCl (245 cm^{-1}) and LiCl (178.4 cm^{-1}) in 1:2 molar ratio was used instead. $Ti_3C_2Cl_2$ MXene was mixed with KCl/LiCl salt at a 100 mg/g concentration (mixture 1). In case of the surface group substitution, 3 times mole excess of Li_2O or K_2Se (w.r.t. $Ti_3C_2Cl_2$ MXene) were added to mixture 1 above (mixture 2). The resultant mixture (mixture 1 or mixture 2) was annealed at 500-550 °C in an alumina crucible for 12-24 h. The annealed mixture was crushed with mortar and pestle and the fine powder was loaded into 0.5 mm borosilicate glass capillary. The capillary was first sealed with epoxy inside the nitrogen filled glovebox before flame sealing outside the glovebox. The in-situ heating experiments were performed in the Linkam stage. The heating rate was 10 K/min and the capillary was allowed to equilibrate for additional 20 minutes before the measurement.

X-ray diffraction (XRD)

The diffraction patterns in the reflection mode were obtained using a Bruker D8 diffractometer with Cu Kα X-ray source (1.5418 Å) operating at 40 kV and 40 mA and Vantec 2000 area detector.

Representative samples of Ti_2CT_n MXenes such as Ti_2CCl_2, Ti_2CBr_2, Ti_2CS and Ti_2AlC MAX phase were additionally collected in the spinning capillary mode using monochromatic Mo Kα1 radiation (0.7093 Å, STOE Stadi-MP) and synchrotron (0.2412 Å, Advanced Photon Source, 17-BM-B) radiation for Ti_2CTe sample.

XRD full pattern fittings (Le Bail and Rietveld) were performed using TOPAS Version 5 software. The Le Bail full pattern fitting was used to extract the unit cell parameters. Each MXene and MAX phase sample was assumed to contain at least two phases: TiC_x (*Fm-3m* space group) and MXene (*P6₃/mmc* or *P-3m1* space group) or MAX phase (*P6₃/mmc* space group). The Stephens model (hexagonal symmetry)[41] was used to account for the anisotropic peak broadening of the XRD patterns of MXenes and MAX phases. The Rietveld refinement of the MXene XRD patterns collected in the reflection mode was impeded by the high anisotropy of the MXene samples due to their 2D nature and lack of the precise ordering in third dimension. Moreover, Rietveld analysis can completely fail for 2D MXenes systems such as recently shown for Mo_2CT_x MXene.[42] The differences between the Le Bail and Rietveld refinements are insignificant and within approximately 0.01 Å for a and 0.1 Å for c axes.

Simulated XRD patterns for three different configurations of surface groups in Ti_2CCl_2 and Ti_2CTe MXenes were generated in BIOVIA's Materials Studio program.

Wide-angle X-ray scattering (WAXS) and Grazing incidence WAXS (GIWAXS)

Transmission WAXS patterns of the MXenes in salt matrices and GIWAXS of delaminated MXene films were collected on SAXSLab Ganesha instrument with Cu Kα X-ray source (1.5418 Å). The GIWAXS measurements were performed at an incident angle of 0.18-0.2°.

X-ray total scattering and pair distribution function (PDF) analysis

High energy X-ray total scattering experiments were performed at 11-ID-B at the Advanced Photon Source, with the X-ray wavelength of 0.2115 Å. The raw 2D data were azimuthally integrated and reduced to 1D intensity *versus* 2θ in GSAS-II[43] using CeO_2 powder as a calibrant to determine sample to detector distance. PDFgetX2 program[44] was used to correct and normalize the diffraction data and then Fourier transform them to obtain the PDF, G(r), according to:

$$G(r) = \frac{2}{\pi} \int_{q_{min}}^{q_{max}} dq q(S(q) - 1)\sin(qr)$$

Here q is the magnitude of the momentum transfer on scattering and S(q) is the properly corrected and normalized powder diffraction intensity measured from q_{min} and q_{max}. G(r) gives the probability of finding a pair of atoms separated by a distance of r.

X-ray absorption (XAS)

Extended X-ray Absorption Fine Structure (EXAFS) spectroscopy and X-ray Absorption Near Edge Structure (XANES) were employed to probe the local environment around Ti using K-edge EXAFS and XANES (4966 eV) at the 20-ID-B beam line at the Advanced Photon Source, Argonne National Laboratory. XAS data were collected in a transmission mode at room

temperature. The incident, transmitted and reference X-ray intensities were monitored using gas ionization chambers. A titanium foil standard was used as a reference for energy calibration and was measured simultaneously with experimental samples. All powder samples were measured as pellets diluted with appropriate amount of BN and sealed in Kapton tape inside a glovebox.

Data collected were processed using Athena software (version 0.9.26)[45] by extracting the EXAFS oscillations $\chi(k)$ as a function of photoelectron wave number k. The theoretical paths were generated using FEFF6[46] and the models were fitted using the program Artemis (version 0.9.26).[45] Data sets were simultaneously fitted in R-space with k-weights of 1, 2 and 3.

Additional fitting details: Incorporation of two scattering Ti-Ti paths for Ti_2CT_n samples is essential to get a good fit in the area between 2-3 Å in R space. The first scattering Ti-Ti path (Ti-Ti1) corresponds to the nearest neighbor Ti on the opposite side of the same Ti_2CT_n 2D sheet. The second scattering Ti-Ti path (Ti-Ti2) corresponds to the Ti neighbor on the same side of the same Ti_2CT_n sheet. Ti-Ti2 distance is approximately equal to the in-plane lattice constant *a* determined from XRD.

Abbreviations used: C.N. Coordination numbers; R, interatomic distances; σ^2, Debye-Waller factors (the mean-square deviations in interatomic distance). The values in parentheses are the estimated standard deviations; ΔE_0, change in the photoelectron energy; S_0^2, amplitude reduction factor.

Scanning transmission electron microscopy (STEM) characterization

Atomic-resolution characterization of the MXene samples was conducted using the JEOL ARM200CF at the University of Illinois at Chicago, which is an aberration-corrected scanning transmission electron microscope (STEM) equipped with a cold field emission gun operated at

200 kV, a Gatan Continuum electron energy-loss spectrometer (EELS) and an Oxford XMAX100TLE X-ray detector, providing a sub-Å probe-size and 350 meV energy resolution. The emission current was reduced to 12 μA in order to reduce damage from the electron beam. An electron probe convergence semi-angle of 24 mrad was used and the inner detector angle for high angle annular dark field imaging was chosen to be 75 mrad, while an inner angle for low angle annular dark field (LAADF) imaging was chosen at 30 mrads.

The MXene samples were initially prepared for STEM analysis by dropcasting particles suspended in isopropyl alcohol onto a 3 mm holey-carbon covered TEM grid. The chalcogenide functionalized MXenes still contained intercalated N_2H_4, which required heating the samples to 100 °C prior to performing the STEM characterization. The samples were heated using the Protochip Aduro Double Tilt heating holder in the column of the JEOL ARM200CF.

Scanning electron microscopy-energy dispersive X-ray spectroscopy (SEM-EDX)

SEM imaging and EDX elemental mapping were performed in a TESCAN LYRA3 field-emission scanning electron microscope equipped with two X-Max-80 silicon drift x-detectors (SDD).

Raman spectroscopy

Raman spectra were obtained with a Horiba LabRamHR Evolution confocal microscope. Si (111) wafer was used for calibration. The samples were excited using a 633 nm light source operating at 1 % of its power or 532 nm light source operating at 2.5 % of its powder and using 100x long path objective and a 600 mm^{-1} grating.

X-ray fluorescence (XRF)

XRF analysis was performed with a benchtop Energy Dispersive Rigaku NEX DE VS X-ray fluorimeter equipped with a Peltier cooled FAST SDD Silicon Drift Detector. All analyses were carried out under He atmosphere to increase sensitivity for lighter elements. Elemental ratios were determined using the standardless thin films fundamental parameters method as programmed in QuantEZ software provided by Rigaku. For the consistent analysis, the samples were prepared by drop casting powders dispersed in anhydrous MeOH on a Si substrate of an approximate 1 by 1 cm square size to provide uniform thin films throughout the series. The films were loaded into the instrument and the analysis window was set at 10 mm radius. All samples were measured and analyzed in the same manner.

X-ray photoelectron spectroscopy (XPS)

XPS analysis was performed on a Kratos Axis Nova spectrometer using monochromatic Al Kα source (1486.6 eV). Te 3d, Ti 2p, N 1s, C 1s, Cl 2p, S 2p and Br 3d high-resolution spectra were collected using an analysis area of 0.3 x 0.7 mm^2 and 20 eV pass energy with the step size of 100 meV. Charge neutralization was performed using a co-axial, low energy (≈ 0.1 eV) electron flood source to avoid shifts in the recovered binding energy. C 1s peak of adventitious carbon was set at 284.8 eV to compensate for any remaining charge-induced shifts. Deconvolution of the high-resolution XPS spectra was performed in CasaXPS software using symmetric Lorentzian-Gaussian curves and a Shirley background. The Ti 2p region consists of the two $2p_{3/2}$ and $2p_{1/2}$ spin-orbit split components. The peak area ratio of $2p_{3/2}$ to $2p_{1/2}$ was fixed to 2 to 1. The Ti 2p region was fit using 4 pairs of $2p_{3/2}$ and $2p_{1/2}$ components for each sample. The Ti-C contribution of the C 1s region was fit with the two curves in order to account for the peak asymmetry. The peak asymmetry is caused by the extrinsic loses due to delocalized states.[47]

Zeta potential and Dynamic light scattering (DLS)

Zeta potential and DLS of a dilute filtered solution of $Ti_3C_2Cl_2$ MXene in NMF was measured with a Zetasizer Nano-ZS (Malvern Instruments). The sample was held in a glass cuvette with an immersed dip cell with palladium electrodes.

3.9 Chapter 3 bibliography.

1. Khazaei, M.; Arai, M.; Sasaki, T.; Chung, C.-Y.; Venkataramanan, N. S.; Estili, M.; Sakka, Y.; Kawazoe, Y., Novel Electronic and Magnetic Properties of Two-Dimensional Transition Metal Carbides and Nitrides. *Adv. Funct. Mater.* **2013,** *23* (17), 2185-2192.

2. Zhou, L.; Zhang, Y.; Zhuo, Z.; Neukirch, A. J.; Tretiak, S., Interlayer-Decoupled Sc-Based Mxene with High Carrier Mobility and Strong Light-Harvesting Ability. *J. Phys. Chem. Lett.* **2018,** *9* (23), 6915-6920.

3. Liu, Y.; Xiao, H.; Goddard, W. A., Schottky-Barrier-Free Contacts with Two-Dimensional Semiconductors by Surface-Engineered MXenes. *J. Am. Chem. Soc.* **2016,** *138* (49), 15853-15856.

4. Si, C.; Zhou, J.; Sun, Z., Half-Metallic Ferromagnetism and Surface Functionalization-Induced Metal–Insulator Transition in Graphene-like Two-Dimensional Cr2C Crystals. *ACS Applied Materials & Interfaces* **2015,** *7* (31), 17510-17515.

5. Pang, S.-Y.; Wong, Y.-T.; Yuan, S.; Liu, Y.; Tsang, M.-K.; Yang, Z.; Huang, H.; Wong, W.-T.; Hao, J., Universal Strategy for HF-Free Facile and Rapid Synthesis of Two-dimensional MXenes as Multifunctional Energy Materials. *J. Am. Chem. Soc.* **2019,** *141* (24), 9610-9616.

6. Li, T.; Yao, L.; Liu, Q.; Gu, J.; Luo, R.; Li, J.; Yan, X.; Wang, W.; Liu, P.; Chen, B.; Zhang, W.; Abbas, W.; Naz, R.; Zhang, D., Fluorine-Free Synthesis of High-Purity Ti3C2Tx (T=OH, O) via Alkali Treatment. *Angew. Chem., Int. Ed.* **2018,** *57* (21), 6115-6119.

7. Li, M.; Lu, J.; Luo, K.; Li, Y.; Chang, K.; Chen, K.; Zhou, J.; Rosen, J.; Hultman, L.; Eklund, P.; Persson, P. O. Å.; Du, S.; Chai, Z.; Huang, Z.; Huang, Q., Element Replacement Approach by Reaction with Lewis Acidic Molten Salts to Synthesize Nanolaminated MAX Phases and MXenes. *J. Am. Chem. Soc.* **2019,** *141* (11), 4730-4737.

8. Li, Y.; Hui Shao, H.; Lin, Z.; Lu, J.; Persson, P. O. A.; Eklund, P.; Hultman, L.; Li, M.; Chen, K.; Zha, X.-H.; Du, S.; Rozier, P.; Chai, Z.; Raymundo-Piñero, E.; Taberna, P.-L.; Simon, P.; Huang, Q., A general Lewis acidic etching route for preparing MXenes with enhanced electrochemical performance in non-aqueous electrolyte. arXiv:1909.13236: arXiv.org e-Print archive, 2019.

9. Kim, D.; Ko, T. Y.; Kim, H.; Lee, G. H.; Cho, S.; Koo, C. M., Nonpolar Organic Dispersion of 2D Ti3C2Tx MXene Flakes via Simultaneous Interfacial Chemical Grafting and Phase Transfer Method. *ACS Nano* **2019,** *13* (12), 13818-13828.

10. Sokol, M.; Natu, V.; Kota, S.; Barsoum, M. W., On the Chemical Diversity of the MAX Phases. *Trends in Chemistry* **2019,** *1* (2), 210-223.

11. Srivastava, V.; Kamysbayev, V.; Hong, L.; Dunietz, E.; Klie, R. F.; Talapin, D. V., Colloidal Chemistry in Molten Salts: Synthesis of Luminescent In1–xGaxP and In1–xGaxAs Quantum Dots. *J. Am. Chem. Soc.* **2018,** *140* (38), 12144-12151.

12. Dash, A.; Vaßen, R.; Guillon, O.; Gonzalez-Julian, J., Molten salt shielded synthesis of oxidation prone materials in air. *Nat. Mater.* **2019,** *18* (5), 465-470.

13. Liu, X.; Fechler, N.; Antonietti, M., Salt melt synthesis of ceramics, semiconductors and carbon nanostructures. *Chem. Soc. Rev.* **2013,** *42* (21), 8237-8265.

14. Hu, T.; Wang, J.; Zhang, H.; Li, Z.; Hu, M.; Wang, X., Vibrational properties of Ti3C2 and Ti3C2T2 (T = O, F, OH) monosheets by first-principles calculations: a comparative study. *Phys. Chem. Chem. Phys.* **2015,** *17* (15), 9997-10003.

15. Fu, Z. H.; Zhang, Q. F.; Legut, D.; Si, C.; Germann, T. C.; Lookman, T.; Du, S. Y.; Francisco, J. S.; Zhang, R. F., Stabilization and strengthening effects of functional groups in two-dimensional titanium carbide. *Phys. Rev. B* **2016,** *94* (10), 104103.

16. Saha, N. C.; Tompkins, H. G., Titanium nitride oxidation chemistry: An x-ray photoelectron spectroscopy study. *J. Appl. Phys.* **1992,** *72* (7), 3072-3079.

17. Jansen, M., A Concept for Synthesis Planning in Solid-State Chemistry. *Angew. Chem., Int. Ed.* **2002,** *41* (20), 3746-3766.

18. Zhang, N.; Hong, Y.; Yazdanparast, S.; Asle Zaeem, M., Superior structural, elastic and electronic properties of 2D titanium nitride MXenes over carbide MXenes: a comprehensive first principles study. *2D Materials* **2018,** *5* (4), 045004.

19. Zhang, H.; Dasbiswas, K.; Ludwig, N. B.; Han, G.; Lee, B.; Vaikuntanathan, S.; Talapin, D. V., Stable colloids in molten inorganic salts. *Nature* **2017,** *542*, 328.

20. Shi, C.; Beidaghi, M.; Naguib, M.; Mashtalir, O.; Gogotsi, Y.; Billinge, S. J. L., Structure of Nanocrystalline ${\mathrm{Ti}}_{3}{\mathrm{C}}_{2}$ MXene Using Atomic Pair Distribution Function. *Phys. Rev. Lett.* **2014,** *112* (12), 125501.

21. Wang, H.-W.; Naguib, M.; Page, K.; Wesolowski, D. J.; Gogotsi, Y., Resolving the Structure of Ti3C2Tx MXenes through Multilevel Structural Modeling of the Atomic Pair Distribution Function. *Chem. Mater.* **2016,** *28* (1), 349-359.

22. Troyanov, S. I.; Snigireva, E. M.; Rybakov, V. B., X-ray diffraction study of phase transition in alfa-TiCl3. *Zh. Neorg. Khim.* **1991,** *36*, 1117-1122.

23. Troyanov, S. I.; Ionov, V. M.; Rybakov, V. B., Synthesis and crystal structures of $TiBr_4$,$TiBr_3$ and $Ti(AlBr_4)_2$. *Zh. Neorg. Khim.* **1990,** *35*, 882-887.

24. Ehrlich, P.; Gutsche, W.; Seifert, H.-J., Darstellung und Kristallstruktur von Titandibromid. *Z. Anorg. Allg. Chem.* **1961,** *312* (1-2), 80-86.

25. Ehrlich, P., Über Titanselenide und -telluride. *Zeitschrift für anorganische Chemie* **1949,** *260* (1-3), 1-18.

26. Onoda, M.; Wada, H., The titanium-sulphur system: Structures of Ti6.9S9(18H) and Ti8.2S11(33R) and the unit cells of 45R and 57R types of titanium sulphide. *Journal of the Less Common Metals* **1987,** *132* (2), 195-207.

27. Hope, M. A.; Forse, A. C.; Griffith, K. J.; Lukatskaya, M. R.; Ghidiu, M.; Gogotsi, Y.; Grey, C. P., NMR reveals the surface functionalisation of Ti3C2 MXene. *Phys. Chem. Chem. Phys.* **2016,** *18* (7), 5099-5102.

28. Persson, I.; Näslund, L.-Å.; Halim, J.; Barsoum, M. W.; Darakchieva, V.; Palisaitis, J.; Rosen, J.; Persson, P. O. Å., On the organization and thermal behavior of functional groups on Ti3C2 MXene surfaces in vacuum. *2D Materials* **2017,** *5* (1), 015002.

29. Qin, Y.; Zha, X.-H.; Bai, X.; Luo, K.; Huang, Q.; Wang, Y.; Du, S., Structural, mechanical and electronic properties of two-dimensional chlorine-terminated transition metal carbides and nitrides. *J. Phys.: Condens. Matter* **2020,** *32* (13), 135302.

30. Richardson, J. H., Thermal Expansion of Three Group IVA Carbides to 2700°C. *J. Am. Ceram. Soc.* **1965,** *48* (10), 497-499.

31. Lu, J.; Persson, I.; Lind, H.; Palisaitis, J.; Li, M.; Li, Y.; Chen, K.; Zhou, J.; Du, S.; Chai, Z.; Huang, Z.; Hultman, L.; Eklund, P.; Rosen, J.; Huang, Q.; Persson, P. O. Å., Tin+1Cn MXenes with fully saturated and thermally stable Cl terminations. *Nanoscale Advances* **2019,** *1* (9), 3680-3685.

32. Berdiyorov, G. R., Optical properties of functionalized Ti3C2T2 (T = F, O, OH) MXene: First-principles calculations. *AIP Advances* **2016,** *6* (5), 055105.

33. Meng, Q.; Ma, J.; Zhang, Y.; Li, Z.; Zhi, C.; Hu, A.; Fan, J., The S-functionalized Ti3C2 Mxene as a high capacity electrode material for Na-ion batteries: a DFT study. *Nanoscale* **2018,** *10* (7), 3385-3392.

34. Wang, D.; Li, F.; Lian, R.; Xu, J.; Kan, D.; Liu, Y.; Chen, G.; Gogotsi, Y.; Wei, Y., A General Atomic Surface Modification Strategy for Improving Anchoring and Electrocatalysis Behavior of Ti3C2T2 MXene in Lithium–Sulfur Batteries. *ACS Nano* **2019,** *13* (10), 11078-11086.

35. Ibragimova, R.; Puska, M. J.; Komsa, H.-P., pH-Dependent Distribution of Functional Groups on Titanium-Based MXenes. *ACS Nano* **2019,** *13* (8), 9171-9181.

36. Mashtalir, O.; Naguib, M.; Mochalin, V. N.; Dall'Agnese, Y.; Heon, M.; Barsoum, M. W.; Gogotsi, Y., Intercalation and delamination of layered carbides and carbonitrides. *Nat. Commun.* **2013,** *4* (1), 1716.

37. Lipatov, A.; Lu, H.; Alhabeb, M.; Anasori, B.; Gruverman, A.; Gogotsi, Y.; Sinitskii, A., Elastic properties of 2D Ti₃C₂T_x MXene monolayers and bilayers. *Science Advances* **2018,** *4* (6), eaat0491.

38. Ghidiu, M.; Barsoum, M. W., The {110} reflection in X-ray diffraction of MXene films: Misinterpretation and measurement via non-standard orientation. *J. Am. Ceram. Soc.* **2017,** *100* (12), 5395-5399.

39. Beecher, A. N.; Yang, X.; Palmer, J. H.; LaGrassa, A. L.; Juhas, P.; Billinge, S. J. L.; Owen, J. S., Atomic Structures and Gram Scale Synthesis of Three Tetrahedral Quantum Dots. *J. Am. Chem. Soc.* **2014,** *136* (30), 10645-10653.

40. Alhabeb, M.; Maleski, K.; Anasori, B.; Lelyukh, P.; Clark, L.; Sin, S.; Gogotsi, Y., Guidelines for Synthesis and Processing of Two-Dimensional Titanium Carbide (Ti3C2Tx MXene). *Chem. Mater.* **2017,** *29* (18), 7633-7644.

41. Stephens, P., Phenomenological model of anisotropic peak broadening in powder diffraction. *J. Appl. Crystallogr.* **1999,** *32* (2), 281-289.

42. Deeva, E. B.; Kurlov, A.; Abdala, P. M.; Lebedev, D.; Kim, S. M.; Gordon, C. P.; Tsoukalou, A.; Fedorov, A.; Müller, C. R., In Situ XANES/XRD Study of the Structural Stability of Two-Dimensional Molybdenum Carbide Mo2CTx: Implications for the Catalytic Activity in the Water–Gas Shift Reaction. *Chem. Mater.* **2019,** *31* (12), 4505-4513.

43. Toby, B. H.; Von Dreele, R. B., GSAS-II: the genesis of a modern open-source all purpose crystallography software package. *J. Appl. Crystallogr.* **2013,** *46* (2), 544-549.

44. Qiu, X.; Thompson, J. W.; Billinge, S. J. L., PDFgetX2: a GUI-driven program to obtain the pair distribution function from X-ray powder diffraction data. *J. Appl. Crystallogr.* **2004,** *37* (4), 678.

45. Ravel, B.; Newville, M., ATHENA, ARTEMIS, HEPHAESTUS: data analysis for X-ray absorption spectroscopy using IFEFFIT. *Journal of Synchrotron Radiation* **2005,** *12* (4), 537-541.

46. Rehr, J. J.; Albers, R. C., Theoretical approaches to x-ray absorption fine structure. *Rev. Mod. Phys.* **2000,** *72* (3), 621-654.

47. Halim, J.; Lukatskaya, M. R.; Cook, K. M.; Lu, J.; Smith, C. R.; Näslund, L.-Å.; May, S. J.; Hultman, L.; Gogotsi, Y.; Eklund, P.; Barsoum, M. W., Transparent Conductive Two-Dimensional Titanium Carbide Epitaxial Thin Films. *Chem. Mater.* **2014,** *26* (7), 2374-2381.

4 Electronic transport and superconductivity in Nb_2CT_n MXenes

4.1 Introduction to Nb_2CT_n MXenes with selective surface terminations, T_n.

The examples of Chapter 3 show that the composition and structure of Ti-based MXenes can be engineered with previously unattainable versatility. However, the developed chemistry is not limited to MXenes with Ti as the transition metal. Similar to Ti_3AlC_2 and Ti_2AlC MAX phases, Nb_2AlC MAX phase can be etched resulting in Nb_2CCl_2 MXene (Figure 4.1).

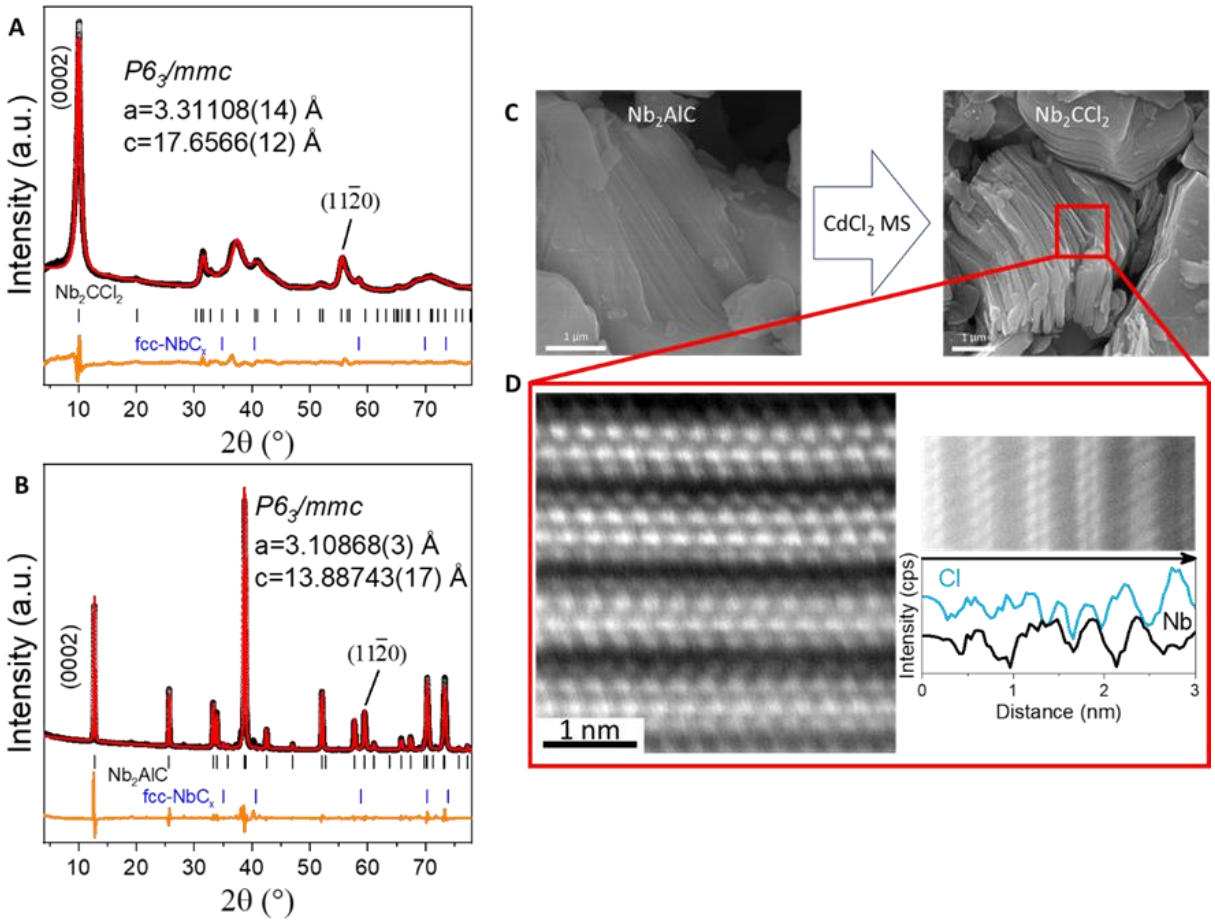

Figure 4.1. Characterization of Nb_2CCl_2 MXene.
Experimental XRD patterns (Cu Kα, reflection, black curves) and Le Bail fits (red curves) of (A) Nb_2CCl_2 MXene derived from Nb_2AlC MAX phase in (B). (C) SEM images of Nb_2AlC MAX phase and Nb_2CCl_2 MXene. (D) STEM low-angle dark-field (LAADF) image of Nb_2CCl_2 MXene. The EDX elemental line scans using Cl Kα and Nb Kα confirm presence of Cl surface groups on each Nb_2C sheet.

Nb_2CCl_2 MXene can be further dispersed in CsBr/KBr/LiBr eutectic (m.p. 236°C) and reacted with LiH, $NaNH_2$ and Li_2O resulting in $Nb_2C□_2$, Nb_2CNH and Nb_2CO_x (Nb/O ratio was not determined) MXenes (Figures 4.2, 4.3).

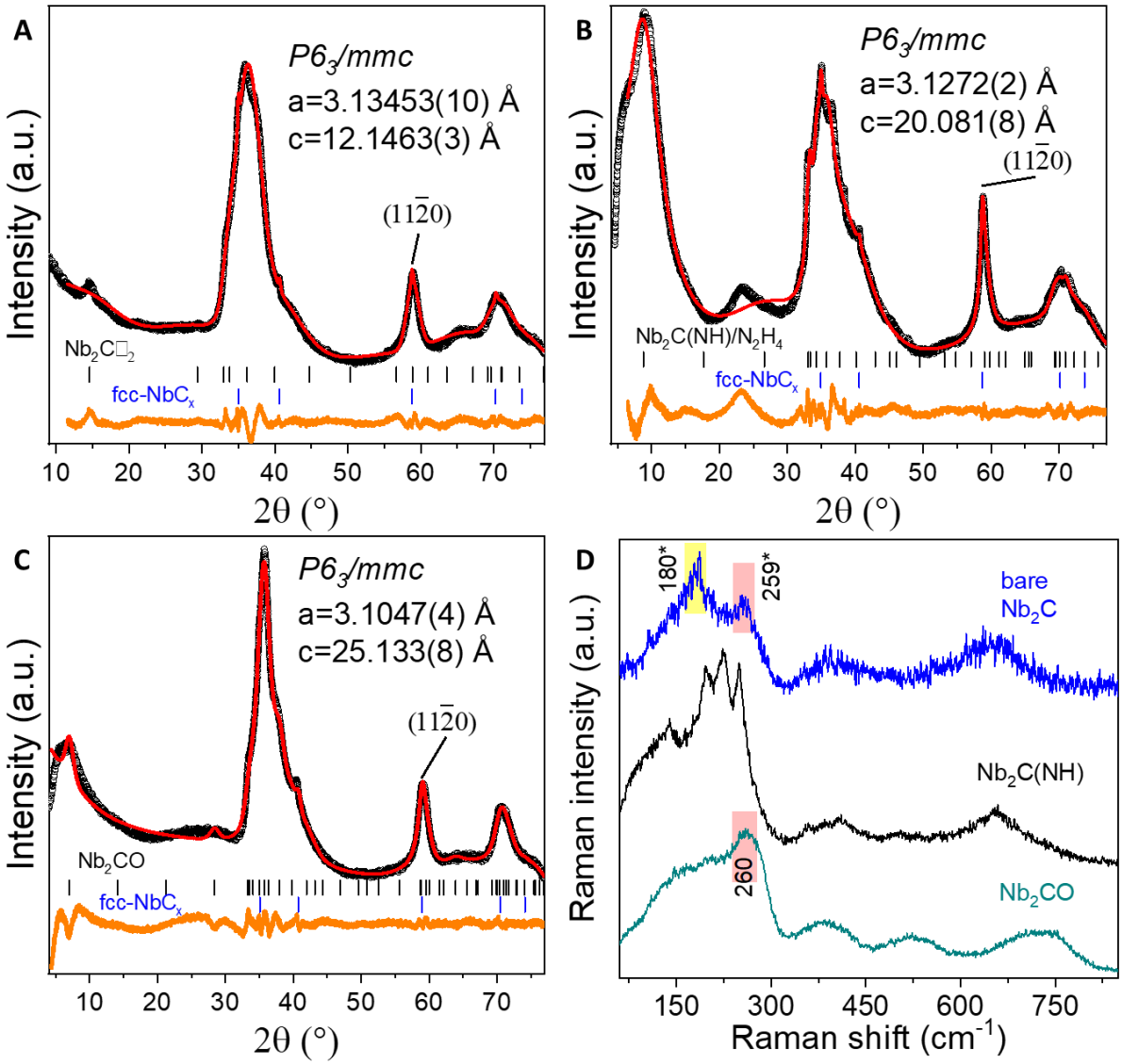

Figure 4.2. Characterization of Nb_2C(□ ,NH, O) MXenes.
Experimental XRD patterns (Cu Kα, reflection, black curves) and Le Bail fits (red curves) of: (A) Bare Nb_2C MXene with the *c* lattice constant larger than that of the bare Ti_2C MXene (Chapter 3.4), probably due to the larger ionic size of Nb atoms; (B) Nb_2C(NH) MXene recovered from the salt matrix using anhydrous hydrazine; (C) Nb_2CO MXene. (D) Raman spectra of the same MXenes. The assignment of the vibrational modes (marked with *) of the bare Nb_2C is based on the work of Hu *et al.*[1]

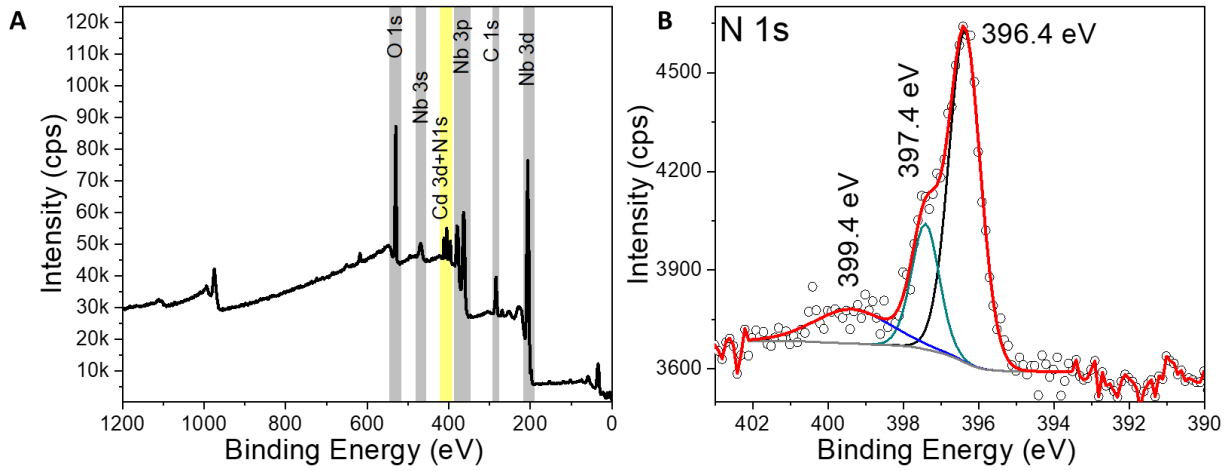

Figure 4.3. XPS spectra of $Nb_2C(NH)$ MXene.

(A) Survey spectrum with the highlighted N 1s region. Elemental analysis of this survey spectrum results in Nb:N ratio of 2:1.1. (B) Analysis of the high resolution N 1s spectrum suggests presence of three components, similar to that of $Ti_3C_2(NH)$ (Chapter 3.2). The 396.4 eV peak (64 %) belongs to the chemisorbed β-N on Nb surface. The 397.4 eV peak (21 %) could correspond to the chemisorbed α-N_2 on Nb surface. The 399.4 eV peak (16 %) likely corresponds to N-H bond.

Similar to T = □ ,NH, O surface functionalization, Nb_2CCl_2 can be reacted with Li_2S and K_2Se to yield Nb_2CS_2 and Nb2CSe MXenes (Figure 4.4). The Raman spectra of Nb_2CS_2 and Nb_2CSe MXenes (Figure 4.5) shows a trend similar to the case of functionalized Ti_3C_2 MXenes (Chapter 3.2): the position of the A_{1g} (red area) and E_g (yellow area) mode is primarily determined by the atomic mass of the surface group with Se resulting in lower frequencies than both Cl and S. Additionally, XPS survey spectra show replacement of Cl peaks with the S peaks after the surface exchange in CsBr/LiBr/KBr molten salt (Figure 4.6). Moreover, high resolution XPS spectra (Figure 4.7) suggest that the Nb-C component binding energy of Nb_2CCl_2 MXene shifts to a lower value after Cl^- has been substituted for S^{2-}. This result is in accordance with S being less electronegative than Cl. S 2p region of Nb_2CS_2 MXene can be modelled using two components: S^{2-} as the major component (70 %) and S in higher oxidation state (probably in the form of S_n^{2-}) as the minor component (30 %) (Table 4.1).

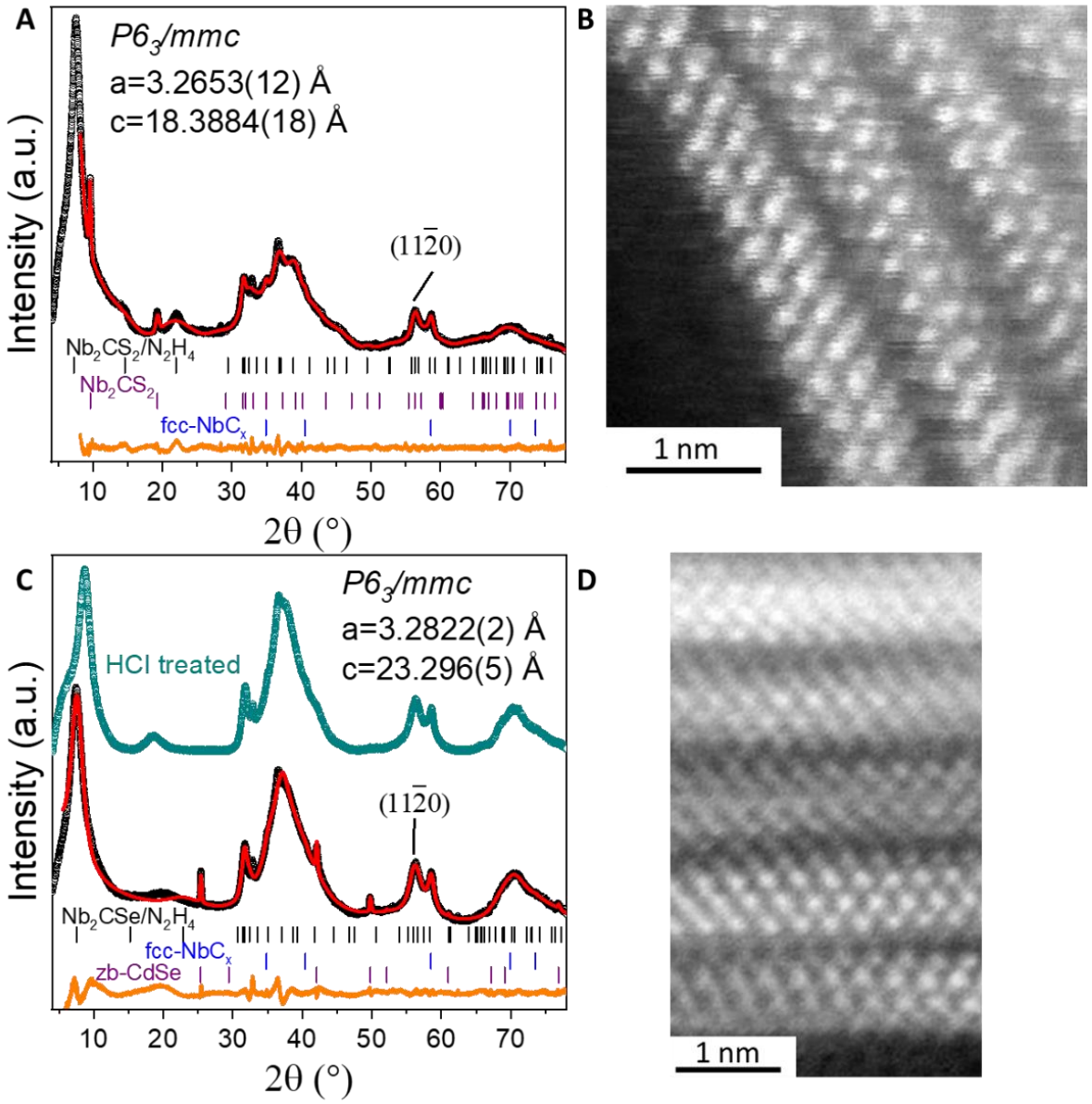

Figure 4.4. Characterization of Nb_2C(S, Se) MXenes.
Experimental XRD patterns (Cu Kα, reflection, black curves) and Le Bail fits (red curves) of: (A) Nb_2CS_2 MXene recovered from the salt matrix using anhydrous hydrazine; (C) Nb_2CSe MXene recovered from the salt matrix using anhydrous hydrazine (black curve) and subsequently washed with aqueous HCl (dark cyan) to remove traces of bulk zb-CdSe. STEM-LAADF images of (B) Nb_2CS_2 MXene and (D) LAADF image of Nb_2CSe MXene.

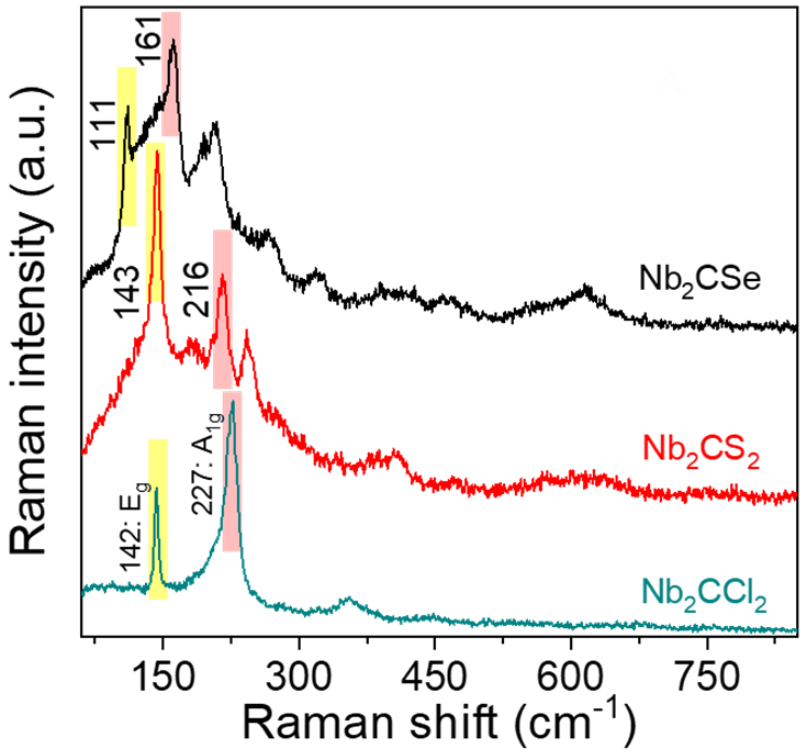

Figure 4.5. Raman spectra of Nb_2C(Cl, S, Se) MXenes.

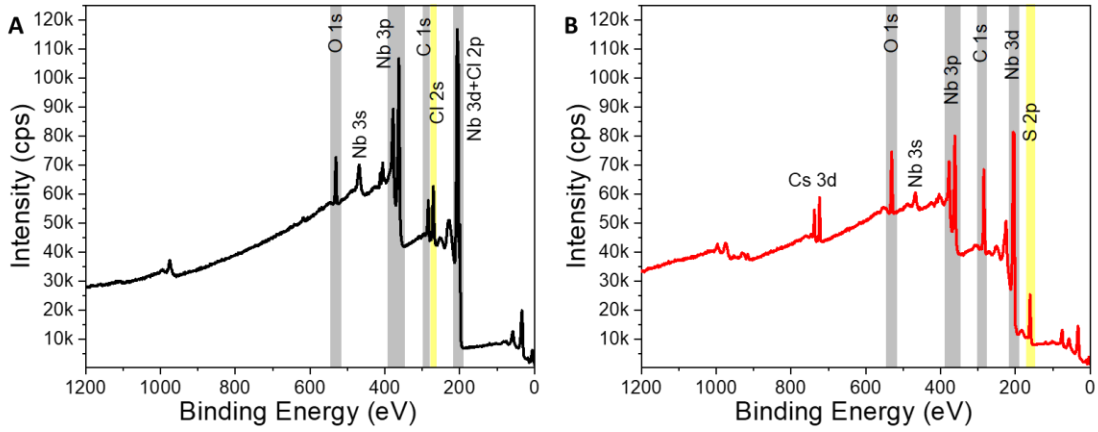

Figure 4.6. XPS survey spectra of Nb_2C(Cl, S) MXenes.

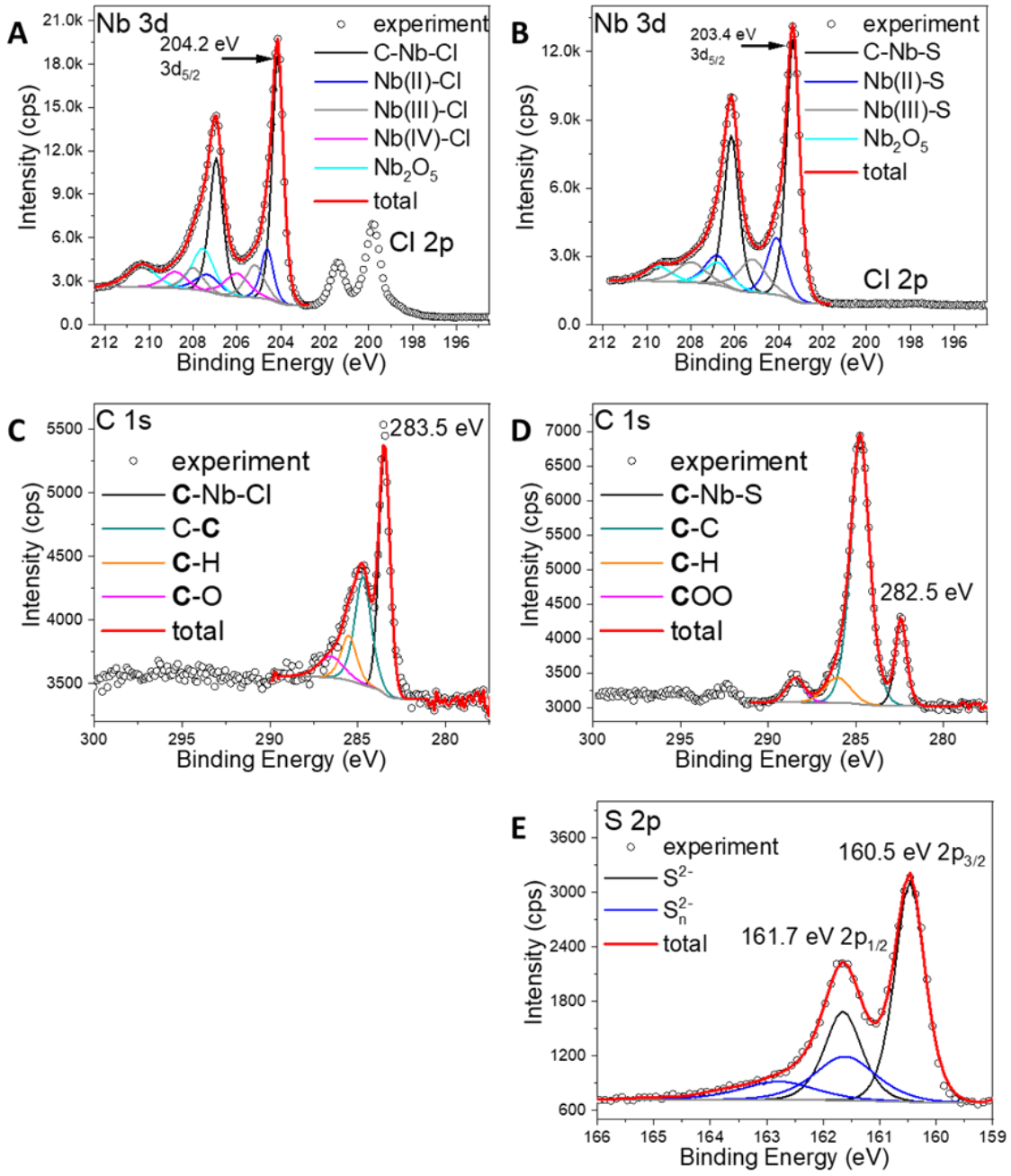

Figure 4.7. High resolution XPS spectra of Nb_2C(Cl, S) MXenes.

Table 4.1. Bond dissociation energies for M-O and M-X bonds relevant for this study.

	BE (eV)	FWHM (eV)	Fraction	Assigned to
Nb $3d_{5/2}$ ($3d_{3/2}$)	204.2 (207.0)	0.6 (0.73)	0.51	C-Nb-Cl
	204.6 (207.3)	0.65 (1.3)	0.11	Nb(II)-Cl
	205.2 (208.0)	1.00 (1.00)	0.11	Nb(III)-Cl
	206.0 (208.8)	1.29 (1.21)	0.10	Nb(IV)-Cl
	207.6 (210.4)	1.18 (1.49)	0.17	Nb_2O_5
C 1s	283.5	0.74	0.46	C-Ti-Te
	284.8	1.09	0.32	C-C
	285.5	1.03	0.13	C-H
	286.5	1.65	0.09	C-O

	BE (eV)	FWHM (eV)	Fraction	Assigned to
Nb $3d_{5/2}$ ($3d_{3/2}$)	203.4 (206.2)	0.7 (0.8)	0.57	C-Nb-S
	204.1 (206.8)	1 (1.3)	0.18	Nb(II)-S
	205.2 (208.0)	1.46 (1.58)	0.15	Nb(III)-S
	206.8 (209.5)	1.4 (1.42)	0.10	Nb_2O_5
C 1s	282.4	0.76	0.14	C-Nb-S
	284.8	1.26	0.71	C-C
	286.0	1.75	0.09	C-H
	288.5	1.21	0.06	-COO
S $2p_{3/2}$ ($2p_{1/2}$)	160.5 (161.7)	0.62 (0.77)	0.7	S^{2-}
	161.6 (162.8)	1.28 (1.55)	0.3	S_n^{2-}

4.2 Electronic transport of Nb_2CT_n MXenes.

Chemical functionalization of MXene surfaces is expected to impact nearly every property of these materials. Next, we will show that the surface groups define the nature of electronic transport in Nb_2CT_n MXenes. We measured temperature dependent four-probe resistivity (ρ) on cold-pressed pellets of Nb_2CT_n (T = □, Cl, O, S, Se) MXenes (Figure 4.8), all synthesized by the procedures described above.

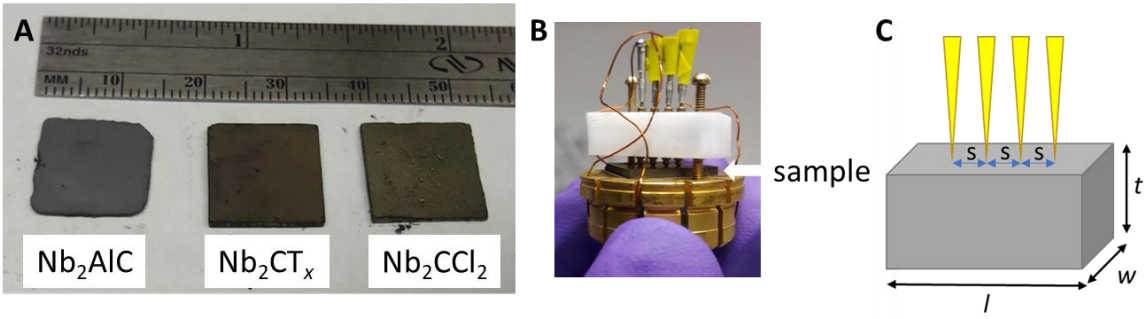

Figure 4.8. Scheme for four-probe resistivity measurement.
(A) Photographs of cold pressed pellets of Nb_2AlC MAX phase and representative Nb_2CT_n MXenes. (B) Photograph of a typical sample pellet connected to the PPMS puck. (C) Schematics of the in-line four-probe resistivity measurement.

Figure 4.9A compares the conductivity of the parent Nb_2AlC MAX phase with that of Nb_2CCl_2 MXene. Above 30 K both MAX phase and MXene samples show similar specific resistivity, which decreases when the sample is cooled. Such behavior is often associated with metallic conductivity. The ultraviolet photoelectron spectroscopy (UPS) confirms nonzero density of electronic states at the Fermi energy E_F (Figure 4.10), which is consistent with the metallic behavior. When the Nb_2CCl_2 MXene is cooled below 30 K, the resistivity starts increasing, possibly due to the beginning of localization. This is followed by a sharp drop of resistivity by several orders of magnitude at a critical temperature T_c ~ 6.0 K (Fig. 4A), which is reminiscent of a superconductive transition. The magnetic susceptibility measurements show the development of

a strong diamagnetism below 6.3 K interpreted as the Meissner effect (Figure 4.9A). From the magnitude of zero-field-cooled (ZFC) data at 1.8 K, the superconducting volume fraction of Nb_2CCl_2 MXene is ~ 35 %. Expectedly, the transition broadens, and T_c shifts to lower temperatures with the application of external magnetic field (Figure 4.9B). In contrast, the parent Nb_2AlC MAX phase behaves as a normal metal down to the lowest measured temperature (1.8 K), which is consistent with T_c ~ 0.44 K previously reported for Nb_2AlC.[2] To the best of our knowledge, this is the first experimental observation of bulk superconductivity in top-down fabricated MXenes. For reference, Nb_2CT_x MXene with mixed O, OH, F termination prepared by the traditional aqueous HF etching route shows two orders of magnitude higher resistivity and no superconductivity (Figure 4.11).[3]

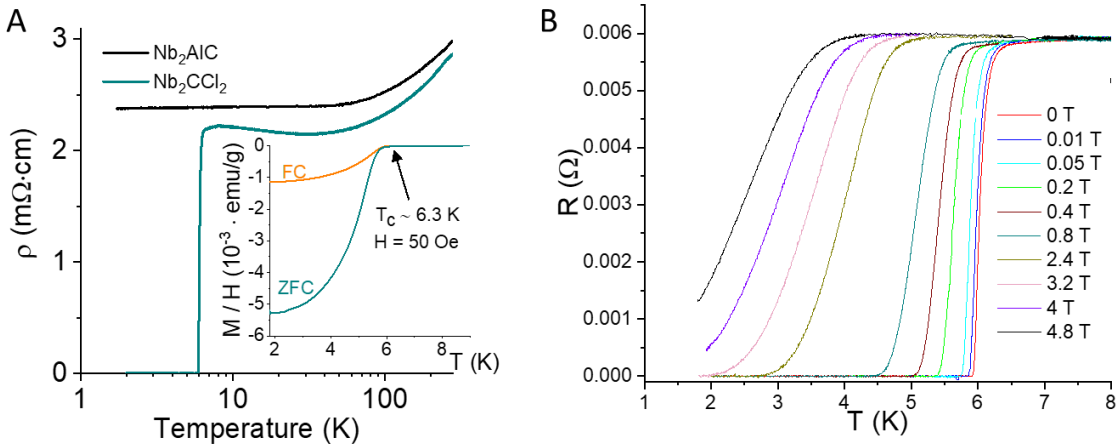

Figure 4.9. Electronic transport of Nb_2CCl_2 MXene.
(A) Temperature-dependent resistivity for the cold-pressed pellets of Nb_2AlC MAX phase and Nb_2CCl_2 MXene. Inset: Magnetic susceptibility of Nb_2CCl_2 MXene as a function of temperature. (B) Resistance as a function of temperature at different applied magnetic fields (0 to 4.8 T) for the cold pressed pellet of Nb_2CCl_2 MXene. The T_c shifts to a lower temperature with the increase in the magnetic field.

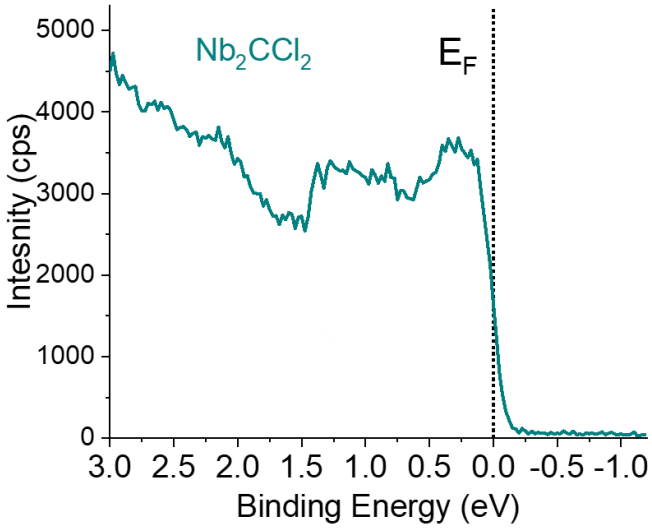

Figure 4.10. UPS spectrum of the valence band region of Nb_2CCl_2 MXene.

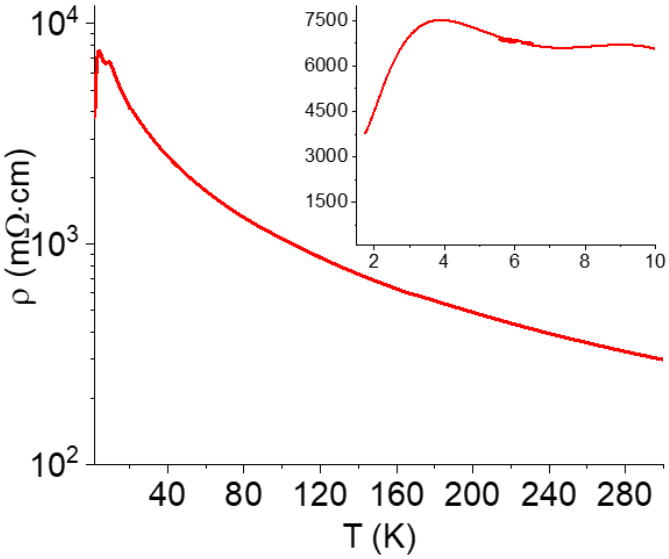

Figure 4.11. Electronic transport of Nb_2CT_x MXene.
Resistivity as a function of temperature for the cold pressed pellet of Nb_2CT_x MXene. The observed sharp increase in resistivity with decreasing temperature is consistent with the previously reported transport behavior of epitaxial Nb_2CT_x MXene thin films.[3]

In contrast to Nb_2CCl_2 MXene, the resistivity of MXenes terminated with chalcogenide ions (O, S, Se) gradually increases when the sample is cooled (Figure 4.12A), consistent with the activated transport regime. Since UPS shows the finite density of states at E_F in Nb_2CS_2 (Figure 4.13), it is reasonable to hypothesize that the localization is controlled by the tunneling rates for

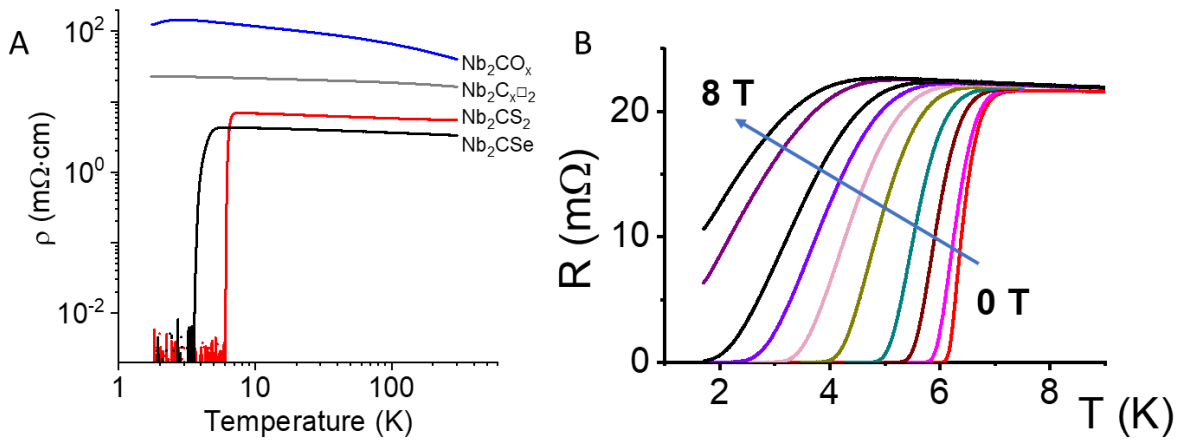

Figure 4.12. Electronic transport of Nb_2C(O, □, S, Se) MXenes.
(A) Temperature-dependent resistivity for the cold pressed pellets of Nb_2CT_n MXenes. (B) Resistance as a function of temperature at different applied magnetic fields (0 to 8 T) for the cold-pressed pellets of Nb_2CS_2 MXene.

charge carriers between metallic MXene sheets. The oxo-terminated Nb_2CT_n MXene shows the highest, and the seleno-terminated MXene the lowest resistivity, consistent with the reduction of the tunneling barrier heights between the MXene sheets. In the low-temperature region, we observed superconducting transitions in Nb_2CS_2 (T_c ~ 6.4 K), Nb_2CSe (T_c ~ 4.5 K), and $Nb_2C(NH)$ (T_c ~ 7.1 K, Figure 4.14), while Nb_2CO_x did not enter the superconducting state (Figure 4.14). In granular metals, the development of macroscopic superconductivity can be suppressed by weak coupling of individual superconducting domains, which is also reflected by the high resistivity in the normal state.[4] The upper critical field (μ_0H_{c2}) shows strong dependence on the surface functional groups. For example, Nb_2CS_2 MXene exhibits higher μ_0H_{c2} compared to Nb_2CCl_2 (Figure 4.15). Interestingly, bare $Nb_2C□_2$ MXenes showed no transition to the superconducting state down to 1.8 K (Figure 4.12A).

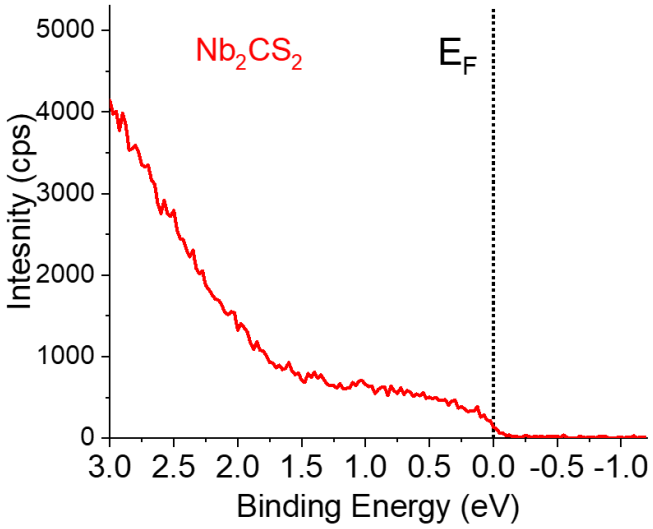

Figure 4.13. UPS spectrum of the valence band region of Nb_2CS_2 MXene.

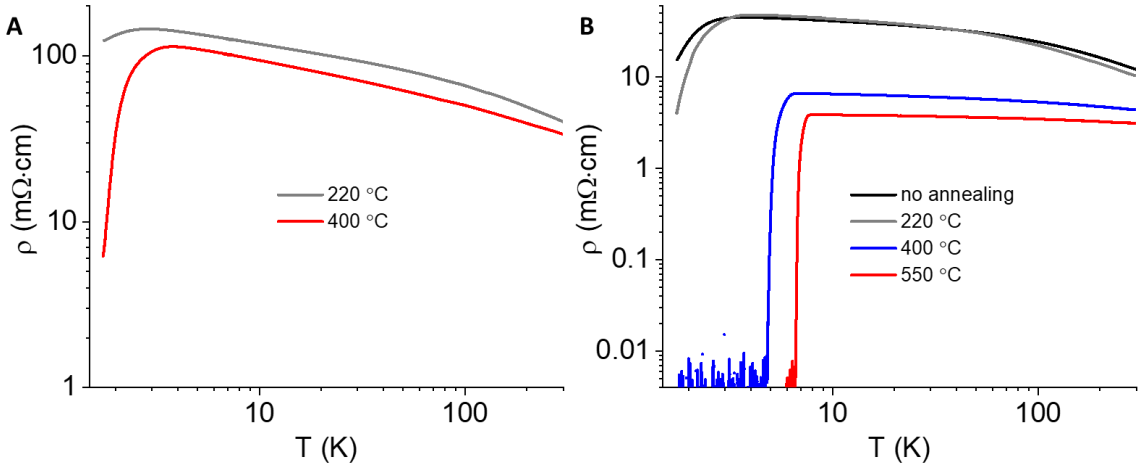

Figure 4.14. Electronic transport of Nb_2CO_x and $Nb_2C(NH)$ MXenes.
Resistivity as a function of temperature for the cold pressed pellet of: (A) Nb_2CO_x MXene after thermal annealing at 220 °C and 400 °C; (B) $Nb_2C(NH)$ MXene before and after thermal annealing at 220 °C, 400 °C and 550 °C. The cold pressed pellet of Nb_2CO_x MXene did not enter the superconducting state even after thermal annealing at 400 °C. The cold pressed pellet of $Nb_2C(NH)$ MXene before thermal processing behaves as an insulator, presumably due to the poor electronic coupling between the sheets. After thermal annealing (under vacuum) at 400 °C, $Nb_2C(NH)$ MXene becomes a superconductor with a T_c of 5.5 K. Additional annealing at 550 °C results in $Nb_2C(NH)$ MXene with a T_c of 7.1 K.

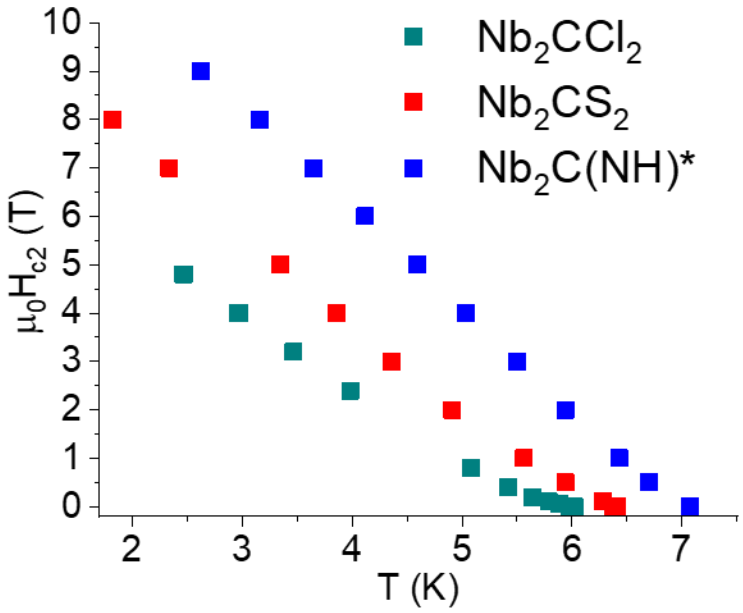

Figure 4.15. Electronic transport of Nb_2CO_x and $Nb_2C(NH)$ MXenes.

Dependence of the upper critical field (μ_0H_{c2}) on the surface group of the superconducting Nb_2CT_n MXenes. *$Nb_2C(NH)$ MXene pellet was annealed at 550 °C under vacuum (Figure 4.14).

4.3 Conclusion.

This chapter demonstrates that the surface groups are not spectators but active contributors to the MXene superconductivity. In addition to rendering MXenes with tunable transport and superconducting properties, surface groups allow to tune MXenes' work function (WF). The WF of Nb_2CCl_2 MXene measured is 4.3 eV, while that of Nb_2CS_2 MXene is 3.7 eV (Figure 4.16).

Further studies will be needed to clarify the underlying physics, which likely reflects the effects of surface groups on the biaxial lattice strain, phonon frequencies, and strength of electron-phonon coupling in surface-engineered MXenes. The superconductivity of MXenes calls for further systematic investigations before it will be possible to make any definitive claims about the parameters determining superconductive transition in these materials. In addition to the classical BCS considerations, we should keep in mind that MXenes are not classical long-range ordered solids – they represent 2D crystalline sheets where the inter-layer coupling is expected to

contribute to the macroscopic properties (T_c, upper and lower critical fields, etc.) of MXene superconductors.

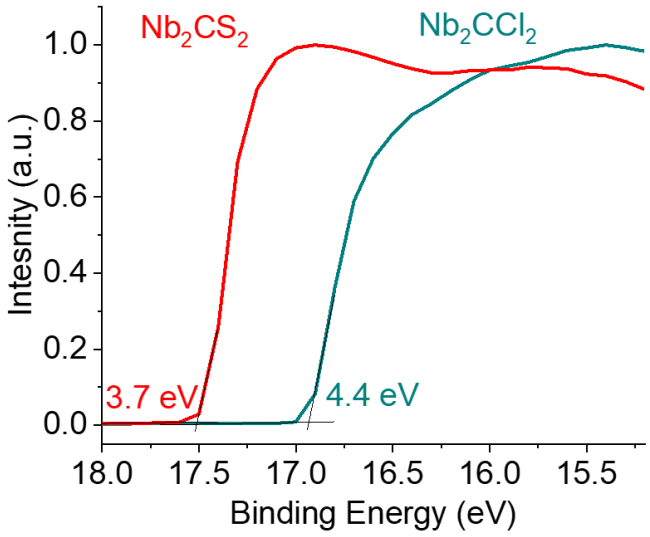

Figure 4.16. Tunable work function in Nb_2CT_n MXenes.

4.4 Materials and methods.

Chemicals and materials

Nb_2AlC (200 mesh, Forsman Scientific). Same ultra-dry inorganic salts and anhydrous solvents were used as in case of the synthesis of Ti based MXenes (Chapter 3).

Synthesis of Nb_2CT_n MXenes

Nb_2AlC MAX phase (0.578 g) was mixed with $CdCl_2$ salt in 1:10 molar ratio using mortar and pestle. The resultant mixture was heated in an alumina crucible at 710 °C for 36 h. The Cl functionalized MXenes were recovered from the reaction mixture by dissolving excess $CdCl_2$ and Cd metal in concentrated HCl followed by washing with deionized water until neutral pH.

In case of the scaled-up synthesis of Nb_2CCl_2 MXene (> 1 g of MXene powder), the recovered powder still contained unreacted Nb_2AlC MAX phase (as evidenced by XRD analysis). In order to increase the reaction yield, the product after 36 h of etching in $CdCl_2$ molten salt was recovered from the reaction mixture. The recovered powder containing Nb_2CCl_2 MXene and unreacted Nb_2AlC MAX phase was mixed with new $CdCl_2$ salt and further annealed at 710 °C for another 36-48 h.

Substitution/elimination of Cl groups of Nb_2CCl_2 MXenes followed the same procedure as outlined for Ti based MXenes in Chapter 3. The amounts used in this work were not optimized and the MXene/molten salt ratio can be increased in order to reduce the cost of using ultra dry salts per surface functionalization reaction. For example, in the case of the scaled-up conversion of Nb_2CCl_2 MXene to Nb_2CS_2 MXene (required for pressing a pellet), the MXene concentration in CsBr/KBr/LiBr eutectic was as high as 122 mg/g, yielding ~ 600 mg of Nb_2CS_2 MXene product per synthesis.

Synthesis of Nb_2CT_x MXenes

Mixed terminated Nb_2CT_x MXenes were synthesized by etching Nb_2AlC MAX phase in 48 wt. % HF as described in details elsewhere.[5]

Temperature dependent resistivity

Dried powders of MXenes were pressed under the load of ~ 0.8 GPa into square pellets of 13 mm in length or disks of 15 mm in diameter and 0.7-1 mm in thickness. Nb_2CS_2 and Nb_2CSe MXene pellets were additionally dried at 100-120 °C under 10^{-5} mbar for 12 h to get rid of excess N_2H_4. Nb_2CO_x and $Nb_2C(NH)$ MXene pellets were additionally annealed at 220-550 °C under

vacuum to investigate the effect of thermal post processing on the superconducting properties if any.

Four gold plated spring-loaded electrodes positioned in-line 2 mm apart were used to electrically contact the MXene pellet to a puck. The puck was then loaded into a physical property measurement system (PPMS, Quantum design) under He-filled inert atmosphere. The 4-probe resistivity measurements were carried out in an AC mode with a DC excitation of 1 mA. The temperature dependent resistivity measurements were performed from 300 K to 1.8 K.

Ultraviolet photoelectron spectroscopy (UPS)

UPS measurements were performed on a Kratos Axis Nova spectrometer using He I line (21.21 eV). Samples were in the form of the cold pressed pellets used for the resistivity measurements. During the measurements, a bias of -9 V was applied between the sample and the analyzer. The step size was 100 meV.

Magnetization measurements

Magnetic measurements were performed on a Quantum Design MPMS 3 instrument equipped with a superconducting quantum interference device (SQUID). Corrections were made for the diamagnetic contributions from the polycarbonate capsules and eicosane used to secure the sample.

From the zero-field-cooled curve of Nb_2CCl_2 MXene, the magnetic susceptibility at 1.82 K is -0.00529 emu/(g·Oe) (Figure 4.9). Given the crystallographic density is 5.3 g/cm^3, the diamagnetic volume fraction is $0.00529*5.3*4\pi*100\ \% = 35.2\ \%$.

4.5 Chapter 4 bibliography.

1. Hu, T.; Hu, M.; Gao, B.; Li, W.; Wang, X., Screening Surface Structure of MXenes by High-Throughput Computation and Vibrational Spectroscopic Confirmation. *J. Phys. Chem. C* **2018,** *122* (32), 18501-18509.

2. Scabarozi, T. H.; Roche, J.; Rosenfeld, A.; Lim, S. H.; Salamanca-Riba, L.; Yong, G.; Takeuchi, I.; Barsoum, M. W.; Hettinger, J. D.; Lofland, S. E., Synthesis and characterization of Nb2AlC thin films. *Thin Solid Films* **2009,** *517* (9), 2920-2923.

3. Halim, J.; Persson, I.; Moon, E. J.; Kühne, P.; Darakchieva, V.; Persson, P. O. Å.; Eklund, P.; Rosen, J.; Barsoum, M. W., Electronic and optical characterization of 2D Ti2C and Nb2C (MXene) thin films. *J. Phys.: Condens. Matter* **2019,** *31* (16), 165301.

4. Beloborodov, I. S.; Lopatin, A. V.; Vinokur, V. M.; Efetov, K. B., Granular electronic systems. *Rev. Mod. Phys* **2007,** *79* (2), 469-518.

5. Naguib, M.; Halim, J.; Lu, J.; Cook, K. M.; Hultman, L.; Gogotsi, Y.; Barsoum, M. W., New Two-Dimensional Niobium and Vanadium Carbides as Promising Materials for Li-Ion Batteries. *J. Am. Chem. Soc.* **2013,** *135* (43), 15966-15969.

5 Nanocomposites of MXenes and lightweight metals

5.1 Introduction to lightweight metal matrix composites (MMCs).

Particle-reinforced MMCs are an important class of composite materials consisting of lightweight elements (Al, Mg, Li) as the metal matrix and ceramic particle reinforcements. Properties of the soft metal matrix, such as yield strength, fatigue, and corrosion resistance, can be significantly improved with the addition of hard ceramic nanostructures.[2] Commercially available ceramic and carbon nanostructures such as SiC,[3] Al_2O_3,[4] graphene platelets,[5] and carbon nanotubes,[6] have been integrated into metals *via* powder metallurgy techniques, usually resulting in weak interfacial bonding between the metal matrix and the nano-inclusions.[2] As an alternative to the powder metallurgy methods, direct dispersion of nanostructures in liquid metals for fabricating MMCs has several advantages, such as stronger bonding between the components[7-8] and greater compatibility with large scale manufacturing.[9] However aggregation and subsequent macroscopic phase segregation of particles in liquid metals presents a major challenge in achieving uniform MMCs.

In addition, given the high reactivity of molten Al, Mg, and Li at elevated temperatures, the choice of nanostructures suitable for MMC fabrication is limited to materials stable in these media. Carbon-deficient early transition metal carbides (such as TiC_y, $y < 1$) are stable in molten Mg and Li across a broad range of temperatures.[10] Unfortunately, these metal carbide particles show a strong tendency toward aggregation in metal matrices,[11] preventing their uniform distribution in MMCs. Here, we discuss the peculiarities of liquid metals as the particle dispersion media and introduce a promising class of MMCs utilizing 2D metal carbide nanostructures (MXenes).

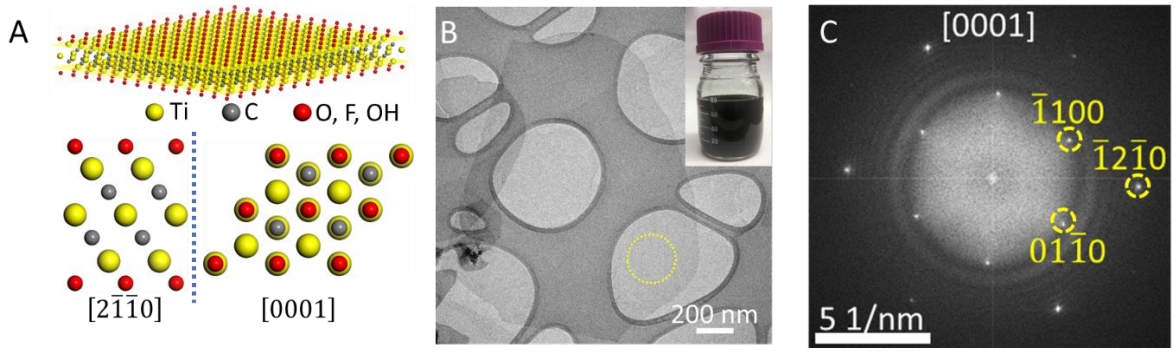

Figure 5.1. Structure of mixed terminated $Ti_3C_2T_x$ MXene used for MMC fabrication. (A) Structure of the monolayer $Ti_3C_2T_x$. (B) TEM image of a $Ti_3C_2T_x$ flake deposited from the colloidal solution on a lacey carbon grid (inset: photograph of the colloidal solution of 2D MXene sheets in water). (C) FFT of the circled region in panel (B) showing single-crystallinity and hexagonal symmetry of the individual flake.

$Ti_3C_2T_x$, the most studied MXene today, has a thickness of ~ 1 nm and hexagonal close-packed (hcp) structure (Figure 5.1A) with a Ti terminated (0001) surface, thus potentially providing means of bonding with the metal matrix, directly or *via* surface oxygen atoms. Strong covalent bonding between in-plane Ti and C atoms is responsible for MXenes' excellent mechanical properties. The experimentally measured 2D Young modulus of an individual $Ti_3C_2T_x$ sheet is 326±29 N/m (corresponding to 330±30 GPa bulk modulus), which is the highest among solution processable 2D materials.[12] The calculated bending rigidity of 49.6 eV[13] far exceeds that of graphene (1.2 eV)[14] and other classes of 2D materials due to the greater thickness (~ 1 nm) of an individual MXene sheet. The combination of metal terminated surfaces, strong in-plane bonding and excellent mechanical properties make $Ti_3C_2T_x$ attractive reinforcements for lightweight MMCs.

In this work, we first develop a general method for achieving a uniform distribution of MXenes in liquid metals by creating a colloidal gel. In this gelled state, the particles are able to form self-supporting networks, which are stable against macroscopic phase segregation. By using a Mg-Li alloy as an example of an ultra-lightweight structural alloy,[15] we further demonstrate the successful

integration of 2D $Ti_3C_2T_x$ flakes in Mg-Li alloy *via* the liquid metal gelation route. The $Ti_3C_2T_x$ flakes retain their 2D morphology after processing in molten Mg-Li alloy in the form of Ti_3C_2 nanoplatelets (NPLs). The composites show a uniform distribution of Ti_3C_2 NPLs and enhanced specific yield strength over the neat metal alloy while fully retaining the base metal's plasticity. Interestingly, the 2D Ti_3C_2 NPLs experience biaxial strain while inside the metal matrix. This biaxial straining is attributed to the formation of a strong semi-coherent interface between the NPLs and metal matrix.

5.2 Preparation and exfoliation of MXene sheets.

Exfoliated MXene sheets were synthesized following an established procedure.[16] Briefly, $Ti_3C_2T_x$ sheets were obtained from the corresponding Ti_3AlC_2 MAX phase *via* simultaneous etching of Al and intercalation with Li^+ ions in LiF/HCl solution. The final product of this process is a colloidal solution of single- to few-flake $Ti_3C_2T_x$ MXene (Figure 5.1B). Fast Fourier transform (FFT) analysis of a representative transmission electron microscopy (TEM) image (Figure 5.1C) shows a hexagonal pattern corresponding to the [0001] zone axis of the single-crystal $Ti_3C_2T_x$ structure. Atomic force microscopy (AFM) confirms the presence of monolayer MXene flakes with a thickness of 1.5 nm (Figure 5.2). Thickness of a single flake of $Ti_3C_2T_x$ MXene is ~ 1 nm. The larger measured thickness in AFM is due to the presence of water molecules between MXene and the substrate.[12] The Li^+ intercalated MXene powder was further treated with aqueous tetramethylammonium hydroxide (TMAOH) to substitute the Li^+ ions for TMA^+ ions. This substitution increased the center-to-center interlayer spacing in MXene films from 10.9 Å to 14.6 Å (Figure 5.3). The resulting increased interlayer spacing was found to be advantageous for the subsequent liquid metal infiltration in between MXene sheets.

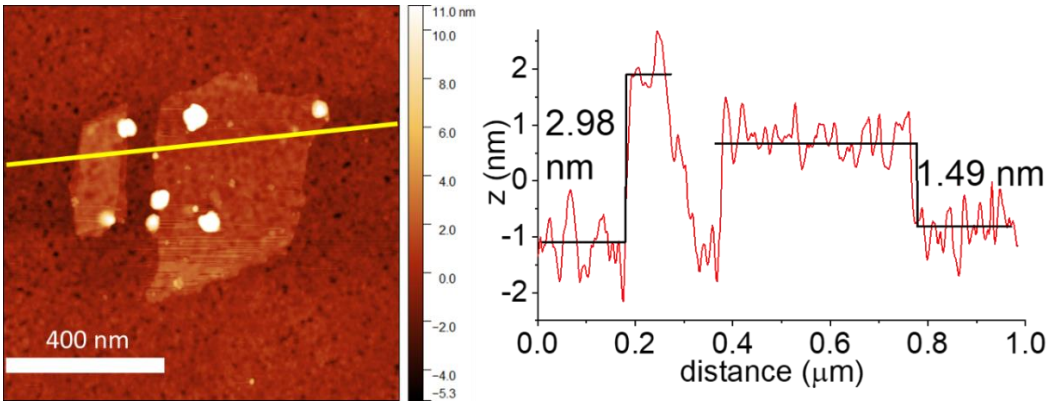

Figure 5.2. AFM study of $Ti_3C_2T_x$ MXene.
AFM topography of mono- and bilayer $Ti_3C_2T_x$ sheet with the height profile along the yellow line. A slightly bigger than theoretical (0.98 nm) thickness measured by AFM can be attributed to the trapped interfacial water.

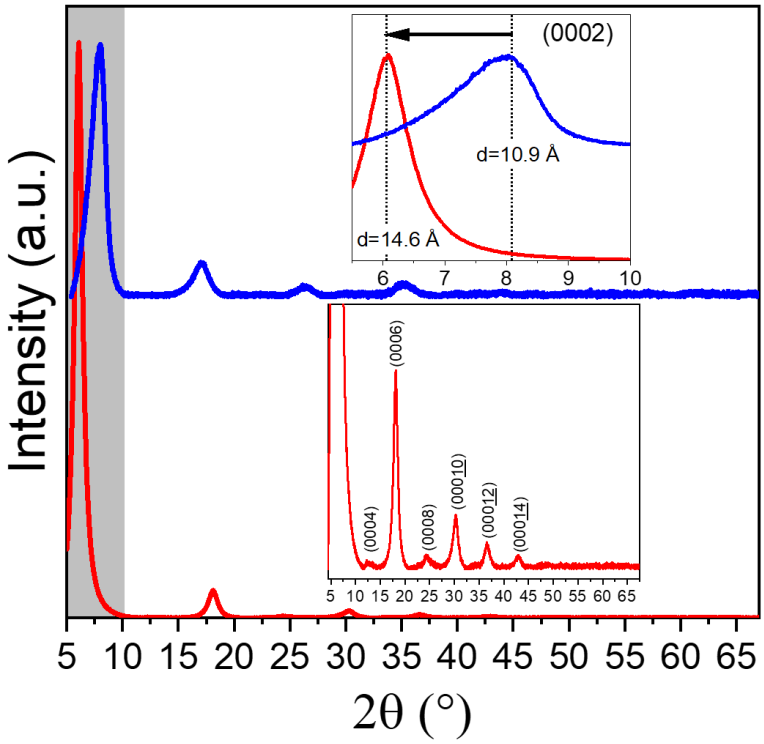

Figure 5.3. Characterization of $Ti_3C_2T_x$ MXene films.
XRD (reflection mode, Cu Kα) for the two MXene films after vacuum-drying at 120 °C overnight: $Ti_3C_2T_x$ intercalated with TMA^+ cations (red); $Ti_3C_2T_x$ intercalated with Li^+ cations (blue). In both cases the peak positions are consistent with highly ordered lamellar. The in-plane reflections are suppressed due to MXene stacking parallel to the substrate plane.

In addition to increasing the interlayer spacing, the TMAOH treatment results in MXenes with reduced lateral dimensions (Figure 5.4)[17] which is also advantageous for fabricating uniform MMCs due to the reduced van der Waals (vdW) attraction between the smaller MXene flakes. TMAOH adsorbed on $Ti_3C_2T_x$ surface decomposes cleanly forming gaseous $NH_2/NH_3/NH_4^+$ and CO/CO_2 at above 300 °C and hence does not leave any organic residue behind.[18] The TMA^+ intercalated $Ti_3C_2T_x$ flakes were used throughout this study, unless stated otherwise.

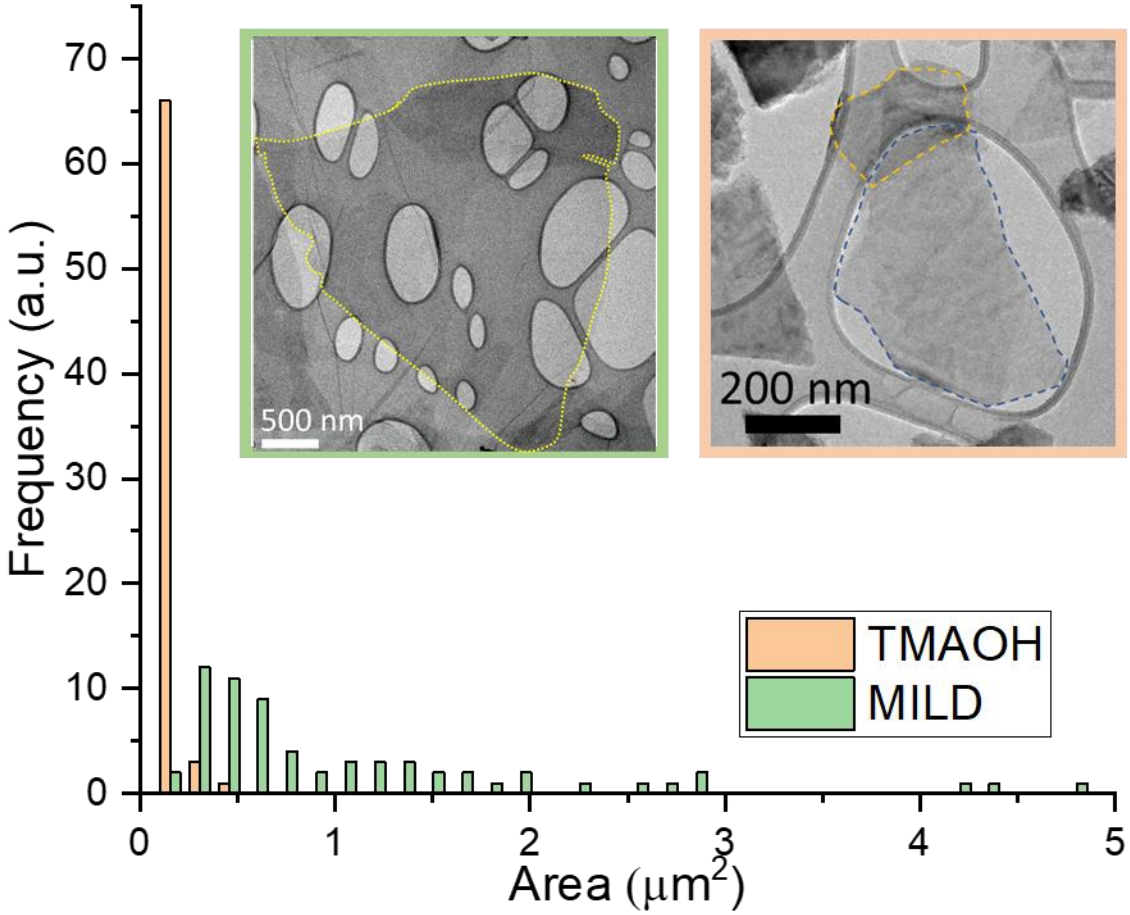

Figure 5.4. Size distributions of MXene flakes.
Comparison of the lateral area distribution for MILD $Ti_3C_2T_x$ and after additional treatment with TMAOH. Insets: representative TEM images for MILD and TMAOH MXene.

5.3 Liquid metals as particle dispersion media.

One of the challenges for dispersing nanostructures directly into a liquid metal is poor wetting of ceramic surfaces by liquid metals.[19] From a thermodynamic point of view, NCs are wetted by liquids when the work of adhesion between the liquid and the NC surface ($-W_{ad}$) exceeds the liquid-vapor surface tension (σ_{LV}). This wetting condition can be easily satisfied in the case of traditional solvents, such as water at 25 °C with σ_{LV} of 0.072 J/m^2. However, this condition becomes more severe in the case of liquid metals, such as liquid Al at 660 °C (melting point) with σ_{LV} of 0.871 J/m^2.[20] Adhesion energy on the order of 1 J/m^2 between a liquid metal and ceramic surface can be achieved through direct chemical bonding.[21] However, the chemical reaction at the interface should not compromise the phase or structure of the ceramic NCs. The Ti rich facets of carbon deficient TiC_y ($y < 1$) are known to exhibit enhanced wettability by liquid metals compared to the mixed atom (C and Ti)-terminated surfaces. This is related to the stronger liquid metal-Ti interfacial bonding when the surface Ti atoms have fewer C neighbors.[22]

From a colloidal science perspective, particles disperse uniformly in liquids if the repulsive terms dominate the long-range interparticle potentials. Typically, the repulsive forces have a steric or electrostatic origin while the attractive interactions come from vdW forces.[23] However, due to perfect polarizability, liquid metals efficiently screen the electrostatic potential immediately next to the NC surface, suggesting that classical electrostatic double layer repulsion is not possible. Moreover, the absence of solvated long chain ligands at the NC surfaces eliminates the possibility of steric stabilization. In analogy with NCs in molten inorganic salts,[24] the chemical affinity of the liquid metal to a ceramic surface can, in principle, induce liquid metal restructuring[25-27] leading to oscillatory solvation interactions. However, this mode of interaction is expected to be short ranged (~ 0.5 nm) in liquid metals and can be both attractive and repulsive between planar surfaces.[28] The

vdW interaction potential *V(l)* for two parallel $Ti_3C_2T_x$ sheets at sub-10 nm distances (*l*), where the retardation effects can be ignored, can be written as:[29]

$$V(l) = -\frac{A}{12\pi}\left(\frac{1}{l^2} - \frac{2}{(l+b)^2} + \frac{1}{(l+2b)^2}\right) \cdot Area$$

where *A* is a Hamaker coefficient and *b* is the thickness of a MXene sheet (~ 1 nm). To assess the attractive potential acting on the particles dispersed in a liquid metal, we used the Lifshitz theory, which expresses the Hamaker coefficient through the complex dielectric functions of the particles and the medium between them. Since the Lifshitz theory does not rely on pairwise additivity of the individual intermolecular forces,[29] it allows for an accurate estimation of the vdW force acting on particles immersed in highly conductive media, such as liquid metals. Using the experimental spectroscopic ellipsometry data for $Ti_3C_2T_x$,[30] we reconstructed the complex dielectric function and calculated Hamaker coefficients (see Supporting Information for details). Table 5.1 summarizes the calculated Hamaker coefficients for the three systems of interest: $Ti_3C_2T_x$ interacting through vacuum, $Ti_3C_2T_x$ interacting through liquid Ga, which is a typical example of liquid metal, and liquid Ga interacting through vacuum. If the Hamaker coefficient of $Ti_3C_2T_x$ in Ga were to be evaluated from the commonly used combining relation,[31] we would arrive at $A = \left(\sqrt{345} - \sqrt{381}\right)^2 = 0.89$ zJ. Clearly the combining relation breaks down when computing Hamaker coefficients for particles interacting through a liquid metal medium. This breakdown of the combining relations in liquid metals can be related to their large dielectric constant.[23] This result demonstrates that the previously used[7, 31] combining relations for the approximation of the vdW attraction between nanoparticles interacting through a liquid metal medium underestimate the Hamaker coefficient and, correspondingly, the vdW attraction, by almost two orders of magnitude.

Table 5.1. Hamaker coefficients for $Ti_3C_2T_x$ and liquid Ga (vac stands for vacuum).

System	$Ti_3C_2T_x$-vac-$Ti_3C_2T_x$	Ga-vac-Ga	$Ti_3C_2T_x$-Ga-$Ti_3C_2T_x$
A [zJ]	381	345	50.4

Figure 5.5A shows the vdW potential between two MXene sheets with surface area of 100^2 nm^2 in a liquid metal at 700 °C (temperature relevant for processing Mg-Li and other lightweight metal alloys) as a function of *l*. The vdW attraction exceeds the thermal energy of 86 meV up to ~ 8 nm of separation. This suggests that, in the absence of long-ranged repulsive forces, dispersions of 10^4 nm^2 MXene sheets in liquid metals will spontaneously aggregate. Even much smaller 10^2 nm^2 MXene flakes are expected to aggregate (Figure 5.5B). A qualitatively similar behavior is also predicted for spherical $TiC_{0.9}$ NCs dispersed in liquid metal (Figure 5.5B): the vdW interactions are too strong to permit the formation of stable colloidal solutions in the absence of long-ranged repulsive interactions. Although change in the T_x composition in harsh liquid metal environment can affect the complex dielectric function of MXenes,[32] the fact that the Hamaker coefficient for $TiC_{0.9}$-Ga-$TiC_{0.9}$ system (39.1 zJ, see Materials and methods for details) is close to that of $Ti_3C_2T_x$-Ga-$Ti_3C_2T_x$ suggests the T_x composition likely plays secondary role in determining the strength of the vdW potential in liquid metals.

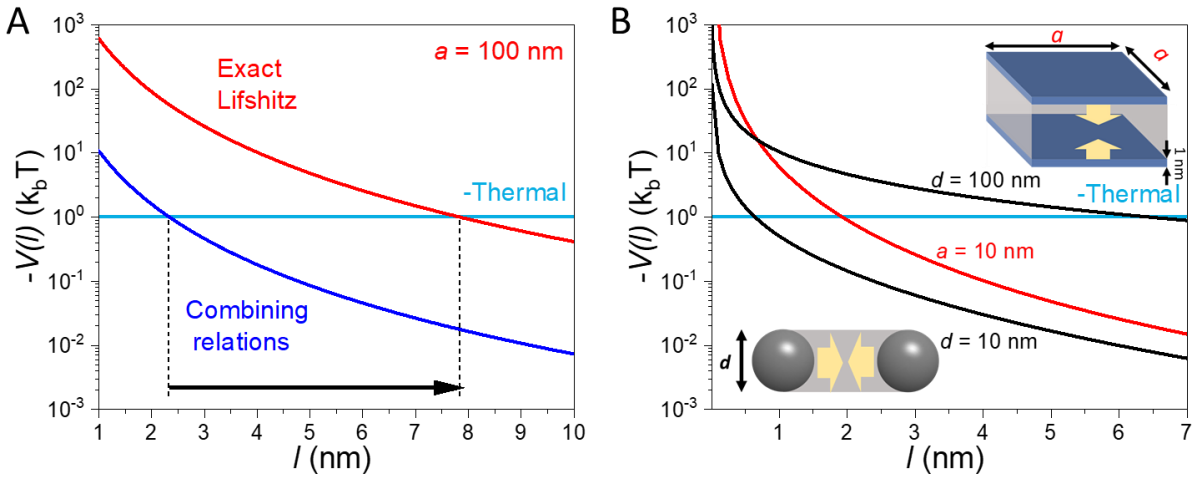

Figure 5.5. vdW potentials for MXenes and TiC NCs in liquid metal.
(A) vdW potential calculated using combining relations and exact Lifshitz approach for the two MXene sheets of lateral dimension *a* interacting through liquid Ga at 700 °C. (b) vdW potential calculated using exact Lifshitz approach for small-area MXene sheets and spherical $TiC_{0.9}$ NCs of diameter *d* interacting through liquid Ga at 700 °C.

5.4 Colloidal gelation in liquid metals.

The strong vdW attraction and lack of long-range repulsive potentials suggest that ceramic particles, including MXene flakes, are not colloidally stable in a liquid metal environment. An alternative approach to prevent macroscopic phase segregation and achieve homogenous distribution of attractive inclusions in a metal is through the dynamic arrest of particles based on colloidal gelation.[33] In a colloidal gel, the volume-spanning network of particles can be stable against settling/creaming under gravity.[34] Such mechanically stable colloidal gels often form when the volume fraction of particles in a solution is high enough to reach a percolation threshold, *i.e.* allow formation of an infinite spanning cluster.[35]

The possibility of colloidal gelation in liquid metals can be probed directly by measuring the composite's viscoelastic properties. The linear viscoelastic storage (G') and loss (G'') moduli

determine the response of the system to a small oscillatory shear strain $\gamma = \gamma_0 \sin(\omega t)$ with amplitude γ_0 and frequency ω (Figure 5.6B). The stress follows as $\sigma = \sigma_0 \sin(\omega t + \delta)$, and the complex modulus of the material $G^* = G' + iG''$ has the storage and loss components determined as $G' = \frac{\sigma_0}{\gamma_0}\cos\delta$ and $G'' = \frac{\sigma_0}{\gamma_0}\sin\delta$. G' gives insight into how a system stores the applied stress, and hence it determines the rigidity and connectivity of the particle network (if any) in the suspension. G'' measures how system dissipates the applied stress. In an elastic material, $G' \gg G''$ while for a viscous fluid $G' = 0$.

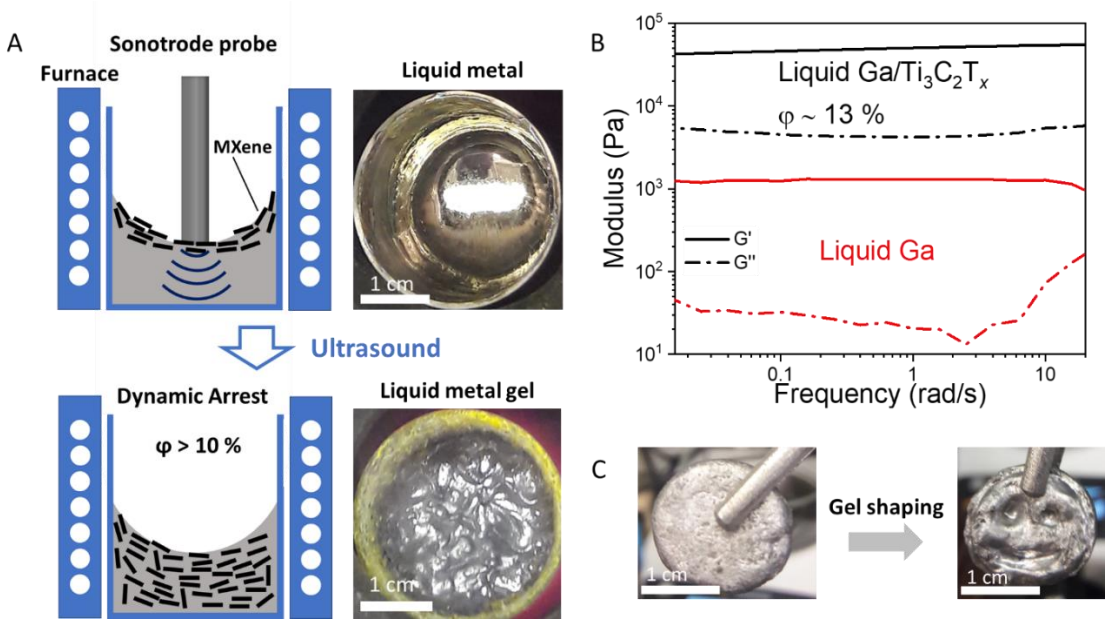

Figure 5.6. Colloidal gelation of MXenes in liquid metals.
(A) Schematic for the preparation of $Ti_3C_2T_x$ MXene dispersions in lightweight metals and photographs of the crucibles. (B) Real (G') and imaginary (G") components of the complex modulus describing viscoelastic properties of liquid Ga with and without $Ti_3C_2T_x$ MXene flakes. (C) Demonstration of shaping the gelated composite of $Ti_3C_2T_x$ MXene in Al-Mg alloy (Figure 5.11) above the alloy melting temperature of 432 °C.

For rheological investigations, we used liquid Ga as a model system to determine conditions that can cause liquid metal gelation through the addition of $Ti_3C_2T_x$ MXene flakes. Ga has a melting point of 29.8 °C and surface tension of 0.711 J/m^2, thus it is a convenient near room

temperature analog of the high melting point Mg-Li alloy discussed in the following sections.[36] The concentration of $Ti_3C_2T_x$ was built up in liquid Ga iteratively at 45 °C, as shown in Figure 5.6A, with the final concentration of $Ti_3C_2T_x$ sheets in liquid Ga set at ~ 13 vol. %. Figure 5.6B shows the frequency dependence of G' and G'' in the linear viscoelastic regime at γ_0 = 0.05 % for the dispersion of $Ti_3C_2T_x$ in liquid Ga. Since γ_0 is small, it only weakly perturbs the equilibrium structure of the suspension (Figure 5.7).[37] Both G' and G'' for the $Ti_3C_2T_x$ flakes suspensions are at least 50 times larger than the corresponding moduli measured for liquid Ga coated with a thin layer of native oxide (Figure 3b, see Supporting Information for further discussion). Therefore, we attribute the observed viscoelastic properties of the composite to the presence of MXene flakes and treat the oxide layer effect as a weak perturbation. The composite's shear moduli are nearly frequency independent with $G' > G''$ across the measured frequency range. This is consistent with the formation of a colloidal gel.[38] The gel structure weakens progressively with time by applying steady shear in one direction (Figure 5.8) suggesting thixotropic behavior, which is also characteristic of gel networks.[39]

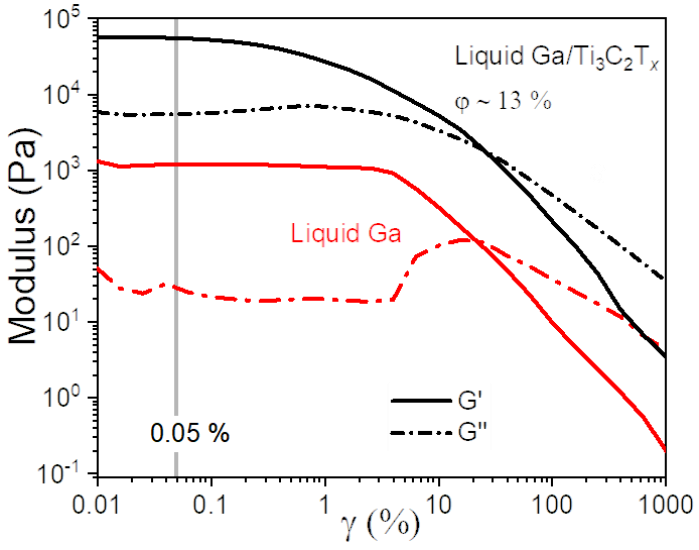

Figure 5.7. Plots showing viscoelastic measurements (at constant ω = 1 rad/s) conducted on Ga with (black) and without (red) $Ti_3C_2T_x$ flakes.

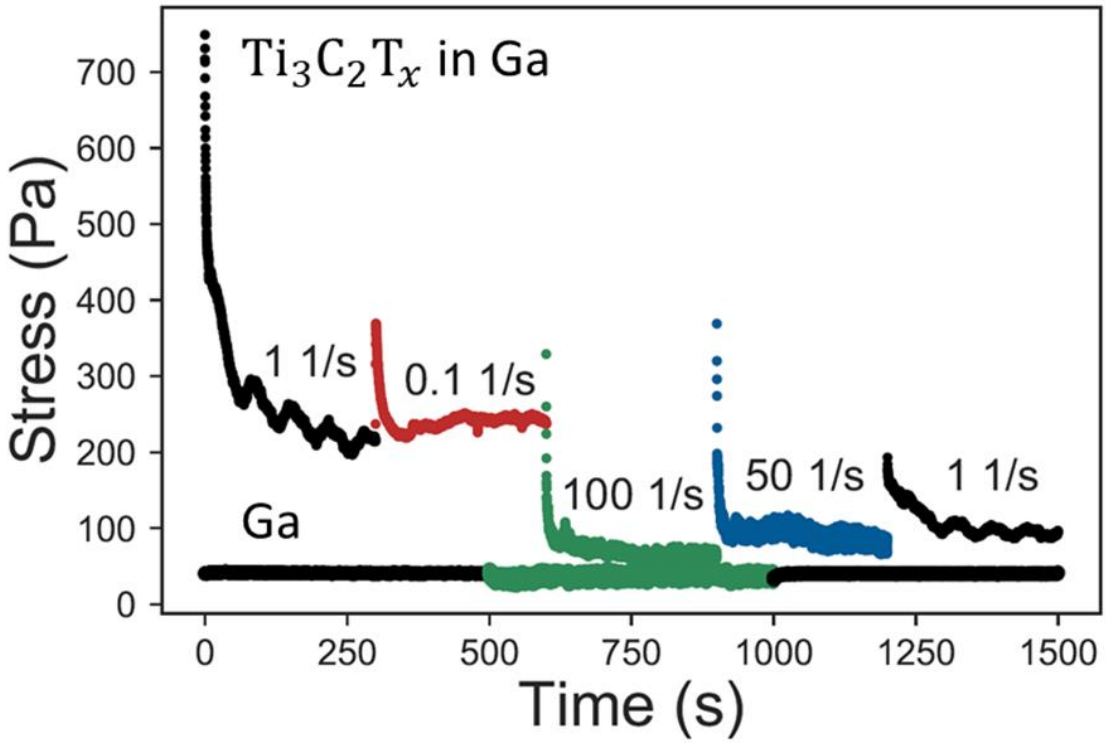

Figure 5.8. Composite's shear stress measured at four different, consecutive shear rates ($\dot{\gamma}$) as a function of time.
Shearing is ceased between each sequential experiment, and thus initial start-up flow decay can be seen at the beginning of each particular rate. The shear stress at constant rate then shows a decay over time, which eventually reaches a constant value. This decay occurs more rapidly the higher the shear rate is. After shearing at 100 s^{-1} and 50 s^{-1}, the stress value nearly drops to that of liquid Ga without MXenes, thus indicating breakage of the particle network. Subsequent shearing at 1 s^{-1} does not restore the stress value to its initial value prior to the shearing at 100 s^{-1}. Similar to the oscillatory shear measurements, the stress value at 1 s^{-1} and 0.1 s^{-1} could be restored after the rheometer tool was raised and lowered back into position. Steady shear experiments performed on Ga without addition of MXenes do not show thixotropic effects with the shear stress being independent of the shear rate. In this case the response is dominated by the Ga_2O_3 surface layer.

The observed aggregation and gelation phenomena for MXene flakes in liquid Ga can be used to predict the behavior of ceramic particles dispersed in liquid metals. At low volume fractions, aggregation of nanoflakes results in a macroscopic phase separation of $Ti_3C_2T_x$ in Ga (Figure 5.9), while at high volume fractions we observed the formation of extended particle networks. A qualitatively similar behavior was observed for $Ti_3C_2T_x$ in Mg-Li alloy (discussed in

the following sections) and $TiC_{0.9}$ microparticles (Figure 5.10) in Al-Mg alloys. In all cases, high particle loading was necessary to achieve a uniform distribution of particles. In addition to rendering uniform composites, the extended particle networks provided sufficient rigidity to shape metals directly in their molten state (Figure 5.6C). In a conventional semi-solid casting, viscoelastic properties of metal slurries are controlled through the volume fraction of the *in situ* nucleated precipitates in the region between solidus and liquidus lines in the equilibrium phase diagram.[40] However, two major limitations of this technique are: (i) it requires careful control over the temperature gradients which are difficult to realize on a large scale; (ii) alloys have to be of a certain composition. Since in our case the liquid metal viscoelastic moduli can be controlled independently through the formation of ceramic particles' networks, the lightweight metal alloys of an arbitrary chemical composition can become amenable to 3D printing above their thermodynamic melting points.[41]

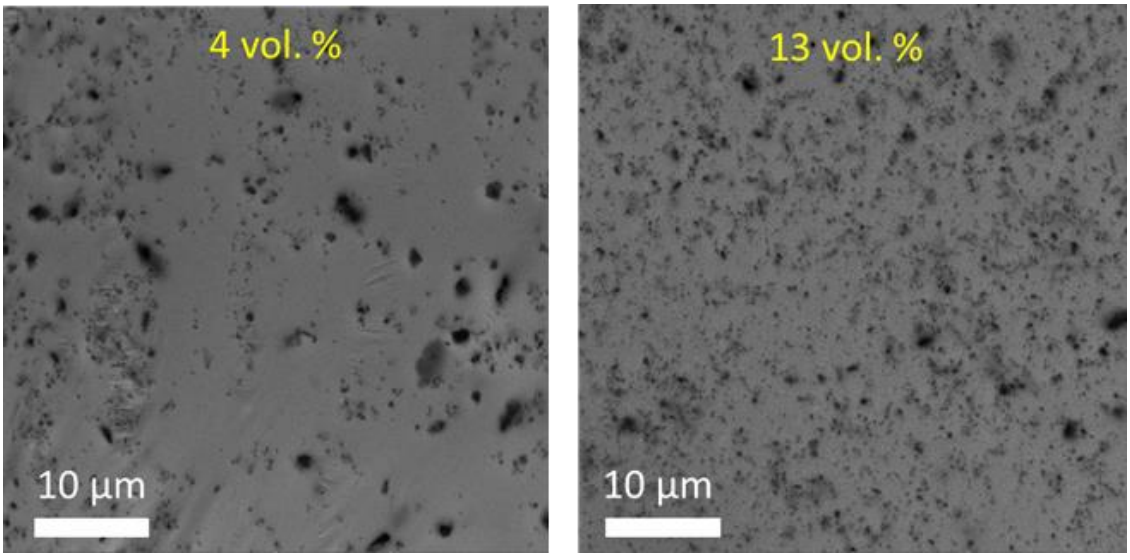

Figure 5.9. SEM images of Ti_3C_2 NPLs in Ga.

SEM images showing distribution of Ti_3C_2 NPLs in liquid Ga (doped with Mg) at two different volume factions of NPLs: 4 and 13 vol. %. The distribution of NPLs is more uniform at a higher volume fraction.

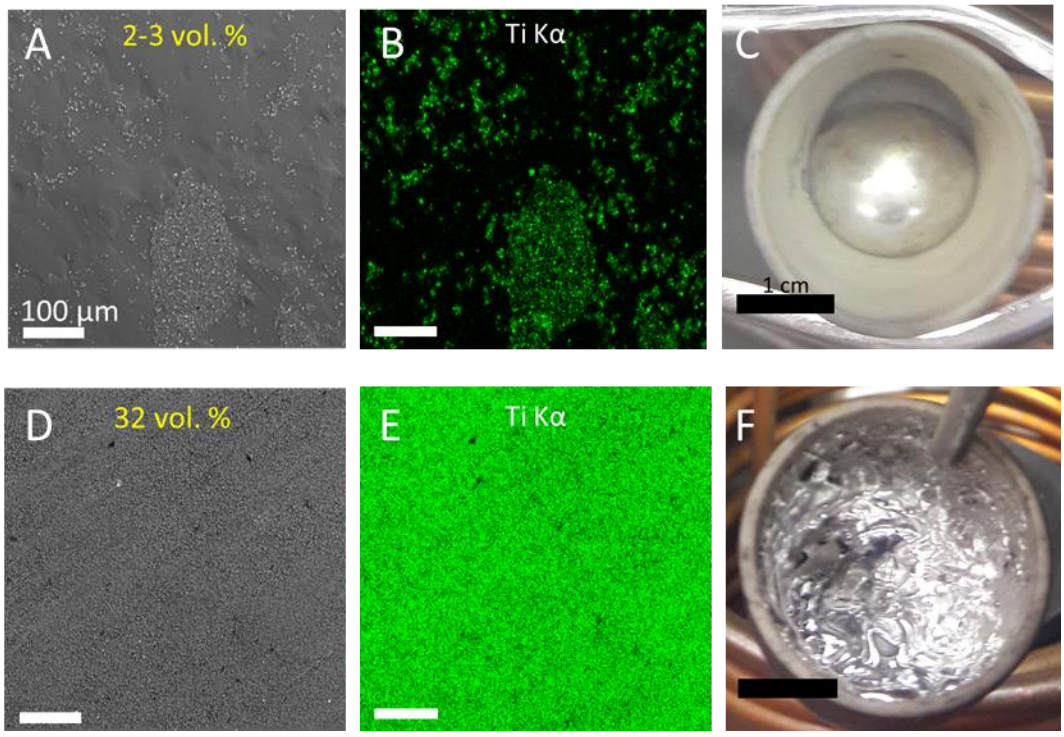

Figure 5.10. $TiC_{0.9}$ microparticles in Al-Mg eutectic alloy.
$TiC_{0.9}$ microparticles in Al-Mg eutectic alloy at two different volume fractions (the Ti:Al:Mg atomic ratio was measured using XRF and converted to the respective volume fraction of particles assuming density of $TiC_{0.9}$ phase of ~ 4.8 g/cm^3). (A, D) SEM images. (B, E) Ti Kα EDX elemental maps of the same area in (A) and (D) respectively. (C, F) Optical appearance of the two MMCs. (F) The 32 vol. % MMC exhibits visible gelation.

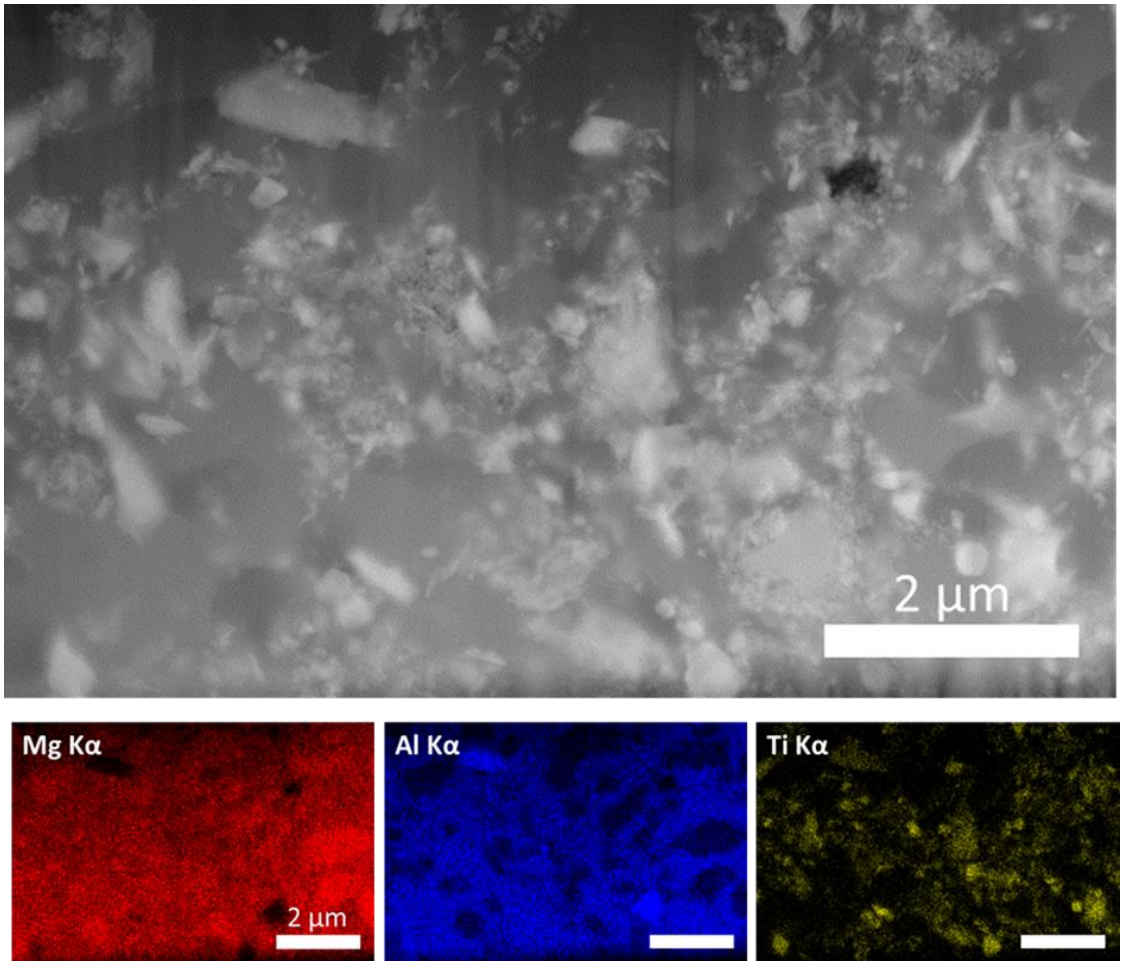

Figure 5.11. Ti_3C_2 NPLs in Al-Mg eutectic.

Dark field TEM image of Ti_3C_2 NPLs in Al-Mg eutectic (Figure 5.6C). The corresponding EDX elemental maps of Mg, Al and Ti are shown at the bottom. The lower scattered intensity regions (darker regions) correspond to the hcp-Mg embedded in $Al_{12}Mg_{17}$ matrix.

5.5 MXene/Mg-Li composite.

As a case study relevant to lightweight MMCs, we further explored $Ti_3C_2T_x$ dispersed in molten and solidified Mg-Li alloy (39 at. % Li). Mg-Li alloys containing more than 30 at. % of Li are the lightest known structural alloys currently investigated for aerospace and other applications. They crystalize in the body centered cubic (bcc) structure which significantly improves their room temperature ductility and corrosion resistance compared to that of Mg alloys with the hcp

structure.[15] The combination of low density and good mechanical properties make bcc Mg-Li alloys an interesting platform to study the effect of ceramic particles on their structural and mechanical properties. Informed by the rheological studies of MXenes in liquid Ga, the concentration of flakes was built up until the liquid Mg-Li alloy exhibited noticeable gel-like viscoelastic behavior, and was able to hold its shape against gravity (Figure 5.6A). Based on the X-ray fluorescence (XRF) elemental analysis (Mg:Ti = 4.2:1), we estimate that the volume fraction of $Ti_3C_2T_x$ MXene in the Mg-Li alloy is ~ 13%, similar to the volume fraction of the same MXenes in liquid Ga. TEM image (Figure 5.12A) and energy dispersive X-ray (EDX) elemental mapping (Figure 5.12B) of the composite show the formation of uniform particle networks consistent with the observation of a colloidal gel in liquid Ga composite containing a similar concentration of particles (Figure 5.6B). A high magnification TEM image (Figure 5.12C) suggests the presence of individual Ti_3C_2 flakes (darker regions) forming a continuous network.

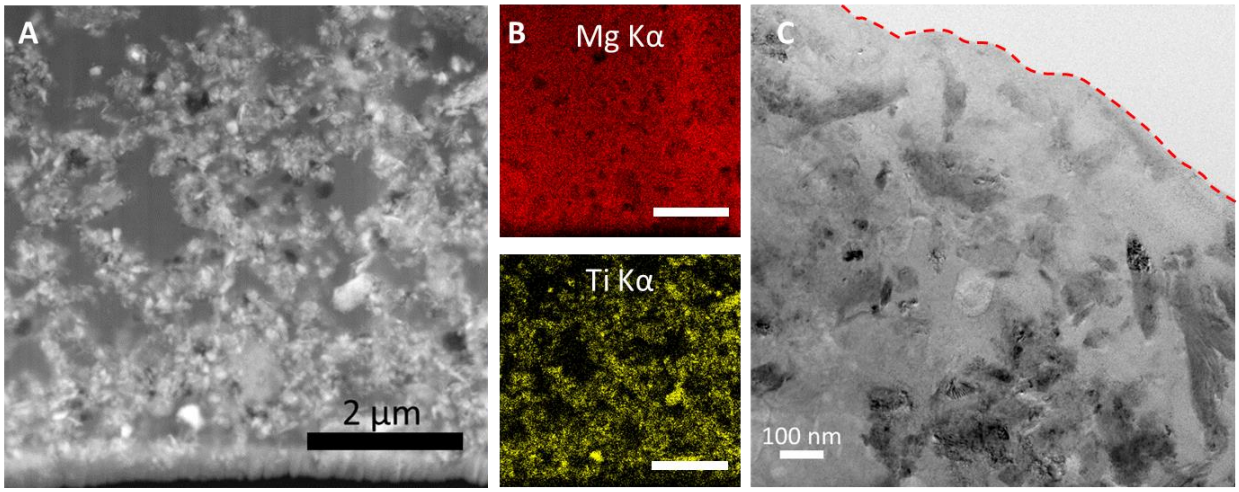

Figure 5.12. Electron microscopy characterization of Ti_3C_2 NPLs in Mg-Li alloy.
(A) Large area dark-field TEM image showing particle network on the several micron scale. (B) Mg Kα and Ti Kα EDX elemental maps of the area shown in (A). (C) Bright field TEM image showing particle network on the submicron scale (dashed red line shows the sample's edge).

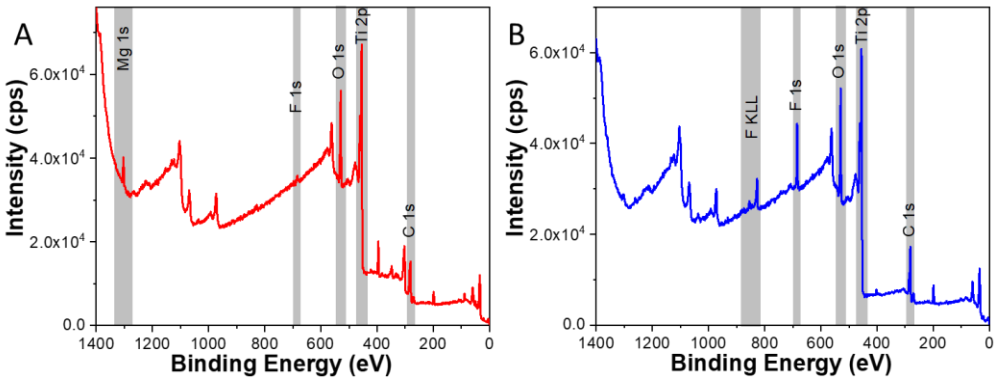

Figure 5.13. XPS survey spectra.
(A) $Ti_3C_{2.2}$ NPLs recovered from Mg-Li alloy after processing at 700 °C; (B) pristine $Ti_3C_2T_x/TMA^+$ before using in MMC fabrication process.

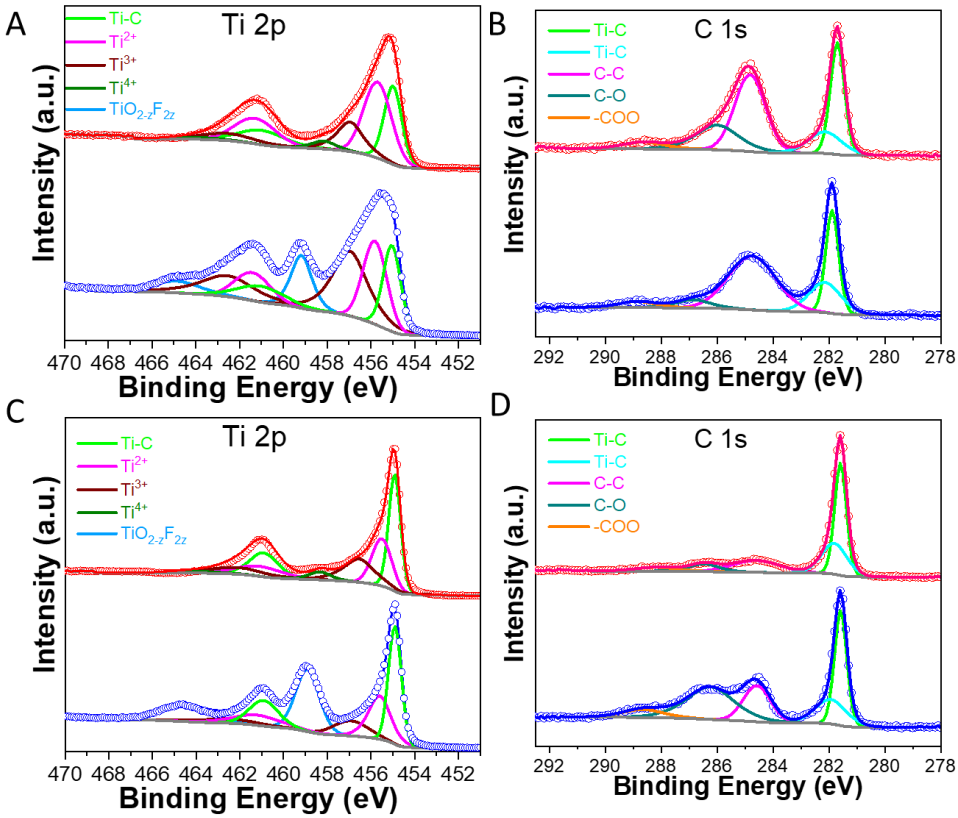

Figure 5.14. High-resolution XPS spectra of Ti 2p and C 1s regions.
(A) and (B) $Ti_3C_2T_x/TMA^+$ (blue curve) and $Ti_3C_{2.2}$ NPLs recovered from Mg-Li alloy (red curve). (C) and (D) isotropic $TiC_{0.88}$ NCs (blue curve) and $TiC_{0.95}$ NCs recovered from Mg-Li alloy (red curve). The recovered particles in both cases did not contain $TiO_{2-z}F_{2z}$ contribution. See "XPS fitting" in Materials and methods section for further details about the components' deconvolution and estimation of the Ti/C (here C is the carbide carbon) elemental ratio.

Table 5.2. XPS fitting results for $Ti_3C_2T_x$/TMA^+ MXenes and $Ti_3C_{2.2}$ NPLs (recovered from Mg-Li alloy).

	BE [eV]	FWHM [eV]	Fraction	Assigned to
Ti $2p_{3/2}$ ($2p_{1/2}$)	455.0 (461.0)	0.95 (2.50)	0.21	Ti-C
	455.8 (461.4)	1.28 (1.90)	0.27	Ti(II) oxide
	457.0 (462.6)	1.89 (2.90)	0.35	Ti(III) oxide
	459.2 (464.9)	1.13 (2.54)	0.17	$TiO_{2-z}F_{2z}$
C 1s	281.9	0.54	0.25	Ti-C
	282.1	1.35	0.18	Ti-C
	284.8	2.00	0.47	C-C
	286.9	1.49	0.06	C-O
	288.9	1.55	0.04	-COO

	BE [eV]	FWHM [eV]	Fraction	Assigned to
Ti $2p_{3/2}$ ($2p_{1/2}$)	455.0 (461.0)	0.95 (2.50)	0.31	Ti-C
	455.7 (461.3)	1.49 (2.22)	0.46	Ti(II) oxide
	457.0 (462.6)	1.41 (2.90)	0.19	Ti(III) oxide
	458.2 (463.9)	1.31 (2.8)	0.04	Ti(IV) oxide
C 1s	281.7	0.59	0.26	Ti-C
	282.1	1.42	0.12	Ti-C
	284.8	1.30	0.39	C-C
	286.0	1.80	0.18	C-O
	288.6	1.79	0.05	-COO

In order to check the stability of $Ti_3C_2T_x$ flakes at 700 ºC in the molten alloy, we assessed the crystalline phase, morphology, and surface functionalization of the materials recovered from the MXene/Mg-Li MMC by dissolving the metal matrix in aqueous HCl solution. X-ray photoelectron spectroscopy (XPS) spectra (Figures 5.13, 5.14 and Table 5.2) indicate that the stoichiometry of the recovered particles is $Ti_3C_{2.2}$ (for simplicity we further refer to it as Ti_3C_2.). Additionally, XPS spectra show that the liquid metal treatment at 700 °C eliminated the fluoride

surface groups and reduced the Ti oxidation state (Figure 5.13) suggesting the presence of bare Ti_3C_2 particles in Mg-Li alloy matrix.

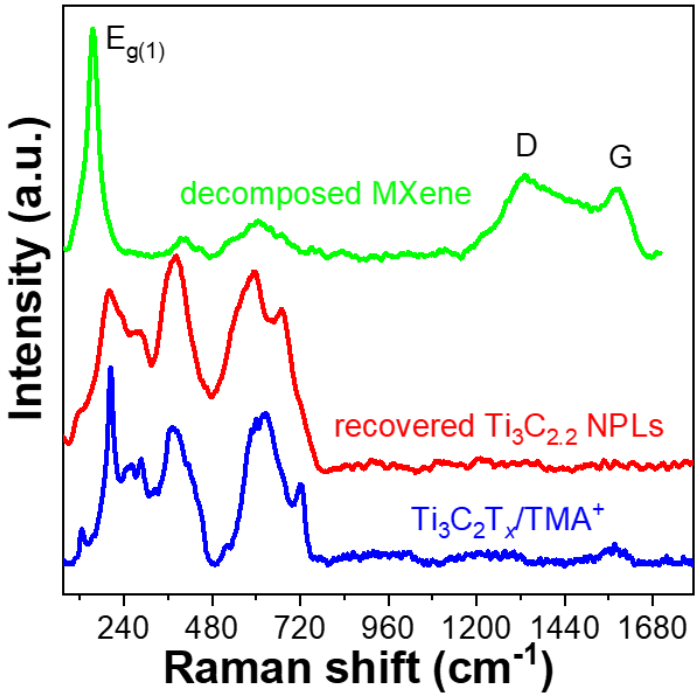

Figure 5.15. Raman spectra for the initial $Ti_3C_2T_x$/TMA^+, recovered NPLs and oxidized $Ti_3C_2T_x$ for comparison.

The recovered NPLs (from Mg-Li alloy) lack the intense peak at 155 cm^{-1} characteristic of $E_{g(1)}$ of anatase TiO_2 as well as D and G bands, characteristic of amorphous carbon, thus confirming that $Ti_3C_2T_x$ phase did not disproportionate during processing in Mg-Li alloy at 700 °C.

The Raman spectrum (Figure 5.15) of the recovered particles does not show peaks corresponding to TiO_2 or amorphous carbon, supporting the stability of titanium carbide phase under our processing conditions. The TEM images of the recovered Ti_3C_2 particles show NPLs with smaller lateral dimensions than the original 2D MXene sheets (Figure 5.16). AFM measurements confirm that the recovered particles retain their 2D morphology, though the thickness increases slightly to ~ 3 nm (Figure 5.17). An FFT of the TEM image of an individual NPL shows a hexagonal pattern consistent with the [0001] zone axis of the hcp structure (Figure

5.18). These results are consistent with a reported *in situ* TEM study where hcp-$Ti_3C_2T_x$ flakes heated above 500 °C grew thicker at the expense of their lateral area, while still preserving hexagonally symmetric Ti-terminated (0001) top and bottom facets.[42] In general, high-temperature stability of $Ti_3C_2T_x$ in molten Mg-Li is encouraging for making a variety of other MMCs by combining different MXenes with various metal matrices.

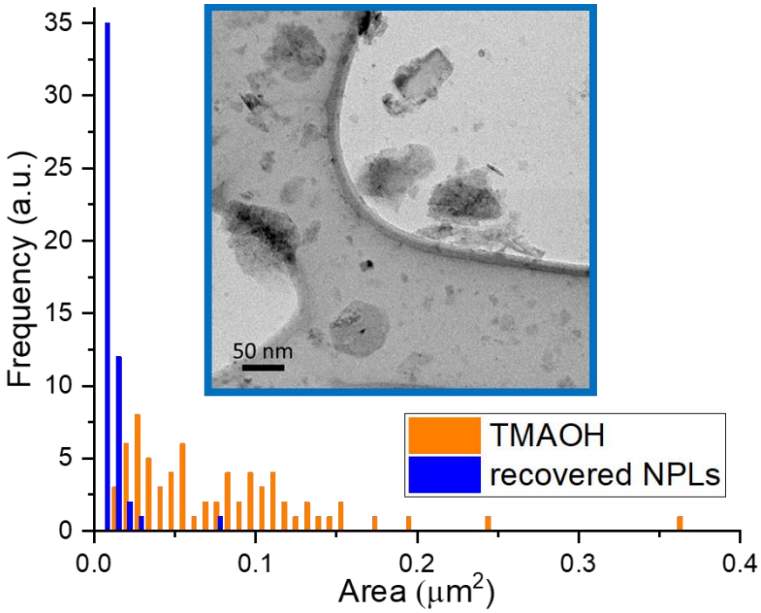

Figure 5.16. Comparison of the lateral area distributions for $Ti_3C_2T_x$/TMA^+ and Ti_3C_2 NPLs recovered from Mg-Li alloy.
Inset: TEM image of Ti_3C_2 NPLs recovered from Mg-Li alloy and deposited from the colloidal solution on a lacey carbon grid. Lacey carbon grid can be seen behind the NPLs suggesting that the recovered particles are very thin.

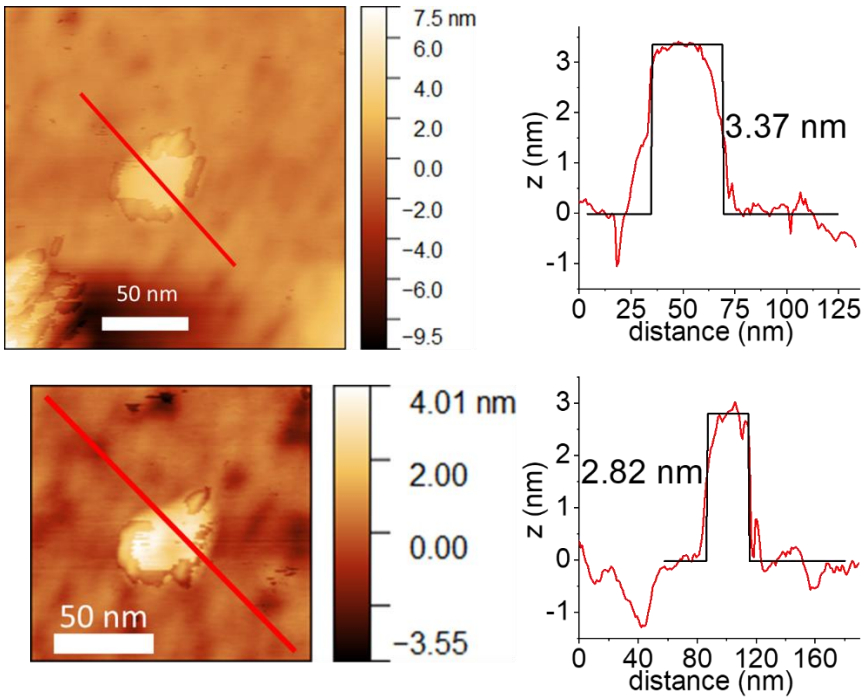

Figure 5.17. AFM topography of the recovered Ti_3C_2 NPLs with the height profile along the red line.

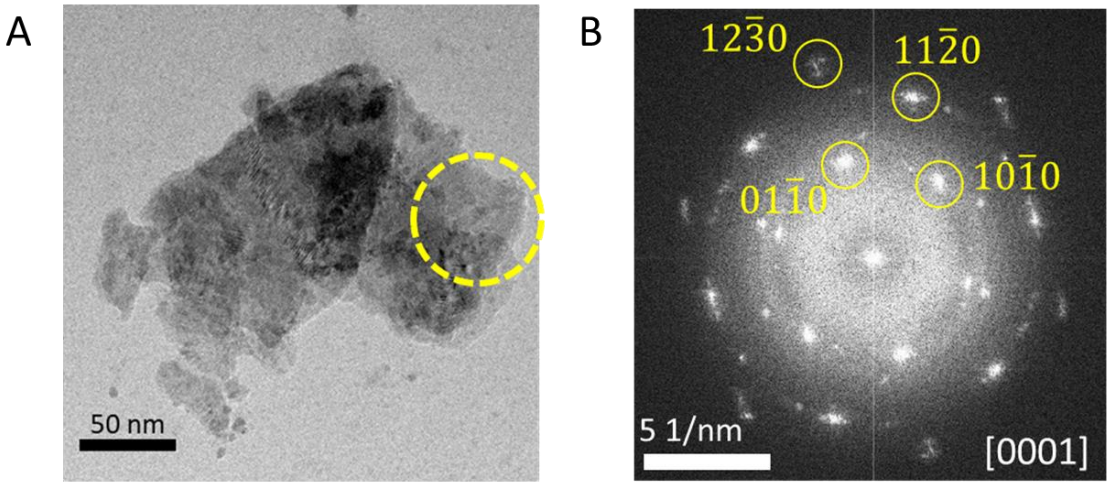

Figure 5.18. TEM image of the recovered NPLs.
(B) FFT of the circled region in (A) showing the hexagonal patterns corresponding to [0001] zone axis. The fact that there is a hexagonal pattern at q ~ 2.4 $Å^{-1}$ allows us to attribute the observed pattern to [0001] zone axis of the hcp component of Ti_3C_2 NPL, rather than to [111] zone axis of the fcc component of Ti_3C_2 NPL for which no reflections at q ~ 3.8 nm^{-1} can be observed. The [111] zone axis of the fcc lattice should contain a hexagonal pattern at q ~ 6.5 nm^{-1} corresponding to planes.

To better understand the role of particle shape, we compared MMCs prepared using 2D $Ti_3C_2T_x$ MXenes with similarly prepared MMCs containing isotropic $TiC_{0.9}$ NCs (Figure 5.19).

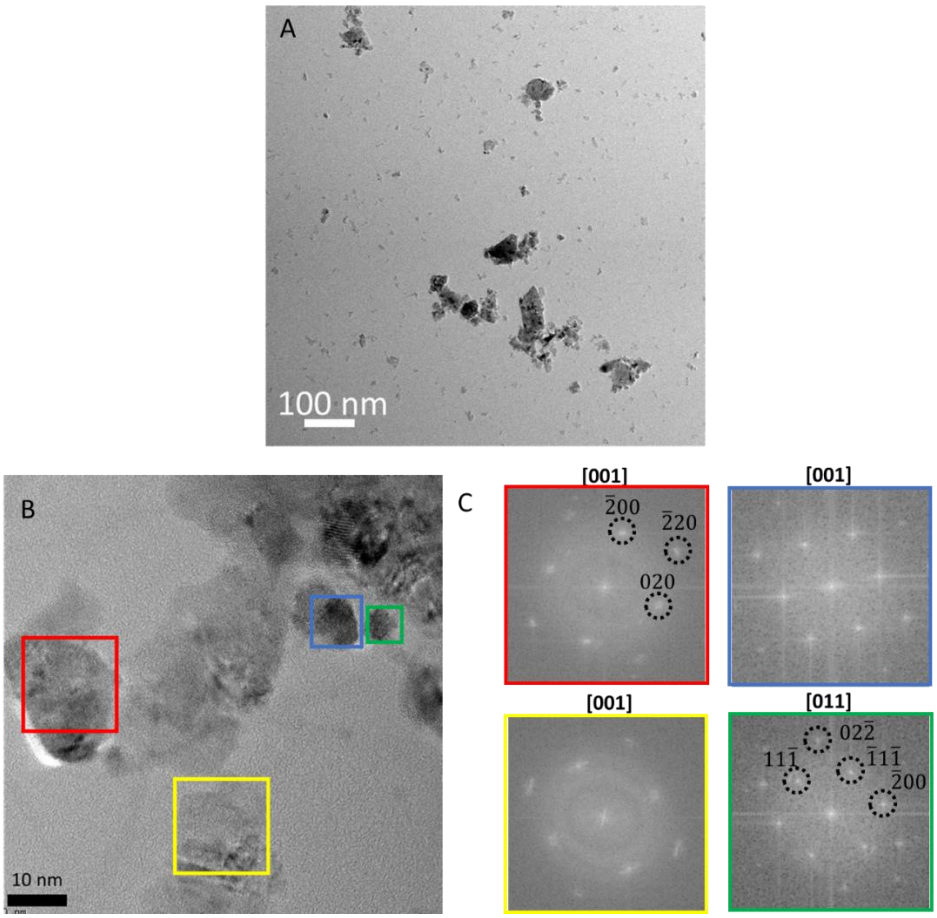

Figure 5.19. TEM characterization of colloidal $TiC_{0.9}$ NCs.
(A) and (B) TEM images of the colloidally stable $TiC_{0.9}$ NCs (in water) used in MMC fabrication. (C) FFT of the selected areas in image (B) showing that majority of NCs are low index {100} facet terminated. In case of TiC, {100} surfaces have significantly lower surface energies that {110} and {111} surfaces. Hence {100} facets should be one of the main faces of TiC powder grains.[22]

The $TiC_{0.9}$ NCs with an average crystalline size of ~ 58 nm were introduced into Mg-Li alloy with a final atomic ratio of Mg:Ti of 4:1 (measured with XRF) corresponding to ~ 12 vol. % $TiC_{0.9}$ phase. Figure 5.20 shows high-resolution synchrotron XRD patterns for the pristine $Ti_3C_2T_x$ MXene powder, recovered Ti_3C_2 NPLs, and recovered isotropic $TiC_{0.9}$ NCs for comparison. The most intense wide-angle peak of the pristine $Ti_3C_2T_x$ flakes corresponds to the diffraction from

$(11\bar{2}0)$ planes, whereas their $(10\bar{1}0)$ peak overlaps strongly with the lamellar $(000L)$ and $(10\bar{1}L)$ reflections.[43] Based on the Rietveld refinement (Figure 5.21, Table 5.3), the recovered $TiC_{0.9}$ NCs did not change their original isotropic rock-salt (fcc) structure. In contrast, the diffraction pattern of the recovered Ti_3C_2 NPLs differs from the original $Ti_3C_2T_x$ MXene phase and qualitatively resembles the recovered isotropic $TiC_{0.9}$ NC phase. However, Rietveld refinement using the pure isotropic fcc structure resulted in poor fitting, with the weighted-profile *R*-factor (R_{wp}) exceeding 10 % (Figure 5.22A). The fitting was significantly improved after introducing a secondary hcp phase and [110] texture for the fcc structure (Figure 5.22B, Table 5.4). The synchrotron XRD results are thus in agreement with the FFT analysis of the high-resolution-TEM images (Figure 5.18): the recovered NPLs have increased thickness (~ 3 nm) compared to the original $Ti_3C_2T_x$ (~ 1 nm) and their structure is a mixture of the hcp (37 %) and [110] textured fcc (63 %) phases.

Next, we compared the synchrotron XRD patterns of Ti_3C_2 NPLs and $TiC_{0.9}$ NCs dispersed in solidified Mg-Li alloy matrix (Figure 5.20B). In both cases the solidified metal matrix consisted of the bcc-MgLi and hcp-MgLi as the major and minor phases, respectively (Figure 5.23).[15, 44] The regions highlighted in yellow correspond to diffraction from the planes of the titanium carbide phase that do not overlap with the strong matrix peaks. The (200) and (220) peaks of the $TiC_{0.9}$ NCs in the Mg-Li matrix are almost identical in their shape and peak position to the peaks of the recovered particles. However, Ti_3C_2 NPLs have a markedly different diffraction pattern while embedded in the matrix compared to their diffraction pattern after removal from the matrix: for the composite sample, the two peaks corresponding to the fcc structure, (200) at 10.95° 2-theta and (220) at 15.50°, each split into two peaks (Figure 5.20B). To further investigate this peak splitting, we used different Mg-Li alloys as the metal matrices and observed similar features in all studied MMCs containing Ti_3C_2 NPLs (Figure 5.24).

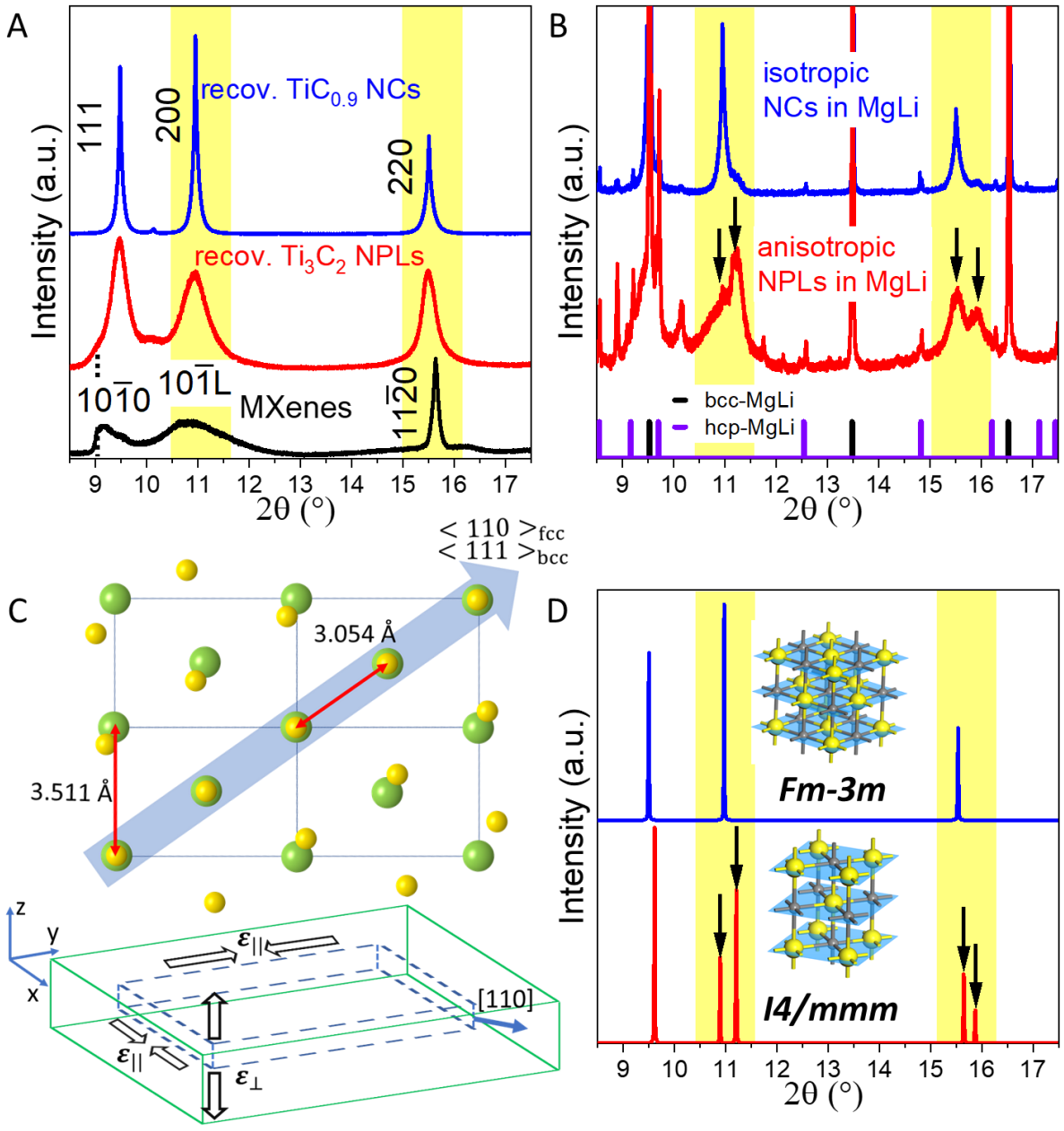

Figure 5.20. Synchrotron XRD characterization of the recovered particles and MMCs. (A) Synchrotron XRD (λ = 0.412779 Å) patterns of the initial $Ti_3C_2T_x$ flakes intercalated with TMA^+ cations (black), flakes recovered from Mg-Li alloy (red) and isotropic $TiC_{0.9}$ NCs recovered from Mg-Li alloy (blue). (B) Synchrotron XRD patterns of the two Mg-Li MMCs containing Ti_3C_2 NPLs (red) and isotropic $TiC_{0.9}$ NCs (blue). (C) Schematic showing the biaxial strain observed in Ti_3C_2 NPLs embedded in Mg-Li matrix due to the Kudjumov-Sachs orientation relationship between (110) plane of bcc-MgLi alloy (green) and (111) Ti-terminated plane of fcc-Ti_3C_2 NPL (yellow). (D) Simulated XRD patterns for TiC in $Fm\bar{3}m$ and $I4/mmm$ space groups.

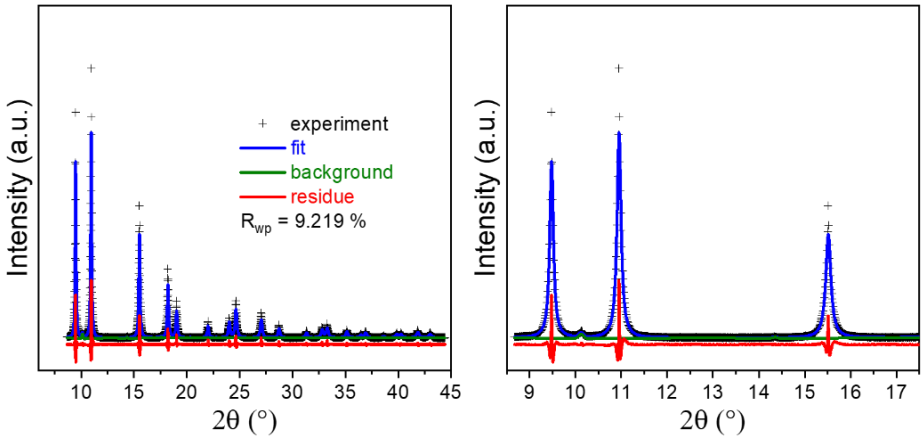

Figure 5.21. Rietveld refinement for $TiC_{0.95}$ NCs recovered from the Mg-Li alloy.
Rietveld refinement of the synchrotron XRD pattern (λ = 0.412779 Å) showing good fit using the isotropic rock-salt (fcc) structure (right panel is a zoom-in of the left panel).

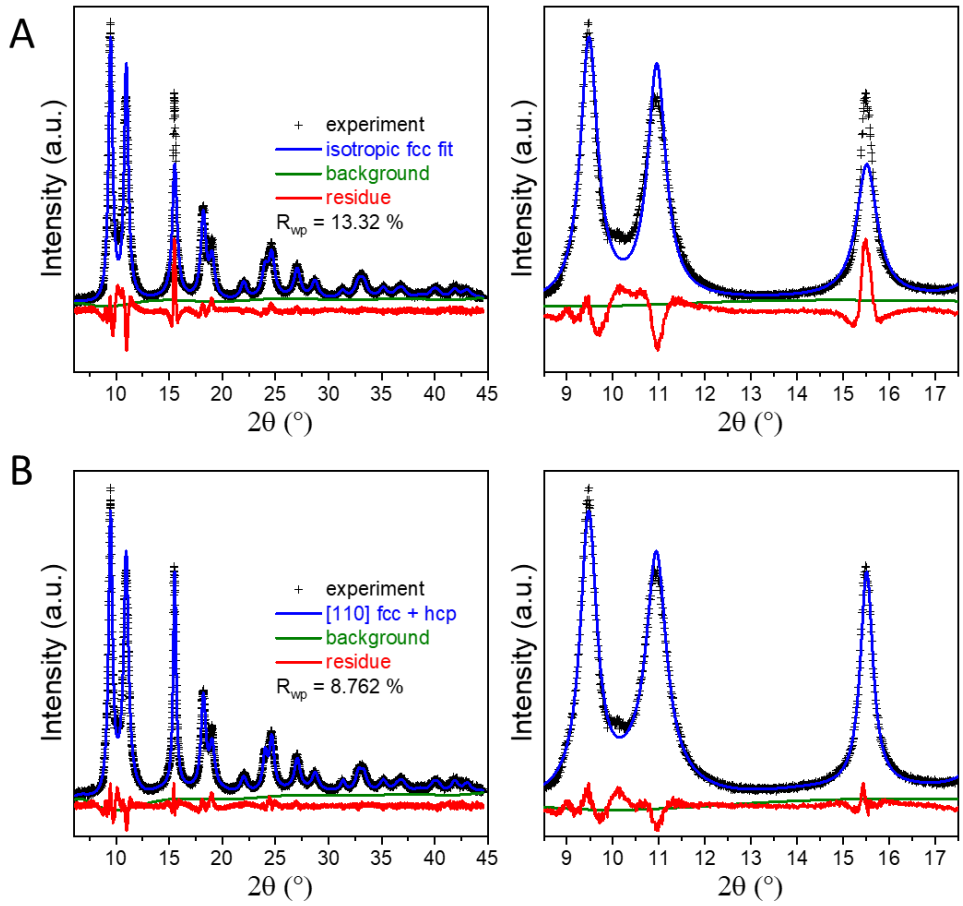

Figure 5.22. Rietveld refinement for Ti_3C_2 NPLs recovered from the Mg-Li alloy.
Rietveld refinement of the synchrotron XRD pattern (λ = 0.412779 Å) using: (A) single phase isotropic rock-salt (fcc-Ti_3C_2) fit; (B) two phase [110] textured fcc-Ti_3C_2 and hcp-Ti_3C_2 fit.

Table 5.3. Rietveld refinement results for $TiC_{0.9}$ NCs recovered from Mg-Li alloy.

$TiC_{0.9}$, Fm-3m, a = 4.32339 Å, V = 80.812 Å^3, domain size 58 nm					
Atom	x	y	z	Occ.	U_{iso} [Å^2]
Ti	0.5	0.5	0.5	1	0.0025
C	0	0	0	0.95	0.0025

Table 5.4. Rietveld refinement results for Ti_3C_2 NPLs recovered from Mg-Li alloy.

$Ti_3C_{2.2}$, Fm-3m, phase fraction 0.6319, a = 4.31857 Å, V = 80.541 Å^3, equatorial size 5 nm, axial size 19 nm, [110] unique axis					
Atom	x	y	z	Occ.	U_{iso} [Å^2]
Ti	0.5	0.5	0.5	1	0.003
C	0	0	0	0.73	0.003

$Ti_3C_{2.2}$, P63/mmc, phase fraction 0.3681, a = 2.92743 Å, c = 4.41613 Å, V = 32.775 Å^3, domain size 39 nm					
Atom	x	y	z	Occ.	U_{iso} [Å^2]
Ti	0.33333	0.66667	0.25	0.5	0.003
Ti	0.66667	0.33333	0.75	0.5	0.003
C	0	0	0	0.73	0.01

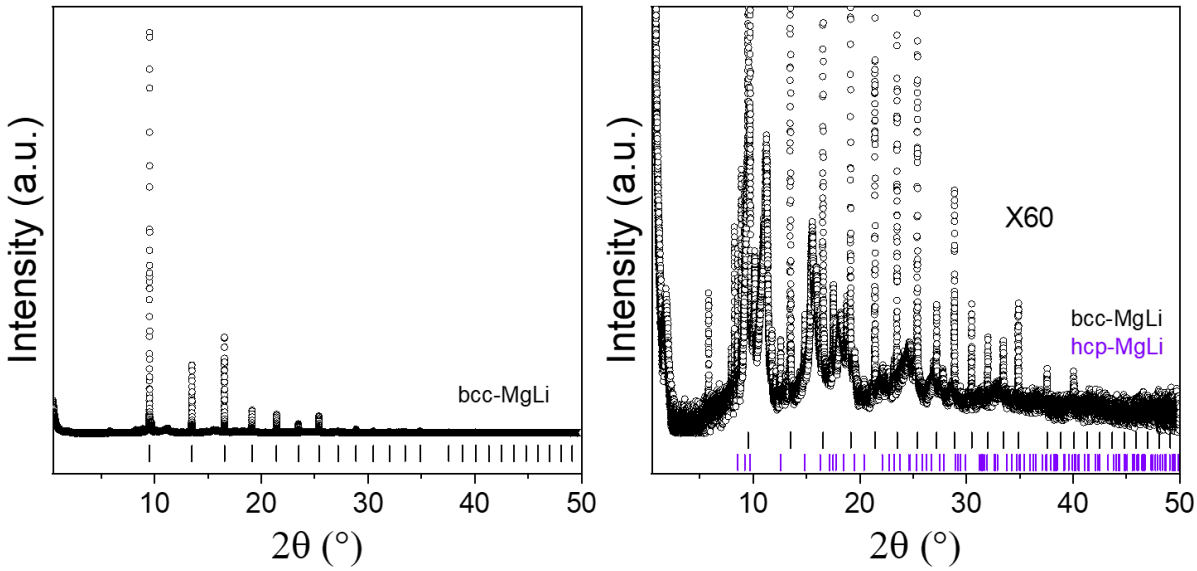

Figure 5.23. Full range synchrotron XRD pattern for the Ti_3C_2 NPLs in Mg-Li alloy. bcc-MgLi phase has *a* = 3.511 Å. Synchrotron radiation, λ = 0.412779 Å.

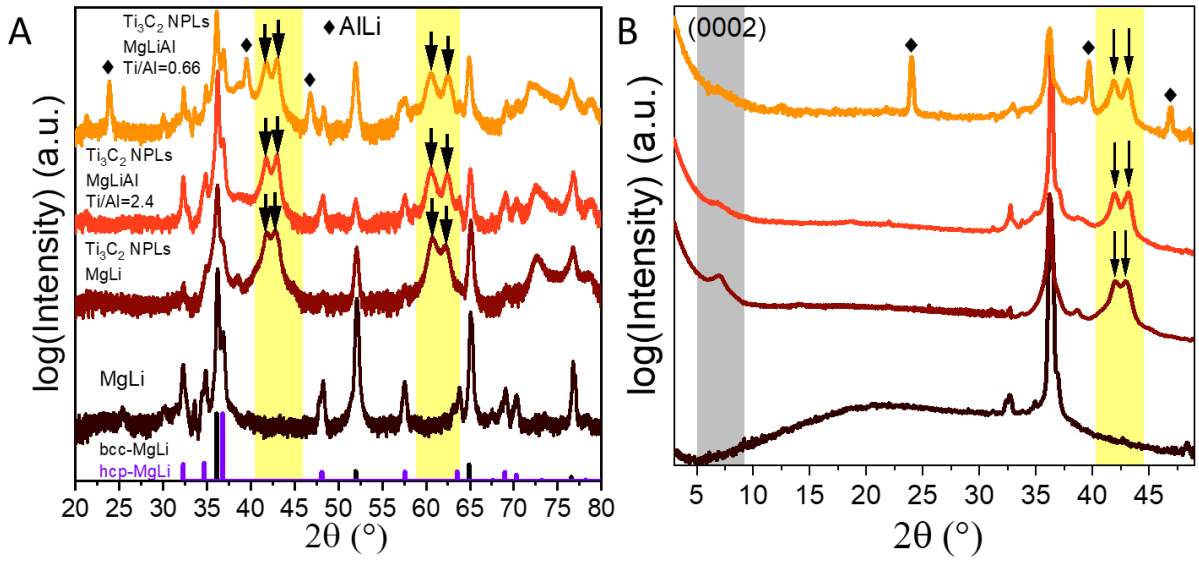

Figure 5.24. XRD characterization of the MXene based MMCs.
(A) XRD pattern (reflection mode, Cu Kα) for Mg-Li alloy (doped with Al) and its composites with Ti_3C_2 NPLs. Black arrows point to the peaks indicating the biaxial straining of Ti_3C_2 NPLs. (B) Wide-angle X-ray scattering (transmission mode, Cu Kα) for samples in (A).

The observed symmetry reduction of the Ti_3C_2 NPLs in Mg-Li alloy is consistent with a tetragonal distortion to the $I4/mmm$ space group, which is a maximal subgroup of the $Fm\bar{3}m$ space group[45] (Figure 5.20D). Since the recovered Ti_3C_2 NPLs lack the (200) and (220) peak splitting (Figure 5.20A, red curve), the tetragonal distortion cannot be attributed to alloying between Mg/Li and Ti. Instead, it may suggest that static strain imposed by the surrounding metal matrix is responsible for the NPL lattice distortion. The amount of the in-plane ($\varepsilon_{||}$) and out-of-plane ($\varepsilon_{\perp}$) strain is -2.09 % (compressive) and 0.72 % (tensile) (Figure 5.20C), respectively. This corresponds to a Poisson ratio (ν) of ~ 0.15 for Ti_3C_2 NPLs and is close to ν of $Ti_3C_2T_x$ MXene.[12, 46] The Poisson ratio is evaluated using the same simple elastic model as outlined in Chapter 3.5.

The observed biaxial straining can originate from the formation of a semi-coherent interface between the matrix and Ti_3C_2 NPLs. Due to the small difference between nearest neighbors' distances in (111) plane of the fcc component of Ti_3C_2 NPLs, 3.054 Å, and in (110)

plane of bcc-MgLi alloy, 3.041 Å, we hypothesize existence of $\{111\} < 110 >_{\mathrm{fcc-Ti_3C_2\ NPL}} || \{110\} < 111 >_{\mathrm{bcc-MgLi}}$ orientation relationship, known as the Kurdjumov-Sachs (KS) orientation (Figure 5.20C).[47] Similarly, the KS orientation can take place between (0001) plane of the hcp component of Ti_3C_2 NPLs (nearest neighbor distance of 2.927 Å) and (110) plane of bcc-MgLi alloy.

The biaxial straining of Ti_3C_2 NPLs inside the metal matrix is a direct consequence of their 2D morphology. $TiC_{0.9}$ NCs, on the other hand, are isotropic particles and hence they can only experience hydrostatic strain inside the metal matrix. However, this strain is confined to the metal-NC interface and cannot significantly perturb the internal structure of $TiC_{0.9}$ NCs.

Table 5.5. Summary of the mechanical properties of the relevant Mg-Li alloy MMCs.

Material	Young modulus [GPa]	Yield strength [MPa]	Ultimate compressive strength [MPa]	Density [g/cm³]	Specific yield strength [kN*m/kg]
Mg-Li	11.8	68	NA	1.24	54
$Ti_3C_2T_x$/TMA^+ Mg-Li	20.6	155	NA	1.82	85
$Ti_3C_2T_x$/TMA^+ Mg-Li-Al Ti/Al=2.4/1	20.9	183	274 (@ 22 %)	1.77	103
$Ti_3C_2T_x$/TMA^+ Mg-Li-Al Ti/Al=2/3	24.5	277	378 (@ 9.7 %)	1.92	144
$Ti_3C_2T_x$ Mg-Li	13.8	120	NA	1.86	65
$TiC_{0.95}$ NCs Mg-Li	11.5	116	NA	1.83	63

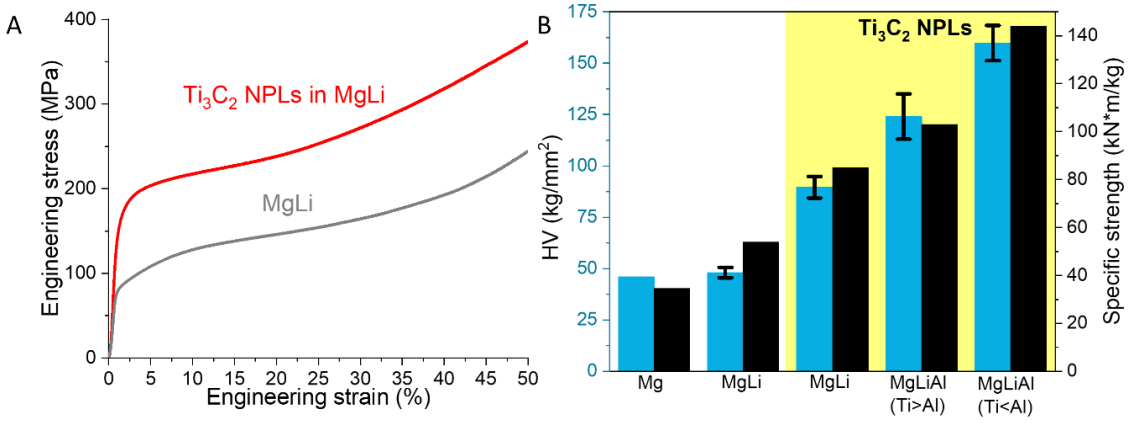

Figure 5.25. Mechanical properties of the MXene based MMCs.
(A) Compressive engineering stress-strain curves for the Mg-Li alloy MMCs containing Ti_3C_2 NPLs (red) and Mg-Li alloy without any particles (grey). (B) Summary of the specific yield strength and Vickers hardness for the composites of Ti_3C_2 NPLs in Mg-Li and Mg-Li-Al alloys. The literature reported specific strength and Vickers hardness for pure Mg are shown for comparison.[48-49]

The biaxial strain observed in the Ti_3C_2 NPLs in Mg-Li alloy reflects strong bonding of the NPLs with the metal matrix, which has important implications on the mechanical performance of these MMCs. The MMC fabricated from $Ti_3C_2T_x$ MXenes shows a 128 % increase in the yield strength and a 57 % increase in the specific yield strength over the base Mg-Li alloy (Table 5.5 and Figure 5.25A). This MMC is able to bear a gradually increasing load smoothly without any signs of crack formation. Additionally, reproducible results were obtained for the replicate samples, suggesting uniform distribution of particles (Figure 5.26A). The MMC fabricated with the isotropic $TiC_{0.9}$ NCs is also able to bear the load smoothly without signs of crack formation (Figure 5.26B). However, this MMC shows only a moderate increase in the yield strength (71 % for the best sample) and specific yield strength (17 % for the best sample) (Table 5.5). This difference in the mechanical performance may be explained by differences at the interfaces due to the interactions between the nanomaterials' surfaces and the metal matrix. The density functional theory (DFT) calculated work of adhesion ($-W_{ad}$) between the metal and ceramic interfaces is larger

for polar ceramic facets.[50] Due to the KS orientation relationship between Ti_3C_2 NPLs and Mg-Li alloy, Ti_3C_2 NPLs maximize the area of polar $(111)_{fcc}$ and $(0001)_{hcp}$ facets per volume of particles in contact with the metal matrix. $TiC_{0.9}$ NCs, on the other hand, have non-polar facets (Figure 5.19) interfacing the metal matrix. Stronger chemical bonding at the interface, in turn, explains increased load transfer from the matrix to Ti_3C_2 NPLs compared to isotropic $TiC_{0.9}$ NCs. As discussed above, 2D Ti_3C_2 NPLs elastically strain inside metal matrix to minimize lattice mismatch at the interface and, correspondingly, maximize the number of chemical bonds per unit area of the NPL-matrix interface.

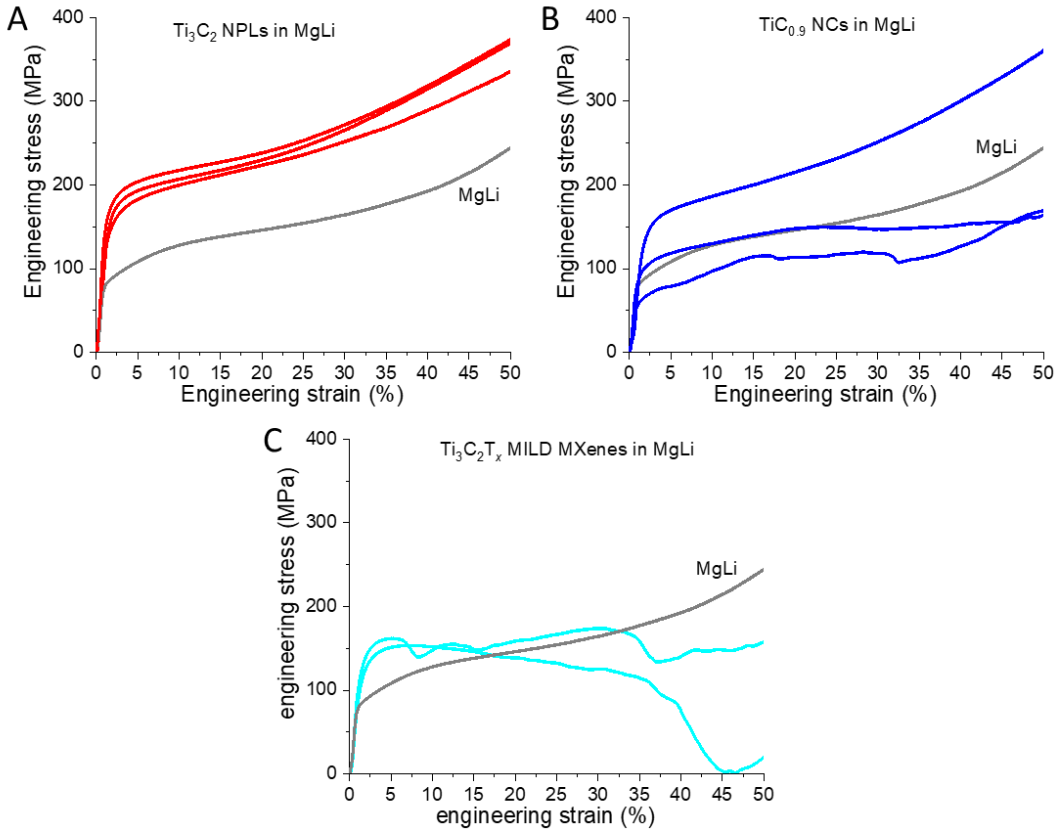

Figure 5.26. **Compressive engineering stress-strain curves for Mg-Li alloy MMC containing 12-13 vol. % of ceramic particles.**
(A) Ti_3C_2 NPLs (fabricated using $Ti_3C_2T_x/TMA^+$). (B) $TiC_{0.9}$ NCs with the crystallite size of ~ 58 nm. (C) $Ti_3C_2T_x$ synthesized *via* the MILD procedure without additional TMAOH treatment. Curves of the same color indicate replicate samples. A stress-strain curve for Mg-Li without any particles is shown for comparison (grey).

The MMCs with the isotropic $TiC_{0.9}$ NCs did not yield reproducible results unlike the MMC with Ti_3C_2 (Figure 5.26B). This can be attributed to the non-uniform distribution of NCs. The volume fraction required to achieve colloidal gelation with attractive isotropic particles is higher than that of attractive anisotropic particles. Our observations are thus qualitatively consistent with the phase diagram for patchy colloids, where colloids with a smaller number of nearest neighbor contacts (such as Ti_3C_2 NPLs) reach gelation and bypass phase segregation at lower volume fractions.[51] The distribution of particles was found to be highly non-uniform in the case of MMCs fabricated with $Ti_3C_2T_x$ without additional TMAOH treatment (MILD MXene), resulting in the composites with irreproducible mechanical properties and reduced plasticity compared to the base Mg-Li alloy (Figure 5.26C). The non-uniform distribution could be related to the stronger vdW attraction between large lateral area MILD $Ti_3C_2T_x$ compared to that between small area $Ti_3C_2T_x/TMA^+$ (Figure 5.4).

We further tested the effect of Al addition on the Ti_3C_2 in Mg-Li MMC. Al is commonly used in small amounts to strengthen Mg-Li alloys[15] and improve the wetting of TiC particles in Mg alloys.[52] Figure 5.25B shows the dependence of the specific yield strength and Vickers hardness (HV) at 0.98 N load for the Ti_3C_2 NPLs in Mg-Li MMCs with different amounts of added Al. With an elemental ratio of Ti to Al of 2.4/1 (measured with XRF), Al did not form any intermetallic compounds with Mg and Li (Figure 5.24), suggesting that Al preferentially interacts with the NPL surface. EDX elemental mapping of a thinned sample (Figure 5.27) further suggests segregation of the majority of the added Al to the Ti_3C_2 NPL-metal interface. In this case the specific strength increased by 91 % and hardness by 158 % over the base Mg-Li alloy. This increase in the strength is accompanied by the broadening of the (0002) reflection possibly suggesting that the addition of Al improves wetting of the individual Ti_3C_2 layers (Figure 5.24B).

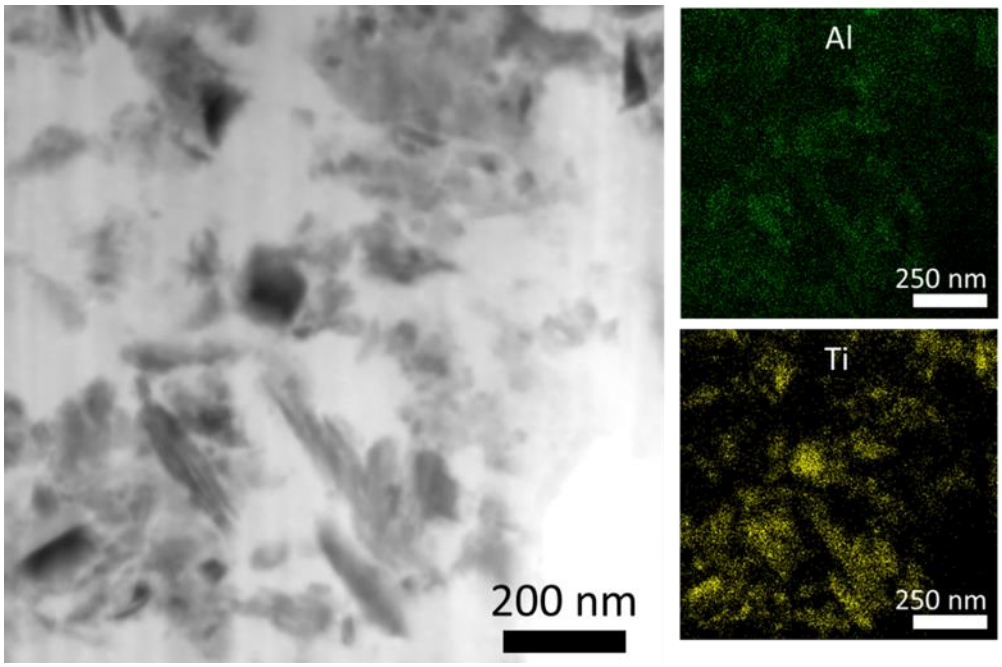

Figure 5.27. Characterization of Ti_3C_2 NPLs in Mg-Li alloy (doped with Al).
Bright field TEM image and corresponding EDX elemental maps of Ti_3C_2 NPLs in Mg-Li alloy (doped with Al) with the elemental Ti/Al ratio of 2.4/1 (estimated from the XRF spectrum).

However, the composite could reach a maximum plastic strain of only 22 % before the first crack reached the surface of the specimen (Figure 5.28), showing more brittle behavior than the no-Al Mg-Li composites. Although Al was effective in increasing the strength of the composite without the formation of intermetallic phases, further optimization is required to improve the composite's plasticity. The introduction of Al at an atomic ratio exceeding that of Ti resulted in the formation of an AlLi intermetallic phase (Figure 5.24A, Figure 5.29), which additionally increased the strength at the expense of the alloy's plasticity with the maximum plastic strain reaching only 9.7 % (Figure 5.28). This initial study shows the potential for developing MXene-reinforced MMCs with greatly improved mechanical properties. It is natural to assume that optimization of MXene content, particle size, dispersion and alloy composition will further improve the mechanical properties.

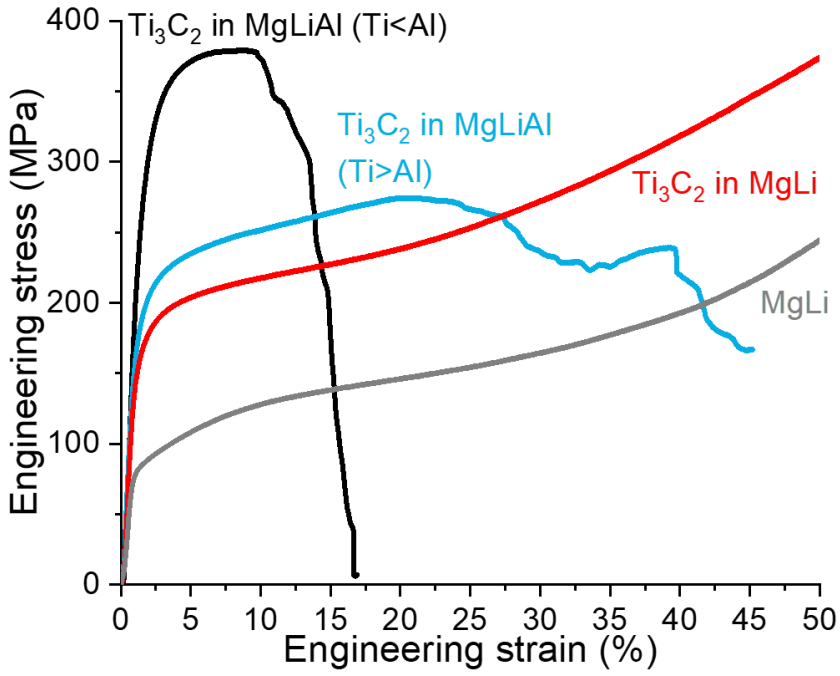

Figure 5.28. **Compressive engineering stress/strain curves for the Mg-Li-Al and Ti_3C_2 NPL MMCs.**
Mechanical properties are summarized in Figure 5.25B.

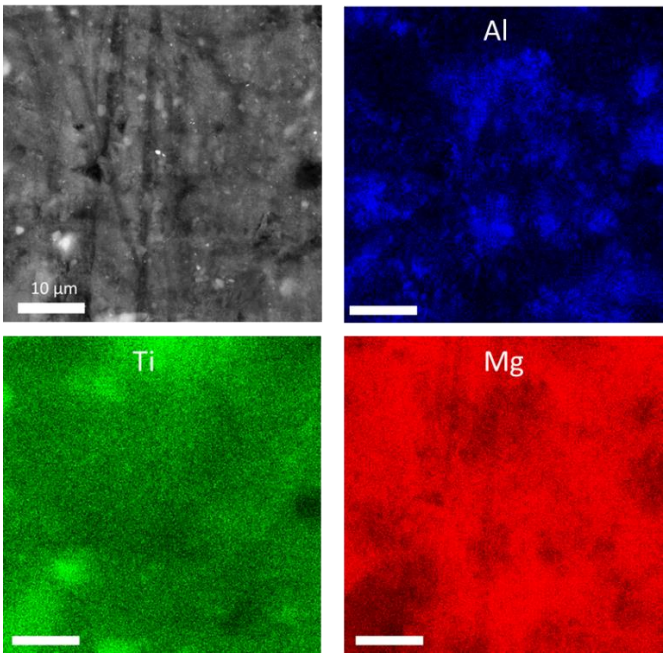

Figure 5.29. SEM characterization of Ti_3C_2 NPLs in Mg-Li-Al alloy.
EDX maps of Ti_3C_2 NPLs in Mg-Li alloy (doped with Al) with the elemental Ti/Al ratio of 0.66/1 (estimated from the XRF spectrum). The AlLi intermetallic phase is phase segregated from the Mg-Li matrix.

5.6 Conclusions.

This work demonstrates promising application for 2D MXenes as a reinforcement component for lightweight structural alloys. Uniform composites of lightweight metals and 2D MXenes have been enabled by the colloidal gelation of liquid metals. $Ti_3C_2T_x$ forms a network of Ti_3C_2 nanoplatelets spanning the volume of Mg-Li alloy matrix. The network formation is believed to be responsible for the lack of particle phase segregation while in the molten state and during melt solidification. The Mg-Li alloy shows increased load transfer to Ti_3C_2 nanoplatelets compared to isotropic $TiC_{0.9}$ NCs due to the favorable orientation relationship between the basal plane of Ti_3C_2 NPLs and the (110) plane of bcc-MgLi, introducing biaxial straining in Ti_3C_2. This leads to the 128% increase in the yield strength of the alloy. By adding Al, one can further improve the mechanical properties of the composite. The specific strength and hardness almost tripled compared to the neat Mg-Li alloy. These numbers for a particular combination of MXene and a metal alloy are probably far from the maximum values possible for MXene-based metal matrix composites. We believe that the developed method for achieving uniform metal-matrix composites, based on the colloidal gelation of liquid metals, can be extended to other metal alloy-MXene systems. While we can assume that Ti_2C, Ti_3CN, Ti_4N_3 and other Ti-terminated MXenes will behave similarly to Ti_3C_2, MXenes based on other transition metals should be investigated. In particular, Zr_3C_2 MXene has been shown to retain its 2D lattice and morphology better than Ti_3C_2 MXene at high temperatures.[53] As a result, Zr_3C_2 MXene can potentially be used as a reinforcement MXene in alloys requiring even higher processing temperatures.

With about 30 MXene species currently available, mechanical and rheological properties of technologically relevant lightweight metal alloys can be controlled by designing specific metal matrix 2D carbide or nitride interfaces. Strong metal-MXene bonding is also required for creating

MXene-metal electrical contacts for MXene antennas,[54] fibers in smart textiles,[55] battery and supercapacitor electrodes.[56] Brazing and soldering of MXenes require good wetting by metal and high interfacial strength. Those applications will benefit from the data reported in this work, even though different metal alloys are used.

5.7 Materials and methods.

Chemicals and materials

Al pellets (99.999 %, Kurt J. Lesker), Mg pellets (99.95 %, Kurt J. Lesker), Li chips (99.9 %, MTI), TiC_y microparticles (~ 2 μm, 99.5 % Alfa Aesar), LiF (98.5 %, Alfa Aesar), HCl (36.5-38 %, Fisher), tetramethylammonium hydroxide (TMAOH, 25 wt. % aqueous solution, Sigma), HF (48 %, Sigma), Ga (99.99 %, Strem). Niobium crucibles were machined from ASTMB 392, R04210 grade Nb rods from Rembar. Alumina crucibles were 99.8 % grade from CoorsTek.

Synthesis of Ti_3AlC_2 MAX

Ti_3AlC_2 MAX phase was synthesized from TiC, Ti and Al powders according to a well-established procedure described in details elsewhere.[16]

Preparation of TiC_y NCs from bulk commercial TiC_y

Ball milling was used to reduce the size of the commercial TiC_y powder (~ 2 μm). 7 g of TiC_y were loaded (inside the Ar glovebox) in the stainless steel cartridge with stainless steel balls (3:1 ball to TiC_y mass ratio) and 15 ml of anhydrous ethanol to prevent particle baking. The slurry was ball milled for 10 h. The ball-milled TiC_y powder was then treated for 12 h with 48 wt. % aqueous HF to dissolve impurities after ball milling and etch passivating TiO_2 layer. The acidic mixture was then thoroughly washed with 1-2 L of deionized H_2O *via* centrifugation/redispersion

cycles. The 48HF-treated particles were further stirred in 100 ml of 25 wt. % aqueous TMAOH solution for 24 h. The particles were then precipitated at 3260g for 5 mins and the supernatant was discarded. 200 ml of deionized H_2O were then added to this precipitate (precipitate 2) and the solution was spun at 3260g for 5 mins. The supernatant containing the colloidal solution of TiC_y NCs was separated from the precipitate. TiC_y NCs were then precipitated with MeOH/acetone mixture *via* centrifugation at 10543g for 45 mins. Another 160 ml of deionized H_2O were added to the precipitate 2 to render more TiC_y NCs colloidally stable. The centrifugation/redispersion cycles were repeated until further addition of deionized H_2O did not result in the colloidally stable TiC_y NCs after 3260g, 5 mins centrifugation. TiC_y NCs were dried at 120 °C under vacuum before further use in composite synthesis. The stoichiometry (y) was determined from the XPS analysis to be ~ 0.9 (Figures 5.13, 5.14).

MXene exfoliation *via* Minimally intensive layer delamination (MILD)

$Ti_3C_2T_x$ was synthesized using the published procedure.[16] The etching solution was prepared by dissolving 4.8 g of LiF in 60 ml of 9 M HCl under continuous stirring. 3 g of Ti_3AlC_2 MAX phase was added slowly (over the course of 5 min) to the etching solution. The mixture was stirred for 24 h at room temperature. The acidic mixture was further washed with 1.6 L of deionized H_2O *via* centrifugation (5 min per cycle at 3260 g)/redispersion cycles. 270 ml of deionized H_2O were then added and the solution was spun at 3260 g for 15 mins to separate the dark-green colloidal solution of delaminated $Ti_3C_2T_x$ sheets from the unetched Ti_3AlC_2 MAX phase and non-delaminated $Ti_3C_2T_x$ sheets (precipitate 1). The colloidal solution was decanted and 300 ml of deionized H_2O were added followed by centrifugation for 1.5 h at 10543 g. Another 270 ml of deionized H_2O were added to precipitate 1 to render more delaminated MXenes. The

centrifugation/delamination cycles were repeated until further addition of deionized H_2O to precipitate 1 did not result in dark green solution after 3260 g, 15 mins centrifugation. The collected precipitate containing delaminated MXenes was dried under vacuum for > 12 h for further use. The typical yield of delaminated $Ti_3C_2T_x$ MXenes was 30-33 %.

Intercalation with Tetramethylammonium hydroxide (TMAOH)

We noticed that the reported procedure of using 48 wt. % HF etching of Ti_3AlC_2 MAX phase followed by TMAOH intercalation of the multi-layer $Ti_3C_2T_x$ sheets was not effective in rendering sufficient yield of the delaminated MXene sheets. Hence TMAOH interaction was performed on MILD MXenes. Typically, ~1 g of MILD synthesized $Ti_3C_2T_x$ MXenes was stirred in 100 ml of 25 wt. % aqueous TMAOH solution for 24 h. The particles were then precipitated *via* centrifugation at 3260 g for 5 mins and 200 ml of deionized H_2O was added. The solution was then ultrasonicated for 1.5 h while continuously bubbling Ar gas to avoid oxidation of flakes. TMA^+ intercalated $Ti_3C_2T_x$ sheets were then precipitated with MeOH/acetone mixture *via* centrifugation at 10543 g for 45 mins. This procedure results in almost quantitative yield of TMA^+ intercalated $Ti_3C_2T_x$ sheets. The collected precipitate was dried at 120°C under vacuum to get rid of intercalated water before further use in the composite synthesis.

Experimental details for handling liquid metals

Special care was taken to manage the heat inside the glovebox while handling liquid metals. Cooling water at 10 °C was continuously supplied into the copper coil around the furnace. During ultrasound processing, the piezoceramic element of the transducer was additionally cooled down with compressed Ar flow.

Mg-Li alloy with $Ti_3C_2T_x$ MXenes

All operations involving composite synthesis were performed in Ar filled glovebox with oxygen and moisture levels below 1 ppm. For ease of handling, Mg-Li alloy containing 60 at. % of Li (m.p. ~ 480 °C) was first prepared by melting Mg ingots (1.04 g) and Li pellets (445 mg) at 660 °C in a niobium crucible. 80-100 mg of $Ti_3C_2T_x$ MXene powder were infused into the melt at 530 °C with the assistance of probe sonication (Sonics Vibra Cell, VCX 750; 20 kHz, 105 µm amplitude, Ti-6Al-4V tip) for 2 mins. Once the required amount of MXenes had been introduced into the melt (~ 1.8 g), Mg ingots (1.37 g) were added at 700°C to the composite to dilute the concentration of Li (w.r.t. Mg) to 39 at. %. The resultant liquid metal alloy with MXenes was additionally ultrasound processed at 700 °C for 5 minutes to ensure complete mixing with the freshly introduced Mg metal. A typical MXene containing Mg-Li alloy composite was viscous enough so that it could be directly shaped while molten into an approximately rectangular shape (thixoforging technique) on a niobium substrate. The composite was allowed to cool down naturally to room temperature. Fabrication of Mg-Li MMC with $TiC_{0.9}$ NCs followed the same procedure as for the fabrication of Mg-Li alloy MMC with MXenes.

Al doped Mg-Li alloy with $Ti_3C_2T_x$ MXenes

In case of additional alloying with Al, the procedure was similar to Mg-Li alloy composite synthesis except that Al pellets were added into Mg-Li alloy (60 at. % of Li) at 530 °C before introducing MXenes.

Ga liquid metal with $Ti_3C_2T_x$/TMA^+ MXenes

1.9 at. % of Mg (50 mg) was dissolved in liquid Ga (7.465 g) at 200 °C in a glass vial. The addition of the small amount of Mg was crucial for liquid Ga to wet MXenes (see Supporting Information for further discussion). $Ti_3C_2T_x$ MXene powder was infused into the alloy at 45 °C (to keep Ga fully molten) with the assistance of ultrasound (Sonics Vibra Cell, VCX 750, 20 kHz, 105 µm amplitude, Ti-6Al-4V tip). The gelated composite was transferred into an alumina crucible and additionally annealed at 700 °C for 30 mins to mimic the high temperature processing conditions in Mg-Li alloy.

Al-Mg eutectic alloy with $TiC_{0.9}$ microparticles

Al-Mg eutectic (31:69 atomic ratio, m.p. 432 °C) liquid metal alloy was first prepared by melting 1.001 g of Al with 2.128 g of Mg ingots in alumina crucible at 740 °C. The liquid metal eutectic was allowed to cool down to 490 °C. 100-200 mg of $TiC_{0.9}$ microparticles were infused into the melt at 490 °C with the assistance of probe sonication (Sonics Vibra Cell, VCX 750; 20 kHz, 105 µm amplitude, Ti-6Al-4V tip) for 2 mins. Once the required amount of particles had been introduced into the melt, the composite was additionally ultrasound processed at 700 °C for 5 minutes.

Mechanical testing

Samples were machined into rectangular pillars with aspect ratio between 1:2 and 1:3. The compressive tests were performed on an Instron 5800 series materials tester using a 50 kN load cell at a strain rate of 10^{-3} s^{-1}. At least three replicate samples were tested for each composite. Vickers hardness tests were conducted on a Duramin 5 hardness tester using 0.98 N load for 5 s.

Indentation was performed at least 17 times on the same sample to determine the average HV value and its standard deviation.

Synchrotron X-ray diffraction (XRD)

The high-resolution synchrotron XRD data were collected using mail-in program available at 11-BM beamline at the Advanced Photon Source (APS) at Argonne National Laboratory with the X-ray wavelength of 0.412779 Å and 0.001° 2θ binning. Data were subsequently re-binned using a coarser spacing of 0.01° 2θ in order to facilitate convergence of the Rietveld refinements. All samples were sealed in Kapton capillaries (0.8 mm inner diameter) with epoxy. The capillaries were spun at 60 Hz during the measurement to maximize random orientation of the powders. The samples were measured for 60 minutes each.

The Rietveld refinement of the high-resolution synchrotron XRD data was performed using GSAS II software.[57] The atom occupancy was not refined and determined independently from the XPS elemental analysis (Ti/C elemental ratio).

Transmission electron microscopy (TEM)

The TEM images were obtained using a 300 kV FEI Tecnai F30 microscope. Samples for TEM were prepared by dropcasting a dilute sample of MXene solution onto a lacey carbon grid from Ted Pella. The MMC samples for TEM were prepared using FIB-SEM.

Focused Ion Beam-Scanning Electron Microscopy (FIB-SEM)

Thin samples of MMCs for TEM analysis were prepared in a TESCAN LYRA3 field-emission scanning electron microscope equipped with a Cobra liquid metal ion gun for focused

ion beam operation and two X-Max-80 silicon drift x-detectors (SDD) for energy dispersive X-ray (EDX) analysis. A thin lamellar was first lifted out of the bulk MMC sample and mounted onto a TEM half-grid using E-beam deposited Pt. The attached lamellar was further thinned to ~100 nm using 30 kV (voltage), 150-500 pA (current) FIB.

XRD (reflection)

The diffraction patterns were obtained using a Bruker D8 diffractometer with Cu Kα X-ray source operating at 40 kV and 40 mA and Vantec 2000 area detector.

WAXS (transmission)

Transmission SAXS and WAXS on the MMCs were collected on SAXSLab Ganesha instrument with Cu Kα X-ray source.

Raman spectroscopy

Raman spectra were obtained with a Horiba LabRamHR Evolution confocal microscope. The samples were excited using a 633 nm light source operating at 1 % of its power and using 100x long path objective and a 600 mm^{-1} grating.

XRF

XRF analysis was performed with a Rigaku NEX DE using a helium atmosphere.

XPS

XPS analysis was performed on a Kratos Axis Nova spectrometer using monochromatic Al K_α source (1486.6 eV). Ti 2p, C 1s and Mg 1s high-resolution spectra were collected using an analysis area of 0.3X0.7 mm^2 and 20 eV pass energy with the step size of 0.1 eV. Charge neutralization was performed using a co-axial, low energy (≈0.1 eV) electron flood source to avoid shifts in the recovered binding energy. See "XPS fitting" section below for details about fitting.

Deconvolution of the high-resolution XPS spectra was performed in CasaXPS software using symmetric Lorentzian-Gaussian curves and a Shirley background.

For $Ti_3C_2T_x/TMA^+$, recovered Ti_3C_2 NPLs, isotropic TiC_y NCs and recovered isotropic TiC_y NCs, Ti 2p region (Figure 5.14) consists of the two $2p_{3/2}$ and $2p_{1/2}$ spin-orbit split components. The peak area ratio of $2p_{3/2}$ to $2p_{1/2}$ was fixed to 2 to 1. The Ti 2p region was fit using 4 pairs of $2p_{3/2}$ and $2p_{1/2}$ components for each sample.

The C 1s region (Figure 5.14) was fit with five symmetric Lorentzian-Gaussian curves. Ti-C contribution was fit with the two curves in order to account for the peak asymmetry. The asymmetry is caused by the extrinsic loses due to delocalized states.

The Ti/C (here C is the carbide carbon) of the initial and recovered particles was determined as following. The survey spectra (Figure 5.13) was used to calculate the elemental ratio of Ti to total available C (including Ti-**C**, C-C, C-O and -COO). Then the C contribution was multiplied by the Ti-**C** fraction determined from the deconvolution of the high resolution XPS spectra (Table 5.2).

Rheology measurements

Rheology measurements were performed on an Anton Paar MCR 301 rheometer equipped with a Peltier temperature control system. Measurements were taken in parallel plate geometry, using a 25 mm-diameter tool. The temperature was maintained at 45 ºC.

Rheology apparatus set-up and measurement protocol

Because the samples are air sensitive, a custom-built, clear acrylic chamber with a port for introducing argon flow, was used when conducting measurements (Figure 5.30). In this inner chamber, the sample was contained in a 3D-printed cup (inner diameter 35 mm, inner height 1 cm), which was affixed to the bottom plate of the rheometer using double-sided tape. Prior to measurements, the rheometer tool zero-position check and air check were performed with the empty 3D printed cup in place, in the presence of flowing argon.

Secondary protection was provided by a glove bag (Spilfyter) covering the whole rheometer. To load the sample, the 3D-printed cup was removed from the rheometer setup and brought into a glove box where the sample was prepared and loaded into the cup. The cup was covered with Parafilm and transferred to a sealed plastic bag, which was removed from the glove box and placed inside the rheometer glove bag. The glove bag was then sealed to the rheometer frame using electrical tape. Argon was flowed into the inner acrylic chamber at an overpressure, and allowed to purge for at least 40 minutes. Using the access granted by the glove bag, the cup with the sample was removed from its container, placed into the inner acrylic chamber, uncovered, and affixed in its original position to the bottom plate.

The rheometer tool was then lowered into position. The gap was between 1.25-1.37 mm, depending on the volume of sample loaded. Because of the high surface tension of gallium, the

most reproducible measurements were obtained by filling the cup with a full layer of sample, and then resting the plate on top of this layer. To ensure the accuracy of this method, the viscosity of water was measured (at 25 ºC) as a test case and found to be within 5 % of its literature value.

Figure 5.30. Experimental set-up for the rheological measurements of liquid Ga and liquid Ga based composites under the inert atmosphere.

Oscillatory Rheology

Oscillatory measurements as a function of amplitude were taken at a frequency of 1 rad/s. The amplitude was ramped from 0.01-1000 % strain, with 5 data points per decade. The Anton Paar MCR 301's No Time Setting option was used to determine the appropriate waiting time at each measured amplitude. Replicate measurements were taken. In between measurements, the rheometer tool was raised and lowered back into position. This was found to "reset" the initial conditions and resulted in reproducible measurements, preventing memory of the prior measurements from creating drift in the data. Oscillatory measurements as a function of frequency were taken following these same steps; the amplitude was held constant at 0.05 % strain (shown to be within the linear regime from the amplitude measurement as a function of frequency), and the frequency was ramped from 100-0.015 rad/s. Due to the low bulk viscosity of liquid Ga, the rheological properties of liquid Ga are dominated by its thin oxide layer in all but the most well-

controlled inert environment.[58-59] Although Ga with and without Ti_3C_2 flakes showed $G' > G''$ for sufficiently small frequencies (Figure 5.6B), both G' and G'' for pure liquid Ga show strong frequency dependence at $\omega > 10$ rad/s (Figure 5.31). This could be attributed to the breakage of the oxide skin with $G' < G''$ at $\omega > 25$ rad/s.

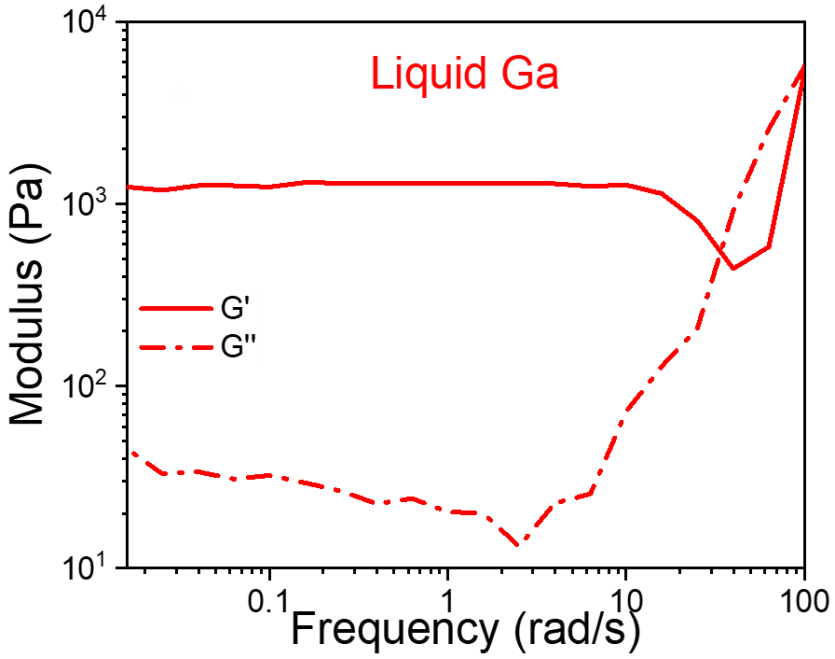

Figure 5.31. Viscoelastic property of liquid Ga measured up to 100 rad/s.
$G' < G''$ at $\omega > 25$ rad/s suggesting breakage of the Ga_2O_3 skin at higher frequencies.

Constant Shear Rheology

Following the oscillatory measurements, experiments at constant shear rate over time were conducted. Individual measurements at a given shear rate were conducted for 3000 seconds, with data taken every 0.1 seconds. These measurements were conducted at the following shear rates (1/s): 0.01, 0.1, 1, 10, 50 100. The Ar protection allowed Ga to have a consistently low shear stress of < 50 Pa. The steady shear measurement performed on Ga liquid metal without Ar gas protection showed a continuous rise in the shear stress which is consistent with the metal's progressive oxidation (Figure 5.32).

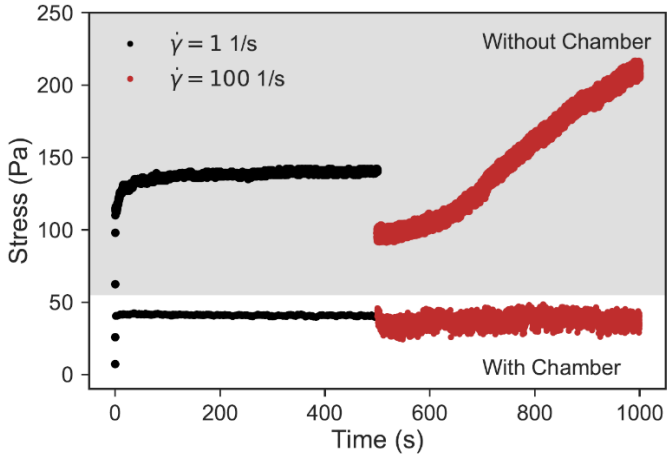

Figure 5.32. Steady shear measurement performed on liquid Ga with and without a chamber filled with Ar gas.

Estimation of the vdW potential in liquid metals

For spherical particles of radius *R*, the vdW potential is calculated using the Hamaker hybrid form:

$$V_{VdW}(l) = -\frac{A}{6}\left(\frac{2R^2}{(4R+l)l} + \frac{2R^2}{(2R+l)^2} + \ln\left(\frac{(4R+l)l}{(2R+l)^2}\right)\right) \quad (1)$$

The Hamaker coefficient (*A*) is defined by the medium's and interacting particles' dielectric functions:

$$A = \frac{3}{2}k_bT\sum_{q=1}^{\infty}\frac{1}{q^3}\sum_{n=0}^{\infty}{}'\left[\Delta(i\omega_n)\right]^{2q} \quad (2)$$

$$\Delta(i\omega_n) = \frac{\varepsilon_1(i\omega_n) - \varepsilon_3(i\omega_n)}{\varepsilon_1(i\omega_n) + \varepsilon_3(i\omega_n)} \quad (3)$$

Here *T* is temperature (in K) and k_b is the Boltzmann constant; ε_1 and ε_3 are the complex dielectric functions of particles (MXenes) and medium (liquid metal) respectively evaluated at imaginary Matsubara frequencies, $\omega_n = n \cdot 2\pi k_bT/\hbar$. The subscript (') in the second sum in eq. 2 indicates

that the zero frequency ($n = 0$) term has contribution of ½. However, since liquid metals are infinitely polarizable media, the zero frequency term (equivalent to the electrostatic interaction) is screened as $e^{-\frac{l}{l_d}}$. Hence, we can ignore the $n = 0$ term contribution to the Hamaker coefficient in eq. 2.

The liquid metal dielectric function is described with the Drude free-electron model whose parameters are readily available in the literature (parameters are given in Table 5.6):[60]

$$\varepsilon_3(i\omega_n) = 1 + \frac{\omega_{p3}^2}{\omega_n^2 + \gamma_3\omega_n} \tag{4}$$

Table 5.6. Drude parameters for the dielectric function of liquid Ga.

ω_{p3}(eV)	γ_3 (eV)
15.57	1.01

As for $Ti_3C_2T_x$, we base our calculations on the ellipsometric data available in the Supporting Information of Dillon *et al.*[30] The complex dielectric function presented in this reference is fitted using a combination of the Drude-like function and Lorentz harmonic oscillators. Following the conventions of the fit, the imaginary part of the dielectric function of $Ti_3C_2T_x$ is defined as (parameters are given in Table 5.7):

$$\varepsilon''(\omega_R) = \frac{\omega_R}{\varepsilon_0\rho\left(\tau^2\omega_R^4 + \omega_R^2\right)} + \sum_{j=1}^{2}\frac{\omega_R f_j\Gamma_j + g_j\Gamma_j\omega_j(\omega_j^2 - \omega_R^2)}{\left(\omega_j^2 - \omega_R^2\right) + \omega_R^2\Gamma_j^2} \tag{5}$$

This function is transformed into ε_1 using the Kramers-Kronig relation:

$$\varepsilon_1(i\omega_n) = 1 + \frac{2}{\pi}\int_0^\infty d\omega_R \frac{\omega_R\varepsilon''(\omega_R)}{\omega_R^2 + \omega_n^2} \tag{6}$$

Table 5.7. Parameters for the dielectric function of $Ti_3C_2T_x$.

Drude parameters

ρ (Ohm cm)	τ (fs)
1/9100	2.1

Lorentz parameters

f_1	g_1	Γ_1 (eV)	ω_1 (eV)	f_2	g_2	Γ_2 (eV)	ω_2 (eV)
7.1	1.1	0.61	1.5	14	-0.69	5.6	6.3

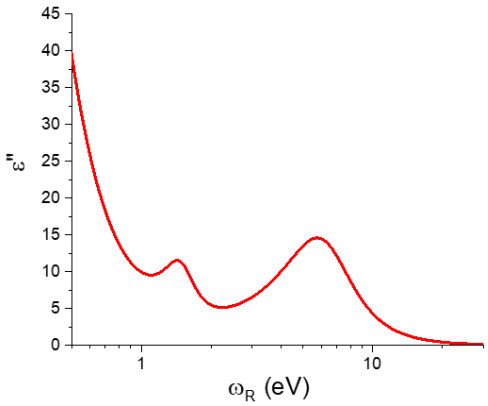

Figure 5.33. ε" of $Ti_3C_2T_x$ used for the evaluation of the Hamaker coefficient.

For $TiC_{0.9}$ NCs, the Hamaker coefficient calculations are based on the ellipsometric data of Koide et al.[61] The real and imaginary part of the dielectric function presented in this references were fit using Drude-like function and 3 Lorentz harmonic oscillators (Table 5.8).

Table 5.8. Parameters for the dielectric function of $TiC_{0.9}$ NCs.

Drude parameters

ω_p(eV)	γ(eV)
6.21	1.13

Lorentz parameters

f_1 (eV)	Γ_1 (eV)	ω_1 (eV)	f_2 (eV)	Γ_2 (eV)	ω_2 (eV)	f_3 (eV)	Γ_3 (eV)	ω_3 (eV)
8.07	3.04	5.81	13.36	5.28	3.47	13.95	6.18	14.44

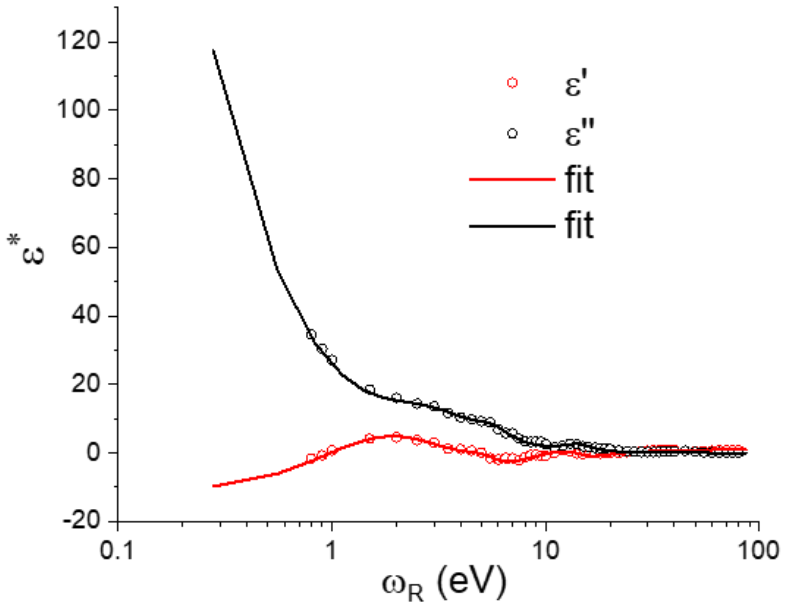

Figure 5.34. *ε”* and *ε’* and the corresponding fits of $TiC_{0.9}$ NCs used for the evaluation of the Hamaker coefficient.

Table 5.1 summarizes calculated Hamaker coefficients (q_{max}=30 and n_{max}=20000) for the three systems of interest (at 973 K): $Ti_3C_2T_x$ interacting through vacuum, Ga interacting through vacuum and $Ti_3C_2T_x$ interacting through Ga. The Hamaker coefficient for $TiC_{0.9}$ NCs interacting through liquid Ga is 39.1 zJ.

The q=1 term in the summation in Eq. (2) dominates the Hamaker coefficient. Hence it is instructive to plot $\left[\Delta(i\omega_n)\right]^2$ (Eq.(3)) as a function of ω_n to determine at which frequency range the electromagnetic fluctuations have the greatest contribution to the Hamaker coefficient. Figure 5.35 shows that the finite frequency fluctuation forces are easily dominated by the action in the UV region for Ga-vac-Ga and $Ti_3C_2T_x$-vac-$Ti_3C_2T_x$ systems. However, in case of $Ti_3C_2T_x$-Ga-$Ti_3C_2T_x$ system the IR and visible regions have significant contribution to $\left[\Delta(i\omega_n)\right]^2$. The presence of the deep around 6.86 eV accounts for the reduction of the Hamaker coefficient for $Ti_3C_2T_x$ in Ga compared to that of $Ti_3C_2T_x$ in vacuum.

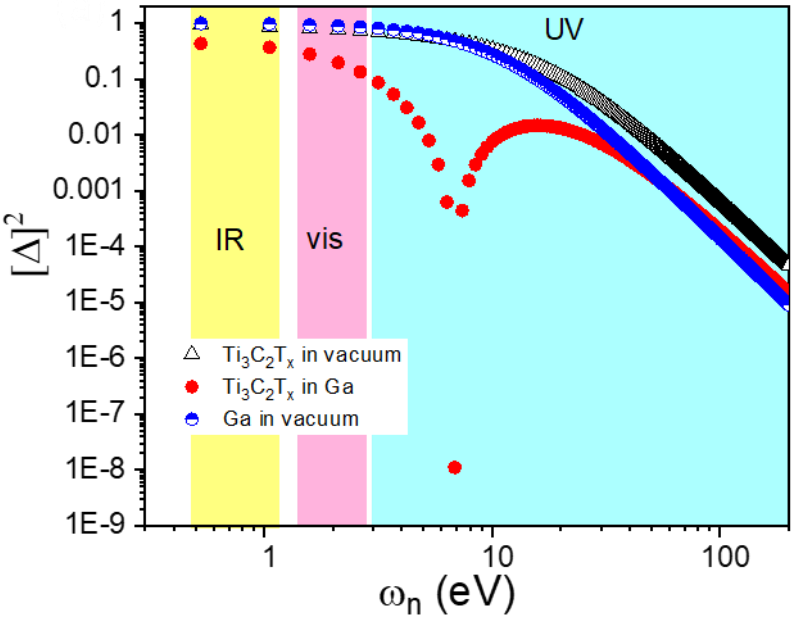

Figure 5.35. Delta function defined in Eq. (3).

5.8 Chapter 5 bibliography.

1. Kamysbayev, V.; James, N. M.; Filatov, A. S.; Srivastava, V.; Anasori, B.; Jaeger, H. M.; Gogotsi, Y.; Talapin, D. V., Colloidal Gelation in Liquid Metals Enables Functional Nanocomposites of 2D Metal Carbides (MXenes) and Lightweight Metals. *ACS Nano* **2019,** *13* (11), 12415-12424.

2. Casati, R.; Vedani, M., Metal Matrix Composites Reinforced by Nano-Particles—A Review. *Metals* **2014,** *4* (1), 65.

3. Kollo, L.; Leparoux, M.; Bradbury, C. R.; Jäggi, C.; Carreño-Morelli, E.; Rodríguez-Arbaizar, M., Investigation of planetary milling for nano-silicon carbide reinforced aluminium metal matrix composites. *J. Alloys Compd.* **2010,** *489* (2), 394-400.

4. Thakur, S. K.; Srivatsan, T. S.; Gupta, M., Synthesis and mechanical behavior of carbon nanotube–magnesium composites hybridized with nanoparticles of alumina. *Materials Science and Engineering: A* **2007,** *466* (1), 32-37.

5. Nieto, A.; Bisht, A.; Lahiri, D.; Zhang, C.; Agarwal, A., Graphene reinforced metal and ceramic matrix composites: a review. *Int. Mater. Rev.* **2017,** *62* (5), 241-302.

6. Esawi, A. M. K.; Morsi, K.; Sayed, A.; Gawad, A. A.; Borah, P., Fabrication and properties of dispersed carbon nanotube–aluminum composites. *Materials Science and Engineering: A* **2009,** *508* (1), 167-173.

7. Chen, L.-Y.; Xu, J.-Q.; Choi, H.; Pozuelo, M.; Ma, X.; Bhowmick, S.; Yang, J.-M.; Mathaudhu, S.; Li, X.-C., Processing and properties of magnesium containing a dense uniform dispersion of nanoparticles. *Nature* **2015,** *528*, 539.

8. Kok, M., Production and mechanical properties of Al2O3 particle-reinforced 2024 aluminium alloy composites. *J. Mater. Process. Technol.* **2005,** *161* (3), 381-387.

9. Dorri Moghadam, A.; Omrani, E.; Menezes, P. L.; Rohatgi, P. K., Mechanical and tribological properties of self-lubricating metal matrix nanocomposites reinforced by carbon nanotubes (CNTs) and graphene – A review. *Composites Part B: Engineering* **2015,** *77*, 402-420.

10. Cook, W. H. *Corrosion reisistance of various ceramics and cermets to liquid metals*; Oak Ridge National Lab: Oak Ridge, TN, 1960.

11. Wu, R.; Yan, Y.; Wang, G.; Murr, L. E.; Han, W.; Zhang, Z.; Zhang, M., Recent progress in magnesium–lithium alloys. *Int. Mater. Rev.* **2015,** *60* (2), 65-100.

12. Lipatov, A.; Lu, H.; Alhabeb, M.; Anasori, B.; Gruverman, A.; Gogotsi, Y.; Sinitskii, A., Elastic properties of 2D Ti₃C₂T_x MXene monolayers and bilayers. *Science Advances* **2018,** *4* (6), eaat0491.

13. Borysiuk, V. N.; Mochalin, V. N.; Gogotsi, Y., Bending rigidity of two-dimensional titanium carbide (MXene) nanoribbons: A molecular dynamics study. *Computational Materials Science* **2018,** *143*, 418-424.

14. Nicklow, R.; Wakabayashi, N.; Smith, H. G., Lattice Dynamics of Pyrolytic Graphite. *Phys. Rev. B* **1972,** *5* (12), 4951-4962.

15. Xu, W.; Birbilis, N.; Sha, G.; Wang, Y.; Daniels, J. E.; Xiao, Y.; Ferry, M., A high-specific-strength and corrosion-resistant magnesium alloy. *Nat. Mater.* **2015,** *14*, 1229.

16. Alhabeb, M.; Maleski, K.; Anasori, B.; Lelyukh, P.; Clark, L.; Sin, S.; Gogotsi, Y., Guidelines for Synthesis and Processing of Two-Dimensional Titanium Carbide (Ti3C2Tx MXene). *Chem. Mater.* **2017,** *29* (18), 7633-7644.

17. Wang, Z.; Xuan, J.; Zhao, Z.; Li, Q.; Geng, F., Versatile Cutting Method for Producing Fluorescent Ultrasmall MXene Sheets. *ACS Nano* **2017,** *11* (11), 11559-11565.

18. Seredych, M.; Shuck, C. E.; Pinto, D.; Alhabeb, M.; Precetti, E.; Deysher, G.; Anasori, B.; Kurra, N.; Gogotsi, Y., High-Temperature Behavior and Surface Chemistry of Carbide MXenes Studied by Thermal Analysis. *Chem. Mater.* **2019**.

19. Ibrahim, I. A.; Mohamed, F. A.; Lavernia, E. J., Particulate reinforced metal matrix composites — a review. *Journal of Materials Science* **1991,** *26* (5), 1137-1156.

20. Daeneke, T.; Khoshmanesh, K.; Mahmood, N.; de Castro, I. A.; Esrafilzadeh, D.; Barrow, S. J.; Dickey, M. D.; Kalantar-zadeh, K., Liquid metals: fundamentals and applications in chemistry. *Chem. Soc. Rev.* **2018,** *47* (11), 4073-4111.

21. Dezellus, O.; Eustathopoulos, N., Fundamental issues of reactive wetting by liquid metals. *Journal of Materials Science* **2010,** *45* (16), 4256-4264.

22. Dudiy, S. V.; Lundqvist, B. I., Wetting of TiC and TiN by metals. *Phys. Rev. B* **2004,** *69* (12), 125421.

23. Israelachvili, J. N., *Intermolecular and surface forces*. Academic press: London, 2011.

24. Kamysbayev, V.; Srivastava, V.; Ludwig, N. B.; Borkiewicz, O. J.; Zhang, H.; Ilavsky, J.; Lee, B.; Chapman, K. W.; Vaikuntanathan, S.; Talapin, D. V., Nanocrystals in Molten Salts and Ionic Liquids: Experimental Observation of Ionic Correlations Extending beyond the Debye Length. *ACS Nano* **2019**.

25. Oh, S. H.; Kauffmann, Y.; Scheu, C.; Kaplan, W. D.; Rühle, M., Ordered Liquid Aluminum at the Interface with Sapphire. *Science* **2005,** *310* (5748), 661-663.

26. Reichert, H.; Klein, O.; Dosch, H.; Denk, M.; Honkimäki, V.; Lippmann, T.; Reiter, G., Observation of five-fold local symmetry in liquid lead. *Nature* **2000,** *408* (6814), 839-841.

27. Huisman, W. J.; Peters, J. F.; Zwanenburg, M. J.; de Vries, S. A.; Derry, T. E.; Abernathy, D.; van der Veen, J. F., Layering of a liquid metal in contact with a hard wall. *Nature* **1997,** *390* (6658), 379-381.

28. Zhang, H.; Dasbiswas, K.; Ludwig, N. B.; Han, G.; Lee, B.; Vaikuntanathan, S.; Talapin, D. V., Stable colloids in molten inorganic salts. *Nature* **2017,** *542*, 328.

29. Parsegian, V. A., *Van der Waals Forces: A Handbook for Biologists, Chemists, Engineers, and Physicists*. Cambridge University Press: Cambridge, 2005.

30. Dillon, A. D.; Ghidiu, M. J.; Krick, A. L.; Griggs, J.; May, S. J.; Gogotsi, Y.; Barsoum, M. W.; Fafarman, A. T., Highly Conductive Optical Quality Solution-Processed Films of 2D Titanium Carbide. *Adv. Funct. Mater.* **2016,** *26* (23), 4162-4168.

31. Xu, J. Q.; Chen, L. Y.; Choi, H.; Li, X. C., Theoretical study and pathways for nanoparticle capture during solidification of metal melt. *J. Phys.: Condens. Matter* **2012,** *24* (25), 255304.

32. Berdiyorov, G. R., Optical properties of functionalized Ti3C2T2 (T = F, O, OH) MXene: First-principles calculations. *AIP Advances* **2016,** *6* (5), 055105.

33. Trappe, V.; Prasad, V.; Cipelletti, L.; Segre, P. N.; Weitz, D. A., Jamming phase diagram for attractive particles. *Nature* **2001,** *411*, 772.

34. Eberle, A. P. R.; Wagner, N. J.; Castañeda-Priego, R., Dynamical Arrest Transition in Nanoparticle Dispersions with Short-Range Interactions. *Phys. Rev. Lett.* **2011,** *106* (10), 105704.

35. Tsurusawa, H.; Leocmach, M.; Russo, J.; Tanaka, H., Direct link between mechanical stability in gels and percolation of isostatic particles. *Science Advances* **2019,** *5* (5), eaav6090.

36. Keene, B. J., Review of data for the surface tension of pure metals. *Int. Mater. Rev.* **1993,** *38* (4), 157-192.

37. Mason, T. G.; Weitz, D. A., Linear Viscoelasticity of Colloidal Hard Sphere Suspensions near the Glass Transition. *Phys. Rev. Lett.* **1995,** *75* (14), 2770-2773.

38. Gisler, T.; Ball, R. C.; Weitz, D. A., Strain Hardening of Fractal Colloidal Gels. *Phys. Rev. Lett.* **1999,** *82* (5), 1064-1067.

39. Moller, P.; Fall, A.; Chikkadi, V.; Derks, D.; Bonn, D., An attempt to categorize yield stress fluid behaviour. *Philosophical Transactions of the Royal Society A: Mathematical, Physical and Engineering Sciences* **2009,** *367* (1909), 5139-5155.

40. Fan, Z., Semisolid metal processing. *Int. Mater. Rev.* **2002,** *47* (2), 49-85.

41. Chen, W.; Thornley, L.; Coe, H. G.; Tonneslan, S. J.; Vericella, J. J.; Zhu, C.; Duoss, E. B.; Hunt, R. M.; Wight, M. J.; Apelian, D.; Pascall, A. J.; Kuntz, J. D.; Spadaccini, C. M., Direct metal writing: Controlling the rheology through microstructure. *Appl. Phys. Lett.* **2017,** *110* (9), 094104.

42. Sang, X.; Xie, Y.; Yilmaz, D. E.; Lotfi, R.; Alhabeb, M.; Ostadhossein, A.; Anasori, B.; Sun, W.; Li, X.; Xiao, K.; Kent, P. R. C.; van Duin, A. C. T.; Gogotsi, Y.; Unocic, R. R., In situ atomistic insight into the growth mechanisms of single layer 2D transition metal carbides. *Nat. Commun.* **2018,** *9* (1), 2266.

43. Ghidiu, M.; Barsoum, M. W., The {110} reflection in X-ray diffraction of MXene films: Misinterpretation and measurement via non-standard orientation. *J. Am. Ceram. Soc.* **2017,** *100* (12), 5395-5399.

44. Tang, S.; Xin, T.; Xu, W.; Miskovic, D.; Sha, G.; Quadir, Z.; Ringer, S.; Nomoto, K.; Birbilis, N.; Ferry, M., Precipitation strengthening in an ultralight magnesium alloy. *Nat. Commun.* **2019,** *10* (1), 1003.

45. Aroyo Mois, I.; Perez-Mato Juan, M.; Capillas, C.; Kroumova, E.; Ivantchev, S.; Madariaga, G.; Kirov, A.; Wondratschek, H., Bilbao Crystallographic Server: I. Databases and crystallographic computing programs. In *Zeitschrift für Kristallographie - Crystalline Materials*, 2006; Vol. 221, p 15.

46. Fu, Z. H.; Zhang, Q. F.; Legut, D.; Si, C.; Germann, T. C.; Lookman, T.; Du, S. Y.; Francisco, J. S.; Zhang, R. F., Stabilization and strengthening effects of functional groups in two-dimensional titanium carbide. *Phys. Rev. B* **2016,** *94* (10), 104103.

47. Bauer, E.; van der Merwe, J. H., Structure and growth of crystalline superlattices: From monolayer to superlattice. *Phys. Rev. B* **1986,** *33* (6), 3657-3671.

48. Yu, Z.; Tang, A.; Wang, Q.; Gao, Z.; He, J.; She, J.; Song, K.; Pan, F., High strength and superior ductility of an ultra-fine grained magnesium–manganese alloy. *Materials Science and Engineering: A* **2015,** *648*, 202-207.

49. Kawamori, S.; Machida, T., Microstructure and Mechanical Properties of Alumina-Dispersed Magnesium Fabricated Using Mechanical Alloying Method. *MATERIALS TRANSACTIONS* **2007,** *48* (3), 373-379.

50. Siegel, D. J.; Hector, L. G.; Adams, J. B., Ab initio study of Al-ceramic interfacial adhesion. *Phys. Rev. B* **2003,** *67* (9), 092105.

51. Bianchi, E.; Largo, J.; Tartaglia, P.; Zaccarelli, E.; Sciortino, F., Phase Diagram of Patchy Colloids: Towards Empty Liquids. *Phys. Rev. Lett.* **2006,** *97* (16), 168301.

52. Anasori, B.; Caspi, E. a. N.; Barsoum, M. W., Fabrication and mechanical properties of pressureless melt infiltrated magnesium alloy composites reinforced with TiC and Ti2AlC particles. *Materials Science and Engineering: A* **2014,** *618*, 511-522.

53. Zhou, J.; Zha, X.; Chen, F. Y.; Ye, Q.; Eklund, P.; Du, S.; Huang, Q., A Two-Dimensional Zirconium Carbide by Selective Etching of Al3C3 from Nanolaminated Zr3Al3C5. *Angew. Chem.* **2016,** *128* (16), 5092-5097.

54. Sarycheva, A.; Polemi, A.; Liu, Y.; Dandekar, K.; Anasori, B.; Gogotsi, Y., 2D titanium carbide (MXene) for wireless communication. *Science Advances* **2018,** *4* (9), eaau0920.

55. Wang, Q.-W.; Zhang, H.-B.; Liu, J.; Zhao, S.; Xie, X.; Liu, L.; Yang, R.; Koratkar, N.; Yu, Z.-Z., Multifunctional and Water-Resistant MXene-Decorated Polyester Textiles with Outstanding Electromagnetic Interference Shielding and Joule Heating Performances. *Adv. Funct. Mater.* **2019,** *29* (7), 1806819.

56. Xia, Y.; Mathis, T. S.; Zhao, M.-Q.; Anasori, B.; Dang, A.; Zhou, Z.; Cho, H.; Gogotsi, Y.; Yang, S., Thickness-independent capacitance of vertically aligned liquid-crystalline MXenes. *Nature* **2018,** *557* (7705), 409-412.

57. Toby, B. H.; Von Dreele, R. B., GSAS-II: the genesis of a modern open-source all purpose crystallography software package. *J. Appl. Crystallogr.* **2013,** *46* (2), 544-549.

58. Liu, T.; Sen, P.; Kim, C. J., Characterization of Nontoxic Liquid-Metal Alloy Galinstan for Applications in Microdevices. *Journal of Microelectromechanical Systems* **2012,** *21* (2), 443-450.

59. Xu, Q.; Oudalov, N.; Guo, Q.; Jaeger, H. M.; Brown, E., Effect of oxidation on the mechanical properties of liquid gallium and eutectic gallium-indium. *Phys. Fluids* **2012,** *24* (6), 063101.

60. Morales, D.; Stoute, N. A.; Yu, Z.; Aspnes, D. E.; Dickey, M. D., Liquid gallium and the eutectic gallium indium (EGaIn) alloy: Dielectric functions from 1.24 to 3.1 eV by electrochemical reduction of surface oxides. *Appl. Phys. Lett.* **2016,** *109* (9), 091905.

61. Koide, T.; Shidara, T.; Fukutani, H.; Fujimori, A.; Otani, S.; Ishizawa, Y., Optical Constants of TiC0.95, VC0.86and NbC0.93from 0.8 to 80 eV. *Jpn. J. Appl. Phys.* **1993,** *32* (Part 1, No. 3A), 1130-1134.